

ALMA MATER STUDIORUM  
UNIVERSITÀ DEGLI STUDI DI BOLOGNA

---

---

Dipartimento di Fisica e Astronomia

DOTTORATO DI RICERCA IN  
ASTROFISICA

Ciclo XXX

Tesi di Dottorato

STAR FORMATION HISTORIES IN THE NEARBY UNIVERSE:  
THE HST LEGACY

**Presentata da: Elena Sacchi**

**Coordinatore Dottorato:  
Francesco Rosario Ferraro**

**Supervisore:  
Monica Tosi**

**Co-supervisore:  
Michele Cignoni**

Esame finale anno 2018

---

---

Settore Concorsuale: 02/C1 – Astronomia, Astrofisica, Fisica della Terra e dei Pianeti  
Settore Scientifico Disciplinare: FIS/05 – Astronomia e Astrofisica



*“Stars are beautiful, but they may not take an active part in anything, they must just look on for ever. It is a punishment put on them for something they did so long ago that no star now knows what it was. So the older ones have become glassy-eyed and seldom speak (winking is the star language), but the little ones still wonder.”*

Sir James Matthew Barrie, *Peter Pan*



# ABSTRACT

---

This thesis has been devoted to a research project selected and funded by INAF (the Italian National Institute for Astrophysics) within the framework of the formal agreement between INAF and the Bologna University for the PhD program in Astrophysics.

The aim of the project is to study star-forming galaxies in the local Universe, and in particular the distribution of their stellar populations and their star formation histories, to understand how the clustering of star formation evolves both in space and time.

The data I analyzed have been acquired with the Hubble Space Telescope (*HST*), whose spatial resolution and sensitivity allow to measure individual stars with the highest possible accuracy even in crowded and relatively distant galaxies. Thanks to its exquisite performances, *HST* is still the most powerful facility for this kind of studies.

The method I used to derive the star formation histories of the examined galaxies is based on the color-magnitude diagram (CMD), one of the best information desks on the evolution of a galaxy or stellar system. More specifically, I applied to the observational color-magnitude diagrams the synthetic CMD technique, a reliable tool to explore the detailed star formation history of nearby galaxies and refine stellar evolution models by comparing them with the data. This method was implemented in the code SFERA, which I have contributed to improve and that will be extensively described in this thesis.

Within this framework, I discuss the results obtained for three galaxies of different morphological type which have been targeted by the *HST* Treasury program LEGUS (Legacy ExtraGalactic Ultraviolet Survey), a large international collaboration whose aim is to investigate and connect the different scales of star formation, from young stellar clusters to local Universe galaxies. The galaxies I analyze are DDO 68, a dwarf irregular, NGC 4449, a Magellanic irregular, and NGC 7793, a flocculent spiral, which were studied both in the UV and optical bands, in order to recover their star formation histories from very recent to older epochs and to understand whether and how the star formation process may depend on the morphological, dynamical and environmental properties of the galaxies.



# CONTENTS

---

<b>Abstract</b>	<b>v</b>
<b>List of Abbreviations</b>	<b>ix</b>
<b>1 Introduction</b>	<b>1</b>
1.1 The context: galaxies in the local Universe . . . . .	1
1.2 Star Formation Histories of nearby galaxies . . . . .	4
1.3 A new survey: LEGUS . . . . .	11
<b>2 From theory to practice</b>	<b>13</b>
2.1 The Color-Magnitude Diagram and its power . . . . .	13
2.1.1 Age indicators on a CMD . . . . .	16
2.1.2 Optical versus UV . . . . .	18
2.2 The synthetic CMD method: strengths and uncertainties . . . . .	21
2.2.1 How to build a synthetic CMD: the SFERA approach . . . . .	21
2.2.2 Comparing models and data . . . . .	22
2.2.3 All kinds of uncertainties . . . . .	23
2.3 Matching the two worlds: SFERA . . . . .	30
2.3.1 Time resolution tests . . . . .	31
<b>3 The dwarf: DDO 68</b>	<b>35</b>
3.1 Observations and Data Reduction . . . . .	38
3.2 Incompleteness and Errors . . . . .	40
3.3 The Color-Magnitude Diagram . . . . .	42
3.4 Distance Determination . . . . .	45
3.5 Stellar populations in DDO 68 . . . . .	47
3.5.1 Spatial distribution . . . . .	47
3.5.2 H II regions . . . . .	49
3.6 Star Formation History . . . . .	51
3.6.1 Basis Functions . . . . .	51
3.6.2 REGION 1 . . . . .	53
3.6.3 REGION 2 . . . . .	54
3.6.4 REGION 3 . . . . .	57
3.6.5 REGION 4 . . . . .	57
3.6.6 DDO 68 B . . . . .	59
3.7 A Flea with Smaller Fleas than on Him Prey . . . . .	61
3.7.1 Physical properties of the substructures . . . . .	63
3.7.2 Dynamics of DDO 68 . . . . .	64
3.8 Discussion . . . . .	66

<b>4</b>	<b>The starburst: NGC 4449</b>	<b>69</b>
4.1	Observations and Data . . . . .	70
4.2	Artificial Star Tests . . . . .	72
4.3	Distribution of the stellar populations . . . . .	74
4.4	The UV perspective . . . . .	77
4.5	Star Formation History . . . . .	80
4.5.1	Whole galaxy . . . . .	80
4.5.2	Central fields . . . . .	86
4.5.3	External fields . . . . .	91
4.6	Results . . . . .	98
4.7	Discussion . . . . .	100
<b>5</b>	<b>The spiral: NGC 7793</b>	<b>103</b>
5.1	Observations and Data . . . . .	104
5.2	Distribution of the stellar populations . . . . .	107
5.3	Distribution of dust . . . . .	110
5.4	Star Formation History . . . . .	112
5.4.1	Inner region . . . . .	112
5.4.2	Middle region . . . . .	113
5.4.3	Outer region . . . . .	113
5.5	Discussion . . . . .	117
<b>6</b>	<b>A picture of Star Formation in nearby Galaxies</b>	<b>121</b>
6.1	Three different galaxies: a comparative study . . . . .	123
6.2	The Schmidt-Kennicutt law . . . . .	127
6.3	The Role of Interaction . . . . .	132
<b>7</b>	<b>Concluding remarks</b>	<b>135</b>
	<b>Acknowledgements</b>	<b>137</b>
	<b>Bibliography</b>	<b>141</b>

# LIST OF ABBREVIATIONS

---

<b>ACS</b>	Advanced Camera for Surveys
<b>AGB</b>	Asymptotic Giant Branch
<b>ALMA</b>	Atacama Large Millimeter Array
<b>ANGST</b>	ACS Nearby Galaxy Survey Treasury
<b>AST</b>	Artificial Star Test
<b>BCD</b>	Blue Compact Dwarf
<b>BF</b>	Basis Function
<b>BL</b>	Blue Loop
<b>BSG</b>	Blue SuperGiant
<b>CMD</b>	Color-Magnitude Diagram
<b>CMF</b>	Cumulative Mass Fraction
<b>CTE</b>	Charge Transfer Efficiency
<b>dE</b>	dwarf Elliptical
<b>dIrr</b>	dwarf Irregular
<b>DM</b>	Distance Modulus
<b>dSph</b>	dwarf Spheroidal
<b>dTrans</b>	dwarf Transition type
<b>FoV</b>	Field of View
<b>GMC</b>	Giant Molecular Cloud
<b>H-R</b>	Hertzsprung-Russell
<b>HB</b>	Horizontal Branch
<b>HST</b>	Hubble Space Telescope
<b>IMF</b>	Initial Mass Function
<b>ISM</b>	InterStellar Medium
<b>LBC</b>	Large Binocular Camera
<b>LBT</b>	Large Binocular Telescope
<b>LCID</b>	Local Cosmology from Isolated Dwarfs
<b>LEGUS</b>	Legacy ExtraGalactic UV Survey
<b>LF</b>	Luminosity Function
<b>LG</b>	Local Group
<b>LMC</b>	Large Magellanic Cloud
<b>MS</b>	Main Sequence
<b>MSTO</b>	Main Sequence Turn Off
<b>MW</b>	Milky Way
<b>NNLS</b>	Non-Negative Least-Square
<b>PSF</b>	Point Spread Function
<b>RC</b>	Red Clump
<b>RGB</b>	Red Giant Branch
<b>S/N</b>	Signal-to-Noise

<b>SC</b>	Stellar Cluster
<b>SED</b>	Spectral Energy Distribution
<b>SF</b>	Star Formation
<b>SFE</b>	Star Formation Efficiency
<b>SFERA</b>	Star Formation Evolution Recovery Algorithm
<b>SFH</b>	Star Formation History
<b>SFR</b>	Star Formation Rate
<b>SGB</b>	SubGiant Branch
<b>SK</b>	Schmidt-Kennicutt
<b>SMC</b>	Small Magellanic Cloud
<b>TP-AGB</b>	Thermally Pulsing Asymptotic Giant Branch
<b>TRGB</b>	Tip of the Red Giant Branch
<b>uFd</b>	ultraFaint dwarf
<b>UVIS</b>	UV/VISible channel
<b>VLA</b>	Very Large Array
<b>WFC</b>	Wide-Field Channel
<b>WFC3</b>	Wide-Field Camera 3
<b>WFPC2</b>	Wide-Field Planetary Camera 2
<b>WR</b>	Wolf-Rayet
<b>ZAMS</b>	Zero Age Main Sequence

*Dedicated to my parents and my sister, there for me, always and ever.  
Ai miei genitori e mia sorella, che ci sono e ci saranno per me, sempre.*



# 1. INTRODUCTION

---

## 1.1 The context: galaxies in the local Universe

The local Universe is characterized by a great variety of galaxies and galactic environments. Within the Local Group (LG), we find spirals, Andromeda and the Milky Way (MW) being the biggest ones, their numerous satellites, mainly dwarf spheroidal (dSph), dwarf irregular (dIrr) and ultrafaint dwarf (uFd) galaxies, and several other dwarfs, apparently not connected to larger systems. Going beyond, within a few tens of Mpc from the Milky Way, we find entirely new classes of very interesting galaxies, such as radio galaxies and Seyferts, those with the lowest star formation activity (early-type ellipticals), and those with the highest one (starburst late-type galaxies), including dwarfs as the blue compact dwarfs (BCDs), very active star-forming galaxies characterized by high gas contents and very low metallicities.

Among all these morphological types, dwarf galaxies are the most common but probably least understood objects when we consider their formation and evolution. As for elliptical and spiral galaxies, we can divide dwarfs on the basis of their activity and gas content in early-type, i.e. dSphs and dwarf ellipticals (dEs), and late-type, including dIrrs and BCDs; the uFd class is still poorly defined, because of the low number of these galaxies found so far and of their properties, compatible with those of both low luminosity dwarf galaxies and faint diffuse globular clusters. Even in the comparison among dwarfs of the same class, we find a wide range of chemical, dynamical and star formation (SF) properties, and the evolutionary processes taking place in these systems are still highly debated, as much as the definition of dwarf galaxy itself. Tolstoy, Hill, and Tosi (2009) review the main characteristics of dwarf galaxies in the Local Group, investigating possible connections and correlations among their different properties. In particular, despite the differences, they suggest an evolutionary sequence connecting early-type and late-type dwarfs, though strongly affected by environmental effects. Indeed, if we look at how some structural parameters are related in different kinds of galaxies, such as half-light radius ( $r_e$ ), surface brightness ( $\mu_e$ ) and absolute magnitude ( $M_V$ ), we find a rather continuous distribution from early- to late-type galaxies (Kormendy and Bender, 2012). Figure 1.1 shows this parameter correlations for spheroidal and late-type galaxies, confirming their close connection. However, a deep understanding of this relation is still lacking, as well as a clear evolutionary process linking the different types of galaxies.

A crucial information to understand galaxy formation and evolution is the star formation history (SFH), which is the result of gas consumption, chemical enrichment and interaction processes experienced by a galaxy. For nearby galaxies, we have the great advantage of resolving their stellar populations, so that we are able to

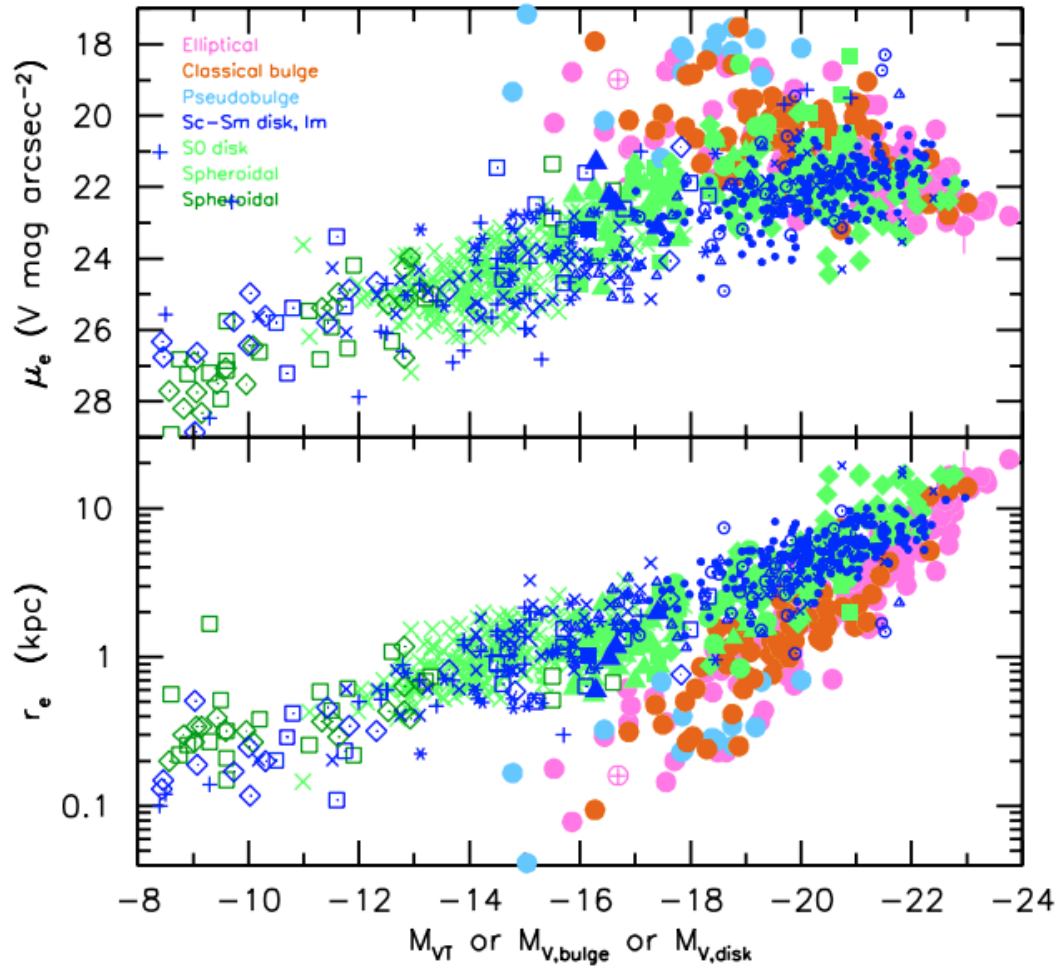


FIGURE 1.1: Relations among structural properties of different kinds of galaxies. *Top panel.* Surface brightness  $\mu_e$  at the effective radius versus absolute magnitude  $M_V$ . *Bottom panel.* Effective radius  $r_e$  versus absolute magnitude. Different galaxy types are marked with different colors: ellipticals (pink), classical bulges (light brown), pseudo-bulges (light blue), spiral disks and irregulars (blue), and spheroidals (green). See Figure 20 of Kormendy and Bender (2012) for more details.

perform spatially resolved studies revealing the variations of their SFH as a function of position, population and metallicity gradients, formation and merger history. Most galaxies show these variations, with old populations being found everywhere whereas the young ones are usually more centrally concentrated or confined to disks and spiral arms.

From a cosmological point of view, the hierarchical formation scenario suggests that big galaxies form through continuous merging and accretion of smaller building blocks. As a consequence, present-day dwarfs may have been sites of the earliest star formation activity in the Universe. On the other hand, given their high gas content and very blue integrated colors, indicative of the prevalence of young stellar populations, the most metal-poor ( $12 + \log(O/H) \lesssim 7.6$ , corresponding to  $Z \lesssim 1/15 Z_{\odot}$ <sup>1</sup>) dwarf irregular and blue compact dwarf galaxies have been often suggested to be “primeval” galaxies, experiencing their first burst of star formation, with ages  $\lesssim 100 - 500$  Myr (Izotov and Thuan, 1999; Pustilnik, Kniazev, and Pramskij, 2005; Pustilnik, Tepliakova, and Kniazev, 2008). However, all dIrr/BCD galaxies resolved and studied so far with the Hubble Space Telescope (*HST*) have been found to harbor stars as old as the look-back time sampled by the depth of the photometry, i.e.  $\sim 1$  Gyr and older (Tolstoy et al., 1998; Schulte-Ladbeck et al., 2002; Izotov and Thuan, 2002; Tosi, 2009; Tolstoy, Hill, and Tosi, 2009). The significance of such studies is clearly illustrated in the long-standing controversial case of I Zw 18, one of the most metal-poor star forming dwarfs and the prototype of the BCD class with  $12 + \log(O/H) = 7.2$  (Skillman and Kennicutt, 1993). Imaging with the Advanced Camera for Surveys (ACS) on board of *HST* performed by Aloisi et al. (2007) provided a deep and uncontaminated color-magnitude diagram (CMD) that indisputably demonstrated the presence of a previously uncertain red giant branch (RGB), thus ruling out its former classification as a truly primordial galaxy (Izotov and Thuan, 2004).

Over the past years, several new dIrr/BCDs with extremely low metallicities and physical properties similar to those of I Zw 18 have been discovered and controversially regarded as “genuine” young galaxies in the nearby Universe, due to a lack of detailed information on their resolved stellar population ages. One of the most recent cases is Leo P, discovered by Giovanelli et al. (2013) within the ALFALFA survey, with a metallicity from H II region spectra of  $12 + \log(O/H) = 7.17 \pm 0.04$  (Skillman et al., 2013). McQuinn et al. (2015) observed it with *HST* and indisputably found RR Lyrae stars, i.e. stars at least 10 Gyr old, from which they also inferred a robust distance estimate of  $1.62 \pm 0.15$  Mpc.

One effective way to check whether or not big galaxies are made only by successive accretions of smaller satellites is to compare the property of massive and dwarf systems. If chemical abundances, kinematics, and star formation histories of the resolved stars of massive galaxies are all consistent with those of dwarf galaxies, then the former can be the result of successive merging of the latter; otherwise, either satellite accretion is not the only channel to build up spiral and elliptical galaxies or the actual building blocks are not alike today’s dwarfs.

<sup>1</sup>Adopting  $12 + \log(O/H)_{\odot} = 8.76 \pm 0.07$  from Caffau et al. (2008).

## 1.2 Star Formation Histories of nearby galaxies

The study of nearby galaxies has been revolutionized by the Hubble Space Telescope. Its high spatial resolution allowed for the first time to resolve and measure individual stars even in the crowded fields of external galaxies and to draw their CMDs, permitting studies of stellar populations, star formation histories, and stellar clusters for galaxies out to several Mpc. The CMD of a stellar system is in fact one of the best information desks on the system evolution, because it preserves the imprinting of all the relevant evolution parameters, such as age, mass, chemical composition, initial mass function (IMF).

Deep CMDs display all the stars still alive born over the whole lifetime of a galaxy, and are indeed fossil records of the SFH. A first qualitative idea of the stellar populations in a galaxy can be obtained simply by looking at a good CMD. Different evolutionary phases trace different epochs: RR Lyrae stars are indicative of a very old population; red giant branch stars are associated with intermediate-age to old star formation activity; asymptotic giant branch (AGB) stars can span from old to intermediate and young ages; the blue, brightest stars, as well as H II regions, are evidence of very recent star formation activity.

Up to the early '90s, stellar ages were derived through isochrone fitting, a simple and effective method to determine the age and metallicity of single stellar populations such as the ones in star clusters, but inadequate to interpret the multiple populations of galaxies, where many different generations of stars can contribute to the morphology of the observed CMD.

A more sophisticated and quantitative technique was then developed by Tosi et al. (1991), the synthetic CMD method, that consists in the extrapolation of the standard isochrone fitting method by creating theoretical CMDs via Monte Carlo extractions from an isochrone set, and comparing them to the observed CMD. It includes the estimate of photometric errors, completeness and crowding, and it is still the most powerful technique available for this kind of analysis and, in general, for SFH studies of resolved stellar populations. A detailed description of this method will be presented in the next Chapter.

One of the first surveys creating a uniform archive of resolved galaxies is the ACS Nearby Galaxy Survey Treasury (ANGST) program (Dalcanton et al., 2009). They built a sample of 69 galaxies within a radius of 3.5 Mpc and included the M81 group (at 3.6 Mpc) and the BGC 253 clump in the Sculptor group (at 3.9 Mpc) to cover a wider morphology and environment range. 60 of these are dwarf galaxies, including 12 dwarf spheroidal/dwarf elliptical galaxies, 5 dwarf spirals, 28 dwarf irregulars, 12 dwarf transition type (dTrans) galaxies and 3 tidal dwarfs. Weisz et al. (2011) analyzed this dwarf sub-sample and uniformly derived the SFHs using the synthetic CMD method. The ANGST dwarf galaxies exhibit a wide variety of complex SFHs, but the mean SFHs of the different morphological types are generally indistinguishable earlier than the most recent  $\sim 1$  Gyr. On average, they find that the typical dwarf galaxy formed the bulk of its stars prior to  $z \sim 1$ , although the uncertainties are relatively large, particularly for dIrrs, which have very different SFHs. Figure 1.2 shows their resulting cumulative SFHs. Despite the variety of the individual curves,

the mean trends are remarkably similar, and the clearest differences between the morphological types arise in the most recent 1 Gyr, where the typical dSph, dTrans, dwarf spiral and dIrr galaxies formed an increasing amount of their total stellar mass ( $\sim 2\%$ ,  $4\%$ ,  $5\%$  and  $8\%$  respectively).

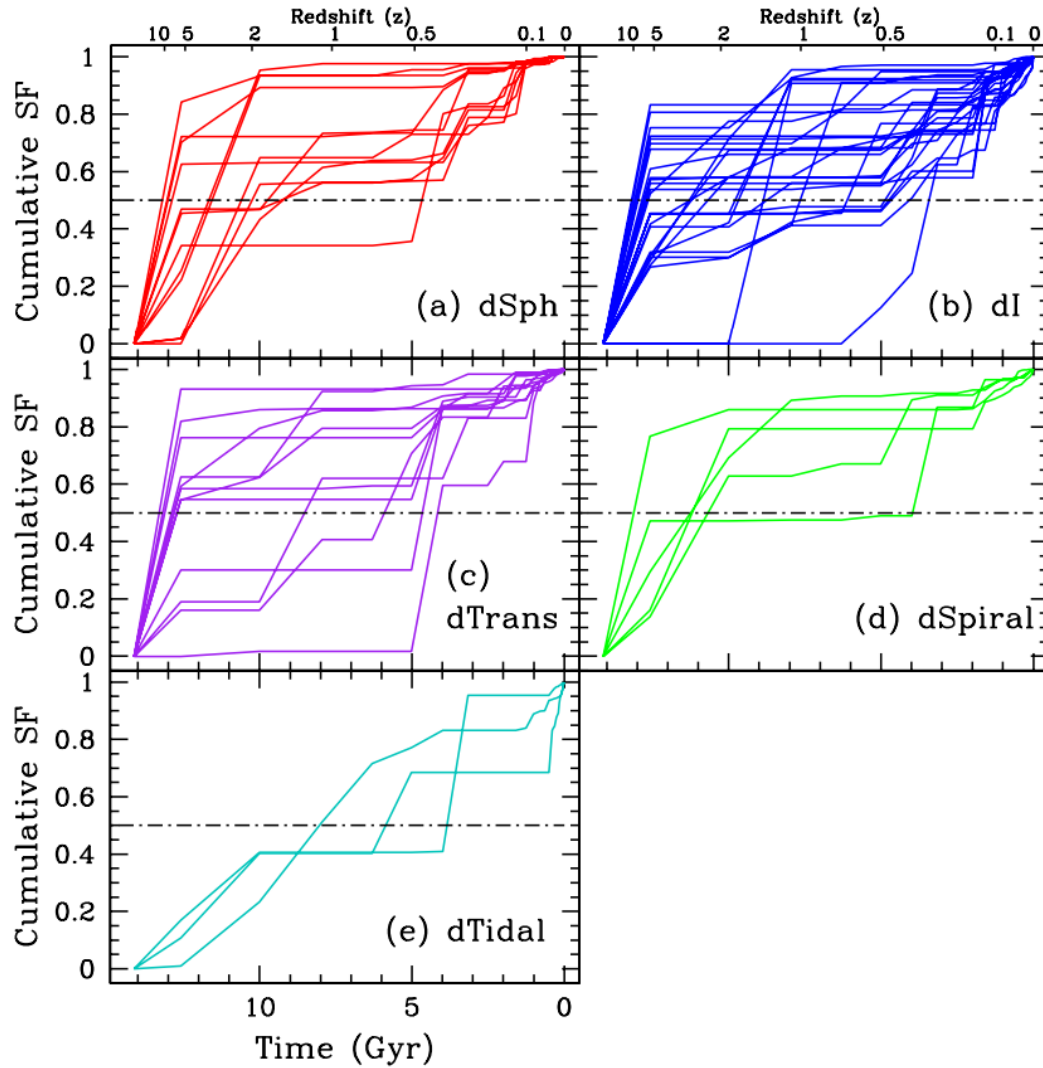


FIGURE 1.2: Cumulative SFHs of the ANGST sample of dwarf galaxies, divided per morphological type. The horizontal dot-dashed line represents 50% of the total stellar mass. Excluding the tidal dwarfs, most dwarf galaxies appear to have formed the bulk of their stellar mass prior to  $z \sim 1$ . See Figure 5 of Weisz et al. (2011) for more details.

A smaller but more precise program was presented by Gallart (2008) and Hidalgo et al. (2013), the Local Cosmology from Isolated Dwarfs (LCID) project, also based on *HST*/ACS observations. They wanted to study the detailed SFHs of six isolated dwarf galaxies of the Local Group, two dIrrs, IC1613 and Leo A, two dTrans, LGS3 and Phoenix, and two dSphs, Cetus and Tucana, in order to investigate the effects of phenomena that may affect the early evolution of dwarf galaxies in the absence of

strong environmental effects; subsequently, another dIrr galaxy, DDO210, has been studied (Cole et al., 2014). As shown in Figure 1.3, they find that Tucana and Cetus share the common characteristic of having formed over 90% of their stars before 10 Gyr ago, and they host no stars younger than 8 – 9 Gyr. The SFHs of the two dTrans galaxies are remarkably similar to those of the dSphs: they formed over 80% of their stars before 9 Gyr ago in spite of having maintained residual star formation during the rest of their evolution. The lower panel of the figure displays the SFHs of the two dIrrs in their sample, Leo A and IC1613. In contrast to the former SFHs, those of the dIrrs do not show a dominant early burst of star formation; instead, over 60% of their stars formed at intermediate and young ages.

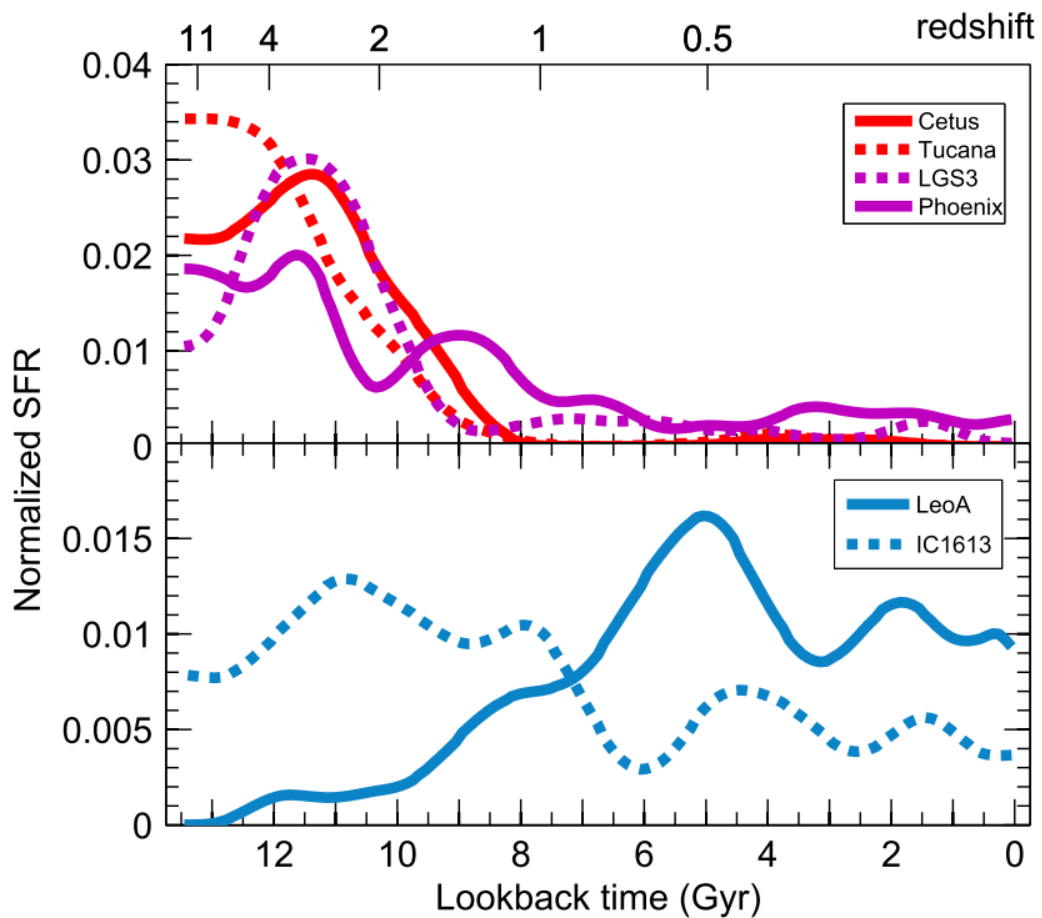


FIGURE 1.3: SFHs of the six LCID galaxies. *Top panel.* SFHs of the dSphs (red) and dTrans (magenta). *Bottom panel.* SFHs of the dIrrs. See Figure 1 of Gallart et al. (2015) for more details.

Gallart et al. (2015) make a very interesting analysis comparing these six isolated dwarfs with dwarfs that are, at present, found close to the large spirals, with SFHs from the literature. Most MW satellites (UMi, Draco, Sextans, Scl, CnVI, plus the very faint dwarfs, Brown et al., 2014) formed most of their stars before  $\sim 10$  Gyr ago. The more distant dSph satellites, Fornax, Leo I, and Carina, show substantial intermediate-age populations: their SFHs peaked at ages younger than 10 Gyr, and

most of their star formation occurred at intermediate ages. In fact, the SFHs of these dSphs are similar to those of dIrr galaxies for most of their lifetimes: they have low initial star formation rates (SFRs) and high SFRs at intermediate ages. The main difference occurs in the last  $\sim 2$  Gyr or less, when their star formation stopped. They are classified as dSphs for their current properties, but their history is similar to that of dIrr galaxies. Based on their full evolutionary histories, they propose a new classification for dwarf galaxies, that can be grouped in two classes (see Figure 1.4):

- *fast* dwarfs that started their evolution with a dominant star formation event, but their period of star formation activity was short (few Gyr);
- *slow* dwarfs that formed a small fraction of their stellar mass at an early epoch, and continued forming stars until the present (or almost).

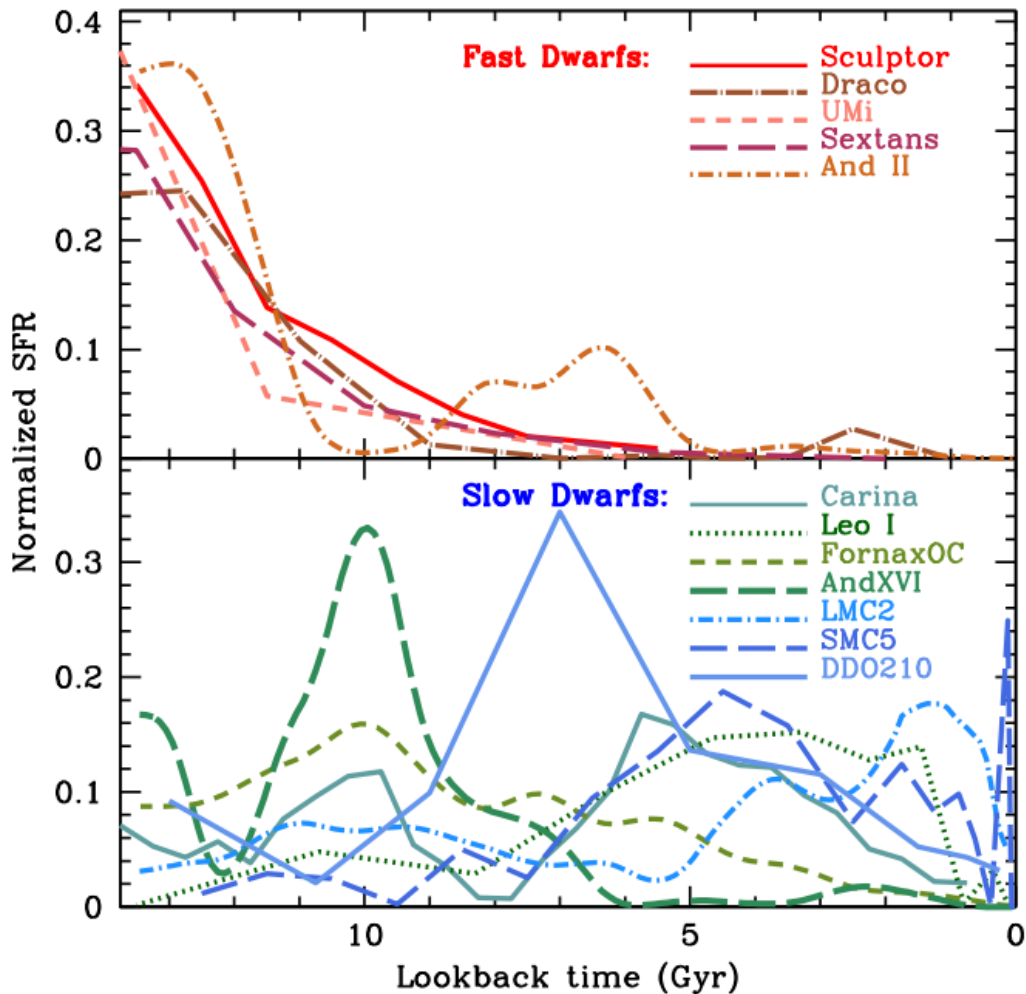


FIGURE 1.4: SFHs of Local Group fast (top panel) and slow (bottom panel) dwarfs. Note that in the bottom panel both slow dwarfs currently classified as dSphs (in green shades) and dIrrs (in blue shades) are represented. See Figure 2 of Gallart et al. (2015) for more details.

These two evolutionary paths do not correspond directly to the current, commonly adopted dwarf galaxy classification (in dIrrs, dTrans and dSphs). Most notably, some dSphs have important intermediate-age and young populations, and thus SFHs that resemble those of dIrrs: in this sample, all dIrrs are slow dwarfs, while some dSphs are fast and others are slow. In addition to SFHs, slow and fast dwarfs also differ in their inferred early location relative to the local large galaxies: as opposed to fast dwarfs, slow dwarfs' positions and radial velocities are compatible with a late first infall into the Local Group, which would imply that they were assembled in lower-density environments than fast dwarfs. They thus suggest that the nature of fast or slow dwarfs is determined by the formation conditions of the galaxy, when the environment influenced the mass-assembly process of the dwarf (which is expected to depend on the formation location) rather than removing the gas later. In this scenario, the progenitor halos of fast dwarfs assembled early and quickly in high-density environments, where interactions triggering star formation were common, likely leading to high SFRs even before reionization. Strong gas loss would follow as a consequence of the effects of reionization and feedback acting together. Slow dwarfs resulted from delayed, slower mass assembly occurring in lower-density environments, which in turn led to a delayed onset of star formation, occurring when the halo had grown massive enough to allow the gas to cool and form stars. This implies milder feedback and gas loss, and the possibility of keeping forming stars on a long timescale. A strong interaction with a large host could play a role in the final removal of gas from the dwarf galaxies that infall late. The morphology-density relation observed (with exceptions) in LG dwarf galaxies today would thus be a consequence of their formation in more or less dense environments around the LG.

A more extended study of LG dwarf galaxies was made by Weisz et al. (2014), who analyzed a sample of 40 galaxies located within  $\sim 1$  Mpc and observed with the *HST*/Wide-Field Planetary Camera 2 (WFPC2). This sample consists of 23 dwarf spheroidals, 4 dwarf ellipticals, 8 dwarf irregulars, and 5 transition dwarfs. Figure 1.5 shows their results. They find several interesting trends for each morphological type, here summarized.

- dSphs are predominantly old systems and have formed the vast majority of their stars prior to  $z \sim 2$  (10 Gyr ago). However, while this behavior holds on average, the individual galaxies show a significant scatter, ranging from purely old to those with nearly constant lifetime SFHs.
- There are few predominantly old dIrrs. On average, dIrrs formed  $\sim 30\%$  of their stellar mass prior to  $z \sim 2$ , and show an increasing SFR toward the present, beginning around  $z \sim 1$  (7.6 Gyr ago). This behavior is generally reflected in the SFHs of individual dIrrs, which show only modest scatter relative to the average.
- On average, dTrans appear to have formed 45% of their total stellar mass prior to  $z \sim 2$ , and have experienced nearly constant SFRs since that time. The SFHs of the individual galaxies show modest scatter over most of their lifetimes.
- dTrans with predominantly old SFHs tend to have lower present day gas fractions, while those with higher gas fraction have had more constant SFHs over most of their lifetimes.

- dEs typically have an initial burst of star formation prior to  $\sim 12$  Gyr ago, followed by a nearly constant SFR. They show little scatter relative to the average value, and all exhibit declining SFHs starting at  $z \sim 0.1$  (2 Gyr ago).

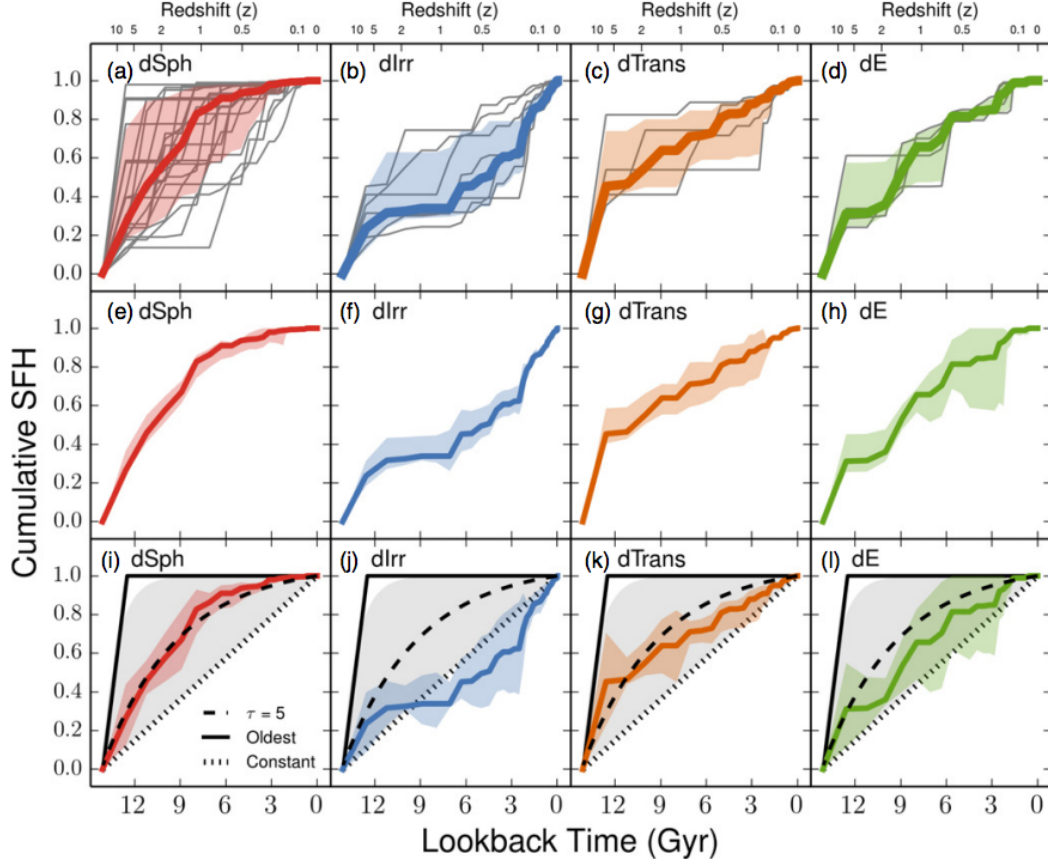


FIGURE 1.5: Unweighted average cumulative SFHs of 40 Local Group dwarf galaxies, grouped by morphological type (dSph red, dIrr blue, dTrans orange, dE green). *Top panels.* The solid line represents the median value of the SFH with the statistical uncertainties, while the gray lines are the individual SFHs. *Middle panels.* Average SFHs with uncertainties given by the root square sum of the differential ensemble systematics and the standard error in the median. *Bottom panels.* Average SFHs with 3 simple SFH models over plotted. See Figure 9 of Weisz et al. (2014) for more details.

As shown in the middle panels of the figure, on average, all morphological types formed  $\sim 30\%$  of their stars prior to 12 Gyr, and are only statistically different after this epoch. In the bottom panels, the average SFHs is compared with simple SFH models (single old population, exponentially declining “ $\tau$ -models”, and constant). The best matches are with the dSphs, whose average SFH is well-approximated by a  $\tau$ -model with  $\tau = 5$  Gyr. Instead, dIrrs, dTrans, and dEs all show a modest initial burst in their SFHs ( $> 10 - 12$  Gyr ago) followed by nearly constant or slightly rising SFHs. The combination of an exponential SFH ( $\tau = 3 - 5$  Gyr) prior to 10 – 12 Gyr ago, followed by a constant SFH thereafter provides a reasonable approximation for the average SFHs of these three groups.

Given their very privileged position very close to the MW, the Magellanic Clouds are another fundamental target for stellar population studies outside our galaxy. They are two interacting satellites of the Milky Way, the Large Magellanic Cloud (LMC) and the Small Magellanic Cloud (SMC), an irregular galaxy at the boundary of the dwarf class. In particular, the SMC can be considered the closest late-type dwarf, given its high gas content, low metallicity ( $Z \sim 0.004$ ), and low mass ( $1 - 5 \times 10^9 M_{\odot}$ ) near the upper limit of the range of masses typical of late-type dwarfs (Tolstoy, Hill, and Tosi, 2009). The first determination of the full, global SFH of the SMC (through the synthetic CMD method), was made by Harris and Zaritsky (2004), thanks to the Magellanic Clouds Photometric Survey (Zaritsky, Harris, and Thompson, 1997), a spatially comprehensive catalog of their stellar populations. However, their ground-based photometry did not reach the oldest main sequence turn off, and this hampered the derivation of the SFH at relatively early epochs. Subsequent deeper studies, as Noël et al. (2009), Cignoni et al. (2013), and Weisz et al. (2013), found that for ages  $> 12$  Gyr, the SFH of the SMC is consistent with a constant lifetime SFH, suggesting either suppressed or under-fueled star formation, relative to other Milky Way satellites at comparable distances; two distinct SF peaks are present at  $\sim 4.5$  and 9 Gyr, which may be due to periodic encounters with the LMC, while the LMC had roughly constant star formation at the same epochs; at  $\sim 3.5$  Gyr ago both galaxies show a sharp increase in SFR, and their SFHs track each other subsequently, consistent with suggestions of a close encounter with the Milky Way at recent times; starting around  $\sim 3.5$  Gyr ago, the SF in the outer regions of the SMC abruptly ceases, while the SFR in the galaxy's center sharply increases, suggesting gas from the outer regions has been centrally funneled.

Another study of nearby dwarf galaxies is the one performed by McQuinn et al. (2010), not based on a specifically designed survey but on archival *HST* observations. They select 18 starburst dwarfs covering a range of brightness, morphologies, and spatial extent, in order to explore the starburst phenomenon in relation to different dwarf galaxy properties. Their SFH derivation shows large variations from galaxy to galaxy, and, while their sample includes a class of objects undergoing significant recent SF, they do not find a common SFR profile that characterizes the starburst phenomenon. In most of their galaxies, elevated levels of SF are sustained over a large interval of time ( $\delta t > \text{few } 100 \text{ Myr}$ ), and there are variations and inhomogeneities in the SFR profiles on small temporal scales ( $\delta t \sim 10 - 20 \text{ Myr}$ ).

The great variety of dwarf galaxies within and outside the Local Group, once again underlines the complexity of this class of objects, and the strong need for detailed studies of their kinematics, metallicities, stellar contents and evolution.

### 1.3 A new survey: LEGUS

The Legacy ExtraGalactic UV Survey (LEGUS) is a Hubble Space Telescope Cycle 21 Treasury program (GO 13364, PI D. Calzetti), whose aim is to provide a homogeneous imaging data set in five bands (from the near ultraviolet to the near infrared) of a sample of 50 local (closer than 12 Mpc) star-forming galaxies. These targets have been selected to sample a full range of global galactic properties such as morphology, star formation rate, mass, metallicity, internal structure, and interaction state, representative of the variety observed within the Local Volume (Calzetti et al., 2015). The main scientific goal of the survey is to link the different scales of star formation, from stellar associations to galaxies, and in particular to investigate how the clustering of star formation evolves both in space and in time, discriminate among different models of star cluster evolution, explore the effects of SFH on the UV star formation rate calibrations, quantify the impact of the environment on star formation and cluster evolution across the full range of galactic and interstellar medium properties.

The LEGUS images were obtained with the Wide-Field Camera 3 (WFC3), in the filters F275W ( $\lambda 2704 \text{ \AA}$ ), F336W ( $\lambda 3355 \text{ \AA}$ ), F438W ( $\lambda 4325 \text{ \AA}$ ), F555W ( $\lambda 5308 \text{ \AA}$ ), and F814W ( $\lambda 8024 \text{ \AA}$ ), plus parallel optical imaging with the ACS, in the filters F435W ( $\lambda 4328 \text{ \AA}$ ), F606W ( $\lambda 5921 \text{ \AA}$ ), and F814W ( $\lambda 8057 \text{ \AA}$ ). Figure 1.6 shows the full LEGUS sample.

Thanks to the multi-band imaging, the LEGUS photometry covers both blue and red, young and old stellar populations, in the field as well as in clusters. Hence, comparisons between recent ( $\lesssim 50 \text{ Myr}$ ) and ancient star formation histories from resolved stellar populations are possible, as well as the investigation of the spatial and temporal evolution of star formation within the galaxies. This can eventually improve the theoretical scenarios on galaxy evolution and help to really understand the physical processes connecting gas and star formation, and possibly their evolution in different environments and at high redshift. One of the goals of LEGUS is to enable accurate ( $\delta(\text{age})/\text{age} \approx 10\% - 20\%$ ) determinations of SFHs in its sample galaxies. The LEGUS UV observations resolve the majority of stars above  $\approx 7 - 10 M_{\odot}$  at all the considered distances, in the disks and in sparse groups and OB associations; the outer regions of star clusters can be partially resolved in the closest ( $< 5 - 6 \text{ Mpc}$ ) galaxies. Using the UV and U bands, we can build color-magnitude diagrams where the main sequence (MS) stars and the blue loop (BL) core helium-burning stars are separated in two cleaner sequences with respect to the optical CMDs, where these stars partially overlap (Tolstoy et al., 1998). With this separation, the correspondence between luminosity and age that is found for BL stars can be a strong constraint to directly convert the luminosity function into the SFH (see Section 2.1). Comparison among different bands can also help to model the extinction and differential reddening that can heavily affect gas- and dust-rich galaxies, and even put constraints on the shape of the stellar IMF.

As a member of the LEGUS collaboration, I am in charge of deriving accurate and reliable SFHs of a subsample of the 50 LEGUS galaxies. The idea was to analyze different galaxy types with a smooth transition from the smallest dwarfs to the biggest spirals. In this thesis, we use LEGUS' data to derive the SFH of three galaxies of different type: a dwarf irregular, DDO 68, a Magellanic irregular, NGC 4449, and

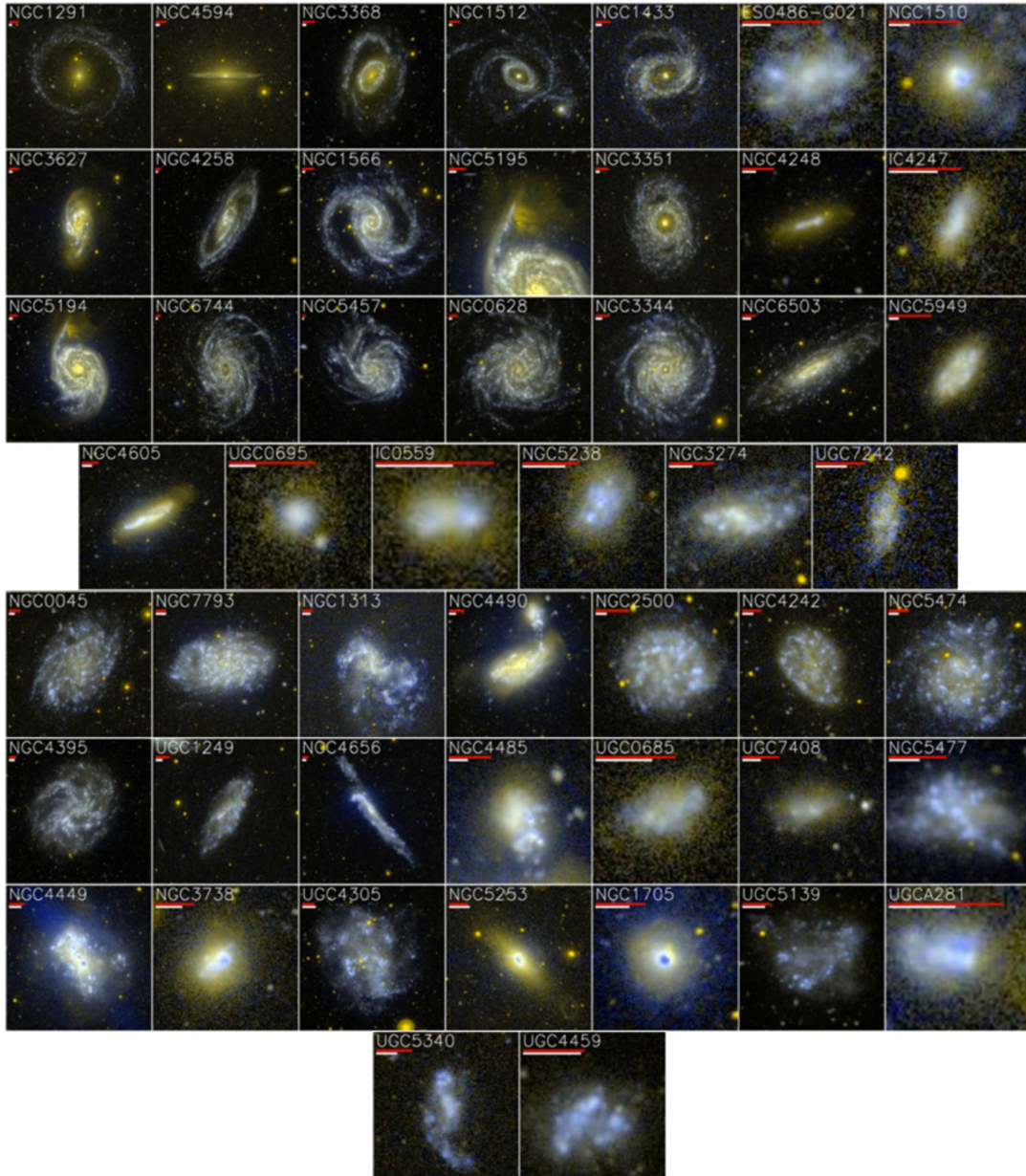


FIGURE 1.6: The full 50 galaxies LEGUS sample shown with GALEX two-color (far-UV and near-UV) images. The two bars under the galaxy name indicate the angular ( $1'$ , red bar) and physical (1 kpc, white bar) scale. See Calzetti et al. (2015) for more details.

a flocculent spiral, NGC 7793. Given the longer timescale covered and the need to build a homogeneous archive to refer to in all future applications, the analyses of the optical stellar populations and SFHs of these galaxies are the first we approached. The corresponding study in the UV and U bands has been carried out in parallel by other members of the team, and will be briefly presented in what follows, as preliminary results.

## 2. FROM THEORY TO PRACTICE

---

### 2.1 The Color-Magnitude Diagram and its power

One of the most useful and fundamental plots in stellar astronomy is the Hertzsprung-Russell (H-R) diagram, which illustrates the relation existing between effective temperature and luminosity of a star. Thanks to the Stefan-Boltzmann equation  $L = 4\pi R^2 \sigma T_e^4$  (where  $L$ ,  $R$  and  $T_e$  are the star luminosity, radius and effective temperature, respectively, and  $\sigma = 5.67 \times 10^{-5} \text{ erg cm}^{-2} \text{ K}^{-4} \text{ s}^{-1}$  is the Stefan-Boltzmann constant), the location of any star of given radius and temperature in the H-R diagram is uniquely defined. This makes the H-R diagram the plot of reference to study stellar evolution.

In practice, the luminosity of a star is commonly measured on a logarithmic scale, going back to the first classification by Hipparchus that divided the observable stars in different classes according to their apparent magnitude  $m$ . Luminosity and apparent magnitude of a star are related by:

$$m = -2.5 \log_{10} \frac{L}{4\pi d^2} + c \quad (2.1)$$

where  $d$  is the star distance and  $c$  is a constant. Since the absolute magnitude is defined as the apparent magnitude of that star if located at 10 pc from us, the difference between the apparent and absolute magnitude  $M$  (the distance modulus, DM) is:

$$m - M = 5 \log_{10}(d) - 5. \quad (2.2)$$

Different stellar temperatures generate different sets of absorption lines, that translate into different spectral types such as O, B, A, F, G, K, M; another estimate of the temperature of a star comes from the so-called color index, which is the difference of the magnitude of the star in two different photometric filters (see Figure 2.1).

The theoretical H-R diagram ( $\log L/L_\odot$  vs  $\log T_e$ , where  $L_\odot = 3.83 \times 10^{33} \text{ erg s}^{-1}$  is the solar luminosity) and its observational counterpart, the color-magnitude diagram (magnitude vs color index), display how luminosity and temperature (or magnitude and color) of a star of a given mass change as a function of time and therefore evolutionary phase (stellar evolution track) or alternatively how luminosity and temperature (or magnitude and color) of a star of a given age change as a function of its mass and therefore evolutionary phase (isochrone).

This tool gave a huge boost to understand how stars and groups of stars evolve, first of all showing that regardless of their mass, stars spend the majority of their lives in the main sequence phase, burning hydrogen in their core. At fixed age, MS

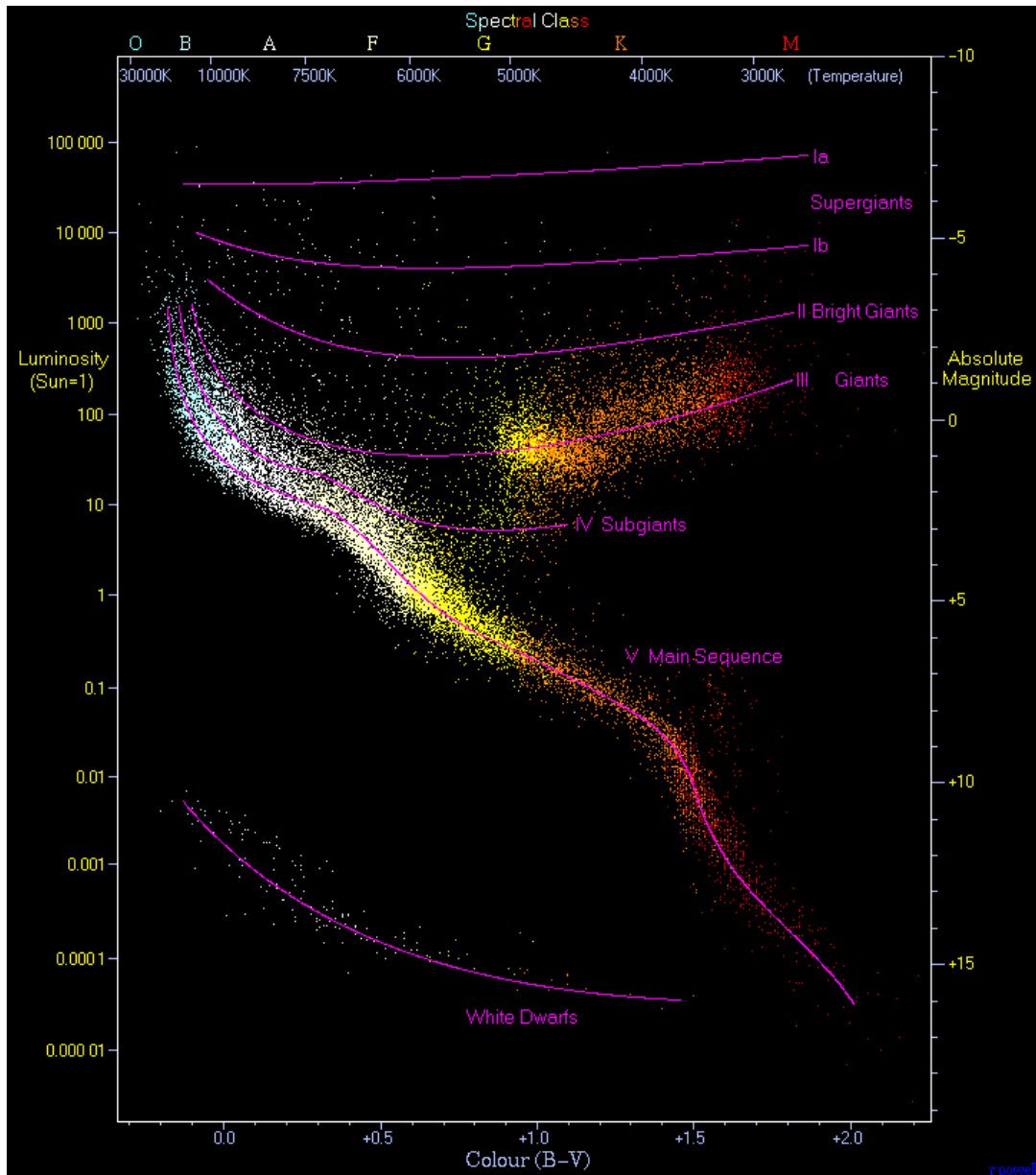


FIGURE 2.1: Luminosity  $L$  (absolute magnitude  $M_V$ ) against effective temperature  $T_e$  (color  $B - V$ ) of stars ranging from the high-temperature blue-white stars on the left side of the diagram to the low-temperature red stars on the right side. The x-axis is also labeled with the main spectral types. The plot includes the 22 000 stars from the Hipparcos Catalogue together with 1000 low-luminosity stars (red and white dwarfs) from the Gliese Catalogue of Nearby Stars. The core hydrogen burning stars are found in a band running from top-left to bottom-right (the main sequence). Giant stars form a clump on the upper-right side of the diagram. Above them lie the bright giants and supergiants. At the lower-left is the band of white dwarfs. (Plot by Richard Powell)

stars follow a well-defined mass-luminosity relation, with  $L \propto M^{3-4}$ . Moreover, the evolutionary timescale on the MS also depends on the mass, so that more massive stars live for shorter times while low-mass stars can sample the whole lifetime of a galaxy, with a relation that is roughly  $t_{MS} \propto M^{-2.5}$ . Thus, combining this two relations gives us a very important time-luminosity relation, i.e. the luminosity of a MS star on the CMD can be directly translated into an age. The intrinsic spread of the MS is given by both binaries and different metallicities in the stellar populations, so the blue edge of the zero age MS (ZAMS) corresponds to the minimum metallicity present in the galaxy, while the red edge is defined by the combination of higher metallicity MS stars with binary MS stars and stars evolving off the MS.

When all the hydrogen in the core has been converted into helium, the off-MS evolution begins. Depending on the mass of the star, this phase can be quite different. In low-mass ( $M \lesssim 2 M_{\odot}$ ) stars the temperature in the core is not high enough to start the fusion of helium, so the core collapses reaching the status of electron degeneracy, while the hydrogen fusion starts in a shell, making the star more luminous and accumulating more helium onto the degenerate core. This phase is called red giant branch and its shape and age are very sensitive to metallicity differences (age-metallicity degeneracy). When the helium core reaches  $M \sim 0.5 M_{\odot}$  the helium ignition starts violently, removing the degeneracy and producing the so-called helium flash, that suddenly ends the RGB phase and starts the horizontal branch (HB) phase (metal-poor stars) or red clump (RC) phase (metal-rich stars), where helium burning proceeds in the core. This process happens at fixed core mass, independently of the initial mass of the star, so the maximum luminosity reached during the RGB is almost constant, and it is called RGB tip (TRGB). This can be a very reliable distance estimator even in distant galaxies.

In intermediate-mass ( $2 M_{\odot} \lesssim M \lesssim 6 - 8 M_{\odot}$ <sup>1</sup>) stars, the helium ignition in the core happens in a non-violent way, and the stars describe large loops in color, the so-called blue loops. The BL luminosity is directly correlated to the total mass, since the mass of the core depends on the extension of the convective core in the previous MS phase, which in turn is a function of the total mass. This makes the blue loops very good age indicators. After the core helium burning phase, low and intermediate mass stars experience the asymptotic giant branch phase. The core is made of carbon and oxygen, as results of the helium burning, while two different shells burn helium (a more internal one) and hydrogen (a more external one). The star expands and develops an extended convective envelope, running almost parallel to the RGB. The shells alternatively stop and re-ignite the nuclear reactions, as the star expands and contracts, producing the so-called thermal pulses during thermally pulsing AGB (TP-AGB) phase. Both during the RGB and TP-AGB phases the stars experience a huge mass loss, that is still very hard to model and quantify.

High-mass stars ( $M \gtrsim 8 - 15 M_{\odot}$ ) form in a small fraction in a galaxy because of the negative slope of the initial mass function (i.e. the distribution of initial masses for

---

<sup>1</sup>The boundary between intermediate- and high-mass stars depends on the evolutionary models. Many groups define high-mass stars all those with a mass above  $8 M_{\odot}$ , while the Padova group uses  $6 M_{\odot}$  as the highest mass intermediate-mass star, due to how they model the effect of overshooting, and  $15 M_{\odot}$  as the lowest mass high-mass star, inserting a “quasi-massive” star category in between.

a population of stars), and their lifetimes are very short ( $< 20$  Myr). Thus, they are indicative of recent or ongoing SF.

### 2.1.1 Age indicators on a CMD

To recover the SFH from the observational CMDs of the considered region through the comparison with synthetic models, the following ingredients are required:

- a set of stellar evolutionary tracks, providing the temperature and luminosity of stars in a (as fine as possible) grid of masses and metallicities according to their evolutionary time scales;
- stellar atmosphere models, to transform the bolometric magnitudes and temperatures into the observational plane;
- an initial mass function, regulating the number of stars born as a function of their mass;
- a star formation rate as a function of time, providing the number of stars born in different time intervals;
- a function regulating the chemical enrichment due to the galaxy chemical evolution, i.e. an age-metallicity relation  $Z(t)$ ;
- a binary fraction and secondary mass distribution.

Eventually, we need to account for the characteristics of any data, as distance, photometric errors and blends, completeness, foreground and internal extinction, differential reddening.

Due to the different assumptions (about not fully constrained quantities) needed for the theoretical calculation and the observational uncertainties, multiple solutions could be possible. As an example, we can consider a test made by Tolstoy, Hill, and Tosi (2009) that shows how CMDs reflect different SFHs in a hypothetical galaxy (see Figure 2.2). They built 6 CMDs with the same distance modulus,  $DM = 19$ , reddening,  $E(B - V) = 0.08$ , and photometric errors and incompleteness typical of *HST*/WFPC2 photometry. In all panels, the number of stars and the IMF are the same, while the metallicity and the SFH change. In the top panels, built with a constant SFR from 13 Gyr ago to the present, all stellar evolution phases are visible: the blue plume typical of late-type galaxies, populated by massive and intermediate-mass stars on the main sequence, and in the most metal-poor case also by brighter blue-loop stars; the red clumps and blue loops of stars in the core helium-burning phase; the AGB and RGB; the subgiant branch (SGB); the oldest MS turn off (MSTO) and the main sequence of the lower mass stars. In the lower panels, the SFH is much simpler, with an old population resembling that of globular clusters. It is clear that interpreting this kind of CMDs (usually even more complex for the presence of different metallicities or reddenings) can be quite challenging, with populations that pile up on each other and mix.

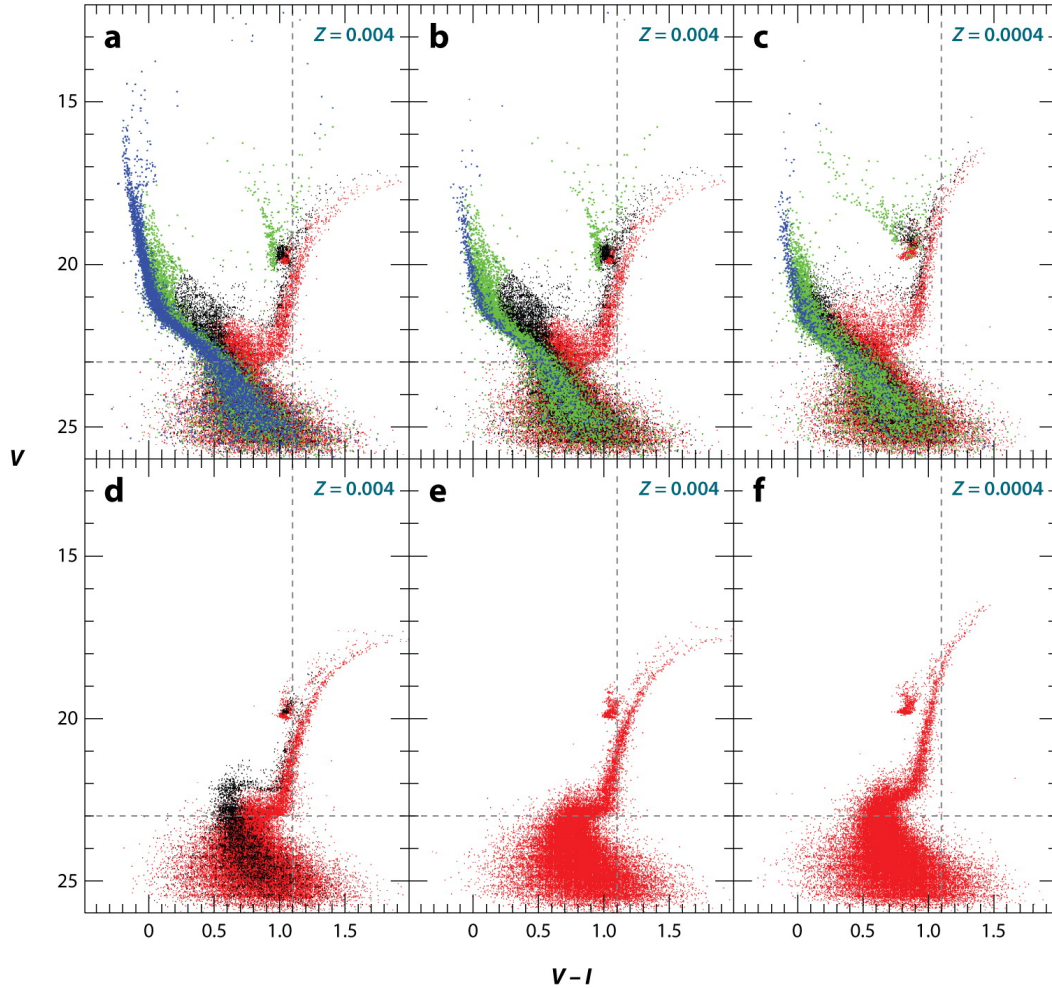


FIGURE 2.2: The effect of different SFHs on the CMD of a hypothetical galaxy. All CMDs contain 50 000 stars, assume a Salpeter IMF (Salpeter, 1955), and are based on the Padova stellar evolution models (Fagotto et al., 1994). A constant metallicity is assumed, indicated in the top-right corner of each panel. In all panels, the colors correspond to different stellar ages (top panels: blue for ages  $< 0.1$  Gyr, green for ages between 0.1 and 1 Gyr, black for ages between 1 and 3 Gyr, red for ages  $> 3$  Gyr; bottom panels: black for ages between 8 and 9 Gyr, red for ages  $> 10$  Gyr). (Panels *b* and *c*) The SFR is constant from 13 Gyr ago to the present. (Panel *a*) A burst of recent ( $< 20$  Myr) SF is added to the constant SFH. (Panels *e* and *f*) An old burst of star formation with a constant SFR from 13 to 10 Gyr ago. (Panel *d*) Two old bursts, one with a constant SFR from 13 to 10 Gyr ago and the other from 9 to 8 Gyr ago (only 10% of the stars were born in the younger burst). See Figure 2 of Tolstoy, Hill, and Tosi (2009) for more details.

### 2.1.2 Optical versus UV

While all studies of SFH performed so far (e.g. Tosi, 2009; Cignoni et al., 2010; McQuinn et al., 2010; Weisz et al., 2011; Hidalgo et al., 2013) cover the longest possible look-back time to infer the SF over the whole lifetime of galaxies, LEGUS allows us to perform a parallel analysis and resolve the details of the SF at very recent epochs ( $\lesssim 50$  Myr) with very high temporal and spatial resolution. Thanks to the UV and U photometry, we can identify the youngest and most massive stars both inside clusters and associations and in the field, and infer the SFH. This can be directly compared to other SFR indicators, such as the  $H\alpha$  emission.

From the CMD point of view, the shorter wavelength bands cover a look-back time of few hundreds of Myr at most, so the main features recognizable are the upper main sequence and the helium burning phases (see Figures 2.3 and 2.4). These synthetic CMDs are computed using a constant SFR (from 13.7 Gyr ago to the present in Figure 2.3, from 300 Myr ago to the present in Figure 2.4), and two different metallicities ( $Z = 0.00152$  and  $Z = 0.00015$ ). The used isochrone set is the PARSEC-COLIBRI stellar evolution library (Marigo et al., 2017) with a Kroupa (2001) IMF and 30% of binaries. The main features discussed in this Section are visible in the CMDs, as well as their dependency on the metallicity. As discussed before, the blue loops luminosity mainly depends on the stellar mass, providing a useful mass-luminosity (thus, luminosity-age) relation, and the great advantage of the BL over the MS is that subsequent generations of BL stars do not overlap as they do on the MS. This is even more evident in Figure 2.4, where this phase dominates the CMDs. From the two shown metallicities we can also note that the more metal-rich simulation exhibits a bigger separation between MS and BL, in both figures.

The UV observations are mainly sampling upper MS and intermediate-to-massive He-burning stars, since stars as those in the RC, RGB, and AGB phases are extremely faint in the UV and U bands. This way, the large majority of stars present in an optical CMD (Figure 2.3) is not observable, and this limits the look-back time reachable with this kind of observations.

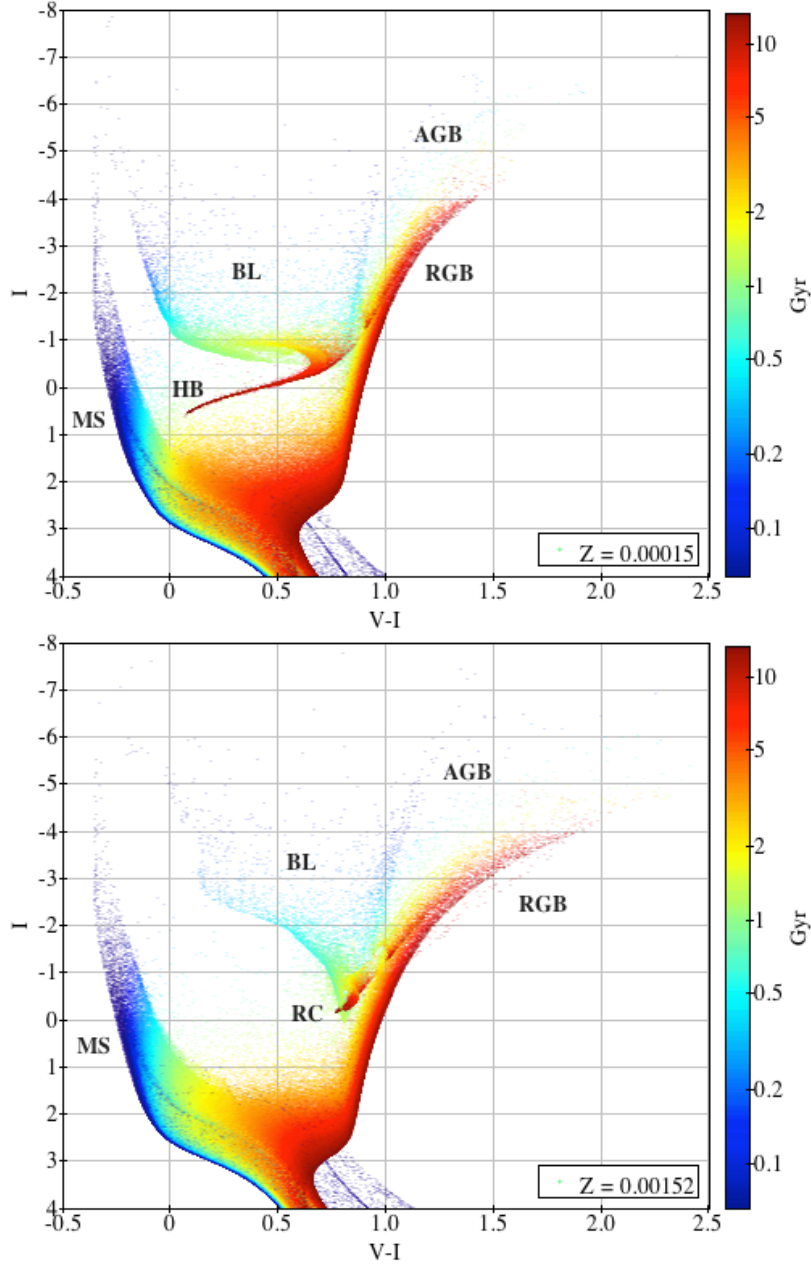


FIGURE 2.3: Synthetic Color-Magnitude Diagrams built with a constant SFR from 13.7 Gyr ago to the present, with two different metallicities ( $Z = 0.00152$  and  $Z = 0.00015$ ), a Kroupa (2001) IMF and a binary fraction of 0.3. The isochrone set used is from Marigo et al. (2017). Stars are color coded according to different age intervals as shown in the color bar. Labels indicate the different evolutionary phases described in the text: main sequence (MS), blue loop (BL), horizontal branch (HB), red clump (RC), red giant branch (RGB) and asymptotic giant branch (AGB). (Plot made with SFERA, see Section 2.3)

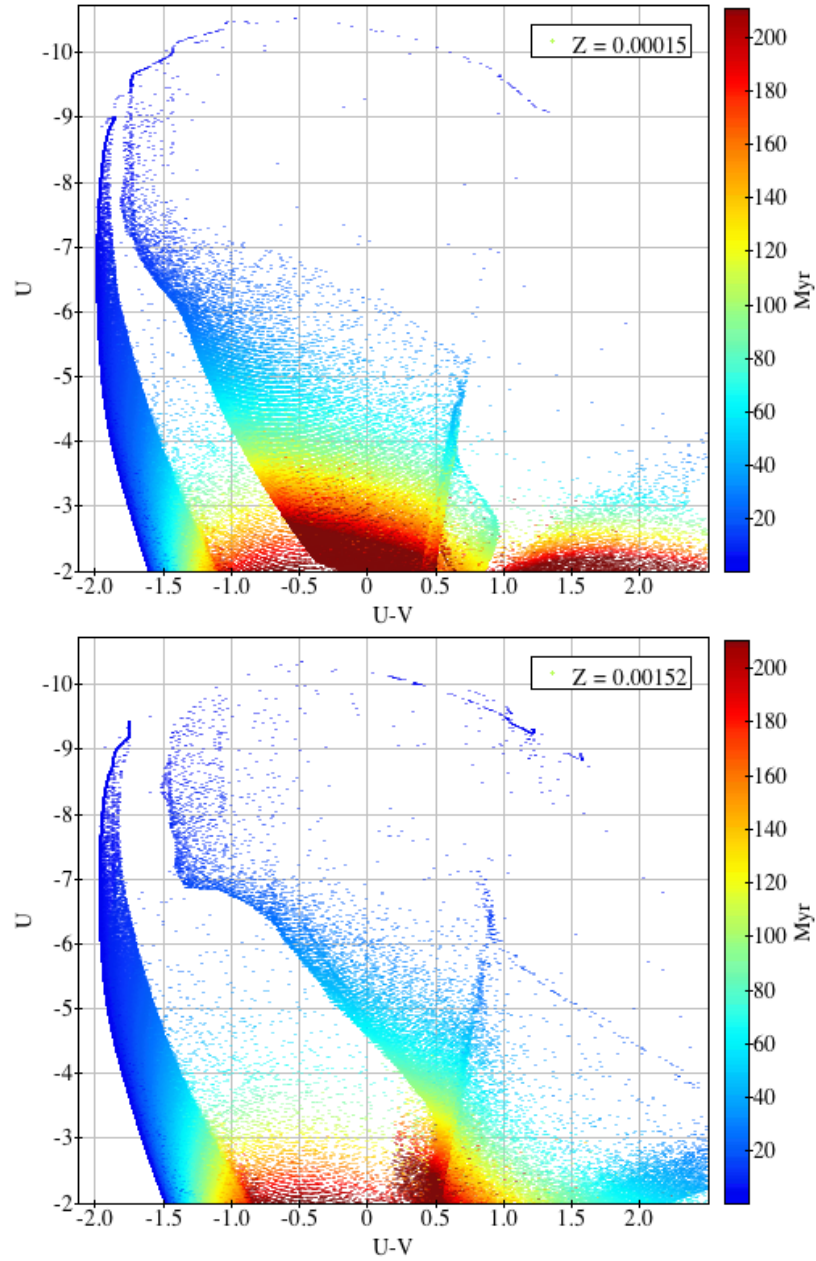


FIGURE 2.4: Synthetic Color-Magnitude Diagrams built with a constant SFR from 300 Myr ago to the present, with two different metallicities ( $Z = 0.00152$  and  $Z = 0.00015$ ), a Kroupa (2001) IMF and a binary fraction of 0.3. The isochrone set used is from Marigo et al. (2017). Stars are color coded according to different age intervals as shown in the color bar. (Plot made with SFERA, see Section 2.3)

## 2.2 The synthetic CMD method: strengths and uncertainties

As already discussed, the CMD of a stellar system holds a great amount of information on its evolution, since it contains the imprinting of all the relevant parameters of the stellar populations composing the system (age, mass, chemical composition, initial mass function). The best tool to analyze it is the synthetic CMD method, that we are going to describe in detail in the following.

The synthetic CMDs are constructed starting from theoretical evolutionary tracks or isochrones by deriving from them the luminosity and temperature corresponding to the mass and age of the synthetic stars, normally extracted with a Monte Carlo approach from a random, IMF weighted, sample. Most of them are built as linear combinations of “basis functions” (BFs), i.e. contiguous star formation episodes whose combination spans the whole Hubble time. Theoretical (luminosity vs temperature) synthetic CMDs need to be converted into the observational (magnitude vs color) plane adopting the proper photometric conversions, the distance and reddening of the examined galaxy, the photometric errors and incompleteness factors of the data.

Observed and synthetic CMDs need then to be compared through a statistical analysis; there are several codes performing such a comparison, as the ones described by Harris and Zaritsky (2001), Dolphin (2002), Aparicio and Gallart (2004), or Grocholski et al. (2012). We used a new one, SFERA, developed by Michele Cignoni at the INAF - Bologna Observatory (see e.g. Cignoni et al., 2015), that will be described in Section 2.3.

It is also useful to compare the SFHs derived with different approaches to estimate which results are robust and which are more uncertain or even artifacts of the chosen minimization algorithms.

### 2.2.1 How to build a synthetic CMD: the SFERA approach

The construction of the BFs is based on the combination between stellar evolution models and observational uncertainties (e.g. photometric errors and incompleteness) of the examined galaxy.

The most common approach uses a Monte Carlo procedure to populate each BF, after choosing the following input parameters:

- initial mass function, typically a Salpeter (Salpeter, 1955) or Kroupa (Kroupa, 2001) one, in a given mass range;
- binary fraction and primary-to-secondary mass ratio;
- metallicity range, possibly from spectroscopic studies of the stellar system under analysis.

Synthetic stars (mass-age pairs) are extracted from the assumed IMF in order to cover a uniform distribution of star formation and metallicity steps; they are then associated with absolute synthetic magnitudes and colors by using a grid of isochrones from the chosen set of stellar models. A given fraction of synthetic stars is randomly

chosen to have a companion, whose mass is extracted from the secondary IMF and whose flux is added to the flux of the primary star. The “theoretical” BFs are then convolved with the characteristics of the data, i.e. distance, foreground and internal extinction, as well as completeness and photometric errors as derived from the artificial star tests (ASTs). To incorporate observational effects and systematic errors (due to e.g. photometric blends) the photometric errors are assigned to the synthetic stars using the difference between output and input magnitudes of the artificial stars. To guarantee that all the stellar evolutionary phases are well populated in spite of the photometric incompleteness and of the short duration of some phases, the synthetic CMDs are generated with a very large number of stars. The comparison between observed and synthetic CMDs is done on the so-called Hess diagrams, i.e. the density of points in the CMD. To this purpose, the BFs, as well as the observed CMD, are pixelated into a grid of  $n$  color-bins and  $m$  magnitude-bins.

The result is a library of  $j \times k$  2D histograms,  $\text{BF}_{m,n}(j, k)$ , that can be linearly combined to express any observed CMD, as in Equation (2.3):

$$N_{m,n} = \sum_j \sum_k w(j, k) \times \text{BF}_{m,n}(j, k). \quad (2.3)$$

The coefficients  $w(j, k)$  are the weights of each  $\text{BF}_{m,n}(j, k)$ , and represent the SFR at the time step  $j$  and metallicity step  $k$ . The sum over  $j$  and  $k$  of  $w(j, k) \times \text{BF}_{m,n}(j, k)$  gives the total star counts  $N_{m,n}$  in the CMD bin  $(m, n)$ .

## 2.2.2 Comparing models and data

The minimization of the residuals between data and models can be implemented in many ways, depending on the statistics one wants to follow. A very common approach is to use a  $\chi^2$ , as implemented by, e.g., Harris and Zaritsky (2001) and Grocholski et al. (2012). The latter solve a non-negative least-squares (NNLS) matrix to identify the SFH that best reproduces the Hess diagram of the observational CMD. The minimization problem is addressed as the solution of a matrix equation:

$$\sum_j w(j) \times \text{BF}_{m,n}(j) = \rho_{m,n} \pm \Delta\rho_{m,n} \quad (2.4)$$

where  $\rho_{m,n}$  is the star density in the observed CMD,  $\Delta\rho_{m,n}$  is the corresponding Poisson uncertainty, and  $m$  and  $n$  are the Hess diagram pixels; the density  $\rho_{m,n}$  is given by the integer number of stars  $L_{m,n} \geq 0$  that is detected in Hess diagram pixel  $(m, n)$ , divided by the area of that pixel. The Poisson error on the detected number of stars is  $\max(1, \sqrt{L_{m,n}})$ , hence:

$$\frac{\Delta\rho_{m,n}}{\rho_{m,n}} = \frac{\max(1, \sqrt{L_{m,n}})}{L_{m,n}}. \quad (2.5)$$

$\text{BF}_{m,n}(j)$  is the density of stars in the BF corresponding to the  $j$ -th time step in the same pixel of the Hess diagram, weighted for the coefficient  $w(j)$ .

However, Mighell (1999) demonstrated that a  $\chi^2$  minimization is generally biased when data are Poisson distributed; in particular, assuming the uncertainty on the data  $\Delta\rho_{m,n} = \max(1, \sqrt{L_{m,n}})$  leads to an underestimation of the true mean of the Poisson distribution. They introduce a modified  $\chi^2$  to obviate this problem, as implemented by Hidalgo et al. (2013) in their code IAC-pop.

Finally, the code we use in this work is based on a Poissonian statistics, as already implemented by Dolphin (2002) in MATCH. Our new code will be described in the next Section.

### 2.2.3 All kinds of uncertainties

There are many uncertainty sources in the determination of the SFH of a galaxy, due to assumptions on some adopted parameters (IMF, binary fraction, distance, extinction), errors from the data (Poissonian noise, photometric errors, completeness), systematics from the stellar evolution models and choices made in the minimization process (SF and metallicity steps, CMD binning).

**Photometric depth** The first aspect we need to consider is the quality of our data, since both distance and crowding and also the instrumental characteristics deteriorate the information available in a CMD by reducing the photometric depth and quality. Increasing the photometric depth means increasing both the number of stars on the CMD and the visibility of age-sensitive CMD features (as discussed in Section 2.1). To have less information implies that the derivation of the SFH is more uncertain, simply because we are not able to find strong constraints to some age intervals or evolutionary stages. Weisz et al. (2011) explore the impact of this limit on the accuracy of the SFH, by constructing a synthetic CMD and recovering the SFH with different completeness limits. In general, when only this aspect is taken into account, the resulting deviations of the SFH are consistent with the expected Poisson precision, even though the results depend on the metallicity. In general, changing the metallicity changes both the evolutionary lifetimes and the stellar luminosity, which can sensibly modify the relation between CMD and SFH as demonstrated by Cignoni and Tosi (2010).

**Photometric error** A related aspect is the resolution of the data, resulting in the photometric error to associate with each star. This is a function of many parameters, such as magnitude, distance, crowding, background noise, whose effect is to scatter the data both in color and magnitude preventing to resolve the different stellar phases. The photometric quality must be carefully evaluated, and the most common and powerful method relies on the artificial star tests.

**Systematic uncertainties** As thoroughly explained by Gallart, Zoccali, and Aparicio (2005), a significant source of uncertainty is given by the choice of the stellar evolution models, that introduces systematic effects in the recovered SFH. Many aspects of the stellar evolution are still not fully understood or properly modeled, such as mass loss, core convective overshooting, stellar rotation, atomic diffusion

in low-mass stars, bolometric corrections for cool stars, uncertainties around the enrichment law, or the abundance of  $\alpha$ -elements. Different sets of isochrones can include these parameters or prescriptions differently, leading to discrepancies in the resulting SFH. While the models by most of the groups reasonably agree on the evolution of MS stars, the stages after the MS can considerably vary from one library to another.

**Random uncertainties** In regions where only few stars are detected, or in poorly populated CMDs, random uncertainties due to stochastic sampling of the CMD can be equally critical (Dolphin, 2013). In particular, they can affect very young time bins, whose SFH is based on few bright supergiants, or phases with a fast evolution resulting in a small number of stars in the observations. The unfortunate circumstance is that the fastest evolutionary phases (hence, the least populated) are those of the brightest stars, whose photometric accuracy is much better, while the longest and most populated phases are those of lower-mass, faintest stars, whose photometric errors and incompleteness are much worse. This issue must be properly taken into account in the algorithms for best SFH identification.

**CMD binning** In the comparison of the star counts between synthetic and observed CMDs, the standard approach is to bin different regions trying to sample as much as possible the observed evolutionary features. In this process, there must be a combination of good statistics in each cell, to minimize the Poisson noise, and good sampling of the fine structure of the CMD, to maximize the time resolution of the results. Aparicio and Hidalgo (2009) propose an *ad hoc* grid whose size varies depending on the density of stars on the CMD and on the reliability of the considered phase. This approach is more “human dependent”, but it can represent a good balance of the different aspects that need to be taken into account. In general, the impact of this choice on the SFH can be relevant, so different combinations should be explored for a safer result.

**Time resolution** Another choice that can affect the quality of this kind of analysis is the number and size of the time bins of the SFH. Since the time resolution is not the same at all ages, but it usually decreases from younger to older epochs, a possibility is to choose logarithmic bins to take into account these variations. In general, the choice of each set of age bins will prevent to identify any SF episode shorter than the bin duration.

**Differential reddening** Another source of uncertainty can come from differential reddening inside a galaxy. In particular, young star forming regions can be surrounded by residual gas and dust from the SF itself, and suffer a major amount of absorption with respect to regions with older populations only. This can affect the morphology of some evolutionary features (e.g. in some galaxies the red clump appears stretched) or hide some important properties of the CMD (as the separation between MS and BL in the UV CMDs).

Other effects (as small variations in the IMF or the binary fraction) have been shown to be smaller than other kinds of uncertainties (Cignoni and Tosi, 2010; Monelli et al., 2010; Dolphin, 2013; Lewis et al., 2015).

As an example, we report the tests made by Cignoni and Tosi (2010), to check the variations in the SFH when the uncertainties related to each parameter are taken into account individually. In particular, to emphasize the effect of each parameter, they show how the recovery of the SFH of a reference fake galaxy is affected by forcing the procedure to adopt a specific (and in most cases wrong) value for the tested parameter. The galaxy was built assuming a constant star formation rate between now and 13 Gyr ago and a metallicity  $Z = 0.004$ . It was put at the distance of the Small Magellanic Cloud,  $(m - M)_0 = 18.9$ , with the same mean foreground reddening  $E(B - V) = 0.08$ . Photometric errors and incompleteness are obtained from actual *HST*/*ACS* observations of the SMC, and applied to the synthetic data, producing a realistic artificial population. The corresponding CMD and recovered SFH are shown in Figure 2.5.

The first test they made is on the completeness limit, thus they performed the star formation recovery using only stars brighter than  $V = 21$  and  $V = 22$ . The results are shown in Figure 2.6. As discussed before, deep CMDs allow to accurately derive the old star formation activity, while the quality already drops when the completeness limit is at  $V = 22$ . The larger error bars at old epochs reflect the fact that the only signature of the oldest activity comes from evolved stars, less frequent, and much more packed in the CMD than the corresponding MS stars. Raising the limiting magnitude at  $V = 21$  further worsens the result, and the recovered SFH is a factor of 2 more uncertain for ages older than 1 – 2 Gyr.

Another tested parameter is the IMF. It is commonly assumed that the stellar IMF has a rather universal slope. Above  $1 M_\odot$  the IMF is well approximated by a power law with a Salpeter-like exponent (Salpeter, 1955), while below  $0.5 M_\odot$  it flattens. According to Kroupa (2001), the average IMF (as derived from local Milky Way star-counts and OB associations) is a three-part power law in the form  $\xi(m) \propto m^{-\alpha}$ , with exponent:

- $\alpha = 1.3 \pm 0.5$  for  $0.08 < m < 0.5 M_\odot$ ,
- $\alpha = 2.3 \pm 0.3$  for  $0.5 < m < 1 M_\odot$ ,
- $\alpha = 2.3 \pm 0.7$  for  $m > 1 M_\odot$ .

Given the degeneracy condition that different combinations of IMF and SFH can equally match the present day mass function (the current distribution of stellar masses) of MS stars, it is interesting to evaluate how this impacts the possibility to infer the SFH. To quantify it, Cignoni and Tosi (2010) generated two populations with different IMF exponents ( $\alpha = 2$ , and  $\alpha = 2.7$ ), but performing the SFH search using always  $\alpha = 2.35$ .

As shown in Figure 2.7 the fit tends to over-estimate the SFR of any population whose IMF is actually steeper than the adopted one, and vice versa, for a flatter IMF. This solution is only the best solution in a parameter space where the IMF is fixed, and not necessarily has to be considered a good one: if the CMD of the recovered SFH is compared with the reference CMD, it is clear that the ratio between low- and

high-mass stars is wrong. In other words, to figure out whether the “best” solution is actually acceptable, it is always crucial to compare all its CMD results with the observed one.

Another source of uncertainty is the percentage of stars in unresolved binary systems and the relative mass ratio. The presence of a given percentage of not resolved binary systems affects the CMD morphology. To see if these effects can alter the recovered information on the SFH, Cignoni and Tosi (2010) built fake populations using different prescriptions for the binary population (10%, 20%, and 30% of binaries

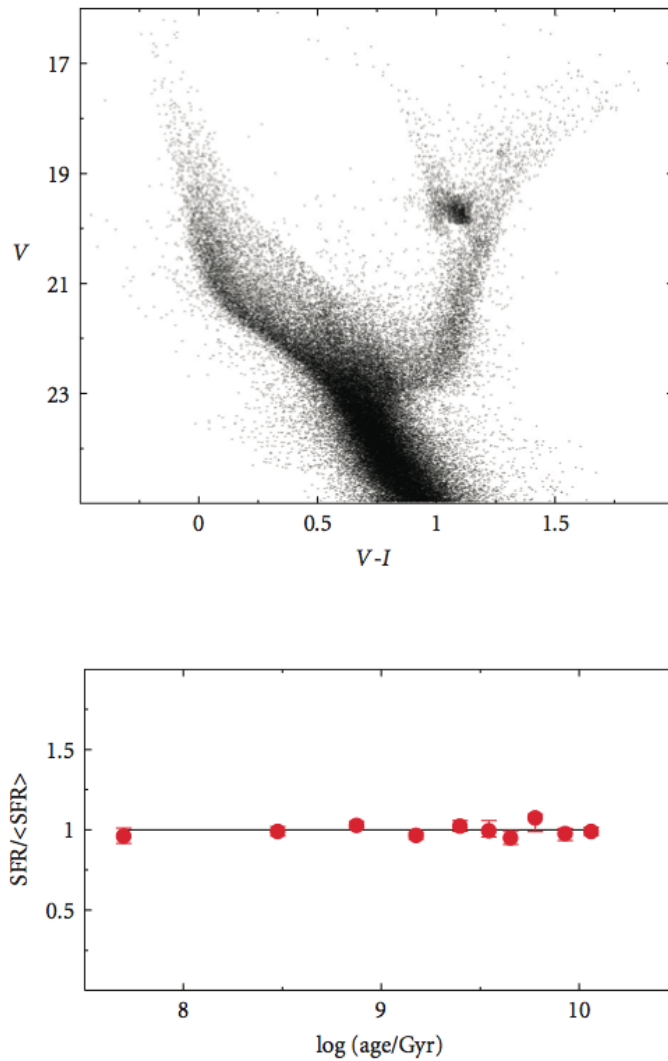


FIGURE 2.5: *Top panel.* CMD of an artificial population of stars generated with constant SFR, Salpeter IMF, constant metallicity  $Z = 0.004$ ,  $(m - M)_0 = 18.9$ ,  $E(B - V) = 0.08$ , and *HST/ACS* photometric errors and completeness. *Bottom panel.* Input (solid black line) and recovered (red dots) SFH. See Figure 6 of Cignoni and Tosi (2010) for more details.

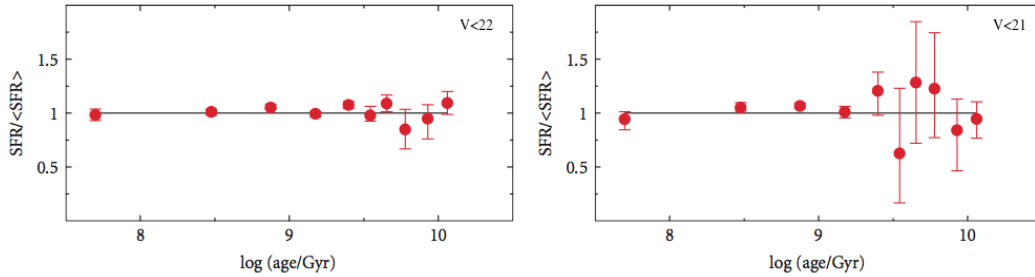


FIGURE 2.6: Effect of different completeness limits on the SFH recovery. *Left panel.* The SFH is recovered using only stars brighter than  $V = 22$ . In this case, most of the information is still retrieved. *Right panel.* The completeness limit is lowered at  $V = 21$  and, as expected, most of the old star formation (older than 1 Gyr) is much more uncertain. See Figure 7 of Cignoni and Tosi (2010) for more details.

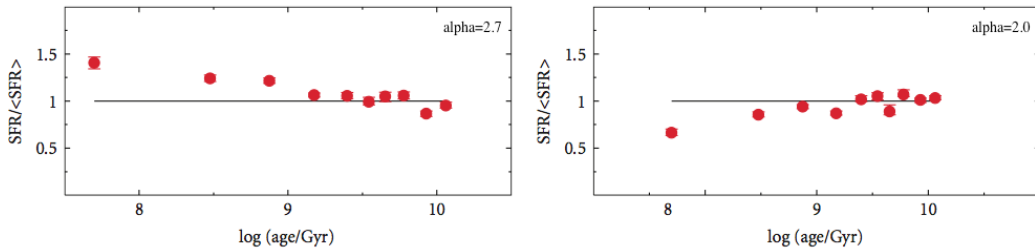


FIGURE 2.7: Effect of different IMF slopes. The SFH was recovered assuming Salpeter's IMF exponent ( $\alpha = 2.35$ ) for synthetic stellar populations actually generated adopting different IMF (labeled in each panel) and a constant SFR. See Figure 8 of Cignoni and Tosi (2010) for more details.

with random mass ratio), but the SFH was searched ignoring any binary population (i.e., assuming only single stars). The adopted stellar models did not include binary evolution with mass exchange, thus each star in a double system is assumed to evolve as a single star.

Figure 2.8 shows the results, and a modest systematic effect is visible. This is because the stars in binary systems are brighter and redder than the average single star population (Olsen, 1999). For the recent SFH, this corresponds to moving lower MS stars from a star formation step to the contiguous older step: in this way, the most recent star formation step is emptied of stars, mimicking a lower activity. Intermediate SF epochs are progressively less affected, because some stars get in and some stars get out of the step bin. For the oldest epochs, the situation is opposite: the binary effect is to move stars toward younger bins.

The precise position of a star on the CMD depends on its chemical composition. The  $Z$  content mainly changes the radiative opacity and the CNO burning efficiency: the result of a decreasing  $Z$  for main sequence stars is to increase the surface temperature and the luminosity of the stars. This has two consequences of relevance for SFH studies: (a) metal poor stars have a shorter lifetime compared to the metal-rich ones

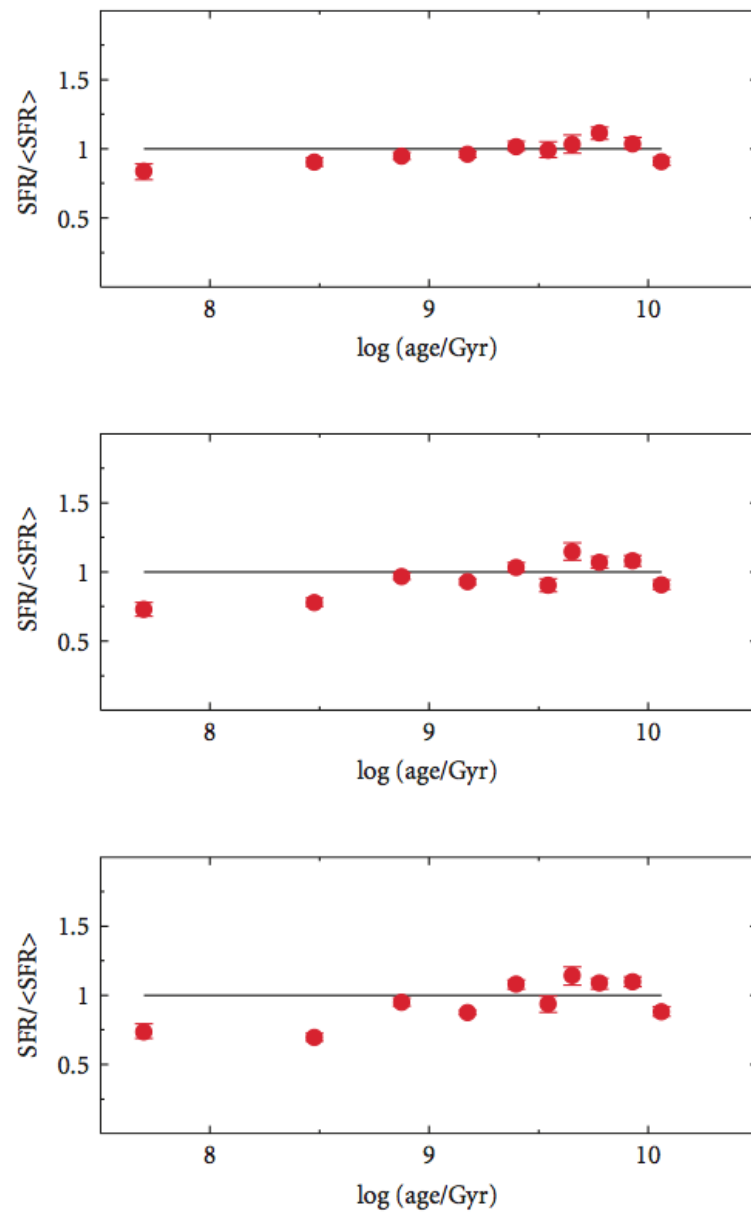


FIGURE 2.8: Effect of unresolved binaries. Three fake populations are built with different percentage of binary stars (10%, 20%, and 30%). The SFH is recovered using only single stars. See Figure 9 of Cignoni and Tosi (2010) for more details.

(because overluminous and hotter), (b) a metal-poorer stellar population is bluer but can be mistaken for a younger but metal-rich population.

To test these effects, the first stars (ages older than 5 Gyr) in the reference fake population are built with a slightly different metallicity ( $Z = 0.002$ ) than the younger objects, which have the usual  $Z = 0.004$ . Then, the SFH is recovered adopting a model with constant  $Z = 0.004$ . The results are shown in Figure 2.9. Neglecting that the oldest population of our galaxy was slightly metal poorer produces systematic, non-negligible discrepancies in the recovered SFH. This is what is called age-metallicity degeneracy: to match the blue-shifted sequences of old metal poorer stars, the models with wrong metallicity must be younger. Note that the overall trend of the young SFR is not significantly biased, while the old SFR is now significantly different.

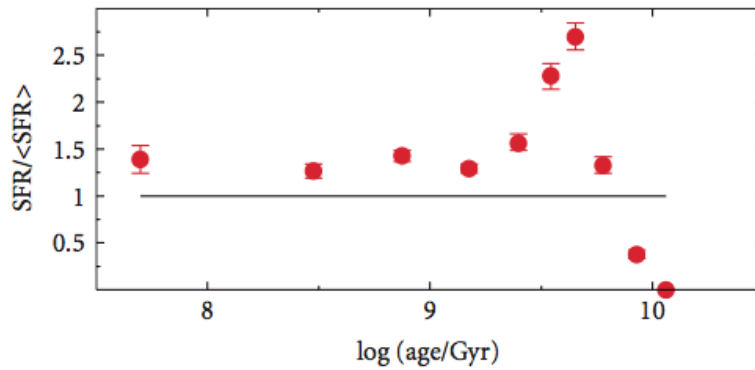


FIGURE 2.9: Sensitivity test to metallicity. The reference fake galaxy has a variable composition:  $Z = 0.004$  for stars younger than 5 Gyr,  $Z = 0.002$  for older stars. The red dots represent the SFR as recovered using a single metallicity,  $Z = 0.004$ , for all epochs. See Figure 10 of Cignoni and Tosi (2010) for more details.

This result is a strong warning against any blind attempt to match the CMD with a single (average) metallicity, especially considering that many galaxies exhibit a pronounced age-metallicity relation.

During and at the end of their life, stars pollute the surrounding medium, so it is natural to expect that more recently formed stars have higher metallicity and helium abundance than those formed at earlier epochs. The progressive chemical evolution with time results from the combined contribution of stellar yields, gas infall and outflows, mixing among different regions of a galaxy. Observational studies have shown that several galaxies reveal a metallicity spread at each given age.

## 2.3 Matching the two worlds: SFERA

To explore the wide parameter space involved in the derivation of the SFHs, Michele Cignoni, at the INAF Bologna Observatory, has developed SFERA (Star Formation Evolution Recovery Algorithm) a hybrid-genetic algorithm that combines a classical genetic algorithm (Pikaia<sup>2</sup>, already implemented in IAC-pop, see Aparicio and Hidalgo, 2009) with a local search (Simulated Annealing, as in, e.g., Cole et al., 2007). This allows to take advantage of the exploration ability of the former, which scans the parameters space in more points simultaneously and thus is not too sensitive to the initial conditions, and the capability of the latter of local exploration of the space and faster convergence. The proposed algorithm alternates two phases: the search for a quasi-global solution by the genetic algorithm and the local search by the other one, whose goal is to increase the solution accuracy (Cignoni et al., 2015).

For this thesis, we further developed the routines dedicated to the grid selection and reddening treatment, we improved the artificial star test technique and inserted the possibility of using different stellar models.

As shown in the scheme in Figure 2.10, the code requires the following input parameters: stellar evolution library, IMF, binary fraction with secondary IMF, metallicity range. If information on the current metallicity of the analyzed galaxy (e.g. from spectroscopy of the H II regions) is available, in the youngest temporal bins the metallicity is allowed to vary in a small range around this value, while the oldest bins have no constraints; this way, we don't assume *a priori* an age-metallicity relation nor the same metallicity for all the stars, and we can check whether we recover physically meaningful  $Z(t)$  relations.

From these inputs the code populates the isochrones in a chosen set of photometric bands via Monte Carlo extraction of stars (mass-age pairs) from the assumed IMF, with a constant SFR; each star will be alive (thus, visible on the synthetic CMD) or dead (thus, contributing only to the astrated total mass) according to its lifetime from the stellar evolution models. These “clean” models are then convolved with the photometric characteristics of the data, as described in Section 2.2.

The minimization of the residuals between data and models is implemented in SFERA taking into account the low number counts in some CMD cells, so we follow a Poissonian statistics, looking for the combination of BFs that minimizes a likelihood distance between models and data. This corresponds to the most likely SFH for these data, with an uncertainty given by the sum in quadrature of the statistical uncertainty (computed through a data bootstrap) and the systematic uncertainty (obtained by re-deriving the SFH with different age and CMD binnings, and using different sets of isochrones).

---

<sup>2</sup>Routine developed at the High Altitude Observatory and available in the public domain: <http://www.hao.ucar.edu/modeling/pikaia.php>.

The Poisson based likelihood function we use is:

$$\chi_P = \sum_{i=1}^{Nbin} obs_i \ln \frac{obs_i}{mod_i} - obs_i + mod_i \quad (2.6)$$

where  $mod_i$  and  $obs_i$  are the models and the data histograms in the  $i$ -bin (Cash, 1979; Dolphin, 2002). This likelihood is minimized with the hybrid-genetic algorithm.

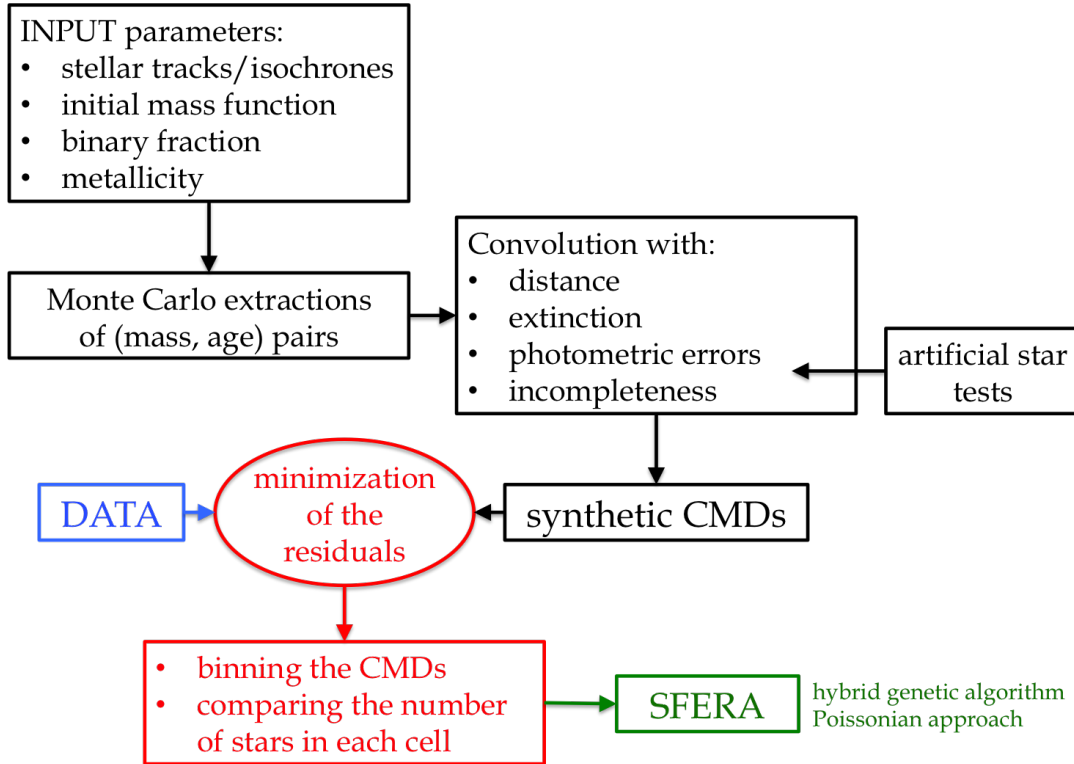


FIGURE 2.10: Schematic view of SFERA, from the computation of the synthetic CMDs to the minimization of the residuals with the data.

Distance and reddening are not fixed parameters; in particular, variations from the assumed distance value (computed from the TRGB luminosity or taken from the literature) are allowed, while the reddening distribution is modeled as a Gaussian (with negative values excluded) with mean value and dispersion (representing total-foreground plus internal- and differential reddening) as free parameters (Harris, Zaritsky, and Thompson, 1997).

### 2.3.1 Time resolution tests

In order to quantify the impact of time resolution on the SFH derivation, we built some tests for our code by using synthetic CMDs generated with a known SFH. We used the typical conditions of a star-forming galaxy located at  $\sim 4$  Mpc from us, and observed with the ACS.

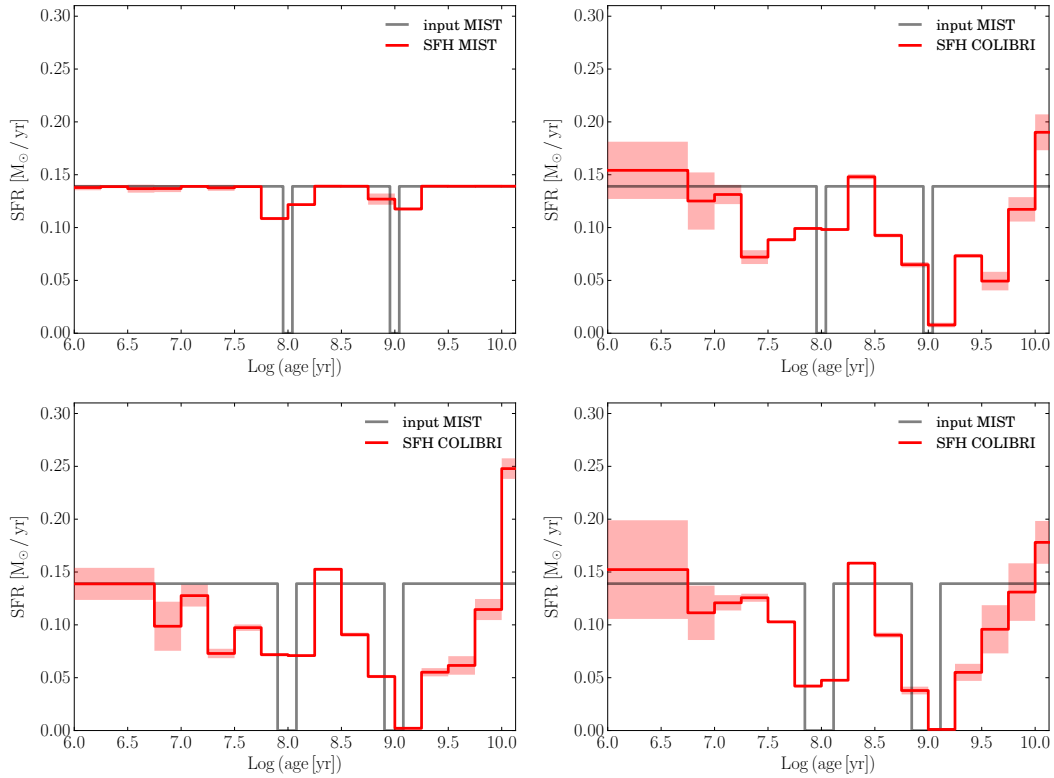


FIGURE 2.11: Test of the time resolution in recovering quiescent phases in the SFH with SFERA. The input SFH was a constant rate with two gaps at 100 Myr and 1 Gyr lasting  $\pm 10\%$  of the age (20 Myr and 200 Myr, respectively) in the top panels,  $\pm 20\%$  of the age in the bottom left panel and  $\pm 30\%$  of the age in the bottom right panel. The models used are the MIST ones for creating the input CMD and as labeled in each panel for recovering the SFH (MIST or PARSEC-COLIBRI) in order to test for systematic uncertainties due to the different stellar models.

To test if we are able to identify and resolve quiescent phases in the life of a similar galaxy, we generated a CMD with a constant SFR with a gap at 100 Myr with a duration of 20 Myr, and another gap at 1 Gyr with a duration of 200 Myr ( $\text{age} \pm 10\%$ ). We simulated a distance of  $\sim 4$  Mpc, and the photometry and completeness conditions from the ACS photometry of a real galaxy (NGC 4449, see Chapter 4). We then ran SFERA with either the same stellar models used for constructing the fake data (MIST) or with a different set of isochrones (PARSEC-COLIBRI). The results are shown in Figure 2.11, and it is evident that, when the same models are used, the lower SFR is perfectly recovered by the code; when we use the other set, although there are some hints, the gaps are not well recovered. However the results improve if we increase the duration of the quiescent phase to  $\pm 20\%$  and  $\pm 30\%$  of the age.

An analogous test was performed by adding two bursts to the constant SFR with the same criteria used before. Again, when the same isochrones are used for both constructing and recovering the SFH, the age resolution is within  $\pm 10\%$  of the age, while if we use different sets, a duration of at least  $\pm 30\%$  of the age is required to well constrain the bursts, in particular for the older one (see Figure 2.12).

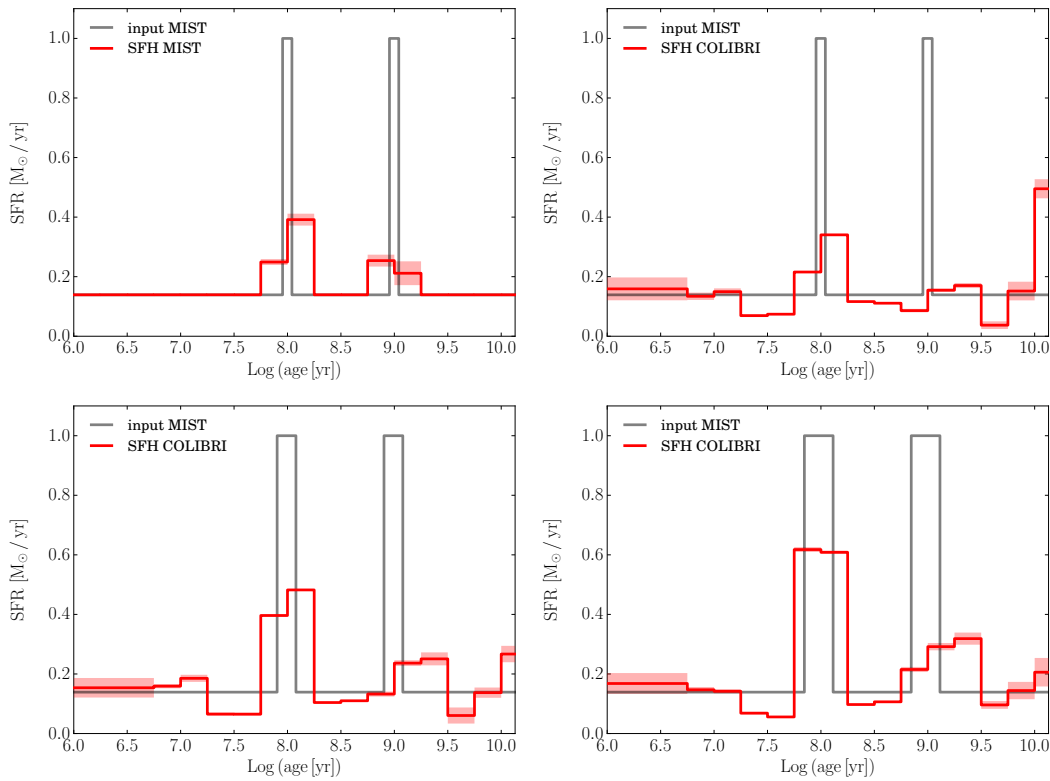


FIGURE 2.12: Test of the time resolution in recovering bursts in the SFH with SFERA. The input SFH was a constant rate with two bursts at 100 Myr and 1 Gyr lasting  $\pm 10\%$  of the age (20 Myr and 200 Myr, respectively) in the top panels,  $\pm 20\%$  of the age in the bottom left panel and  $\pm 30\%$  of the age in the bottom right panel. The models used are the MIST ones for creating the input CMD and as labeled in each panel for recovering the SFH (MIST or PARSEC-COLIBRI) in order to test for systematic uncertainties due to the different stellar models.

These results strongly depend on the fact that our CMDs do not reach the ancient main sequence turnoff, so the resolution at the oldest epochs is a few Gyr only, and the SFH relies on poorer ages chronometers (RGB, AGB and TP-AGB phases). As thoroughly illustrated by Weisz et al. (2011), the ancient MSTO constrains so tightly the SFH that the systematic uncertainties are strongly reduced independently of the stellar models used for the SFH recovery. They indeed find uncertainties larger than 50% when the CMD is too shallow to reach the ancient MSTO. However, limiting the SFH studies to galaxies within 1 – 2 Mpc, where we see the ancient MSTO, would prevent us to cover all the morphological types (e.g. blue compact dwarf galaxies), metallicity ranges and environments that populate the Local Universe.



### 3. THE DWARF: DDO 68

---

In this Chapter, we present the interesting case of DDO 68 (UGC 5340), an extremely metal-poor dwarf irregular galaxy which holds the same record low-metallicity as the mentioned I Zw 18 and Leo P,  $12 + \log(O/H) = 7.15 \pm 0.04$ , from longslit-spectroscopy of the ionized gas in its H II regions (Izotov and Thuan, 2009). After deriving a distance of  $12.74 \pm 0.27$  Mpc, Cannon et al. (2014) estimated for DDO 68 a dynamical mass of  $M_{\text{dyn}} \sim 5.2 \times 10^9 M_{\odot}$  within 11 kpc, and an H I mass of  $M_{\text{H I}} = (1.0 \pm 0.15) \times 10^9 M_{\odot}$ . Their distance, although larger than the  $\sim 9.9$  Mpc predicted by its recession velocity ( $v = 502 \pm 4$  km/s), 6.5 Mpc from the apparent magnitudes of the brightest stars (Pustilnik, Kniazev, and Pramskij, 2005), and 12.0 Mpc derived from the TRGB (Tikhonov, Galazutdinova, and Lebedev, 2014), places DDO 68 close enough to resolve its old stars with *HST*.

DDO 68 is especially appealing as candidate young galaxy because it is located at the periphery of the nearby Lynx-Cancer void (Pustilnik and Tepliakova, 2011) and is at least 2 Mpc away from the closest bright galaxies ( $L > L_{\star}$ , where  $L_{\star}$  corresponds to  $M_B = -19.6$  for  $H = 72 \text{ km s}^{-1} \text{ Mpc}^{-1}$ ). Within the framework of hierarchical formation scenarios, the evolution of galaxies formed in voids could be quite different than in higher density environments because of a much lower probability of being subject to those processes (i.e. encounters and mergers) that are important in shaping and accelerating the evolution of galaxies (Peebles, 2001; Gottlöber et al., 2003; Rojas et al., 2004; Rojas et al., 2005; Hoeft et al., 2006). As a consequence, some void galaxies may have survived in their nascent state of gaseous protogalaxies until the present epoch, and may have just started forming stars as a consequence of a recent disturbance.

DDO 68 presents a very irregular optical morphology, with a long curved Tail on the South and a ring-like structure at the Northern edge consisting of 5 separated H II regions (see Figures 3.1 and 3.2). The neutral gas morphology and kinematics, as inferred from H I maps by Stil and Israel (2002a) and Stil and Israel (2002b), are very disturbed as well. DDO 68 is also an outlier on the mass-metallicity relationship (Pustilnik, Kniazev, and Pramskij, 2005; Berg et al., 2012), being overly massive compared to other systems with comparable metallicity. All these characteristics suggest that DDO 68 may have undergone an interaction event. However, the closest known neighbor galaxy, the dwarf UGC 5427, is at a projected distance of  $\sim 200$  kpc. There is no evidence for a physical association between the two galaxies, and with  $M_B = -14.5$ , UGC 5427 has a too low mass to have significantly affected DDO 68. So, the absence of an easily identifiable companion to DDO 68 leaves the question of how its recent SF was triggered open. From the analysis of the spatial distribution of stars resolved in *HST*/ACS imaging, Tikhonov, Galazutdinova, and Lebedev (2014) argued that DDO 68 consists in fact of two different systems: a central most massive



FIGURE 3.1: ACS/WFC color-combined image of DDO 68 (blue=broad  $V$ , green= $I$ , red= $H\alpha$ )

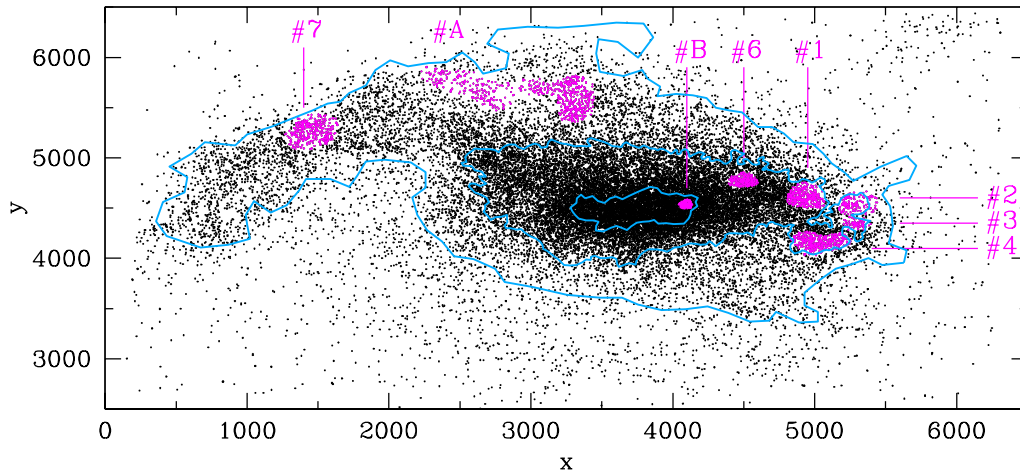


FIGURE 3.2: Map of the stars with the isophotal contours superimposed (light blue lines) which were used to identify the 4 regions for the analysis of the galaxy SFH. Region 1 is the most central one, and Regions 2, 3 and 4 are increasingly more external. The magenta points are the stars within the  $H II$  regions labeled as Pustilnik, Kniazev, and Pramskij (2005) and Izotov and Thuan (2009) except for A and B that they don't take into account in their analysis.

body and an elongated arc-shaped body (DDO 68 B). In a recent work based on Very Large Array (VLA) observations, Cannon et al. (2014) found an object with the same systemic velocity of DDO 68. This gas-rich object (DDO 68 C), has a total neutral hydrogen mass of  $M_{\text{H I}} = (2.8 \pm 0.5) \times 10^7 M_{\odot}$  and lies at a distance of  $\sim 42$  kpc from DDO 68. The claimed detection of a bridge of low surface brightness gas connecting DDO 68 and DDO 68 C may suggest an interaction between the two objects.

In this Chapter we present the star formation history of DDO 68 based on deep *HST*/ACS data. The derived CMD, which reaches down to  $\sim 1$  mag below the TRGB, implies that DDO 68 started its star formation at least  $\sim 1 - 2$  Gyr ago (and possibly up to a whole Hubble time ago) disproving the hypothesis that it is a truly primeval galaxy of recent formation. We analyzed the populations of stars resolved with *HST* in and around DDO 68 and applied the synthetic CMD method (see Section 2.2) to infer its SFH. We also provide a new distance estimate, based both on the TRGB and on the whole CMD fitting.

### 3.1 Observations and Data Reduction

Deep imaging with the ACS Wide-Field Channel (WFC) of DDO 68 was performed on 2010 April 27 and May 2 (GO program 11578; PI Aloisi) using the F606W ( $\sim$  broad  $V$ ) and F814W ( $\sim$   $I$ ) broad-band filters and the F658N ( $H\alpha$ ) narrow-band filter. The total integration time is  $\sim 2400$  s in F658N, and  $\sim 6940$  s in both F606W and F814W. In addition, coordinated observations were made in parallel with the UV/visible channel (UVIS) of the Wide Field Camera 3, in both F606W and F814W filters. The results from the latter are not discussed here and will be presented in a forthcoming publication.

We have observed DDO 68 with standard dither pattern in both filters to fill the gap between the two CCDs of the ACS and improve the sampling of the point-spread function (PSF). All images were processed with the latest version of CALACS, the ACS pipeline. We applied to them all the routine developed by Anderson and Bedin (2010) to corrected for charge transfer efficiency (CTE). Eventually, we combined all the images in the same filter into a single frame using the MULTIDRIZZLE software package (Fruchter et al., 2009). MULTIDRIZZLE allows to fine-tune the alignment of the images, correct for small shifts, rotations and geometric distortions between the images, and remove cosmic rays and bad pixels. The final  $V$  and  $I$  images were eventually resampled to a pixel size of 0.033 arcsec (0.68 times the original ACS/WFC pixel size). Figure 3.1 shows a three-color combined image of DDO 68.

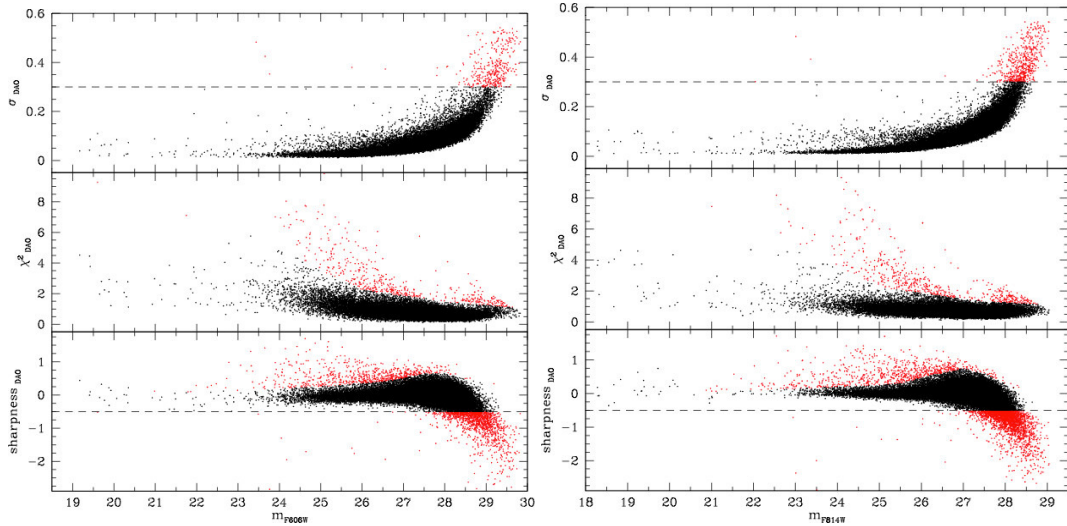


FIGURE 3.3: Selection cuts applied to the photometric error  $\sigma_{\text{DAO}}$  (top panels),  $\chi^2$  (middle panels) and sharpness (bottom panels) for the two filters. The red and black points are, respectively, the discarded and the retained objects.

We have performed PSF-fitting photometry on the  $V$ - and  $I$ - band images using the stand-alone versions of DAOPHOT and ALLSTAR (Stetson, 1987). To create the PSF models, we selected  $\sim 174$  and  $\sim 265$  bright, relatively isolated stars in  $V$  and  $I$ ,

respectively, with good spatial coverage across the entire image. The PSF was modeled with analytic MOFFAT (F606W) and PENNY (F814W) functions plus second-order additive corrections as a function of position derived from the residuals of the fit to the PSF stars. Next, we ran ALLSTAR to fit the PSF models to the sources detected independently in the  $V$  and  $I$  images. To push the photometry as deep as possible, we repeated the procedure on the subtracted images, allowing for the detection of faint companions near brighter stars. The  $V$  and  $I$  catalogs were finally cross-correlated adopting a matching radius of 1 pixel, providing a final matched catalog of  $\sim 35,000$  objects.

The calibration of the instrumental magnitudes into the *HST* VEGAMAG system was performed by applying the Bohlin (2012) time-dependent ACS zero points provided by STScI<sup>1</sup>. To determine the aperture corrections to the conventional  $0''.5$  radius aperture, we performed photometry on several bright and isolated stars in our images<sup>2</sup>.

In order to clean the photometric catalog from spurious objects, we applied selection cuts on the DAOPHOT parameters  $\sigma$  (photometric error),  $\chi^2$  and sharpness, as shown in Figure 3.3: to retain a star, we required that  $\sigma_V < 0.3$ ,  $\sigma_I < 0.3$ ,  $\text{sharp}_V > -0.5$ ,  $\text{sharp}_I > -0.5$ . Furthermore, we applied an additional cut in sharpness and  $\chi^2$  following the upper envelopes of the distributions (see Figure 3.3). A visual inspection in the images of the rejected objects, coupled with an analysis of their radial profiles, revealed that the majority of them are background galaxies, unresolved stellar clusters or blends of two or more stars. The same inspection was performed for objects brighter than  $\sim 23$  mag in  $V$  or  $I$ , independently of their  $\chi^2$  and sharpness. After these selections, we were left with  $\sim 30,000$  objects.

---

<sup>1</sup><http://www.stsci.edu/hst/acs/analysis/zeropoints>

<sup>2</sup>The correction from  $0''.5$  to an infinite aperture was done using the old Sirianni et al. (2005) values instead. However, according to Bohlin (2012) the new Encircled Energy values are within 1-2% of the corresponding Sirianni et al. (2005) results, therefore we expect a negligible effect on our photometry, considering also the typical size of the photometric errors.

## 3.2 Incompleteness and Errors

Incompleteness and errors of our photometry have been evaluated performing artificial star tests on the images. To this aim, we added artificial stars created with the adopted PSF to the images and exploited the DAOPHOT/ADDSTAR routine, that simulates real stars adding the appropriate Poisson noise to the artificial stars, and allows to cover the desired range of positions and magnitudes. The range of magnitudes covered by the artificial stars was chosen to match the data. We divided the images into grids of  $30 \times 30$  pixel<sup>2</sup> cells and placed one artificial star in each cell at each run, to efficiently compute the completeness without altering the crowding on the images. To avoid overcrowding, we also imposed that no two artificial stars laid within 20 pixels of each other, since the PSF radius is 15 pixels. The images were fully sampled because we let the starting position of the grid and the position of the artificial star within each cell vary appropriately. We performed PSF fitting photometry of the images with the added artificial stars with the same procedure as for the real data described in Section 3.1. We then cross-correlated stars in this output catalog with those in the combined catalog that includes both the original photometric catalog and the input artificial star catalog. An input artificial star was considered “lost” when it was not recovered in the output catalog, or when its recovered magnitude differed from the input value by more than 0.75 mag. We then cleaned the artificial star catalog applying the same criteria in photometric error,  $\chi^2$  and sharpness used in the real data. In total, we simulated  $\sim 1,800,000$  stars.

The completeness of our photometry was taken as the ratio of the number of recovered artificial stars over their input number in each magnitude bin. In order to account for variable crowding within the galaxy, as well as for gradients in the stellar populations (see Sections 3.3 and 3.5.1), we identified 4 regions within DDO 68 using isophotal contours, with Region 1 being the most central one and Region 4 the most external one. The contours that identify the four regions are overplotted on Figure 3.2 showing the spatial map of the resolved stars.

In Figure 3.4, left panels, we show the behavior of the  $V$  and  $I$  completeness as a function of magnitude for the four regions. As expected, Region 1 is the most incomplete one due to the largest crowding, with the completeness starting to drop at  $V \sim 26$  and  $I \sim 25$ . On the other hand, the photometry is  $\sim 100\%$  complete down to  $V \sim 28$  and  $I \sim 27$  in the most external Regions 3 and 4. The behavior of the output-input magnitudes, displayed in the right panels of Figure 3.4, provides a more realistic estimate of the photometric errors than  $\sigma_{\text{DAO}}$ . The increasing deviation of the average  $m_{\text{out}} - m_{\text{inp}}$  towards negative values indicates the increasing effect of blending toward fainter magnitudes.

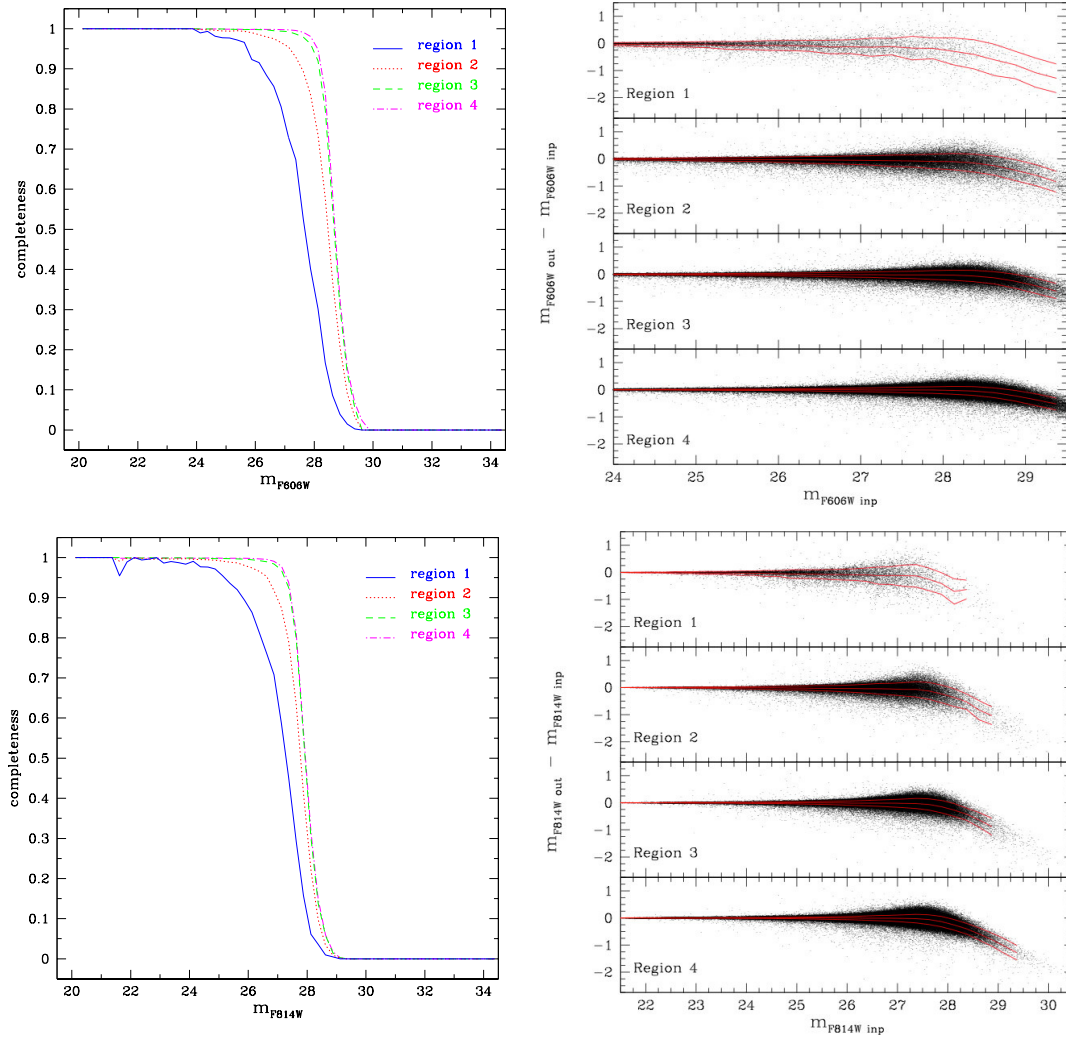


FIGURE 3.4: Completeness (left panels) and photometric errors (right panels) in  $V$  and  $I$  from the artificial star tests. The solid red curves indicate the mean of the  $\Delta\text{mag}$  distribution (central line) and the  $\pm 1\sigma$  standard deviations.

### 3.3 The Color-Magnitude Diagram

Figure 3.5 shows the total  $m_{F814W}$  vs  $m_{F606W} - m_{F814W}$  CMD of DDO 68 after applying the selection cuts described in Section 3.1. The level of the 50% completeness limit as derived from the artificial star experiments is shown in the figure, as well as the location of the TRGB as derived in Section 3.4. Also shown is the average size of the photometric errors in each magnitude bin. These are the errors resulting from the artificial star tests. The CMD shows a blue plume at  $m_{F814W} \lesssim 26.7$  and  $m_{F606W} - m_{F814W} \simeq 0$ , which is the locus of young ( $\lesssim 10$  Myr) main sequence stars and blue supergiants (BSGs, evolved stars at the hot edge of their core He-burning phase), and is typical of star-forming systems. At  $m_{F606W} - m_{F814W} \simeq 0.9$  mag, the red plume is populated by a mix of RGB, He-burning stars near the red edge of the loop and early asymptotic giant branch stars of intermediate mass, implying ages from  $\sim 20$  Myr up to several Gyr. At intermediate colors, the CMD samples the blue loop phase of intermediate mass stars, with ages between  $\sim 100$  Myr and  $\sim 300$  Myr (the oldest and faintest BL sampled by our CMD). The very red objects with  $25 < m_{F814W} < 26$  and  $m_{F606W} - m_{F814W} \gtrsim 1.2$  are thermally pulsing asymptotic giant branch and Carbon stars with ages from  $\sim 300$  Myr to  $\sim 2$  Gyr. More importantly, the presence of a well-populated RGB below  $I \simeq 26.4$  implies a population of stars at least 1 – 2 Gyr old, and possibly as old as the Hubble time. The age-metallicity degeneracy affecting RGB stars normally prevents us from claiming that the redder ones are stars as old as 13 Gyr. However, the extremely low metallicity of DDO 68 makes this claim rather plausible.

In order to account for possible gradients in the stellar populations, we constructed separate CMDs for the 4 regions selected through isophotal contours (see Figure 3.2). The CMDs are shown in Figure 3.6 with superimposed the Padova PARSEC isochrones (Bressan et al., 2012) shifted to a distance of 12.65 Mpc (Section 3.4) and with a foreground Galactic extinction  $E(B - V) = 0.018$  (Schlegel, Finkbeiner, and Davis, 1998) – notice that in the PARSEC isochrones the thermally pulsing AGB phase is not included. These CMDs clearly show a gradient in the stellar populations, with younger stars detected predominantly in the most central regions. However, the comparison with the isochrones reveals a significant population of stars with ages of  $\sim 10$  Myr or younger in Regions 2 and 3, in agreement with the presence there of a large number of H II regions (see Section 3.5.2). The old ( $> 1$  Gyr) RGB population is well detected everywhere but in Region 1. A more detailed analysis of the spatial distribution of the different stellar populations will be discussed in Section 3.5.1.

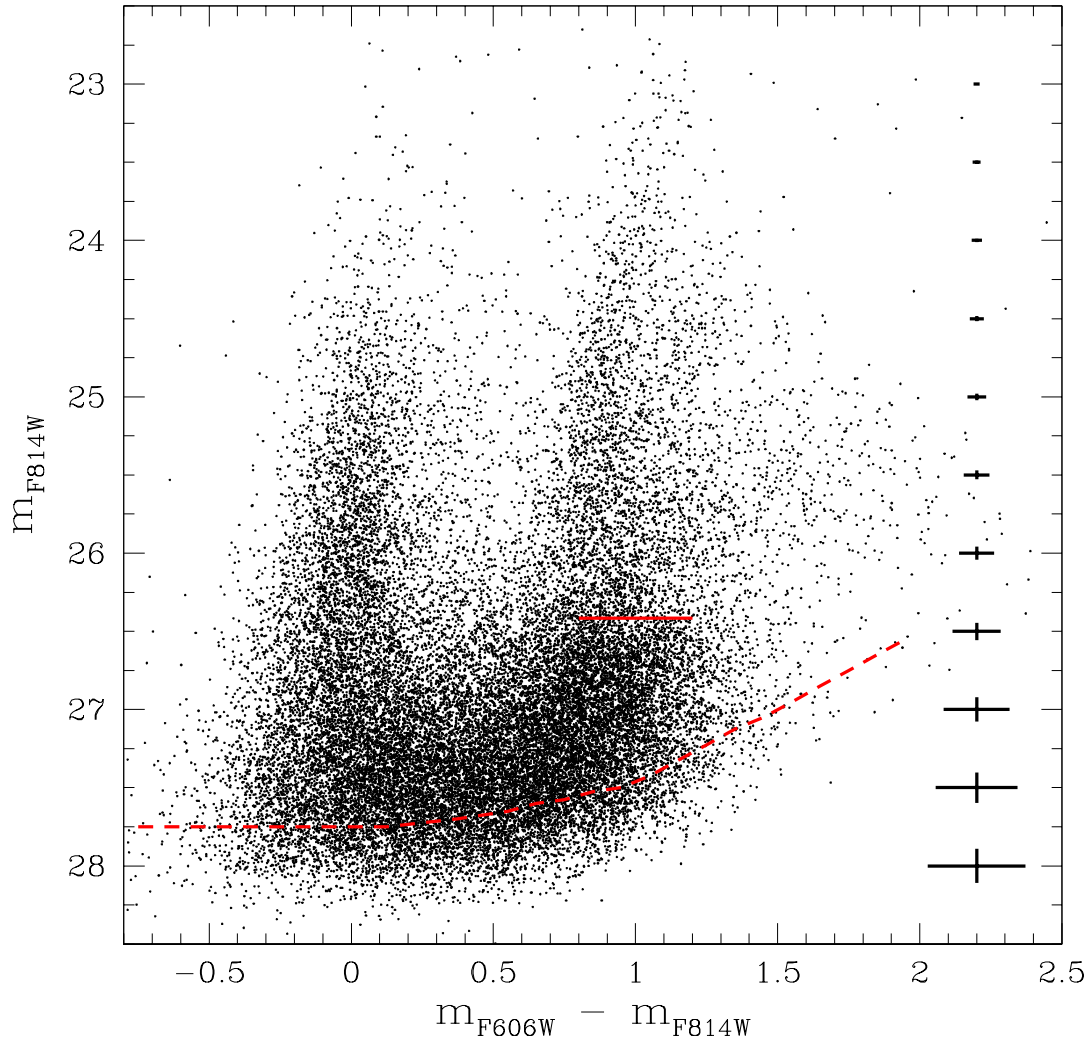


FIGURE 3.5: Total CMD of the resolved stars in DDO 68. The data are corrected for foreground extinction but not for possible extinction internal to the galaxy. The photometric errors on the right are those from the artificial star tests ( $1\sigma$  of the output-input distribution) assuming that the errors are uncorrelated, and that  $V - I = 1$ . The dashed curve provides an estimate of the 50% completeness level. The horizontal red segment indicates the magnitude of the TRGB as computed within this work.

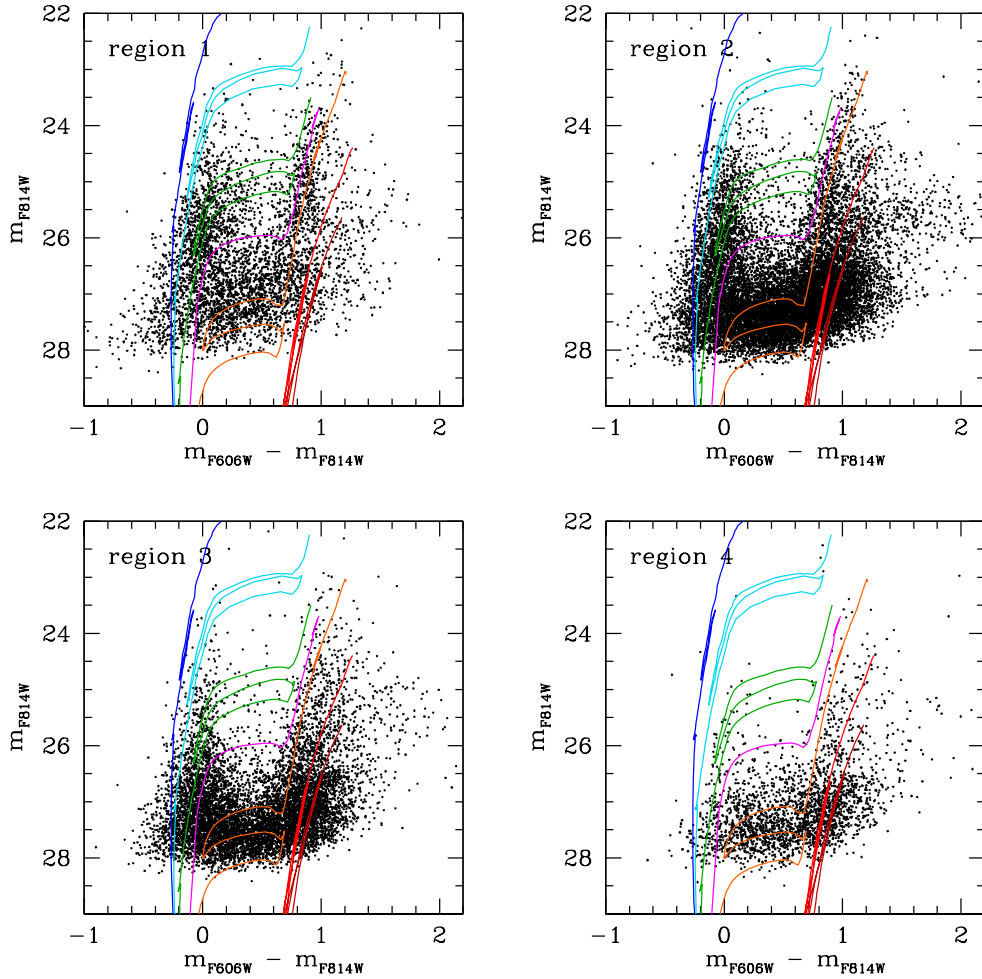


FIGURE 3.6: CMDs for the four regions of the galaxy (the region numbering goes from inside out, so Region 1 is the most internal one). The isochrones superimposed (from left to right) correspond to the following ages: 10 Myr (blue), 20 Myr (cyan), 50 Myr (green), 100 Myr (magenta), 200 Myr (orange), 2 Gyr (red) and 13 Gyr (dark red), and are plotted assuming  $(m - M)_0 = 30.51$  and  $E(B - V) = 0.018$ .

### 3.4 Distance Determination

We derived the distance of DDO 68 using the magnitude of the TRGB. We show in Figure 3.7 the  $I$ -band luminosity function (LF) of stars with color  $0.5 < V - I < 1.3$  in our catalog (the photometry was converted to the Johnson-Cousins system through the procedure outlined in Sirianni et al. 2005 in order to apply the described method).

We visually identified the TRGB as a steep increase in the LF at  $I = 26.416$ . There, RGB stars start to contribute to the LF, while at brighter magnitudes only red supergiants and AGB stars contribute. The dip in the LF fainter than  $I \simeq 27.5$  is due to incompleteness effects. The TRGB magnitude was determined with the approach described by Cioni et al. (2000), that uses the peaks in the first and second order derivatives of the LF to better identify the position of the TRGB. These peaks are shown in the middle and bottom panels of Figure 3.7. Once photometric errors and binning effects are accounted for, the first and second order derivative peaks provide a TRGB magnitude of  $I_{TRGB,1} = 26.424$  and  $I_{TRGB,2} = 26.408$ , respectively. The systematic error of this procedure was estimated by Cioni et al. (2000) to be  $\Delta I_{TRGB} = \pm 0.02$ . The additional systematic errors, due to uncertainties in the photometric zeropoints and conversions, and in aperture corrections (Sirianni et al., 2005), is  $\Delta I_{TRGB} = \pm 0.023$ . The random error on  $\Delta I_{TRGB}$  from the finite number of stars, estimated using bootstrap techniques, was found to be  $\Delta I_{TRGB} = \pm 0.057$ . Addition of these errors in quadrature yields a total (i.e. random plus systematic) error of  $\pm 0.068$  mag. After correcting for an  $I$ -band foreground extinction towards DDO 68 of  $A_I = 0.036$  [ $E(B - V) = 0.018$ ], we derive the final TRGB magnitude estimate of  $I_{TRGB,0} = 26.380 \pm 0.068$ . To derive the distance modulus, we need to compare the observed TRGB magnitude with the absolute one, which was calibrated as a function of metallicity by, e.g., Bellazzini et al. (2004). At the metallicity of I Zw 18, a comparable metallicity to that of DDO 68, this is estimated at  $M_{I,TRGB} = -4.03 \pm 0.10$  (Aloisi et al., 2007) which implies a distance modulus of  $(m - M)_0 = 30.41 \pm 0.12$  mag, i.e.,  $D = 12.08 \pm 0.67$  Mpc, in agreement with the value obtained by Tikhonov, Galazutdinova, and Lebedev (2014) from the same data.

We should however consider that the location of the TRGB is likely affected also by a significant blending of multiple stars in these crowded regions. The effect of blending is always to let the TRGB appear brighter. Indeed, when fitting the observed CMDs with synthetic ones to derive the SFH (see Section 3.6), we always found that all the evolutionary sequences are much better reproduced if the distance modulus is slightly larger, although within the uncertainties. We therefore conclude that the distance modulus of DDO 68 is  $(m - M)_0 = 30.51$ , and  $D = 12.65$  Mpc, in agreement with the independent estimate by Cannon et al. (2014). From now on we therefore adopt the latter distance for all applications.

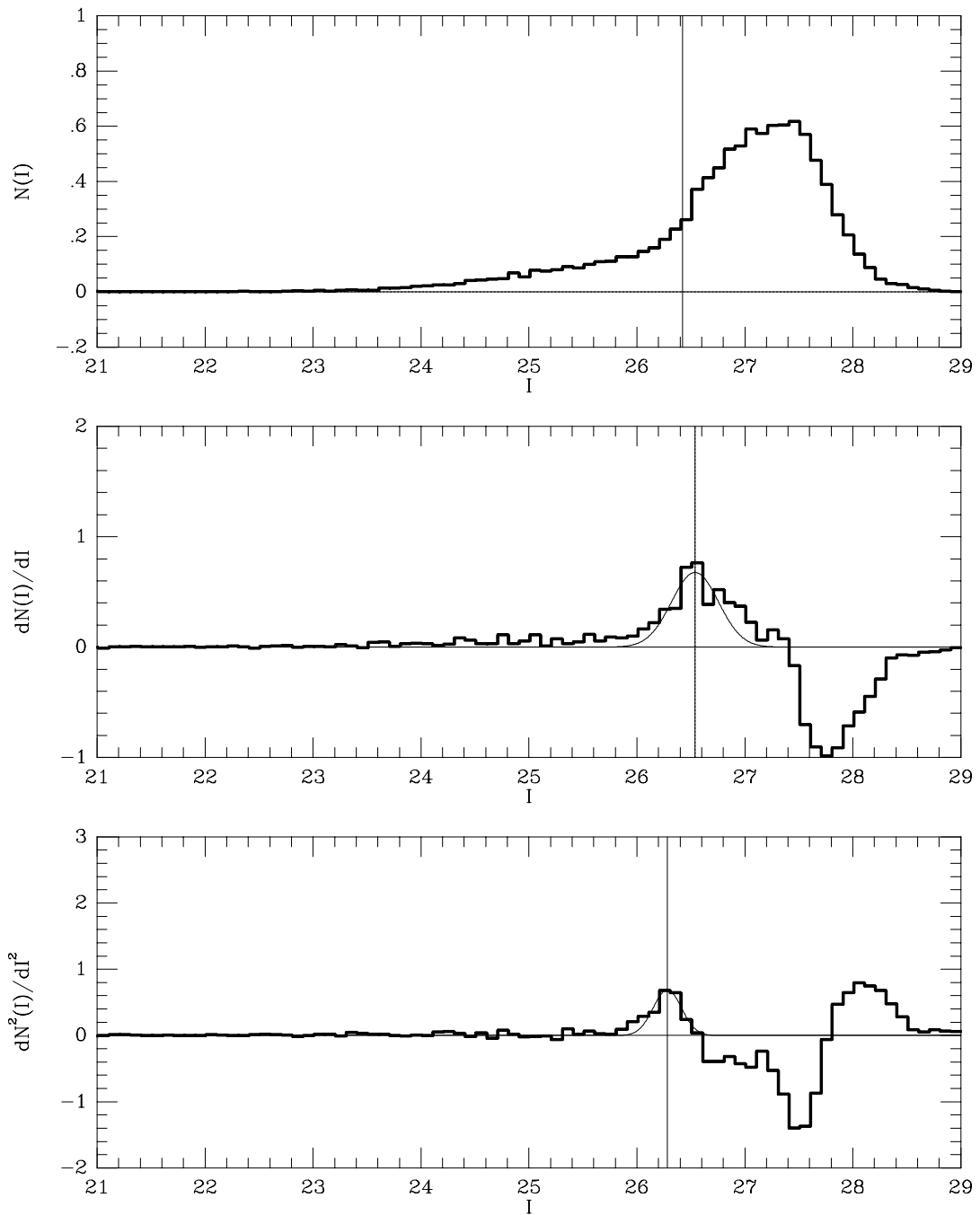


FIGURE 3.7:  $I$ -band LF (top) and its first (middle) and second (bottom) order derivatives for stars with  $V - I$  in the range  $0.5 - 1.3$ . Magnitudes are corrected for extinction. The vertical lines indicate the position of the TRGB as derived in Section 3.4. The normalization of all the vertical scales is arbitrary.

## 3.5 Stellar populations in DDO 68

### 3.5.1 Spatial distribution

As a first qualitative analysis, we looked at how the different stellar populations are distributed over the galaxy. To this purpose, we used the PARSEC (Bressan et al., 2012)  $Z = 0.0004$  stellar isochrones (corresponding to the metallicity of DDO 68's H II regions, Izotov and Thuan 2009) to identify on the CMD a few regions corresponding to different age intervals (see Figure 3.8): age  $< 20$  Myr,  $20 \lesssim$  age  $< 100$  Myr,  $100 \lesssim$  age  $< 300$  Myr, and age  $> 1$  Gyr (the RGB phase); we also identified the region of the Carbon-stars (not covered by the adopted isochrones), with typical ages between  $\sim 0.3$  and 2 Gyr. The spatial distribution of the stars in the different age intervals, as well as the global distribution for the total number of stars in the CMD, are shown in the star count density maps of Figure 3.9. To the purpose of better highlighting some particular features, the images were smoothed and arbitrarily scaled.

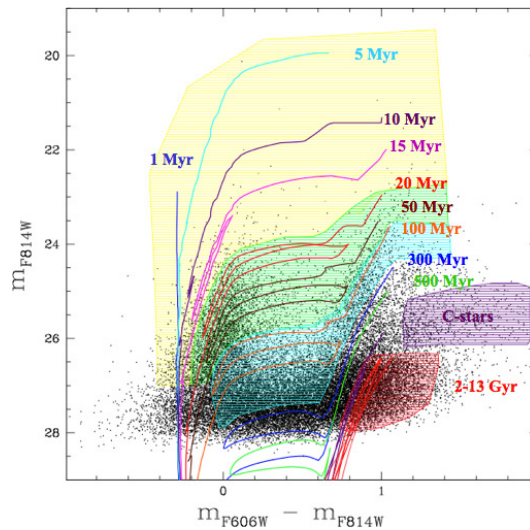


FIGURE 3.8: Selection of different age intervals identified through the  $Z = 0.0004$  stellar isochrones (Bressan et al., 2012) shown and labeled in the image.

From an inspection of the spatial maps in Figure 3.9, we immediately notice an important difference with the typical behavior of the stellar populations in other star-forming dwarfs, where the youngest stellar populations are preferentially concentrated toward the most central galaxy regions: in the case of DDO 68, in fact, stars younger than  $\sim 20$  Myr are also found at relatively large galactocentric distances, and in particular they appear to follow the arc-shaped structure well visible in the total spatial map. This is consistent with the presence there of numerous H II regions, as highlighted in Figure 3.2, which trace stars typically younger than  $\sim 10$  Myr. A similar behavior was also found in the starburst dwarf NGC 4449 (see Chapter 4), for which the presence of young stars at high galactocentric distances is likely due

to an accretion event (Annibali et al., 2012). As we consider increasingly older stellar populations, the distribution becomes more and more homogeneous, until the old ( $> 1$  Gyr) RGB population traces really well the shape of the whole galaxy. Notice that the paucity of RGB stars in the center of DDO 68 is an artifact due to the strong incompleteness affecting the most crowded Region 1, and does not reflect the intrinsic distribution of the old stellar populations.

Interestingly, we can see the disturbed arc-shaped Tail in all the age intervals, meaning that this structure is not made of young stars only, as the distribution of the  $H\alpha$  emission might have suggested. The presence of stars of all ages in the arc-shaped structure suggests that this is a possible dwarf galaxy in interaction with the central body of DDO 68, since stars older than  $\sim 1$  Gyr would not be able to remain in the form of a gravitationally unstable arc. This is in full agreement with the suggestion by Tikhonov, Galazutdinova, and Lebedev (2014) that DDO 68 consists of two distinct objects: a more massive central galaxy, DDO 68 A, traced by the spatial distribution of the bulk of the old stars, and a dwarf galaxy in interaction with DDO 68 A, namely DDO 68 B, corresponding to the arc-shaped structure, an hypothesis that we find very interesting and worth of further investigation (see Section 3.6.6).

In the RGB spatial map we also recognize a small concentration of stars toward the upper right edge of the ACS chip, noticed also by Tikhonov, Galazutdinova, and Lebedev (2014); new results on this feature are presented in Section 3.7 (Annibali et al., 2016), on the basis of new data acquired with the much larger field of view of the Large Binocular Telescope (LBT).

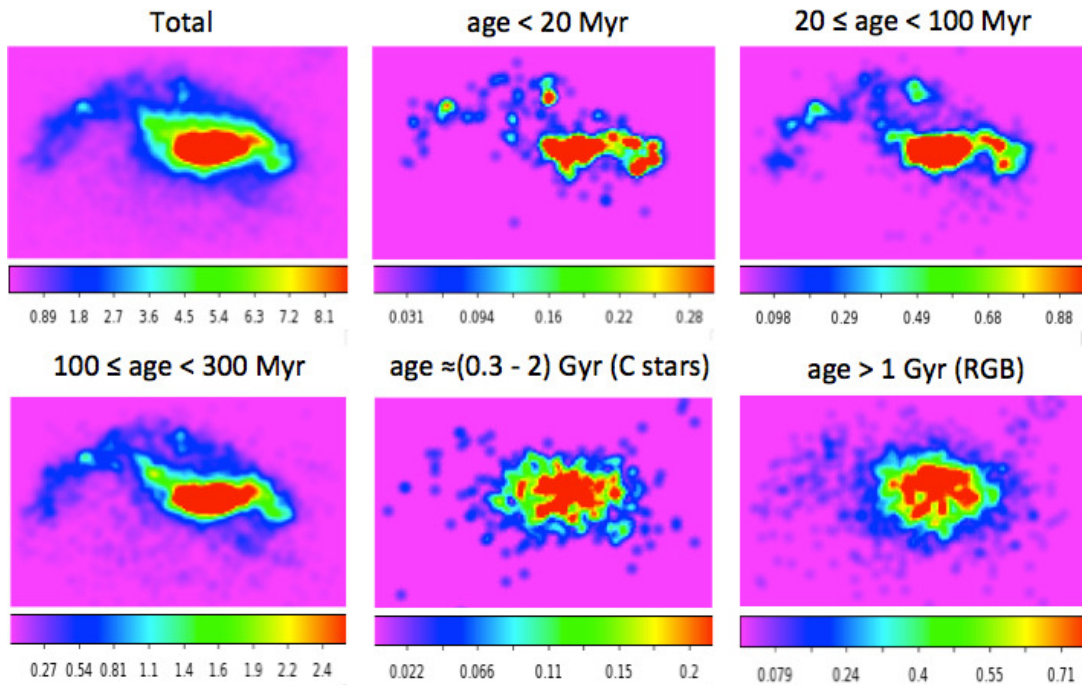


FIGURE 3.9: Density maps of stars observed in different evolutionary phases within DDO 68, as selected through their position in the CMD (see Figure 3.8). The scale is in number of stars/arcsec<sup>2</sup>.

### 3.5.2 H II regions

The F658N narrow-band filter allows us to study how the  $H\alpha$  emission is located within the galaxy and to identify the very recent concentrations of SF. In fact, the  $H\alpha$  recombination line is one of the most widely used tracers of recent SF, since it comes from the recombination of gas ionized by photons of massive stars ( $> 20 M_{\odot}$ ) and thus is expected to be observed over their typical lifetimes ( $< 10$  Myr, Leitherer et al., 1999). Thus, the ionized gas emission traces the youngest SF and provides an important piece of information on the SFH and on the dynamical interactions of the galaxy. A quite interesting and uncommon feature is that the H II regions in DDO 68 are placed mostly in the outer parts (see Figs. 3.1 and 3.2) suggesting some external effect to trigger the SF. As already discussed, this could be the presence of another object which has recently interacted with DDO 68. We selected 8 H II regions based on the gas distribution, and visually analyzed the CMDs of their resolved stars (Figure 3.10) finding that they are predominantly populated by young blue-plume stars. A comparison with stellar isochrones indicates that stars younger than  $\sim 10 - 20$  Myr are found in these regions, in agreement with the presence of ionized gas. The regions in Figure 3.10 were labeled following Pustilnik, Kniazev, and Pramskij (2005) and Izotov and Thuan (2009).

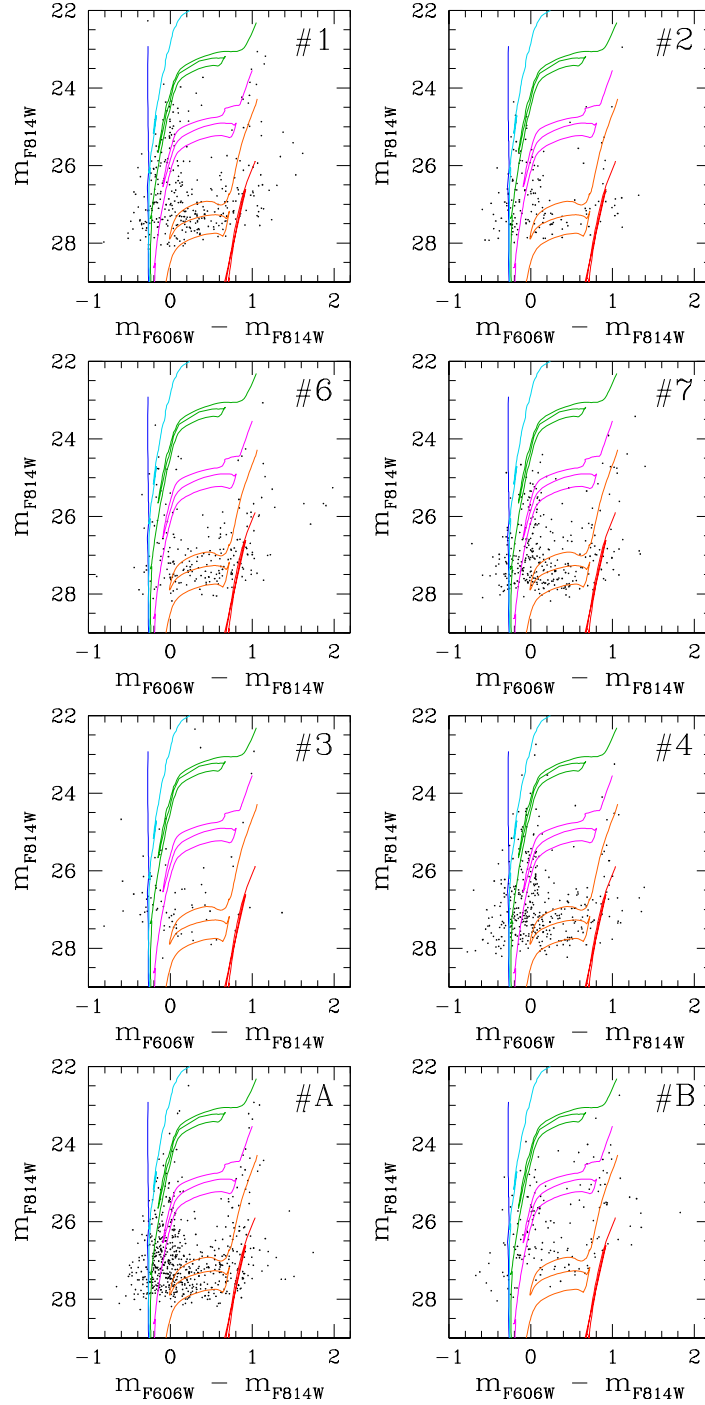


FIGURE 3.10: CMDs of the H II regions in DDO 68. The isochrones superimposed (from left to right) correspond to the following ages: 1 Myr (blue), 10 Myr (cyan), 20 Myr (green), 50 Myr (magenta), 200 Myr (orange) and 2 Gyr (red). The numbers follow the labeling by Pustilnik, Kniazev, and Pramskij (2005) and Izotov and Thuan (2009) except for the last two regions (A and B) that they don't take into account in their analysis.

## 3.6 Star Formation History

The SFH of DDO 68 was derived by comparing the observed CMDs with synthetic ones, following the method described in Chapter 2. To this purpose, we adopted two independent procedures: the one originally developed by R. P. van der Marel and described in Grocholski et al. (2012), SFHMATRIX, based on a NNLS approach, and SFERA (see Section 2.3). The adoption of two different procedures allows us to consider the systematic uncertainties on the derived SFHs.

### 3.6.1 Basis Functions

We created the BFs starting from the Padova PARSEC isochrones V.1.2S (Bressan et al., 2012), which include the pre-main sequence evolutionary phase (while the TP-AGB phase is still not included). We adopted a Kroupa IMF (Kroupa, 2001) from 0.08 to 120  $M_{\odot}$  and assumed a 30% fraction of binary stars, whose masses were extracted from the same IMF of the “main” population. The BFs were computed up to an age of  $\sim 13.5$  Gyr with a logarithmic time duration of  $\Delta \log(\text{age}) = 0.25$ , except for ages younger than 1 Myr which were grouped into a single time bin. The logarithmic step is chosen to take into account the lower time resolution as a function of the look-back time. The star formation rate is assumed to be constant within each episode.

Absolute magnitudes were converted into apparent ones applying a foreground reddening of  $E(B - V) = 0.018$  from the NASA/IPAC Extragalactic Database<sup>3</sup>, and a distance modulus allowed to vary by 1 mag around the value  $(m - M)_0 = 30.41$  derived from the TRGB (see Section 3.4). Eventually, the best value to fit all the evolutionary sequences and LFs turned out to be  $(m - M)_0 = 30.51$ . To incorporate observational effects and systematic errors (due to e.g. photometric blends) we assigned photometric errors to the synthetic stars using the difference between output and input magnitudes of the artificial stars (see Figure 3.4).

We have used the two different procedures SFERA and SFHMATRIX to identify the weighted combination of BFs that best reproduces the observational CMDs and thus the best SFH. In both cases, the metallicity is treated as a free parameter. We don’t assume an age-metallicity relation nor the same metallicity for all the stars; however, since we have information on the current metallicity (corresponding to  $Z \sim 0.0004$ ) from the H II regions, we allow the metallicity to vary in the range  $[0.0002 - 0.002]$ . For all regions, the metallicity inferred by the codes in the youngest bins is between  $Z \sim 0.00035$  and  $Z \sim 0.0005$ , consistent with the observed values from the H II regions.

---

<sup>3</sup>The NASA/IPAC Extragalactic Database is operated by the Jet Propulsion Laboratory, California Institute of Technology, under contract with the National Aeronautics and Space Administration. <https://ned.ipac.caltech.edu>

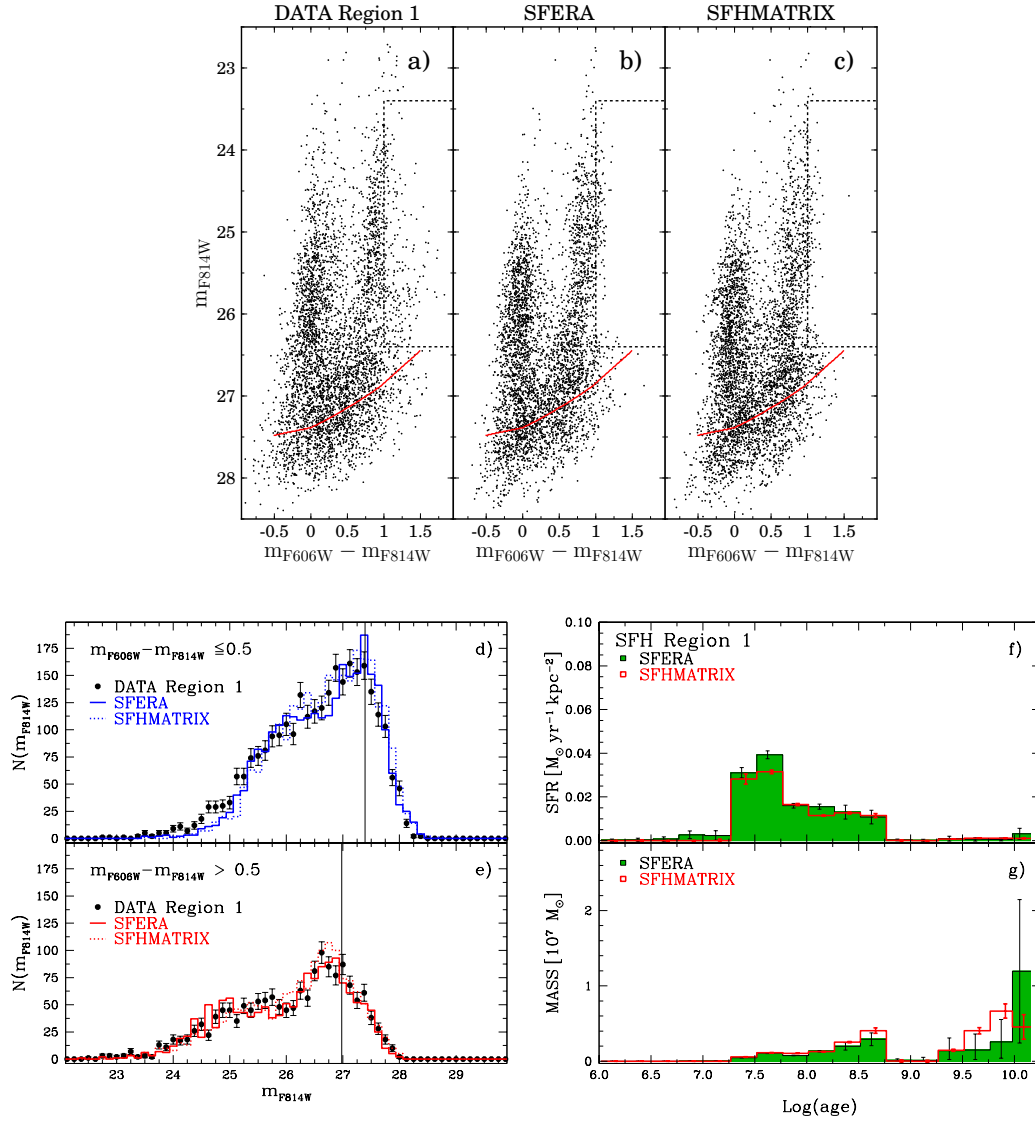


FIGURE 3.11: Results of the synthetic CMD method for Region 1. *Top panels:* a) observed CMD for Region 1, b) best-fit synthetic CMD with SFERA and c) best-fit synthetic CMD with SFHMATRIX (both obtained considering only the region with completeness above 30% indicated by the red solid curve). The dotted box shows the TP-AGB region that was excluded from the minimization. *Middle panels:* LF in the blue (d) and red (e) parts of the observed (black points with Poissonian error) and synthetic CMDs (solid line for SFERA, dotted line for SFHMATRIX). The vertical lines indicate the average faintest magnitudes that were considered for the fit. *Bottom panels:* best-fit SFH (f) normalized over the area of the region and recovered stellar mass (g) with SFERA (green solid histograms) and SFHMATRIX (red histograms). Notice that the error bars coming out from SFHMATRIX have to be considered as lower limits to the real uncertainties of the solution, since only statistical errors are included.

### 3.6.2 REGION 1

Panel a) of Figure 3.11 shows the observed CMD of the most crowded Region 1 of DDO 68, together with the synthetic realizations inferred from the best-fit solutions of the SFERA (panel b) and SFHMATRIX (panel c) codes. We excluded from the minimization the cells of the CMD with a completeness below 30% where the uncertainties become significant. We used a lower completeness threshold with respect to the other regions in order to reach at least the TRGB and have a strong constraint on the CMD. We run several tests using a different completeness limit (up to 50%) and this yielded results that are qualitatively similar. We choose to keep the results with a completeness down to 30% to include the RGB stars, since they are the only signature of epochs older than 1 – 2 Gyr ago; we do take into account the larger uncertainty due to this choice and we are confident that this does not affect the main conclusions of the analysis.

When using SFHMATRIX, we created a grid with a constant cell size of 0.5 both in color and in magnitude: given the low number of stars in Region 1, this cell size allows to minimize the statistical fluctuations without losing information on the CMD. For the same reason, we treated the box at  $0.5 < m_{F606W} - m_{F814W} < 1.3$  and  $26.4 < m_{F814W} < 29$  (i.e. the RGB) as a single pixel, while we excluded from the minimization the box at  $1 < m_{F606W} - m_{F814W} < 2$  and  $23.4 < m_{F814W} < 26.4$ , corresponding to the TP-AGB phase which is not included in the PARSEC isochrones we used here.

In SFERA, where flexibility in the construction of the grid is possible, we chose a quite large cell size (0.5 both in color and magnitude) for the brightest stars with  $m_{F814W} < 24$  to balance the low statistics caused by the few number of bright stars; we chose an intermediate cell size (0.1 in color, 0.2 in magnitude) for the blue and red plumes and for the lower MS; for the RGB instead we implemented a variable random binning from 1 to 16 cells in the box  $0.5 < m_{F606W} - m_{F814W} < 1.3$  and  $26.4 < m_{F814W} < 29$ , that we changed at every bootstrap in order to minimize the bin dependence of the results.

To reproduce the observed CMD and LF in Region 1, as well as in all the other regions of DDO 68, we found more satisfactory to adopt a slightly higher distance modulus than that derived from the TRGB [that is  $(m - M)_0 = 30.51$  instead of  $(m - M)_0 = 30.41$ ]; this larger distance modulus, which is still inside the errors of the previous determination, implies a distance of 12.65 Mpc.

We show in Figure 3.11 the solutions found by the two codes for the best CMD (b-c), LF (d-e) and SFH (f-g). It is evident that the codes are both able to well reproduce the overall morphology of the observed CMD, although with some differences. In particular, both codes tend to under-predict the number of stars in the blue LF ( $m_{F606W} - m_{F814W} \leq 0.5$ ) at  $24 < m_{F814W} < 25.25$ , i.e. the blue supergiants. A similar problem was found for another very low-metallicity dwarf galaxy, I Zw 18, for which we derived the SFH (Annibali et al., 2013). As already discussed in that study, possible explanations for the observed discrepancy are: i) the completeness behavior with magnitude is not properly taken into account, because of the severe crowding of this central region; ii) some of the most luminous blue stars in the CMD are not actually single objects but blends of two or more blue stars; iii) the timescales

for the evolution of massive stars in the brightest post-MS phase are not properly modeled.

It is plausible that models including additional parameters, like stellar rotation (Meynet and Maeder, 2002), could improve the fit of the brightest objects in the CMD, but these models are not implemented yet for DDO 68's metallicity.

Panels f) and g) of Figure 3.11 show the best-fit SFHs (normalized over the area of the region) and the stellar mass assembled in the different time bins, where the solid green and the red histograms are the output of SFERA and SFHMATRIX, respectively. These SFHs are quite in agreement with each other, and clearly show an old activity, once again confirming the presence of a population of stars at least 1 Gyr old and probably as old as the Hubble time. Notice that the low uncertainty inferred for some bins with very low SF (e.g. 8.75 – 9.25) could be an artifact of the bootstrap approach (see Dolphin 2013 for a detailed discussion). The mass in stars at epochs older than 1 Gyr is  $\sim 70\%$  of the total stellar mass formed in this region. There is no evidence of a very young ( $< 5$  Myr) SF episode, while the strongest burst ( $\text{SFR}_{peak} \simeq 3.9 \times 10^{-2} M_{\odot}/\text{yr}/\text{kpc}^2$ ) occurred between 20 and 60 Myr ago.

The results for the average SFR and for the stellar mass formed in different time intervals are summarized in Table 3.1.

### 3.6.3 REGION 2

Figure 3.12 shows the results for Region 2. We excluded from the fit the region of the CMD where the completeness is below 50%. Given the larger number of stars with respect to Region 1, we chose to use a pixel size of 0.25 both in color and magnitude when running SFHMATRIX. We masked again the region of the TP-AGB phase. For SFERA we kept the same (variable) binning as for Region 1.

The blue LF in panel d) of Figure 3.12 shows that SFHMATRIX under-predicts the counts at  $27 < m_{F814W} < 27.5$ , while SFERA does so between 27 and 27.25, and both codes slightly over-predict the counts below 27.5; these regions correspond to the lower part of the MS where probably both the spatial resolution and the completeness of the photometry are degrading fast. For what concerns the red LFs ( $m_{F606W} - m_{F814W} > 0.5$ ), SFERA provides a quite good agreement in the brightest bins, and at  $\sim \pm 0.5$  magnitudes around the TRGB; on the other hand, we notice an under-prediction of counts at  $25 < m_{F814W} < 26$ , where the (not-simulated) TP-AGB stars are located, and at  $27 < m_{F814W} < 27.5$ . The SFHMATRIX code, instead, provides a better agreement in this magnitude range, but tends to over-predict the counts around the TRGB.

The SFH shows an overall trend very similar to that of Region 1, but the SFRs are almost 10 times lower ( $\text{SFR}_{peak} \simeq 0.6 \times 10^{-2} M_{\odot}/\text{yr}/\text{kpc}^2$  between 20 and 60 Myr) and were in fact multiplied by a factor of 10 in the plot to make them more visible. Also in this region we find the majority of the mass locked in the oldest ( $> 1$  Gyr) stars, while there is no evidence for a significant recent activity.

This is the region where we find the largest differences between the results from the two codes, in particular in the formed stellar mass. In general, we consider SFERA

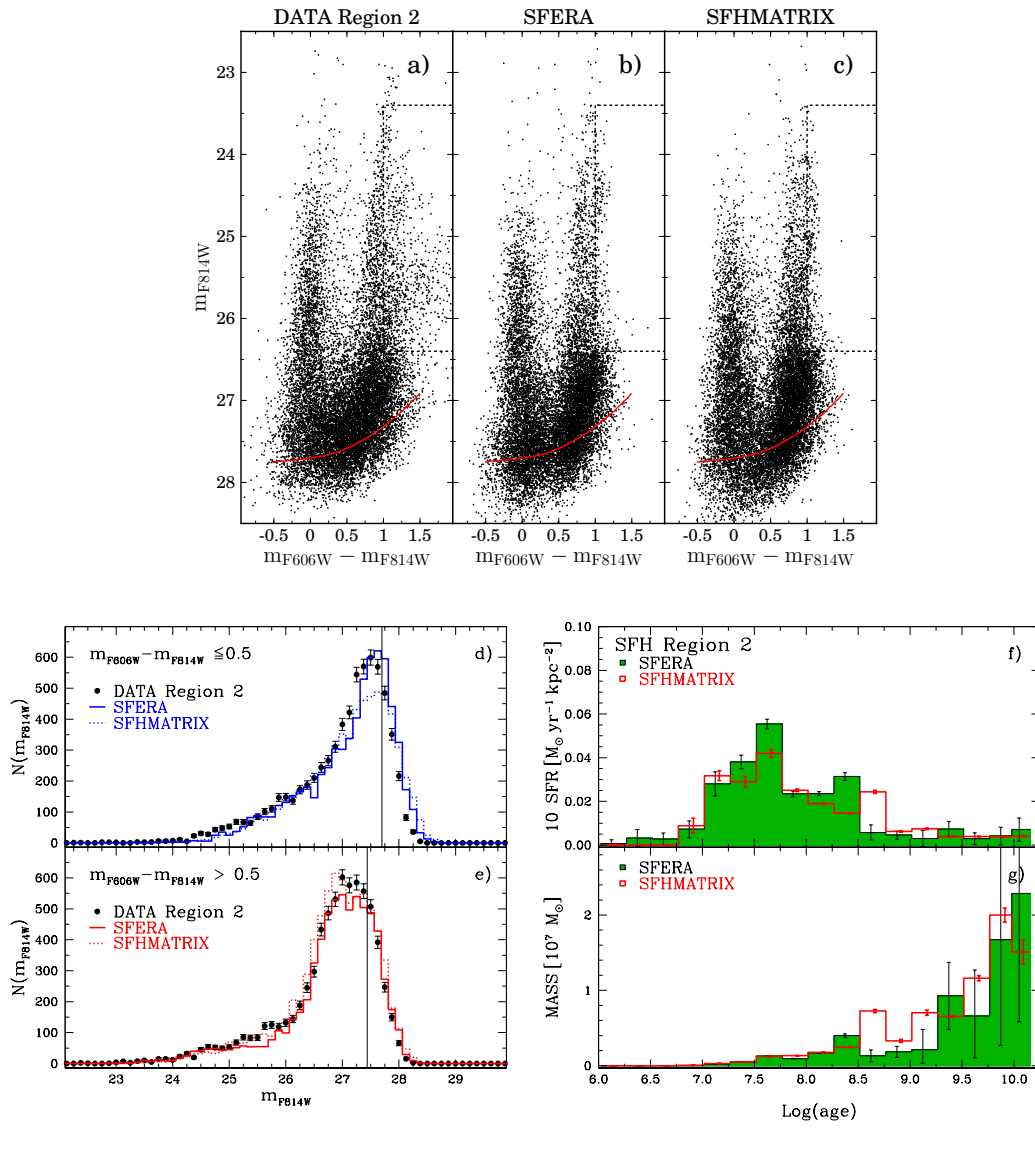


FIGURE 3.12: Same as Figure 3.11 but for Region 2 (the best-fit is performed in the region with completeness above 50%). Notice that in this case the SFRs of panel f) are multiplied by 10.

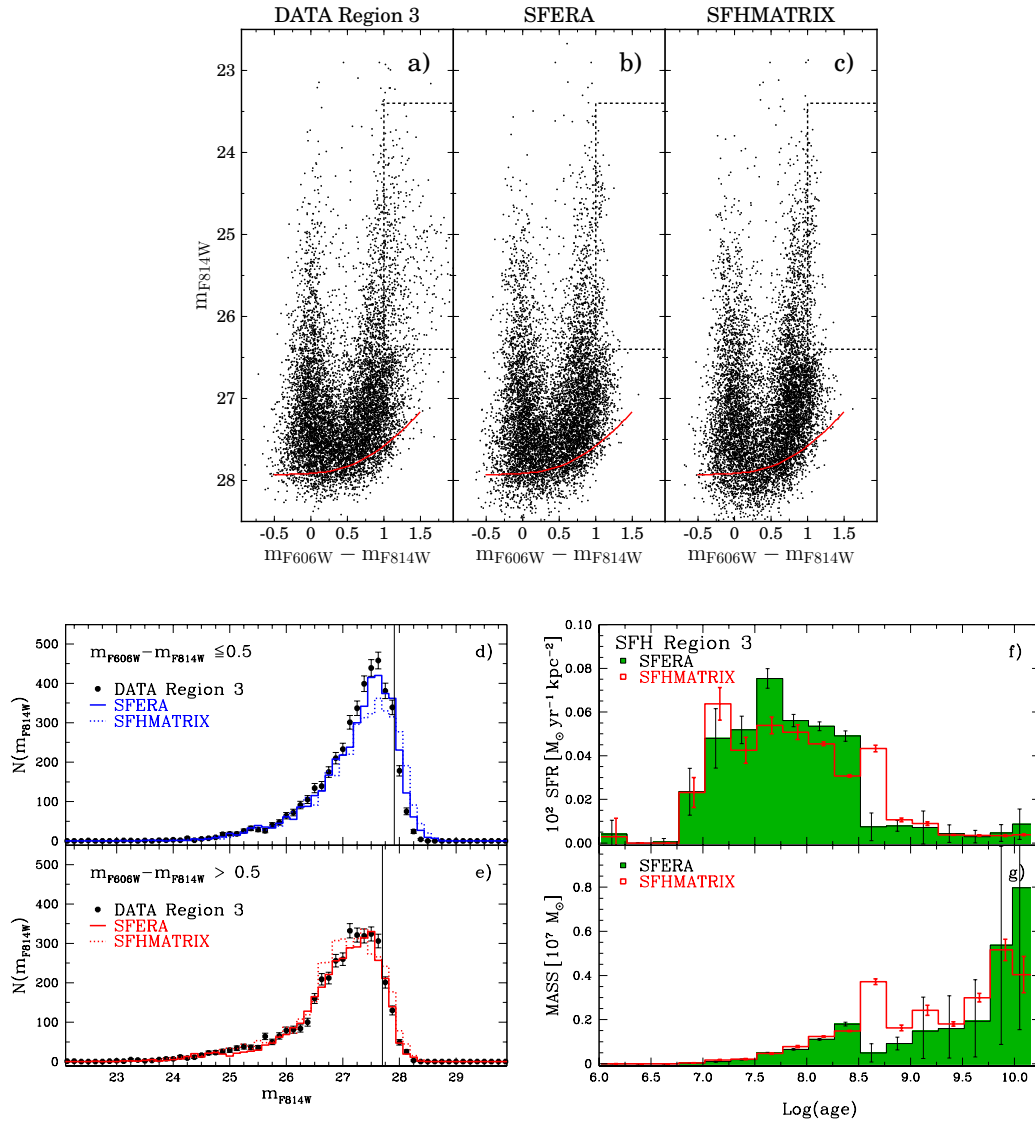


FIGURE 3.13: Same as Figs. 3.11 and 3.12 but for Region 3. Notice that in this case the SFRs of panel f) are multiplied by 100.

more reliable, because it minimizes an actual likelihood using Poissonian statistics, and does not make the simplifying assumption of Gaussian statistics that is inherent to the  $\chi^2$  minimization of SFHMATRIX. However, for the main characteristics of DDO 68 implied by our SFHs, the codes yield broadly consistent results (see Table 3.1).

### 3.6.4 REGION 3

For Regions 3 and 4 of DDO 68 we kept the same binning of Region 2 and the same completeness limit of 50%. As shown in Figure 3.13, Region 3 has the best reproduced CMD and LFs. With SFERA there are no relevant discrepancies between the data and the models, while with SFHMATRIX there is an under-prediction of the blue counts at  $m_{F814W} \sim 27.5$  and an over-prediction of the red counts at  $26.5 < m_{F814W} < 27$ .

The SFRs per unit area plotted in panel f) are multiplied by a factor of  $10^2$  to make them more visible; this is the region where a very recent SF activity is found by both codes. This is in agreement with the fact that the majority of the nebular emission is found in this region. The remaining evolution of the SF is quite similar to the other regions, but with lower rates ( $SFR_{peak} \simeq 7.5 \times 10^{-4} M_{\odot}/\text{yr}/\text{kpc}^2$  between 20 and 60 Myr).

### 3.6.5 REGION 4

Figure 3.14 shows the CMD, LFs and SFH of the most external region of the galaxy. There are very few stars here and a strong contamination from background galaxies. In fact, as expected, SFHMATRIX has some troubles in reproducing the right number of stars as can be noticed from the LFs. In both the blue and red LFs SFHMATRIX under-predicts the counts, also in the RGB region. SFERA instead well reproduces the blue LF, while it under-predicts the number of stars in the red LF at  $27 < m_{F814W} < 27.5$ . The plotted SFRs are multiplied by a factor of  $10^3$ , and in general are very low, showing a peak two bins older than the previous regions ( $SFR_{peak} \simeq 0.8 \times 10^{-4} M_{\odot}/\text{yr}/\text{kpc}^2$  between 100 and 200 Myr). This is not surprising since we expect this region to host mainly old populations of stars as discussed in Section 3.5.1. The oldest bins provide again the most relevant contribution to the formed stellar mass.

The total average SFR over the whole galaxy is  $\simeq 0.01 M_{\odot}/\text{yr}$ , and the corresponding astrated mass over the whole Hubble time is  $M_{\star, \text{TOT}} \simeq 1.3 \times 10^8 M_{\odot}$ .

Overall, the general good agreement between the solutions of SFHMATRIX and SFERA seems to suggest that the  $\chi^2$  bias is not significantly affecting the results.

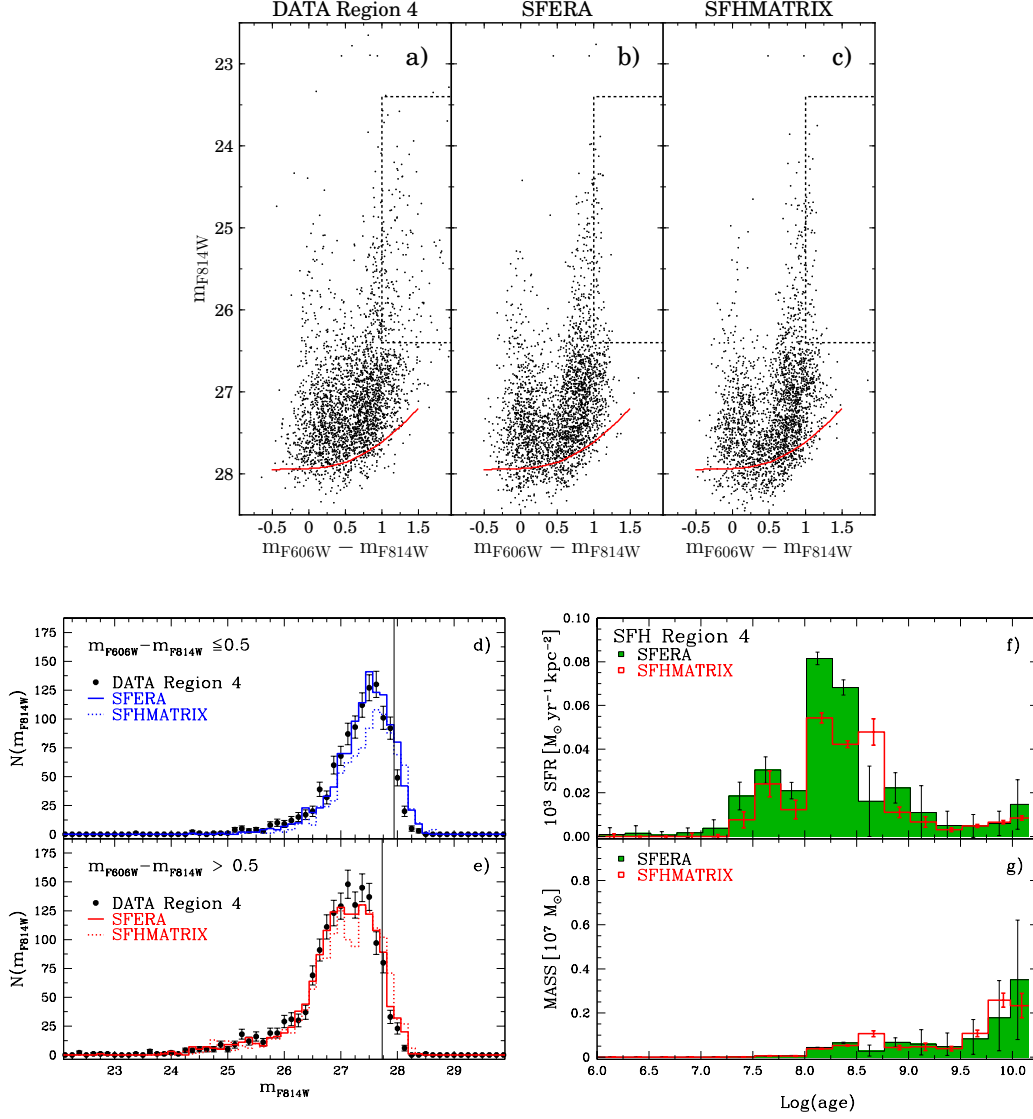


FIGURE 3.14: Same as Figs. 3.11–3.13 but for Region 4. Notice that in this case the SFRs of panel f) are multiplied by 1000.

TABLE 3.1: Summary of the results for SFRs and stellar mass in the four regions.

region	area [kpc <sup>2</sup> ]	(SFR) <sub>age&lt;1 Gyr</sub> [M <sub>⊙</sub> /yr/kpc <sup>2</sup> ]		M <sub>★TOT</sub> [10 <sup>7</sup> M <sub>⊙</sub> ]		M <sub>★age&gt;1 Gyr</sub> [10 <sup>7</sup> M <sub>⊙</sub> ]	
		SFERA	SFHMATRIX	SFERA	SFHMATRIX	SFERA	SFHMATRIX
1	1.1	$(7.91 \pm 0.91) \times 10^{-3}$	$(9.68 \pm 0.37) \times 10^{-3}$	$2.62 \pm 1.04$	$2.74 \pm 0.20$	$1.75 \pm 1.03$	$1.67 \pm 0.19$
2	9.2	$(1.28 \pm 0.12) \times 10^{-3}$	$(1.98 \pm 0.03) \times 10^{-3}$	$6.94 \pm 2.49$	$7.85 \pm 0.19$	$5.76 \pm 2.49$	$6.03 \pm 0.19$
3	26.5	$(2.17 \pm 0.20) \times 10^{-4}$	$(3.66 \pm 0.07) \times 10^{-4}$	$2.41 \pm 0.84$	$2.61 \pm 0.10$	$1.83 \pm 0.84$	$1.64 \pm 0.10$
4	68.5	$(0.31 \pm 0.05) \times 10^{-4}$	$(0.37 \pm 0.02) \times 10^{-4}$	$0.93 \pm 0.34$	$0.94 \pm 0.07$	$0.72 \pm 0.34$	$0.68 \pm 0.07$

### 3.6.6 DDO 68 B

The peak in the star formation activity between  $\sim 30$  Myr and  $\sim 50$  Myr that we find in all regions of DDO 68 hints that this epoch may have been affected by a merging/accretion event between two different bodies, as suggested by Tikhonov, Galazutdinova, and Lebedev (2014). For this reason we performed a separate analysis of the arc-shaped structure (dubbed by Tikhonov, Galazutdinova, and Lebedev 2014 DDO 68 B) to explore the possibility that the increased young star formation in Region 3 could be the result of this interaction.

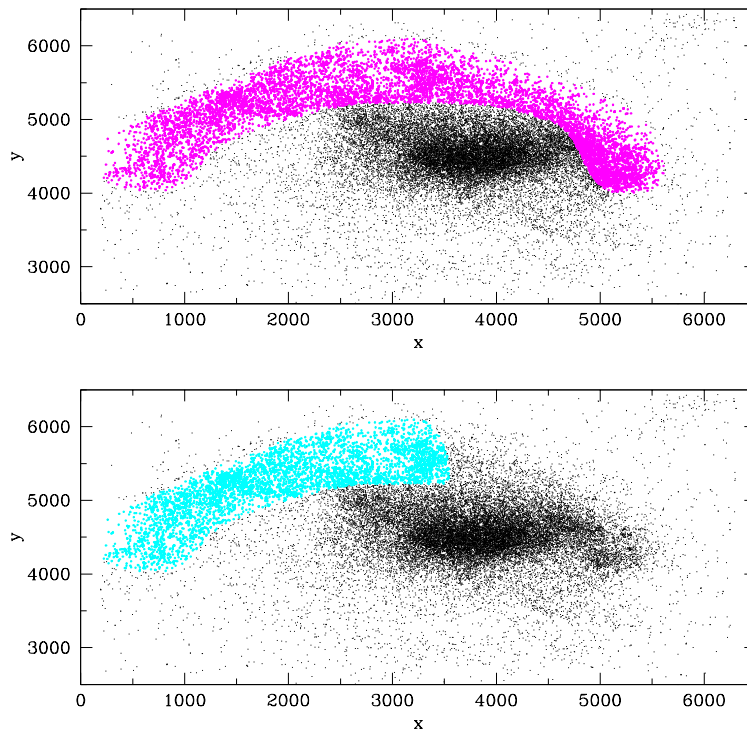


FIGURE 3.15: Map of the stars in DDO 68 with enhanced in magenta and cyan two possible configurations of the arc-shaped structure identified as DDO 68 B and used for a separate derivation of the SFH.

In Figure 3.15 we show two selections of stars falling in the Tail for which we re-derived the SFH. The results are shown in Figure 3.16 (the SFRs per unit area are multiplied by a factor of  $10^2$  as for Region 3). The SFH of the candidate accreted satellite in the last hundreds Myr is qualitatively similar to that of Region 2, that can be considered as representative of the main body, although the SF activity in the configuration 2 of the Tail is definitely more skewed towards more recent epochs, and close to absent at epochs older than 1 Gyr, as if the activity in the candidate satellite was mostly triggered when the interaction with the main body became strong. The young peak is the same as in Region 3, as expected since most of the  $H\alpha$  emission is in common. However, the SFR normalized over the area in each bin is roughly

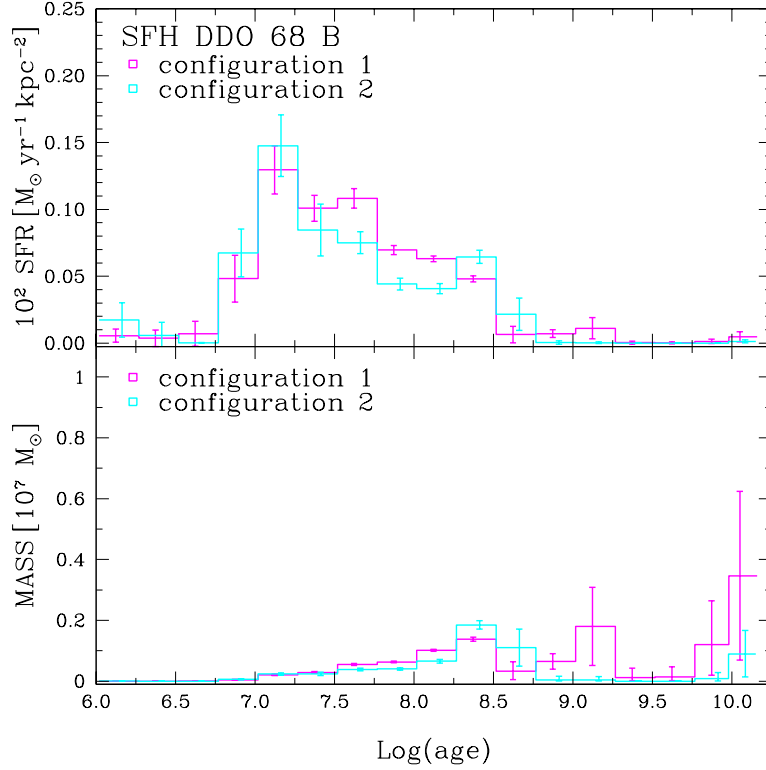


FIGURE 3.16: SFHs for stars in magenta and cyan in Figure 3.15. Notice that in this case the SFRs are multiplied by 100.

double in the Tail with respect to the whole Region 3, since it has a smaller area but the majority of the young and intermediate-age stars.

The average SFR over the last  $\sim 1$  Gyr in the Tail Configuration 1 is  $\langle \text{SFR} \rangle_{\text{Tail 1}} \simeq 3 \times 10^{-4} M_{\odot}/\text{yr}/\text{kpc}^2$  while the total formed stellar mass is  $M_{\star \text{Tail 1}} \simeq 1.2 \times 10^7 M_{\odot}$  that is  $\sim 1/10$  of the stellar mass of the whole galaxy. In Configuration 2 they are  $\langle \text{SFR} \rangle_{\text{Tail 2}} \simeq 4 \times 10^{-4} M_{\odot}/\text{yr}/\text{kpc}^2$  and  $M_{\star \text{Tail 2}} \simeq 0.6 \times 10^7 M_{\odot}$  respectively. The metallicity in the most recent bin of Configuration 2 is  $Z \sim 0.0008$ , slightly higher than that of the other regions; however, the uncertainties on this determination prevent a firm conclusion.

The presence of recent SF in Region 3 is thus compatible with the merging/accretion scenario, that is explored in more details in the next Section.

### 3.7 A Flea with Smaller Fleas that on Him Prey <sup>4</sup>

To obtain very deep imaging that could reveal the presence of previously unknown faint stellar substructures connected to DDO 68, we exploited the perfect combination of large field of view and excellent photometric depth of the LBT Large Binocular Camera (LBC) covering a large area around our target. Here we report the successful results obtained from the LBT photometry, with clear evidence that, in addition to the Tail and DDO 68 C, the system also hosts an independent small stream and several arclike structures. To better interpret the LBT data in terms of the dynamical status of the system, we have also run N-body simulations and found that the observed configuration is consistent with the presence of at least two different satellites being accreted by the galaxy main body.

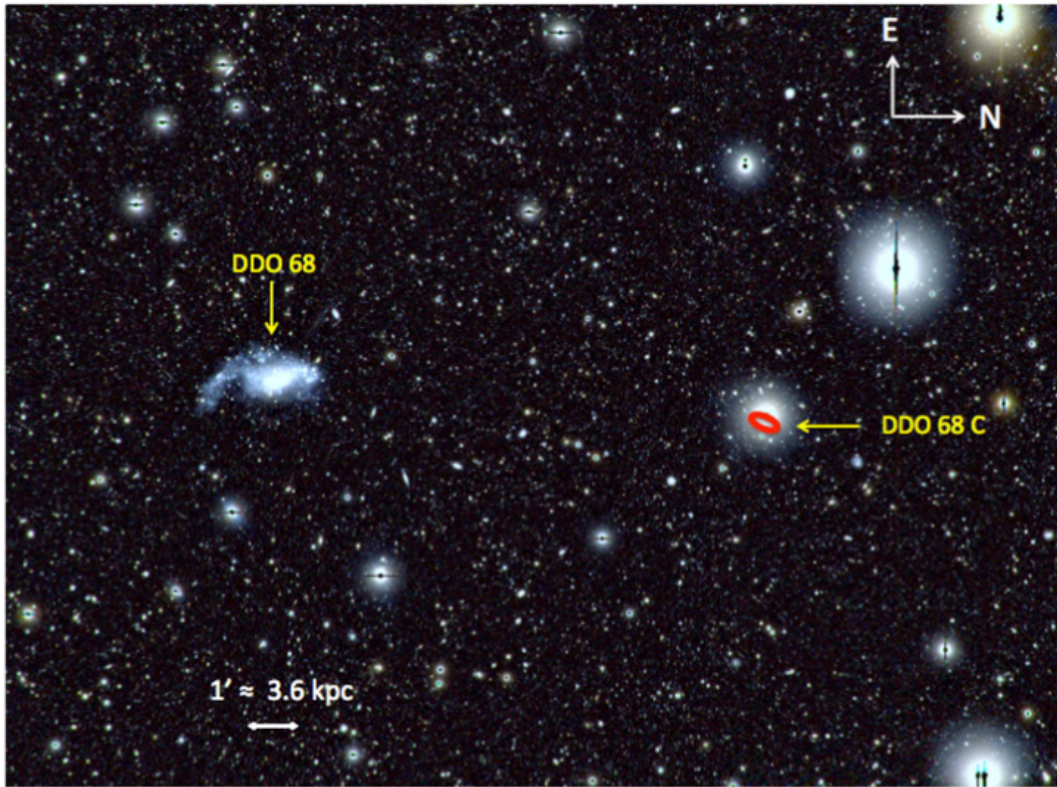


FIGURE 3.17: Deep LBC g and r color-combined image of DDO 68. The positions of DDO 68 and of the candidate H I companion DDO 68 C are indicated. DDO 68 C is masked by a bright foreground star, but we have drawn its spatial extension (red ellipse) as detected in the ultraviolet GALEX images. The total displayed field of view is  $\sim 0.4 \times 0.3$  square degrees, corresponding to  $\sim 90 \times 70$  kpc<sup>2</sup> at DDO 68 distance of  $\sim 12.7$  Mpc.

<sup>4</sup>From Jonathan Swift's *On Poetry: a Rhapsody*: So, naturalists observe, a flea/has smaller fleas that on him prey/and these have smaller still to bite em/and so proceed ad infinitum.

Our color-combined LBT image is displayed in Figure 3.17, where both DDO 68 and the position of the candidate companion DDO 68 C (Cannon et al., 2014) are indicated. The new substructures/satellites discovered here are much closer to the main body of DDO 68 and are visible in Figure 3.18, where blow-ups of some portions of the whole image are displayed. Remarkably, Figure 3.18, besides the already well known Tail, reveals several previously undetected faint stellar substructures. The most prominent of these are an arc embracing the western side of DDO 68 for a projected extension of  $\sim 5$  kpc (hereafter the Arc) and a stream (which we dub DDO 68 S1, i.e., Stream 1) as faint as  $\mu_r \sim 28.7$  mag arcsec $^{-2}$  that extends for  $\sim 4.6$  kpc along the NE-SW direction (the system at the NE end of S1 is most likely a background spiral galaxy). While S1 is well detected in both the g and r images, the Arc is mostly visible in g, due to the presence of younger stars than in S1.

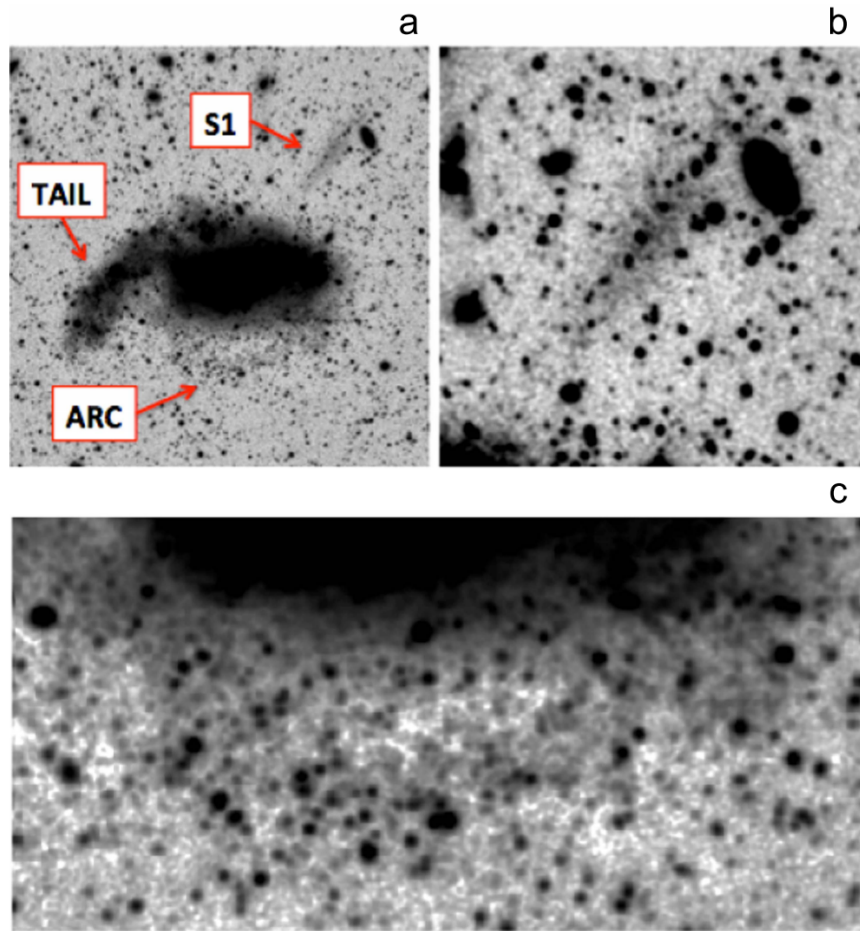


FIGURE 3.18: Blow-ups of key portions of the LBT image of DDO 68. (a) Portion of the g-band image (FoV  $\sim 280 \times 280$  arcsec $^2$ , or  $17 \times 17$  kpc $^2$ ) showing the Tail, Arc, and Stream S1. A Gaussian smoothing has been applied to the image to better highlight low surface-brightness features. (b) Further blow-up (FoV  $\sim 90 \times 90$  arcsec $^2$ , or  $5 \times 5$  kpc $^2$ ) in the r band showing S1 in detail. (c) Blow-up of panel (a) (FoV  $\sim 140 \times 60$  arcsec $^2$ , or  $8.4 \times 3.6$  kpc $^2$ ) in the g band showing the Arc in detail.

### 3.7.1 Physical properties of the substructures

Both the Arc and a small portion of S1 fall into our ACS images and are resolved into individual stars. Their CMDs host RGB stars with luminosities compatible with the distance of DDO 68 (see Figure 3.19). This indicates that both structures are physically associated with the galaxy.

The CMD of the Arc implies a wide range of ages, with most of the measured stars  $\sim 200 - 300$  Myr old, a few as young as 50 Myr, and several RGB stars older than 2 Gyr and possibly up to 13 Gyr old. Unfortunately, the age-metallicity degeneracy of the RGB colors, coupled with the large photometric errors, prevents us from safely distinguishing a 2 Gyr old from a 13 Gyr old population in DDO 68.

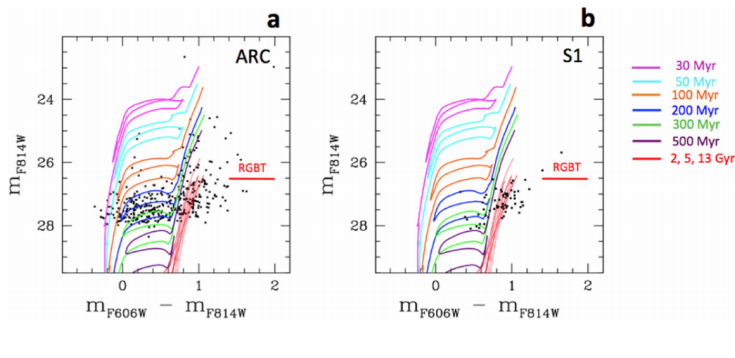


FIGURE 3.19: (a) CMD of the stars resolved in our *HST*/ACS images that belong to the region outlined by the Arc. Superimposed are the PARSEC isochrones (Bressan et al., 2012) for a metallicity  $Z = 0.0004$  and for different ages, shifted according to DDO 68's distance and foreground reddening. The horizontal segment indicates the location of the tip of the red giant branch. (b) Same as panel (a), but for the small portion of S1 falling within the *HST* images. S1 is mainly populated by RGB stars, implying ages older than 2 Gyr.

The resolved portion of S1 exhibits a population older than the Arc since its CMD is only populated by RGB stars, with ages  $\gtrsim 2$  Gyr. To further characterize the stellar population of S1, we compared its intrinsic color derived in the previous section with the PARSEC v1.2S + COLIBRI PR16 simple stellar population models (Bressan et al., 2012; Marigo et al., 2013; Rosenfield et al., 2016), for a Kroupa IMF (Kroupa, 2001), at DDO 68's metallicity of  $Z = 0.0004$  ( $\sim 1/40$  of solar, where  $Z_{\odot} = 0.0152$ ) and at a lower metallicity of  $Z = 0.0001$  ( $\sim 1/150$  solar). The S1 color implies, within a  $1\sigma$  error, a population older than 5 Gyr, and possibly as old as the age of the universe. This is in agreement with the fact that the portion of S1 sampled by our *HST* data is resolved into RGB stars, which can have ages in the range 2 – 13 Gyr. From the models we derive a total S1 luminosity of  $\sim 3.5 \times 10^5 L_{\odot}$ . To derive a stellar mass range for S1, we conservatively adopted two age extremes at 2 and 13 Gyr, which provide a current stellar mass in the range  $1.5 - 6 \times 10^5 M_{\odot}$ . S1 is then comparable to the ultra-faint satellites of the Milky Way (Belokurov et al., 2007; Belokurov et al., 2010), although it may also be just a portion of a larger disrupted progenitor. The significantly different stellar populations of the Arc and S1 suggest that the two substructures originated from two different systems.

### 3.7.2 Dynamics of DDO 68

A possible interpretation of the morphology of DDO 68 is that the Tail, the Arc, and S1 are tidal features due to the stripping effect of a passing body. However, no nearby objects in the direction of the Tail, the Arc, or S1 are detected in Figure 3.17 or in the SDSS images. A simple estimate of the mass  $M_p$  of a putative perturber at distance  $d$  from the main body of DDO 68 is given by the fact that a significant stripping can be produced only for  $M_p \simeq M_{tot} d^3 / R^3$  where  $M_{tot}$  is the total mass and  $R$  is a fiducial radius of DDO 68. This leads us to deduce implausibly high values for the mass of an otherwise undetected perturber. For example, the minimum mass of a perturber located at a distance  $d$  three times the length of the Tail ( $R \sim 5$  kpc) would be  $M_p \sim 30 M_{tot}$ . This argument excludes that the Tail, the Arc, and S1 are tidal features due to DDO 68 C, which is at a distance of 42 kpc (Cannon et al., 2014) from the main body and has a baryonic mass  $\sim 10$  times smaller than that of DDO 68.

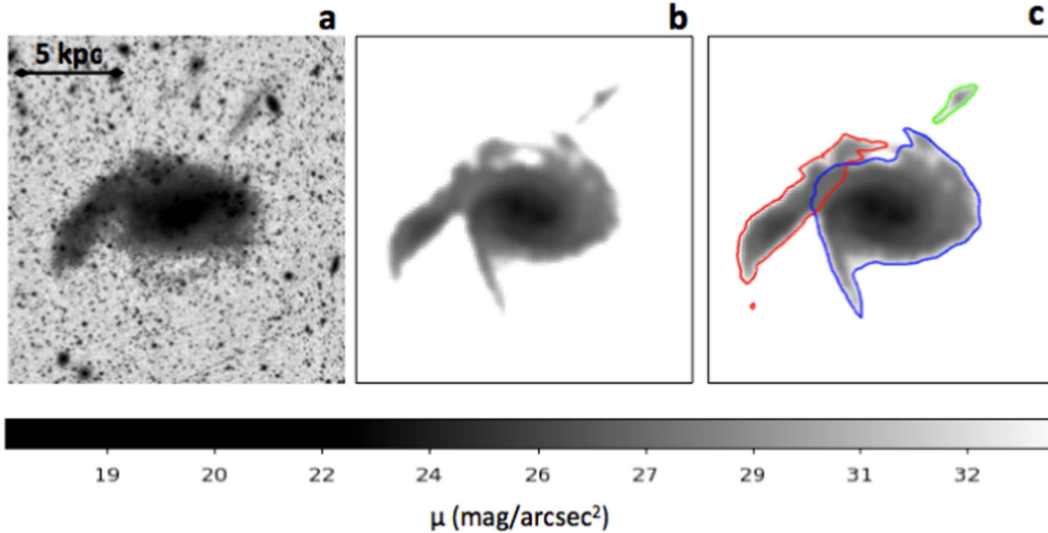


FIGURE 3.20: (a) g-band image of DDO 68 in surface-brightness scale. (b) Snapshot of the stellar component of the multiple-merger N-body simulation. The observed and the simulated images are displayed on the same spatial and surface-brightness scales. We note that elongated arc-like substructures, akin to the observed Arc (see Figure 3.18 Panel (a)), are present in the mock image. (c) Final snapshot of the N-body simulation with superimposed contours delimiting the regions whose bulk stars originally belong to the main galaxy (blue), to satellite T (red), and to satellite S (green).

Since tidal stripping is excluded as the cause of the three non-equilibrium features, the alternative is that they are due to the accretion of smaller companions. Support for the interpretation of DDO 68 as an ongoing multiple merger comes from the results of N-body simulations. We ran several simulations of possible merging events in DDO 68 with the parallel collisionless N-body code FVFPS (Nipoti, Londrillo, and Ciotti, 2003). For simplicity, we included only the collisionless component (stars and dark matter) in the simulations, and we did not model the physics of the gas. We found that while the Tail and a structure similar to the Arc are reproduced by

the accretion of a 10 times less massive satellite galaxy (with the Tail surviving for  $\sim 100$  Myr and consisting mainly of stars of the satellite), the formation of S1 requires an additional accreting system. We thus performed simulations (see the Appendix of Annibali et al. 2016 for details) in which the main galaxy of mass  $M_{tot}$  interacts simultaneously with two smaller satellites, named T and S, of mass  $M_{tot}/10$  and  $M_{tot}/150$ , respectively. As an example, we compare in Figure 3.20 the LBT image of DDO 68 with a snapshot of one of these N-body simulations that reproduces well all its main morphological features. In this snapshot, the spatial distributions of the stars of satellites T and S correspond, respectively, to the Tail and to S1.

### 3.8 Discussion

In this Chapter, we presented several results on the star forming dwarf DDO 68, i.e. an accurate distance determination, a qualitative analysis of the spatial distribution of the different stellar populations, a detailed SFH based on the synthetic CMD method, and some preliminary dynamical considerations. Here we summarize and discuss the main results we obtained.

From the TRGB method, we derived a distance modulus of  $(m - M)_0 = 30.41 \pm 0.12$  mag, i.e. a distance  $D = 12.08 \pm 0.67$  Mpc. However, during our synthetic CMD analysis, we found more satisfactory using a slightly higher distance modulus, i.e.  $(m - M)_0 = 30.51$ , implying a distance  $D = 12.65$  Mpc, still inside the errors of our TRGB determination, and closer to the distance  $D = 12.74 \pm 0.27$  Mpc inferred by Cannon et al. (2014). From the presence of a well-populated RGB, we concluded that DDO 68 hosts a population of stars at least 1 – 2 Gyr old (and possibly as old as a Hubble time), allowing us to reject the hypothesis that this is a young system experiencing its first burst of SF at recent epochs. The same conclusion was reached for the BCD I Zw 18, with a similarly low metallicity, for which we clearly detected the RGB (Aloisi et al., 2007), and were able to provide a lower limit for the stellar mass formed at epochs older than 1 – 2 Gyr ago (Annibali et al., 2013). Another galaxy worth mentioning in this context is Leo P, a recently discovered star forming dwarf galaxy that has the same extremely low metallicity of DDO 68 and I Zw 18. Leo P is much closer (1.62 Mpc), so that its oldest stars can be detected. In fact, McQuinn et al. (2015) find that it indisputably contains stars as old as 10 Gyr. As a matter of fact, there is no evidence so far for the existence of any really young galaxy in the Local Universe.

From a quantitative derivation of DDO 68’s SFH based on the synthetic CMD method, we estimated that the mass locked up in old (age  $> 1$  Gyr) stars is  $M_* \simeq 1.0 \times 10^8 M_\odot$ , i.e., almost 80% of the total galaxy stellar mass. Obviously, the closer distance of DDO 68 compared to I Zw 18 ( $\sim 12$  Mpc versus  $\sim 18$  Mpc) allowed us to better constrain the total stellar mass formed at these epochs. We consider this result quite robust, while the details on the SFH earlier than 1 – 2 Gyr, as well as the age of the onset of the SF, should be taken with caution, due to the degeneracy of the stellar models on the RGB and to the large photometric errors at the faintest magnitudes. We emphasize however that the low metallicity of DDO 68 mitigates the age-metallicity degeneracy and allows us to argue on safer grounds that the redder RGB stars are likely 10 – 13 Gyr old. On the other hand, the SFH derived at epochs younger than  $\sim 1$  Gyr offers a more realistic view of the recent SF activity in DDO 68.

We derived an average SFR density of  $\simeq 7.1 \times 10^{-4} M_\odot \text{ yr}^{-1} \text{ kpc}^{-2}$  over the last  $\sim 1$  Gyr (the SFR is normalized over the area containing 90% of the stars) which is typical of the majority of star-forming dwarf galaxies; the most recent SF activity is quite modest, and not even comparable to the burst strengths (see e.g. Tolstoy, Hill, and Tosi, 2009; Tosi, 2009, and references therein) in “monsters” like NGC 1569.

Extremely metal poor galaxies are recently being classified in two major groups, namely quiescent and active, in the attempt to understand their evolutionary stage

and why there are so few of them (James et al., 2015). Quiescent ones (like Leo P) are numerous but very faint, and therefore remain undetected when at relatively large distances, whereas active ones (like I Zw 18) are undergoing a starburst and are easily detected even at large distances. DDO 68 is certainly not a starburst dwarf, but its level of star formation is high enough to let it be clearly recognizable in spite of its relatively large distance.

As with all studied star-forming dwarfs, DDO 68 does not show evidence for long interruptions in the SFH, with an overall activity more “gaspings” than bursting; at all ages, the SFR density decreases from the center outwards. The distribution of the old stellar population is quite homogeneous and traces the whole galaxy, while young stars tend to be more concentrated. All these characteristics make DDO 68 quite a “normal” star forming dwarf galaxy.

Nonetheless, there are properties that make it exceptional: its highly disturbed morphology and the presence of an arc-shaped structure populated by stars of all ages, and rich in H II regions, is a very peculiar characteristic which strongly suggests a merging/accretion scenario. Interestingly, a peak in the star formation activity between  $\sim 30$  Myr and  $\sim 50$  Myr is found in all regions of DDO 68, suggesting that this epoch may have been affected by the interaction of two merging bodies. A merging event between DDO 68 and a possible companion could also explain why DDO 68 is an outlier in the mass-metallicity relation for dwarf star-forming galaxies, with a metallicity similar to that of I Zw 18, but with a stellar mass  $\sim 10$  times higher: the H II region abundances derived by Pustilnik, Kniazev, and Pramskij (2005) in the arc-shaped structure could in fact trace the metallicity of the accreted companion DDO 68 B, but not the (possibly higher) metallicity of DDO 68 A (Tikhonov, Galazutdinova, and Lebedev, 2014). A merging event could also have triggered the recent SF observed at relatively large galactocentric distances (as demonstrated by our CMD analysis and by the presence of H $\alpha$  emission), which is a quite uncommon feature.

Finally, we recognized, in the RGB spatial map, a small concentration of stars toward the upper right edge of the ACS chip, noticed also by Tikhonov, Galazutdinova, and Lebedev (2014); in order to better investigate the nature of this feature, we obtained new wide-field imaging data at the Large Binocular Telescope. This study shows clear evidence of stellar streams around a galaxy with stellar mass as low as  $M_* \sim 10^8 M_\odot$  and located in a void. DDO 68 is an extremely isolated system and yet it appears surrounded by smaller, interacting bodies: the Tail (or DDO 68 B, in the notation of Tikhonov, Galazutdinova, and Lebedev 2014), DDO 68 C (discovered by Cannon et al. 2014), the Arc, and S1, detected now with LBT. A simple dynamical analysis suggests that the observed morphological features (Tail, Arc, and S1) are not the effect of tidal interaction with massive companions, but are instead the signature of an ongoing multiple merging, as confirmed by our N-body simulations. The simulation, which is admittedly simplified, must be considered only an illustrative case and not necessarily the best possible way to reproduce the complex morphology of DDO 68.

Multiple accretions of dwarf systems onto a more massive host are expected from observations showing that dwarfs are often found in associations (Tully et al., 2006; Bellazzini et al., 2013) and from cosmological simulations predicting that sub-halos

are often accreted in small groups (Li and Helmi, 2008), a scenario that could explain the association of some Milky Way dwarfs with the plane of the orbit of the Magellanic Clouds (D’Onghia and Lake, 2008). In DDO 68, we are witnessing multiple accretions of smaller systems in action. We suggest that it is not just a coincidence that these *fleas of fleas* are so clearly observed for the first time in such an isolated system: once a group of dwarfs with their satellites falls into a massive host, like the Milky Way, it is eventually disassembled by tidal forces wiping out evidence of coherent structure (Deason et al., 2015; Wheeler et al., 2015). It is natural to expect satellites of satellites residing in small halos, i.e., in lower-density environments, to survive longer than those residing in more massive halos. While all dwarf irregulars show distorted morphologies, by definition, this does not imply that these are produced by recent merging events. Here, we have identified very specific signatures (like, e.g., a stream made of old stars that cannot originate from internal hydrodynamical processes) that are not usually seen in other dIrrs. Yet, lack of evidence is not evidence of lack and might instead be due to insufficient sensitivity of the available observations. Our result demonstrates the potential of wide-field instrumentation at 8–10 m telescopes to search for substructures around dwarfs.

As part of LEGUS, DDO 68 will be further studied to explore its very recent SF and to better understand what triggered its most recent SF activity.

*The work presented in this Chapter has been reported in the following publications:*  
Sacchi et al. (2016)  
Annibali et al. (2016)

# 4. THE STARBURST: NGC 4449

---

In this Chapter, we present a detailed study of NGC 4449, based on both archival and new photometric data from LEGUS obtained with the ACS and WFC3. NGC 4449 is an extremely interesting and well-studied galaxy, which is known to be interacting and currently forming stars at a high rate ( $\text{SFR}_{\text{UV}} \sim 0.94 M_{\odot} \text{ yr}^{-1}$ ,  $M_{*} \sim 1.1 \times 10^9 M_{\odot}$  from Calzetti et al., 2015). It is classified as a Magellanic irregular galaxy; indeed, it has characteristics similar to those of the Large Magellanic Cloud, such as dimensions,  $R_{\text{opt}} \sim 3.3 \text{ kpc}^1$ , and metallicity, between  $12 + \log(O/H) = 8.26 \pm 0.09$  and  $12 + \log(O/H) = 8.37 \pm 0.05$  from spectroscopy of the ionized gas in its H II regions (Berg et al., 2012; Annibali et al., 2017), although its star formation activity is at least two times higher. Moreover, NCG 4449 seems to be interacting with neighboring galaxies, as shown by its stellar and gas distribution (see Figures 4.1 and 4.2). A recent detection highlights a stellar tidal stream that is falling onto the galaxy and whose origin is thought to be the disruption of a smaller dwarf spheroidal galaxy (Rich et al., 2012; Martínez-Delgado et al., 2012). Furthermore, Annibali et al. (2012) reported the discovery of a very massive ( $M \sim 10^6 M_{\odot}$ ) elliptical old star cluster, apparently associated with two tails of blue stars, which may be the nucleus of a former gas-rich satellite galaxy undergoing tidal disruption by NGC 4449.

The H I morphology is highly disturbed, with filaments and giant ring- and shell-shaped complexes extending well beyond the optical galaxy (Figure 4.2). Moreover, the inner and outer parts of the neutral gas form two separate systems that are counter-rotating (Hunter, van Woerden, and Gallagher, 1999) which generally signals the recent accretion of gas.

The star formation history of NGC 4449 was already derived by McQuinn et al. (2010) as part of a study of 18 dwarf galaxies. It was based on archival *V* and *I* ACS images and refers to the whole galaxy. Here we provide a new SFH, inferred with a refined method for comparing synthetic and observational CMDs (SFERA), both in the optical and ultraviolet bands. Our analysis includes a new method to estimate photometric errors and completeness of the catalog, and is based on two different up-to-date sets of stellar evolution models. Moreover, we perform a spatially resolved SFH analysis of the galaxy.

---

<sup>1</sup> $R_{\text{opt}}$  is defined as 3.2 times the exponential scale length (Lelli, Verheijen, and Fraternali, 2014a).

## 4.1 Observations and Data

Figure 4.1 shows the *HST*/ACS Wide Field Channel image of NGC 4449 presented by Annibali et al. (2008). The images were acquired in November 2005 (GO program 10585) in the F435W, F555W, F814W and F658N filters, following a dither pattern. For each of these filters, images with eight exposures of 900 s, 600 s, 500 s and 90 s, respectively, were acquired. These data were included in the LEGUS 5-band image processing together with the new UV and U-band ones (broadband filters F275W and F336W) acquired with the UVIS channel of the Wide Field Camera 3 (GO Treasury program 13364, PI D. Calzetti). Imaging through all five bands were aligned and drizzled onto the same grid, and photometry was performed using the DOLPHOT 2.0 package (Dolphin, 2016). No relevant differences were found with the photometry performed by Annibali et al. (2008). The sensitivity was enough to reach at least one magnitude below the TRGB with a photometric error smaller than 0.1 magnitudes, and detect stars as faint as  $\sim 3$  magnitudes below the tip.

We selected our data with the following DOLPHOT parameters, in F555W and F814W filters: photometric error  $\sigma \leq 0.2$  (meaning a signal-to-noise ratio  $\geq 5$ ), squared sharpness  $\leq 0.2$  (excluding objects with size significantly deviating with respect to the point spread function), crowding  $\leq 2.25$  (excluding only objects in very crowded regions such as candidate clusters), object type  $\leq 2$  (excluding spurious objects such as background galaxies). The final catalog after the quality cuts includes  $\sim 430\,000$  stars in both F555W and F814W.



FIGURE 4.1: Four color composite image of NGC 4449 from *HST*/ACS observations: blue corresponds to F435W ( $B$ ), green to F555W (broad  $V$ ), red to F814W ( $I$ ), magenta to F658N ( $H\alpha$ ). In the upper left corner is indicated the angular scale (30 arcsec) which corresponds to  $\sim 550$  pc at the adopted distance. Original figure from Annibali et al. (2008).

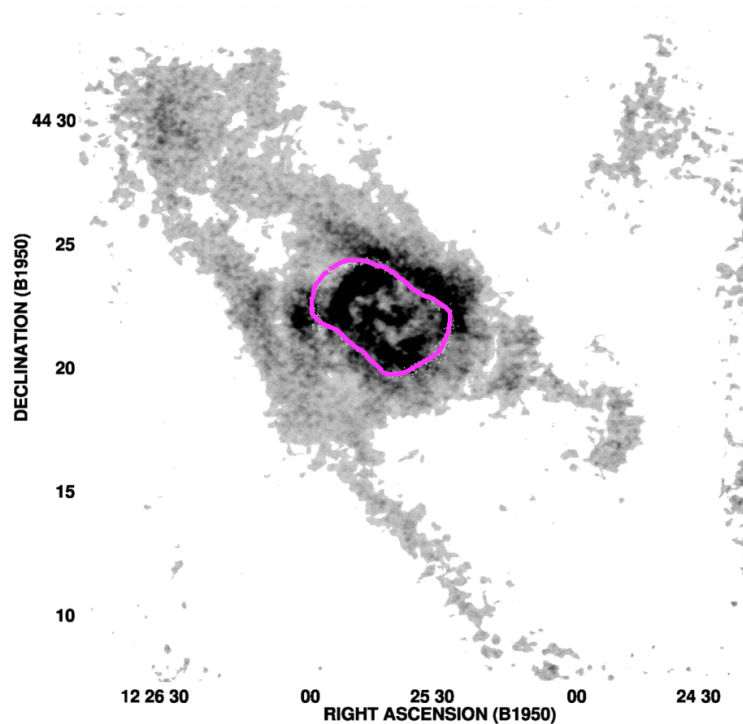


FIGURE 4.2: Integrated H I map of NGC 4449. The magenta line indicates the contour of the optical galaxy. Original figure from Hunter, van Woerden, and Gallagher (1999); notice the different orientation angle (North up, East left) with respect to Figure 4.1.

For the F336W and F555W filters we used: photometric error  $\sigma \leq 0.2$ , squared sharpness  $\leq 0.15$ , crowding  $\leq 1.3$ , object type  $\leq 2$ . The resulting catalog contains  $\sim 78\,000$  stars in both F336W and F555W.

## 4.2 Artificial Star Tests

To estimate the photometric errors and incompleteness of our data, we refined the standard procedure of the artificial star test by following the steps described in Cignoni et al. (2016) and here summarized. First, we put a spatially uniform distribution of artificial stars on the images (one star at a time) and re-process them with DOLPHOT every time we add a new source; this gives us a first estimate of the completeness of the catalog as a function of the magnitude. We then use this function to reconstruct the actual density profile of the galaxy and run a second artificial star test following this profile. We applied this method to each filter separately and then combined the outputs to obtain information of every input star in all filters.

With this iterative procedure, we obtain a more precise description of the completeness as a function of position and magnitude, and we are also able to put more artificial stars in regions that need to be explored in more detail because of their higher crowding. This way, in particular in galaxies with high density gradients from one region to another, we obtain a description of the completeness function not biased by the average density but describing the local incompleteness: the most crowded parts will have a lower and more realistic completeness than the one inferred from the uniform distribution, since they have been explored with a higher number of artificial stars. Notice that this procedure does not create artificial crowding, since we always add only one artificial star at a time. This allows to take into account the very different morphologies we can encounter with a very general procedure, which does not involve galaxy-by-galaxy treatment such as a division of the field following iso-density regions.

In Figure 4.3 we plot the optical completeness derived from our artificial star tests in three different regions of the galaxy (inner, middle and outer, see Section 4.5) to show how the higher crowding of the inner regions severely reduces their completeness. We point out, however, that the complex morphology of NGC 4449 makes crowding (and hence completeness) not a simple function of the galactocentric distance, but rather a patchy pattern following the major star forming regions.

Figure 4.4 shows the  $m_{output} - m_{input}$  versus  $m_{input}$  distribution of the artificial stars in F555W and F814W, that we use to estimate the photometric errors of the optical CMD.

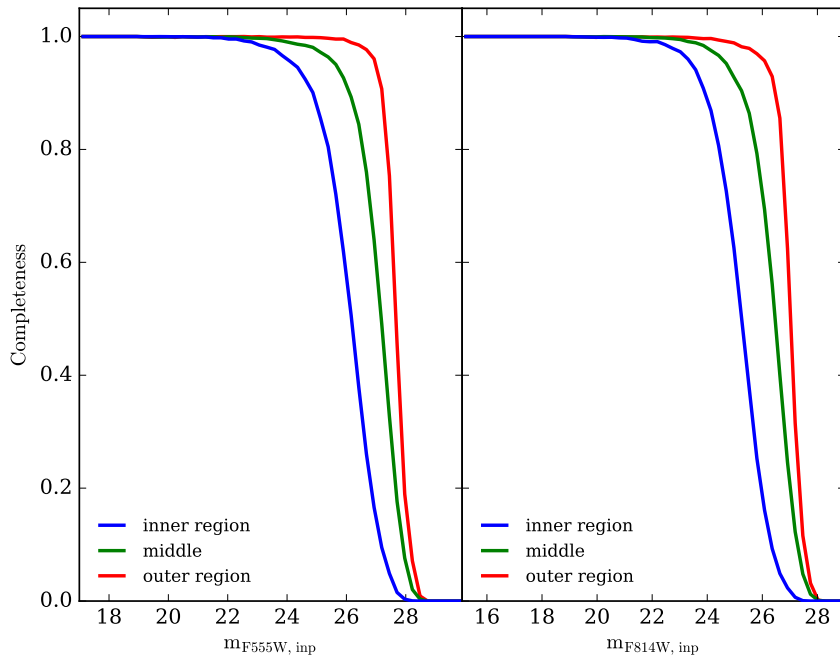


FIGURE 4.3: Completeness in F555W (left panel) and F814W (right panel) from our artificial star tests in three different regions of the galaxy (inner in blue, middle in green, outer in red, see Section 4.5) highlighting the different crowding conditions from inside out.

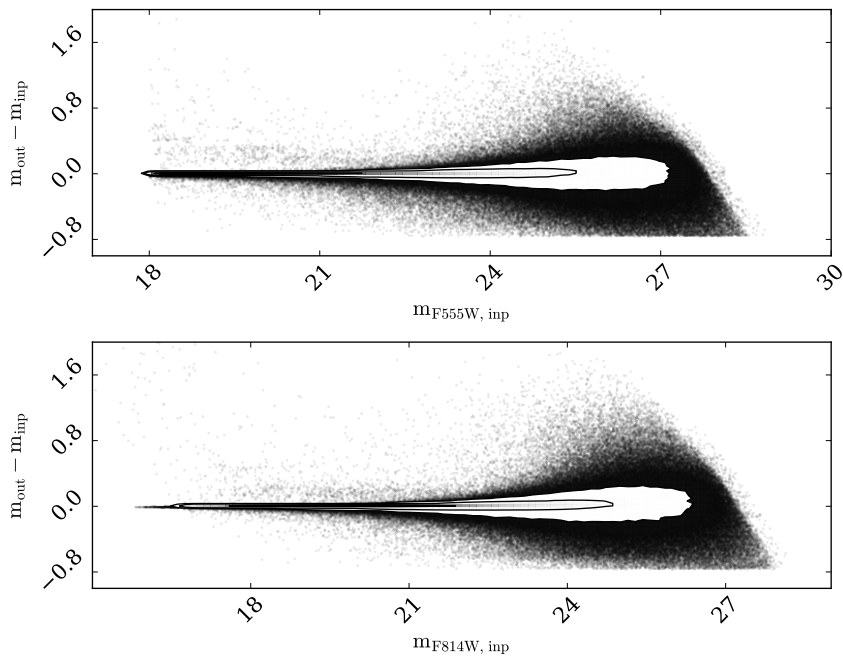


FIGURE 4.4: Photometric errors in F555W (top panel) and F814W (bottom panel) from our artificial star tests; the contours indicate the  $1\sigma$ ,  $2\sigma$  and  $3\sigma$  levels of the distributions.

### 4.3 Distribution of the stellar populations

The optical CMD of the whole catalog we obtained after the quality cuts is shown in Figure 4.5. We can see a large variety of stellar populations and recognize the main features of CMDs typical of this kind of galaxies:

- the blue plume ( $-1 \lesssim m_{F555W} - m_{F814W} \lesssim 0.5$ ) containing stars on the main sequence and at the hot edge of the helium burning phase;
- the red plume ( $1.5 \lesssim m_{F555W} - m_{F814W} \lesssim 2.5$ ,  $m_{F814W} \lesssim 24$ ) made of mainly red helium burning stars;
- the blue loops between the two plumes, populated by helium burning stars;
- the horizontal red tail ( $m_{F555W} - m_{F814W} \gtrsim 1.8$ ,  $m_{F814W} \lesssim 24$ ) made of thermally pulsing asymptotic giant branch stars;
- the red giant branch ( $m_{F555W} - m_{F814W} \gtrsim 0.5$ ,  $m_{F814W} \gtrsim 24$ ) with the oldest population reachable at this distance.

In order to better understand the evolutionary status of NGC 4449, we isolated some of these phases and inspected how they are spatially distributed across the body of the galaxy. We chose three age intervals, corresponding to: very young ( $\lesssim 10$  Myr) blue MS stars, intermediate-age ( $\sim 50 - 300$  Myr) helium burning and AGB stars, and old ( $> 1 - 2$  Gyr) RGB stars. Figure 4.6 shows these selected stars, both in the CMD and in the spatial map. As a general behavior, we find that the younger the stars, the more concentrated and clumped in groups their spatial distribution, as naturally expected for star formation that proceeds hierarchically (Gouliermis et al., 2017).

In addition, there are several very interesting features revealed by the maps. First of all, the young stars seem to form a sort of S-shaped structure crossing the galactic center, that follows the distribution of the  $H\alpha$  gas. These are the loci of very recent SF, as confirmed by the detection of stars in our catalog in the F336W filter (magenta points in the top right panel of Figure 4.6). Their distribution is clearly lopsided, suggesting an external event to cause the asymmetry and to trigger the formation of H II regions on the north side of the galaxy. Moreover, Reines, Johnson, and Goss (2008) identified 13 clusters with thermal radio emission (shown with light blue circles in the figure); they estimate that these sources have ages  $\lesssim 5$  Myr and stellar masses  $\gtrsim 10^4 M_{\odot}$ , and they represent the birthplace of the next generation of stars. The S-shaped structure is still visible in the intermediate-age population, that is however more diffuse. A clump of stars forming a shallow overdensity (highlighted by the red dotted ellipse in the figure) is also visible; if we select these stars on the map and look at where they are on the CMD, we find that their luminosities are all very similar to each other ( $m_{F814W} \sim 21.3$ ), meaning that they are stars of roughly the same age<sup>2</sup>.

<sup>2</sup>During the helium burning phase of intermediate mass ( $> 2 M_{\odot}$ ) stars, there is a direct correlation between mass and luminosity of a star since the core is non-degenerate; this makes the luminosity of the blue loops a very fine age indicator (see Section 2.1).

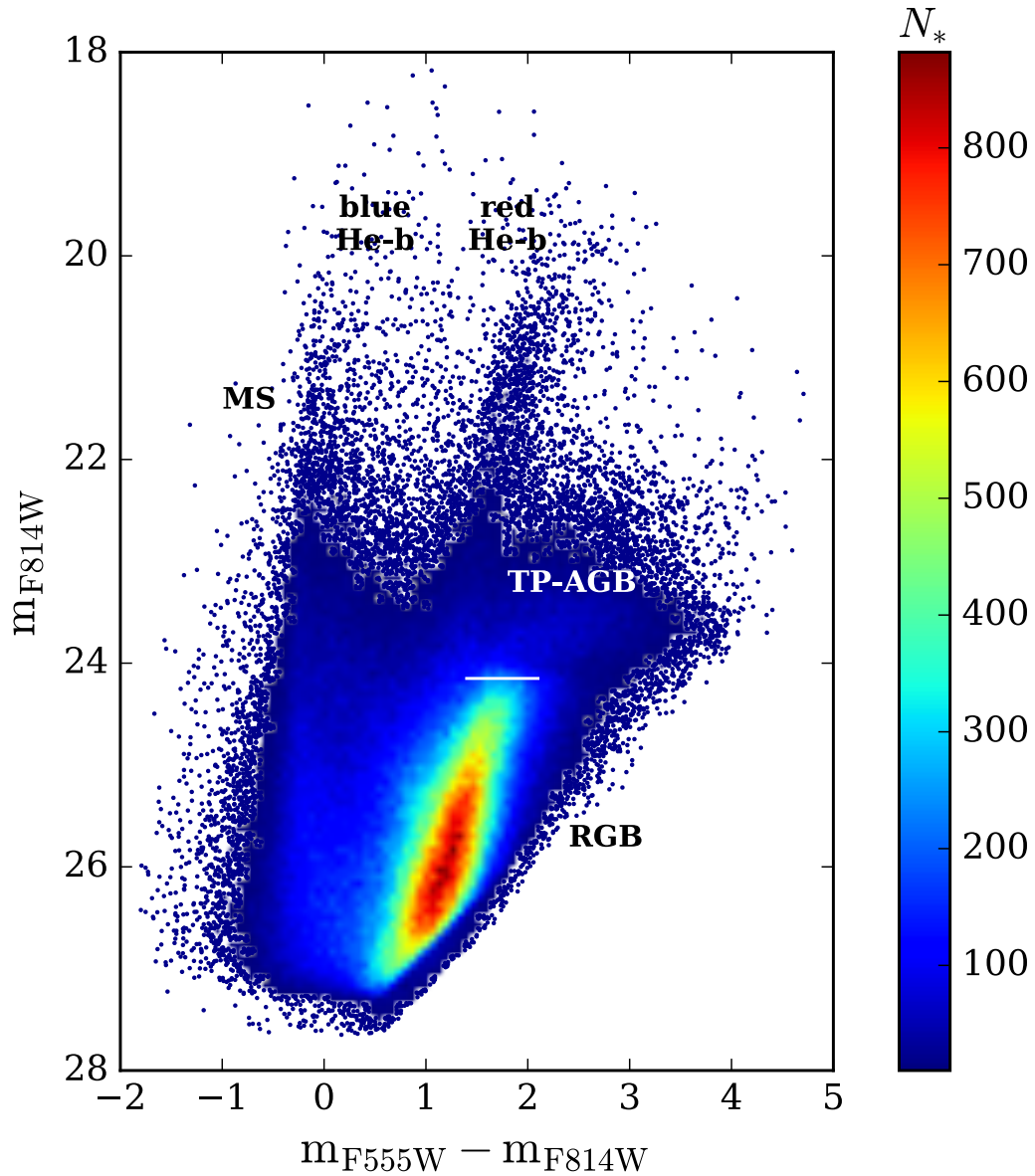


FIGURE 4.5: Optical Color-Magnitude Diagram of the whole field of NGC 4449 covered by the ACS imaging (after the quality cuts, see Section 4.1). The high density regions have been binned and color coded by number density (see the color bar) for a better visualization of the evolutionary features in the diagram. The main stellar evolutionary phases are indicated (see Section 4.3). The horizontal white line represents the magnitude of the red giant branch tip.

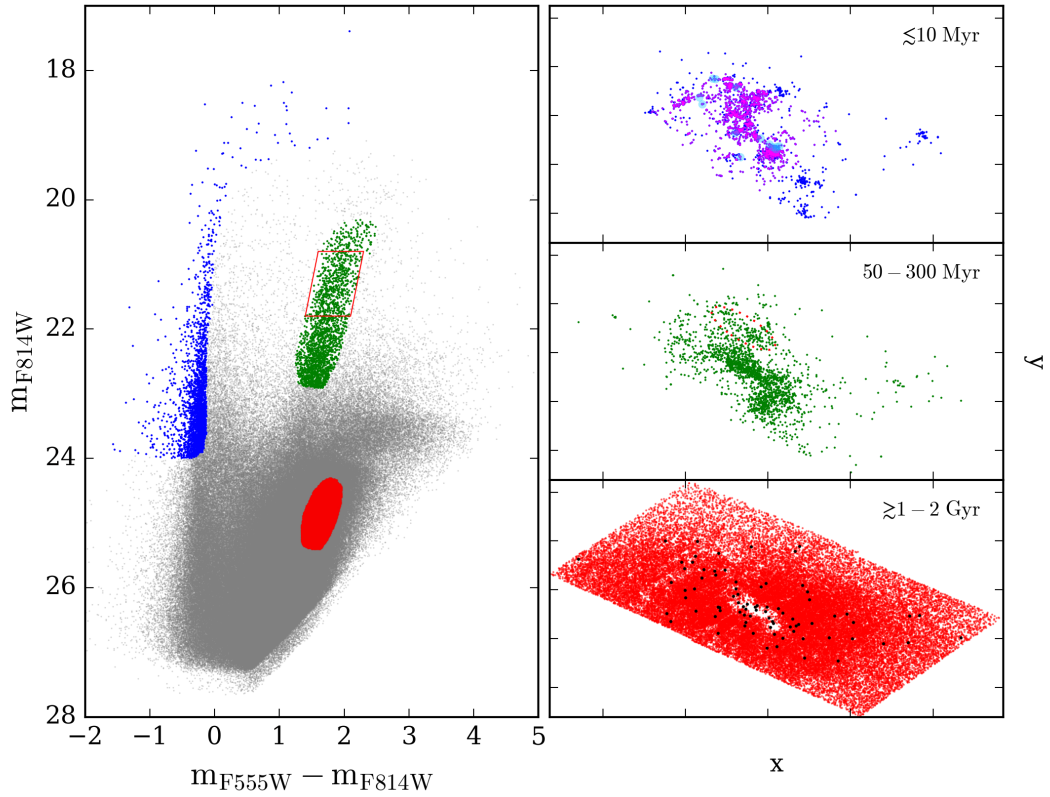


FIGURE 4.6: *Left panel.* Selection of three different stellar populations in the CMD: in blue, stars with ages  $\lesssim 10$  Myr; in green, stars with intermediate ages between  $\sim 50$  and  $\sim 300$  Myr; in red, stars older than  $\sim 1 - 2$  Gyr. *Right panel.* Spatial distribution of the age-selected stars: the magenta points in the top map represent stars that have also a measured flux in the F336W filter, while the light blue circles are clusters with thermal radio emission from Reines, Johnson, and Goss (2008); the red dotted ellipse in the middle map includes stars forming an elongated structure and with roughly the same F814W luminosity (inside the red parallelogram in the CMD); the black dots in the bottom map are the stellar clusters identified by Annibali et al. (2011).

This suggests that the structure originated from a specific episode of SF, maybe triggered by the inflow of new gas from some interaction, that created this small coeval population. Moreover, this region hosts a Wolf–Rayet (WR) massive cluster which is believed to be a young evolutionary stage of a super star cluster as 30 Doradus in the LMC (Sokal et al., 2015). The old stars are spread all over the galaxy, with holes in the distribution only due to incompleteness.

## 4.4 The UV perspective

Figure 4.7 shows the spatial distributions of NGC 4449 in the F336W image, the map in physical units (pc) of all stellar sources identified both in the F336W and in the F555W, color coded with the density estimated using a Gaussian kernel, and the 2D histogram of the densest sub-region ( $\approx 600$  pc wide).

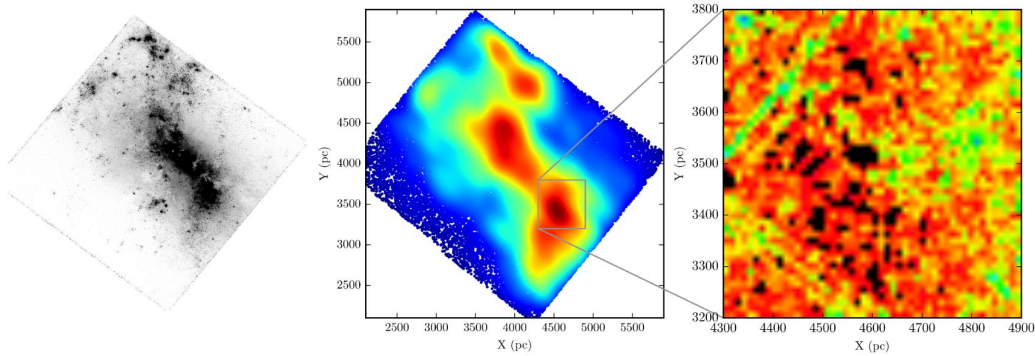


FIGURE 4.7: *Left panel.* F336W image of NGC 4449. *Middle panel.* All stellar sources detected in F336W and F555W, color-coded with the density (estimated with a Gaussian kernel). *Right panel.* Zoom-in on the densest sub-region.

As already clear from the optical analysis, NGC 4449 has multiple overdensities that are irregularly distributed. Zooming in on the densest sub-region (right panel) reveals a very crowded area (as indicated by the almost uniform red color), with multiple peaks (black areas) of higher density.

The F336W versus F336W–F555W CMD, after the quality cuts we applied, is shown in Figure 4.8 together with the latest PARSEC-COLIBRI isochrones (PADova and TRIeste Stellar Evolution Code version 1.2S plus COLIBRI code for AGB thermal pulses Bressan et al., 2012; Tang et al., 2014; Marigo et al., 2017) corresponding to the ages 3, 10, 20, 50, 100 and 200 Myr, corrected for reddening  $E(B - V) = 0.20$  and distance modulus 27.91 (Annibali et al., 2008), with a metallicity  $Z = 0.005$ .

Guided by the isochrones, we can recognize three common stellar phases in the CMD of Figure 4.8: a prominent blue plume of MS stars, a SGB and a He-burning phase. Typical masses populating these CMDs are higher than  $5 M_{\odot}$  and as massive as  $80 M_{\odot}$ . Given the depth of this CMD the maximum age that can be investigated is about 180 Myr.

The MS is very broad, and the luminosity distribution of SGB/He-burning stars appears rather uniform. Concerning the MS spread, it seems unlikely that a metallicity variation can explain it all. In fact, in massive hot stars the opacity is dominated by electron scattering, which depends only on the mass fraction of hydrogen  $X$  as  $0.20(1 + X)$ , and is about constant at  $Z < 0.01$ .

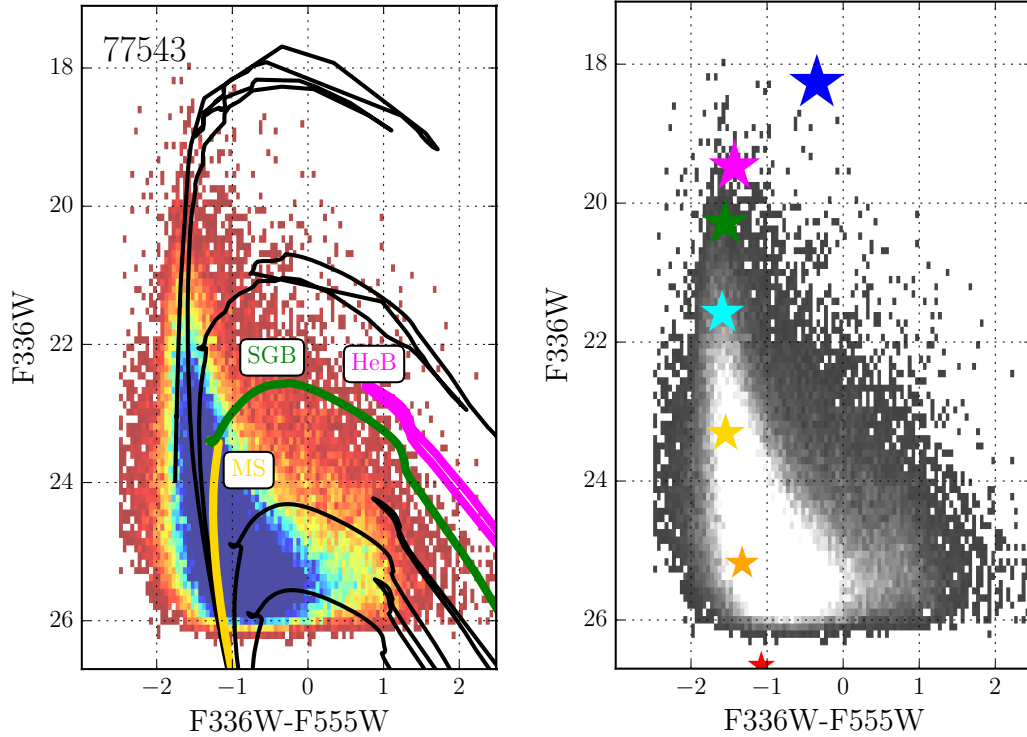


FIGURE 4.8: *Left panel.* F336W versus F336W–F555W CMD of NGC 4449. PARSEC-COLIBRI isochrones of ages 3, 10, 20, 50, 100 and 200 Myr are overlaid. The most relevant stellar phases are also indicated along the 20 Myr isochrone with lines of different colors: orange for the MS, green for the SGB, and magenta for the He-burning phase. *Right panel.* Same CMD with star symbols representing the PARSEC-COLIBRI stellar models of 3 Myr and masses 6 (red), 10 (orange), 20 (gold), 40 (cyan), 60 (green), 70 (magenta) and 80 (blue)  $M_{\odot}$ .

Analogously, the MS of NGC 4449 is significantly broader<sup>3</sup> than that expected from an age spread alone. Given the youth of the population, it seems very likely that differential reddening is artificially inflating the apparent width of the MS. Indeed, using far-ultraviolet and Balmer-line imagery for 22 OB complexes in NGC 4449, Hill et al. (1994) derived from the Balmer decrement reddening  $E(B - V)$  values ranging from 0.25 to 0.60. Alternatively, stellar rotation (see, e.g., Meynet and Maeder, 1997) or core-convective overshooting (see, e.g., Bressan et al., 2015) could be also responsible for broadening the MS.

Beyond the MS, the stellar phases before the red giant branch are so fast (thermodynamical evolution) that the probability of observing stars is low compared to nuclear phases. Generally, this causes the so-called Hertzsprung gap, i.e. the observed lack (or paucity) of stars in the evolutionary phase right after the MS. However, the stellar

<sup>3</sup>The MS width is measured with the standard deviation of the color distribution of stars in the magnitude interval  $22 < F336W < 23$ .

production in this galaxy is such that the number of stars in these fast evolutionary phases is not negligible. Indeed, SGB stars are copious in NGC 4449, with no sign of interruption between  $F336W \approx 19$  and the faint end of the CMD.

The comparison with the isochrones in Figure 4.8 suggests that the blue edge of the BL is redder than  $F336W - F555W \approx 1$ , except for the most massive stars (isochrone younger than 20 Myr). Clearly, the relatively high metallicity of the galaxy prevents the helium burning phase to reach the MS color. The net result is that, depending on the magnitude, stars at intermediate colors are a different mixture of SGB and BL stars. However, the color spread tends to smear out many CMD features already at magnitudes as bright as 24.

Since SGB and BL monotonically fade as the population age increases, both stellar species are fundamental clocks to infer the recent SFH of a galaxy. The route of the BL as age indicator has been pioneered by Dohm-Palmer et al., 1997 on the dwarf irregular galaxy Sextans A and recently applied to several other dwarf irregulars by, e.g., McQuinn et al. (2011) and McQuinn et al. (2012). In particular, McQuinn et al. (2012) studied the concentration of SF for 15 star-forming dwarf galaxies, including NGC 4449, using the position of blue core helium burning stars as tracer of populations younger than few 100 Myr. They find that SF can be both highly concentrated and more distributed depending on the system; in the case of NGC 4449, however, they cannot clearly distinguish the MS and blue He-burning populations, that begin to blend due to photometric crowding and differential extinction. Despite this limitation, they find a very high degree of centralized SF, in according with our findings on its young stellar populations.

As discussed in Section 2.1.2, the main advantage of SGB/BL over the MS is that subsequent generations of SGB/BL stars *do not overlie each other* as they do on the MS. Moreover, the SGB/BL is on average *brighter* than the coeval MSTP. However, since the MS evolutionary times are much longer than post-MS times, star counts along the MS are statistically more robust.

## 4.5 Star Formation History

The SFH of NGC 4449 was studied through the synthetic CMD method (see Section 2.2). The theoretical CMDs used for the comparison with the observed one were built from two different sets of stellar evolution isochrones, PARSEC-COLIBRI (Marigo et al., 2013; Rosenfield et al., 2016) and MIST (Choi et al., 2016). This allowed us to explore the uncertainties arising from the models, and to test the strength and reliability of different evolutionary phases. For both, we used the following input parameters:

- Kroupa initial mass function (Kroupa, 2001) from 0.1 to  $300 M_{\odot}$ ;
- 30% binary fraction;
- metallicity in the range  $Z = [0.0003 - 0.008]$  or  $[M/H]$  from  $-1.7$  to  $-0.3$  in steps of 0.1.

We then convolved the models with the data properties:

- distance modulus  $(m - M)_0 = 27.91 \pm 0.15$  (Annibali et al., 2008) which is allowed to vary in a range around the chosen literature value, in steps of 0.05 mag;
- photometric errors, incompleteness and blending from the Artificial Star Tests;
- total reddening (foreground<sup>4</sup> plus internal) varying from 0.05 to 0.20 mag in steps of 0.05;
- differential reddening (modeled as a Gaussian spread) varying from 0.1 to 0.2 mag.

A crucial point in the analysis of this galaxy is the existence of a rich population of TP-AGB stars, that presents several challenges, both observational and theoretical, such as modeling circumstellar dust obscuration (Boyer et al., 2009), mass loss and evolutionary timescales. Both isochrone sets we used have recently included a detailed treatment of this stellar phase, but they still lack an empirical calibration with a real galaxy (this is typically done with the LMC). Moreover, the models from the two groups are quite different, so we decided to mask the TP-AGB area in the CMD, in order to exclude it from the minimization procedure applied to search for the best star formation history.

### 4.5.1 Whole galaxy

Figure 4.9 shows the results for the total CMD of NGC 4449. In the top panels the observed and recovered CMDs are shown as Hess diagrams, i.e. density plots, as this is the way we perform the minimization of the residuals between them; the dotted black box indicates the TP-AGB region masked for the comparison. To analyze these Hess diagrams we slice them in luminosity intervals and build their color function

<sup>4</sup> $E(B - V) = 0.017$  from Schlafly and Finkbeiner (2011).

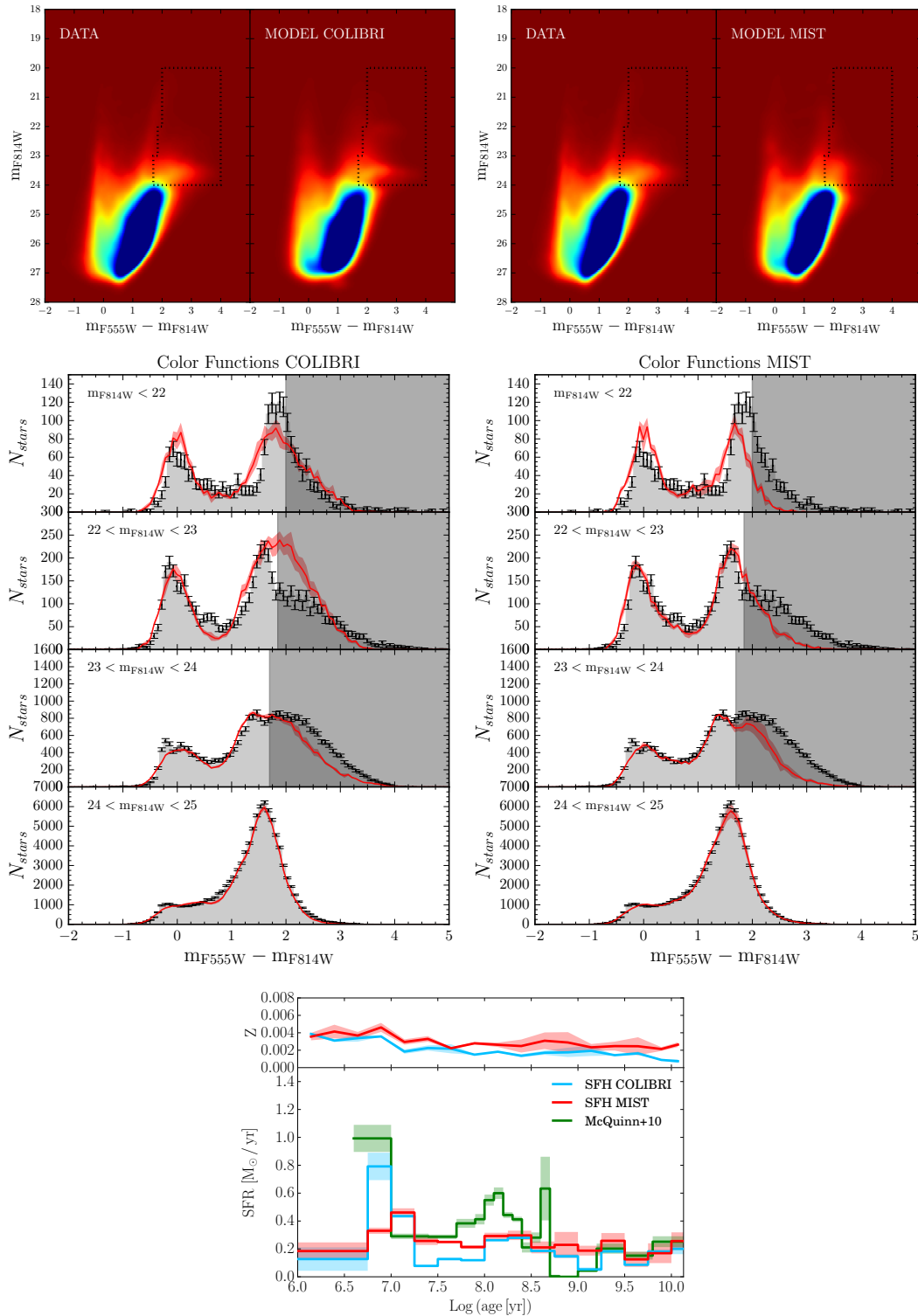


FIGURE 4.9: *Top panels.* Hess diagrams of the whole optical field of NGC 4449: the observational one is on the left and the one reconstructed on the basis of different sets of models on the right; the dotted line shows the region containing TP-AGB stars and excluded from the minimization. *Middle panels.* Color functions of the CMDs in different luminosity bins; the shaded part of the diagrams corresponds to the masked region in the CMD; the data are the grey histograms with a Poissonian uncertainty, while the models are the red lines with the uncertainty from a bootstrap technique. *Bottom panel.* Recovered SFH and metallicity; in green, the SFH from McQuinn et al. (2010) based on older stellar models from the Padova group.

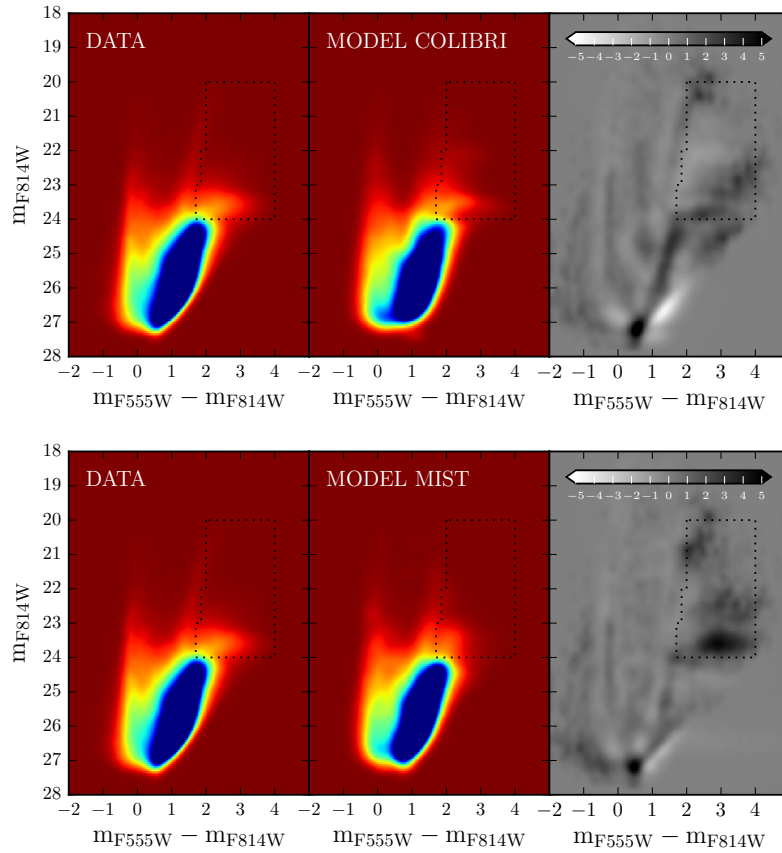


FIGURE 4.10: Observed (left panel), recovered (middle panel) and residuals (right panel) CMDs for the whole galaxy with the two adopted sets of stellar models.

The residuals are in units of Poisson uncertainties:  $(data - model)/\sqrt{model}$ .

for each luminosity slice (middle panels). This way, we can have a clear comparison of the number of stars in the data and the model and directly check the quality of the minimization. In the bottom panel, we show the star formation history and the evolution of the metallicity as a function of the age. For the whole field we show the results for both the COLIBRI and MIST isochrones, to identify their differences and the features that may result from the chosen set of evolutionary tracks.

As suggested by the presence of stellar populations of all ages, the SF of NGC 4449 has been fairly continuous over the lifetime of the galaxy. In particular, we find peaks and dips, but the SFR at the top of the peaks is only a factor of a few higher than at the bottom of the dips. The duration of the peaks is similar to that of the dips. This behavior is not what we would call a “bursting” regime, where bursts should be short episodes, with SFR significantly higher than average, separated by long quiescent phases. What we find for NGC 4449 is instead quite similar to what is found in the Small Magellanic Cloud (e.g. Cignoni et al., 2012; Cignoni et al., 2013) and in other Local Group Irregulars (e.g. Tolstoy, Hill, and Tosi, 2009; Gallart et al., 2015): a “gaspings” (Marconi et al., 1995) more than a “bursting” regime. We find the main peak of SF at ages between 5 and 20 Myr ago, in the same interval found

by McQuinn et al. (2010), with a SFR almost 4 times higher than the average; some low activity is also found in the most recent bin (last 5 – 6 Myr) in agreement with the presence of H $\alpha$  emission in the galaxy. The SFH from McQuinn et al. (2010) has another peak around 100 Myr ago. In our case, the COLIBRI solution shows an enhanced SFR in this time range, but the SFR peak is about half of that of McQuinn et al. (2010). This is due to the very different predictions of the adopted stellar models for stars on the TP-AGB phase (McQuinn’s adopted models did not include this phase at all). Also, the bin duration they use in this time range seems smaller than the time resolution at this look-back time.

There are a few differences between the models, and between models and data: both synthetic CMDs reproduce the overall shape of the observed one, but they hardly reach the very bright tip of the red plume, underestimating the number of red super giants, while they slightly overestimate the blue ones. The COLIBRI CMD also misrepresents the small bump in the blue plume at  $22 < m_{F814W} < 23$ ,  $m_{F555W} - m_{F814W} \sim 0.6$ . Even with the whole CMD fitted, all models fail to reproduce exactly the TP-AGB phase, either in terms of CMD morphology and of star counts. This is due to the well known difficulty in modeling such a rapid phase and is the reason why we decided to mask the entire phase to infer the proper SFH. This is also causing the main difference between our result and the one from McQuinn et al. (2010) between  $\sim 20$  and  $\sim 300$  Myr. The remaining features of the CMD are well fitted within the errors (see also the residuals in Figure 4.10), and the SFH never shows signs of long interruptions within our time resolution. Although the trends are similar, the solutions from the two sets of stellar models show significant differences: the MIST SFH tends to be more constant where the COLIBRI one shows a higher variation around the average. This is a behavior we often find when comparing the two libraries, thus we consider this difference as an estimate of the systematic uncertainty in our SFH.

The metallicity shows a growing trend with time, and in the youngest bins it matches the spectroscopic value inferred from H II region observations (Berg et al., 2012; Annibali et al., 2017).

To better evaluate the differences between the models, and for an easier comparison with other literature results, we show in Figure 4.11 the cumulative stellar mass fraction (CMF), which is less sensitive to the correlated errors between adjacent bins. The two functions are remarkably similar and clearly show that the bulk of SF is older than 1 Gyr, when roughly 90% of the mass was already formed.

As shown by the observational CMD, our photometry reaches the RGB population, but is not deep enough to identify other older features such as the red clump or the horizontal branch; this means that the actual look-back time safely sampled by our CMD is formally 1 Gyr (the minimum age of an RGB star) and in practice around 3 Gyr (since the quite low metallicity allows us to reduce the age-metallicity degeneracy affecting RGB stars and thus have an older age constraint). To quantify the uncertainties related to assuming different look-back times in the derivation of the SFH, we have re-run SFERA assuming the starting epoch of the SF activity to be either  $\sim 5$  Gyr or  $\sim 3$  Gyr ago instead of  $\sim 13$  Gyr ago. In both cases, the CMD is reproduced quite well, with no relevant differences with respect to the ones in Figure

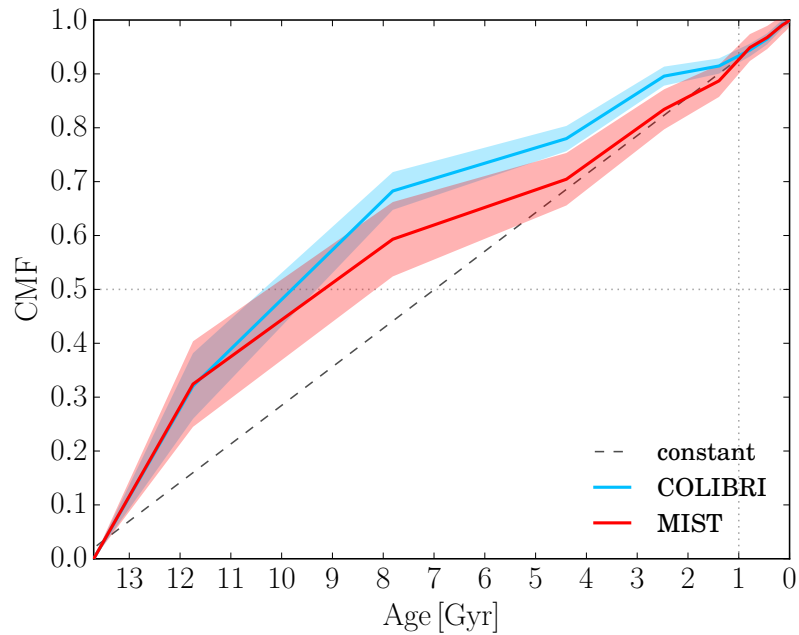


FIGURE 4.11: Cumulative stellar mass fraction for the total field of NGC 4449 recovered with the COLIBRI (light blue) and MIST (red) tracks; the dotted vertical line indicates an age of 1 Gyr whilst the dotted horizontal line shows 50% of the total mass. The dashed curve corresponds to a constant SFH.

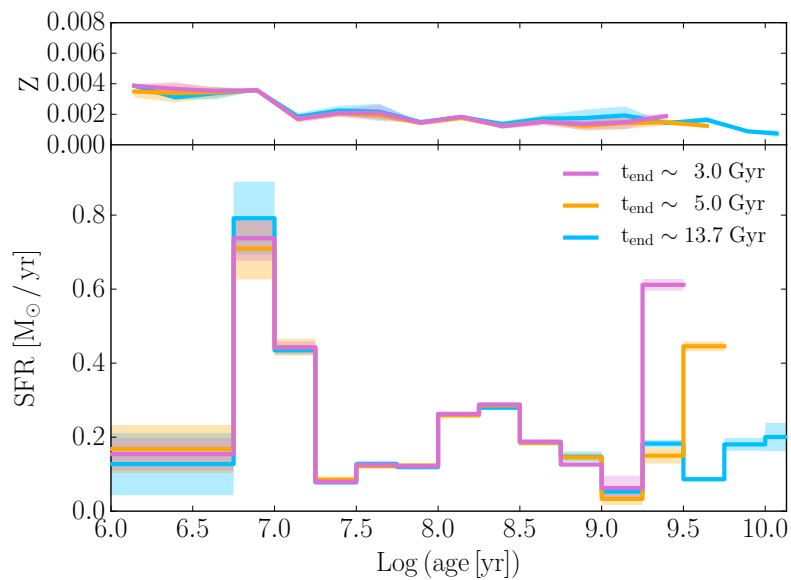


FIGURE 4.12: Comparison among the SFH of the total field of NGC 4449 recovered within three different look-back times: 3 Gyr (pink line), 5 Gyr (orange line) and the whole Hubble time (light blue, same as in Figure 4.9).

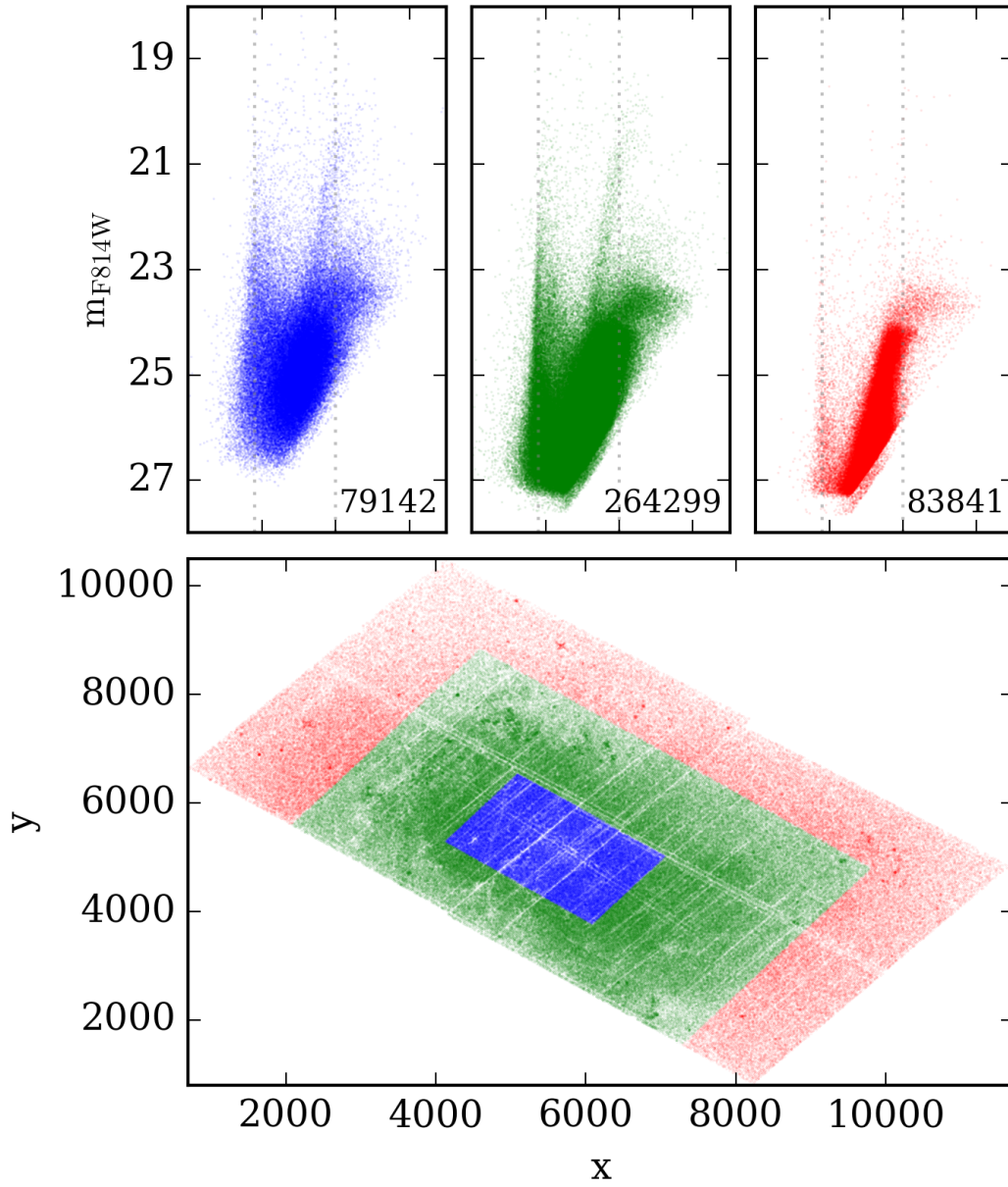


FIGURE 4.13: Map and corresponding CMDs of the 3 regions we identified in the galaxy and used to recover the SFH; the dotted vertical lines are a rough reference of the blue edge of the MS ( $m_{F555W} - m_{F814W} = -0.2$ ) and the red edge of the RGB ( $m_{F555W} - m_{F814W} = 2$ ). In the bottom right corner of every CMD the number of stars in the corresponding field is indicated.

4.9, and the corresponding SFHs are shown in Figure 4.12. The shorter the look-back time, the higher the enhancement of the earliest episode in order to recover the right number of observed stars, while the SFR in all the other bins remains the same within the errors. We thus keep modeling the whole Hubble time in the following, but warn the reader that the actual SFR in the earliest 8 – 10 Gyr may vary within the extremes shown in Figure 4.12.

Despite this observational limit, it is quite reasonable to expect this galaxy to be older than 3 Gyr, possibly as old as a Hubble time, as already demonstrated by spectroscopic studies (Strader, Seth, and Caldwell, 2012; Karczewski et al., 2013). Thus, we are confident that future observations will allow the photometry to go deeper and detect older population tracers.

Given the richness and complexity of this galaxy, we divided the whole field in 3 separate regions, for which we performed the SFH analysis independently. Figure 4.13 shows the division and the corresponding CMDs. Given the boxy shape of the galaxy, an elliptical selection of the regions would have been less representative of the SF region distribution, so we adopted this rectangular selection. The outer field was selected to avoid all the infalling features we see around the galaxy (see Figure 4.1), while the central one includes the strongest  $H\alpha$  emission. The CMDs of these three regions clearly reflect the changing stellar populations, with the central region containing lots of very bright young stars, almost absent in the outer part, and the different completeness conditions of the subregions (the CMD becomes deeper going from inside out, see also Figure 4.3).

However, the presence of different substructures in the intermediate region, made the SFH recovery process very difficult, in particular in the differential reddening treatment. For this reason, we do not show here the corresponding SFH, and we decided to split this field in two different subregions, one including the northern SF region, with the elongated structure discussed above, the other including the southern clumps of stars. To investigate possible local features, we also split the external field in 4 different subfields, as shown in Figures 4.14 and 4.15. Interestingly, Field 2 hosts the globular cluster analyzed by Annibali et al. (2012) that is suggested to be the remnant of a dwarf galaxy disrupted by the interaction with NGC 4449.

## 4.5.2 Central fields

From the point of view of the SF, the three central fields are the most interesting ones, showing that all the main stellar populations are present. Moreover, the Center is also included in the UVIS field, so we can directly compare the optical and UV results. Figures 4.16 and 4.18 show the results for these three regions.

**Center** For the Center, we again show the comparison of the two sets of tracks we used. Both models successfully reproduce the blue part of the CMD, while the red plume still has the problems described for the total field. Overall, the MIST tracks better reproduce the shape of the CMD, even if they underestimate the number of the reddest bright stars more than the COLIBRI tracks. Indeed, the upper red plume predicted by the MIST models is too weak. As a result, to reproduce the total number

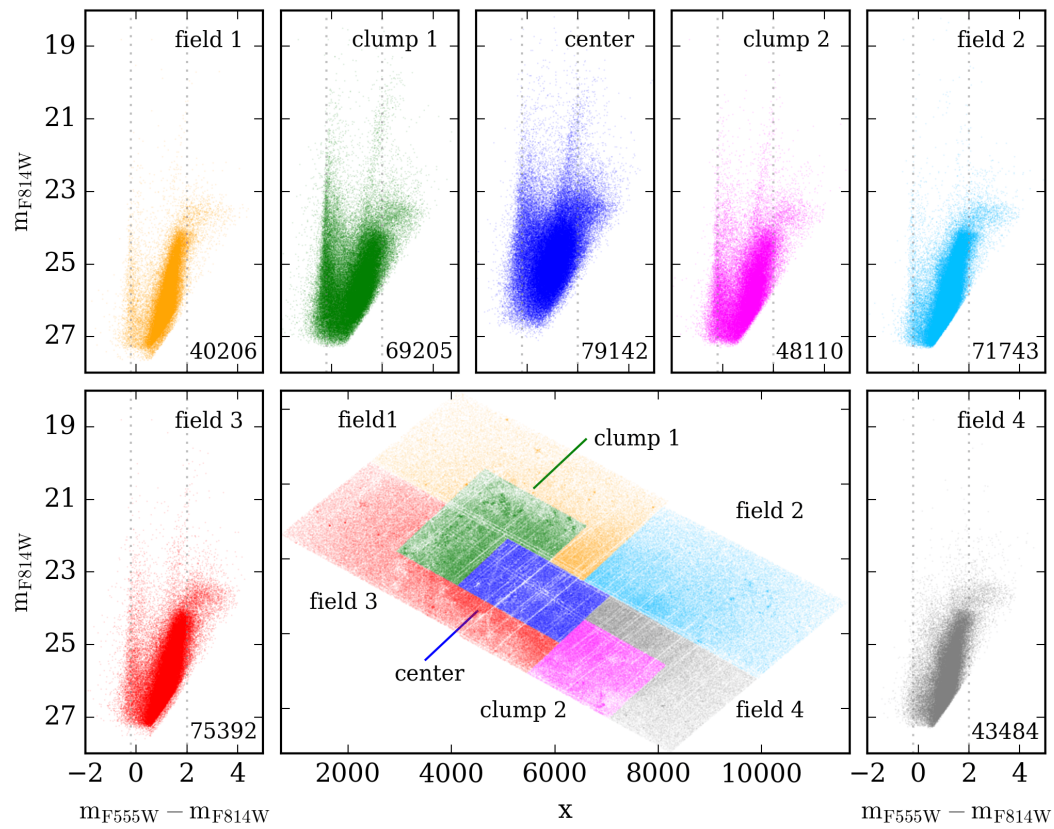


FIGURE 4.14: Map and corresponding CMDs of the 7 subregions we identified in the galaxy and used to recover the SFH; the lines and labels follow that of Figure 4.13.



FIGURE 4.15: Footprints of the seven regions identified in Figure 4.14 on the image of Figure 4.1

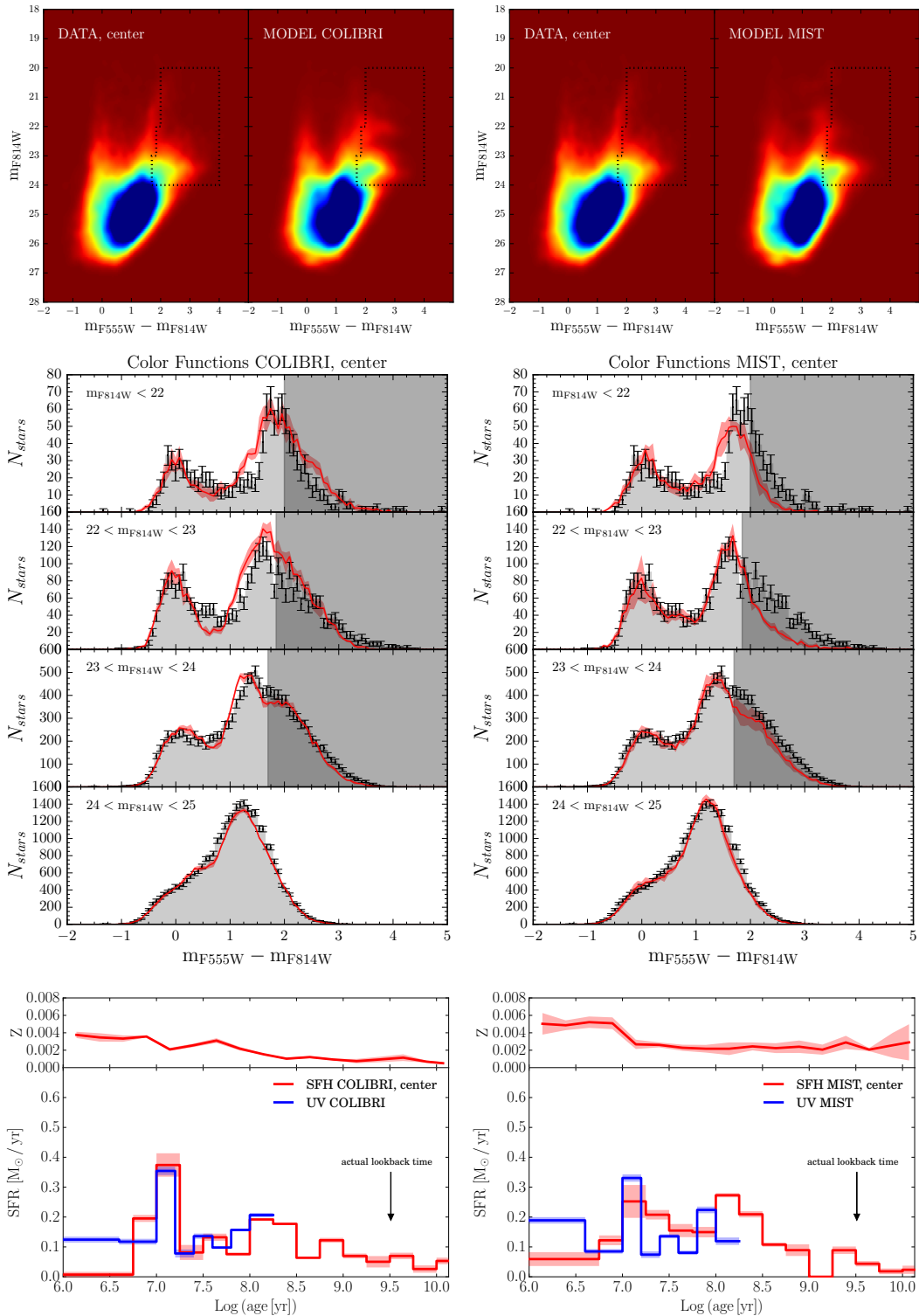


FIGURE 4.16: *Top panels.* Hess diagrams of the Center field of NGC 4449: the observational one is on the left and the one reconstructed on the basis of different sets of models on the right; the dotted line shows the region containing TP-AGB stars and excluded from the minimization. *Middle panels.* Color functions of the CMDs in different luminosity bins; the shaded part of the diagrams corresponds to the masked region in the CMD; the data are the grey histograms with a Poissonian uncertainty, while the models are the red lines with the uncertainty from a bootstrap technique. *Bottom panel.* Recovered SFH and metallicity; in blue, the UV SFHs from Cignoni et al. (2017, submitted). Notice that the SFR scale is different from that in Figure 4.9.

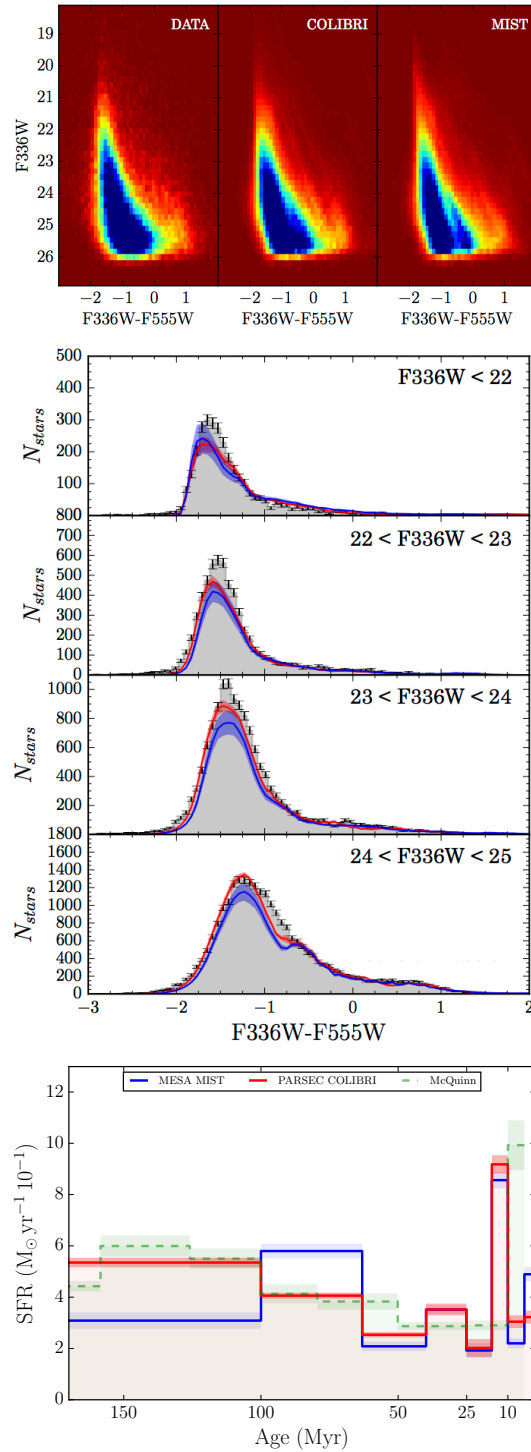


FIGURE 4.17: *Top panels.* Hess diagrams of the UVIS field of NGC 4449: the observational one is on the left and the one reconstructed on the basis of different sets of models on the right. *Middle panels.* Color functions of the CMDs in different luminosity bins; the data are the grey histograms with a Poissonian uncertainty, while the models are the red (PARSEC-COLIBRI) and blue (MIST) lines with the uncertainty from a bootstrap technique. *Bottom panel.* Recovered SFH; the green dashed line is the SFH from McQuinn et al. (2010) based on older stellar models from the Padova group.

of bright stars, the synthetic code must overpopulate the fainter part of the distribution. We find that the SFH of the Center is fairly similar to that of the whole galaxy, with the main peaks (the higher one around 14 Myr ago, the other around 100 Myr ago) and dips in SFR occurring at the same epochs. This is not surprising since the Center contains  $\sim 20\%$  of all the stars measured in NGC 4449.

The UV SFH, plotted in blue in the figure, is in very good agreement with the corresponding optical one, in particular with the COLIBRI tracks, but the overall trends still agree also with the MIST models. For deriving this recent SFH we used 9 logarithmic time bins between  $\log(t) = 5$  and 8.5 with a single age bin for the youngest stars,  $\log(t) = 5 - 6.6$ . The metallicity range, IMF and binary fraction were the same used in the optical case, as well as the distance treatment. Analogously, the extinction distribution is modeled with two parameters: a foreground extinction evenly applied to all stars,  $A_V$ , and a random additional differential extinction, between 0 and  $\Delta A_V$ . The details of our results are shown in Figure 4.17, with the SFH from McQuinn et al. (2010) for reference.

Our average SFH compares well also with  $H\alpha$  and FUV emission rates. Lee et al. (2009) derived SFRs of  $0.66 M_\odot/\text{yr}$  and  $0.89 M_\odot/\text{yr}$  from  $H\alpha$  and FUV respectively. Once corrected for the different IMF, these values are within a factor 2 from our average rates in the last 10 and 100 Myr. The best synthetic CMDs and color distributions show some differences from the observational counterparts. All models show a deficiency of MS stars for magnitudes F336W brighter than 24. The predicted number of post-MS stars (arbitrarily chosen with  $F336W - F555W > -0.5$ ) is instead generally correct, except for  $F336W < 22$  where we have an excess of synthetic post-MS stars. At fainter magnitudes ( $F336W > 24$ ) we have another issue: synthetic models show a star counts drop at colors around  $-1$ , whereas the observed color distribution is instead continuous. The presence of the gap might be an indication that models are not able to produce extended loops during the He-burning phase. Indeed, a similar gap was already devised by Tang et al. (2014) in several dwarf galaxies. Tang et al. (2014) showed that this discrepancy is overcome by extending the overshooting at the base of the convective envelope. Another possibility is that differential reddening  $\Delta A_V$  is underestimated. Indeed: 1) the main effect of differential reddening is to smear CMD features, like the gap between MS and post-MS; 2) our estimate for  $\Delta A_V$  is based on the assumption of a Gaussian reddening distribution (each synthetic star is reddened with a random reddening between  $A_V$  and  $A_V + \Delta A_V$ ), whereas the real distribution might be more complex (see, e.g., Harris, Zaritsky, and Thompson, 1997) and mass/age dependent. However, the color distribution of MS stars is generally *broader* in the model than in the data, suggesting that  $\Delta A_V$  is not significantly underestimated.

It is worth to notice that in the most recent bin the UV SFRs are higher than the corresponding optical ones. We believe that this behavior is due to the better temporal resolution of the UV CMDs, where the characterization of the youngest stellar phases is much more precise. In future analyses of both optical and UV CMDs of other LEGUS galaxies we will be able to check whether or not the UV SFR is systematically higher than the optical one at the most recent epochs, as in NGC 4449. Since the two different sets of stellar evolution models consistently provide the same kind

of results in the various fields, for sake of simplicity in the following we show only the results based on the COLIBRI models.

**Clump 1** This region includes the small elongated structure and the WR cluster mentioned in Section 4.3. As apparent from Figure 4.14, Clump 1 is the area with the tightest and brightest blue and red plumes, suggesting that its SF activity has been more peaked at certain epochs. The CMD in Figure 4.18 clearly reveals the presence of a well populated MS, and a small over-density in the red plume due to the coeval stars in the elongated structure. The model, however, fails to reproduce the very blue peak in the color functions at  $22 < m_{F814W} < 24$ ,  $m_{F555W} - m_{F814W} \sim -0.25$ . The main peak of SF is between 5 and 20 Myr ago. Interestingly, the metallicity appears to decrease with time between 3 and 1 Gyr ago; since this is one of the most active and interacting regions of the galaxy, this could be due to gas infall or a merging with another lower metallicity body.

**Clump 2** The CMDs and color functions in Figure 4.18 show a very good agreement in the fitted area, although the number of red stars just below the tip is slightly underestimated. In the SFH we can find again a peak around 10 Myr, but with lower relative importance over the activity at earlier epochs than in Clump 1. This is consistent with the almost zero  $H\alpha$  emission found in this region.

### 4.5.3 External fields

The external regions show a prevalence of old stellar populations, their CMDs being mainly constituted by TP-AGB and RGB stars. However, while the single outer region was selected to avoid all the SF regions and the streams infalling in the galaxy, the single subfields include some of these features. In fact, with the exception of Field 4, they all also show MS and very few He-burning stars, meaning that a low but non negligible SF is still active in these fields. In Figures 4.19, 4.20 and 4.21 we show their Hess diagrams, color functions and SFHs. As expected, the oldest bins enclose the main activity that generated the well-defined RGB and TP-AGB features; in particular, these RGBs are much tighter than the ones in the central regions, suggesting a lower differential reddening and/or a smaller range of metallicities.

**Field** As expected, the outermost region shows no sign of recent SF, and the SFH is somewhat complementary to that of the three central regions. The peak is in the oldest bins, but a very low activity lasts until  $\sim 300$  Myr ago.

**Field 1** Although dominated by the presence of old RGB stars, the CMD of Field 1 (Figure 4.20) shows a weak but well defined MS, reproduced by our model. In fact, as expected, the SFH has the main peak in the oldest bins, and a secondary peak of activity around 10 Myr.

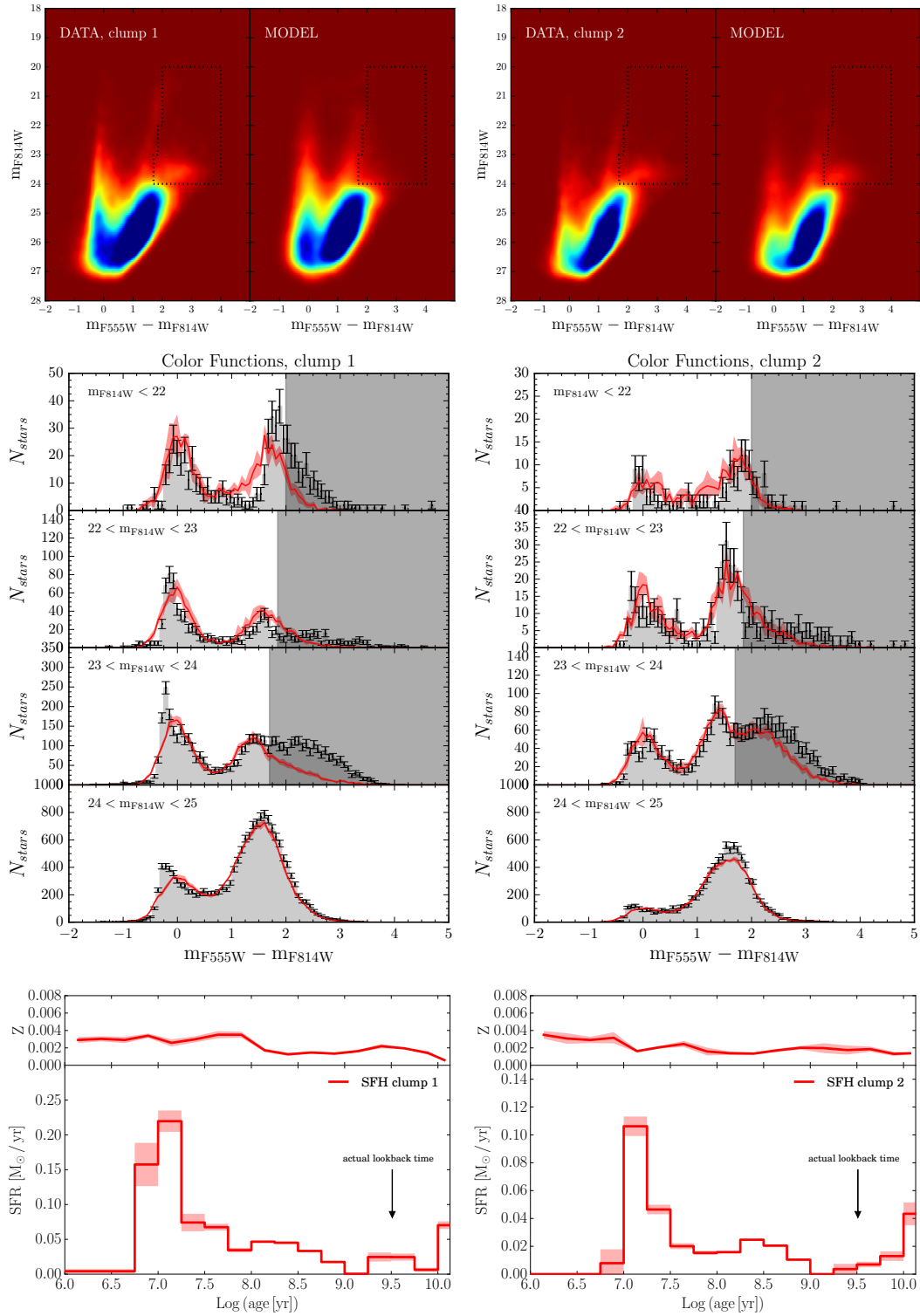


FIGURE 4.18: *Left panels.* Hess diagrams, color functions, age-metallicity relation and star formation history of Clump 1. *Right panels.* Same for Clump 2. Notice that the SFR scales are different from each other and from those of the other figures.

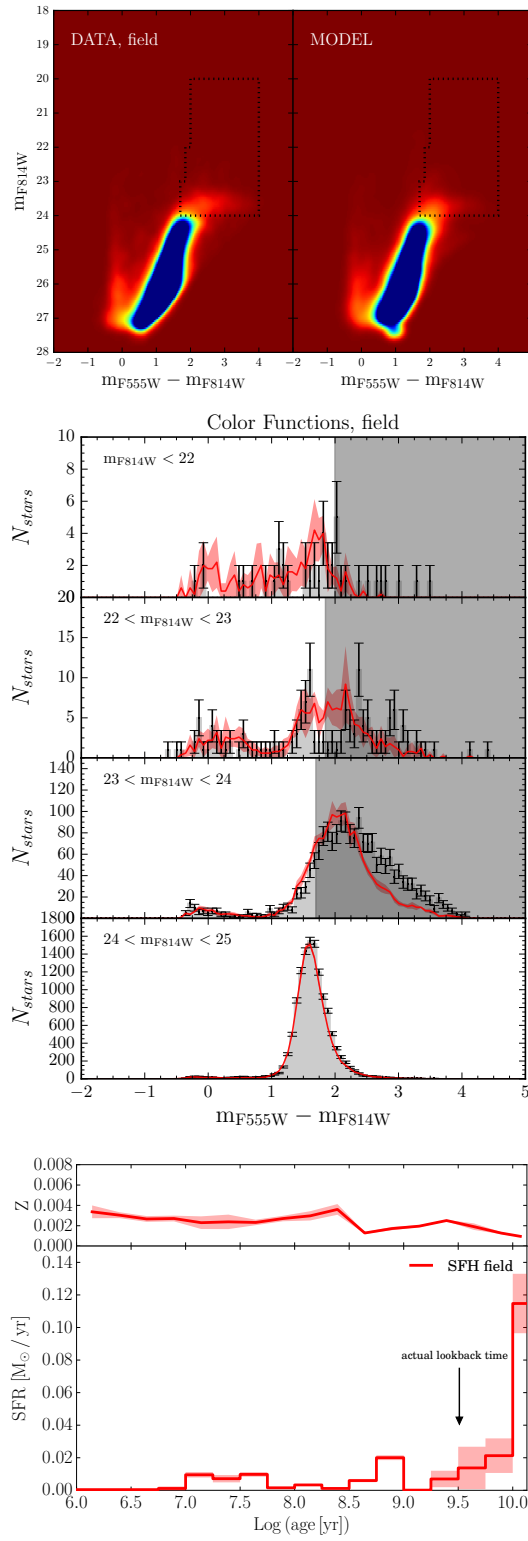


FIGURE 4.19: Hess diagrams, color functions, age-metallicity relation and star formation history of the single outer Field shown in Figure 4.13.

**Field 2** Also in this case we can see a strong RGB population with a larger spread than that of Field 1, and a weak MS. From the CMD of Field 2 also a conspicuous population of TP-AGB stars emerges, forming the horizontal feature above the TRGB.

**Field 3** Although the main features of Field 3 are similar to those of the other external fields, this region shows the strongest young population, indeed reproduced by the recovered SFH (see Figure 4.21). The highest peak remains the oldest one, in good agreement with the well populated RGB observed in the CMD.

**Field 4** Among the four external regions, Field 4 has the lowest ratio between recent ( $\lesssim 10$  Myr) and old ( $> 1$  Gyr) activity, as shown by its CMD (Figure 4.14) and SFH (Figure 4.21); thus, we can consider it completely part of the halo of the galaxy, with a very diffuse emission and no evidence of young bursts of SF.

A summary of the SFRs and stellar masses formed in different epochs for both the whole galaxy and the 7 sub-regions is given in Table 4.1.

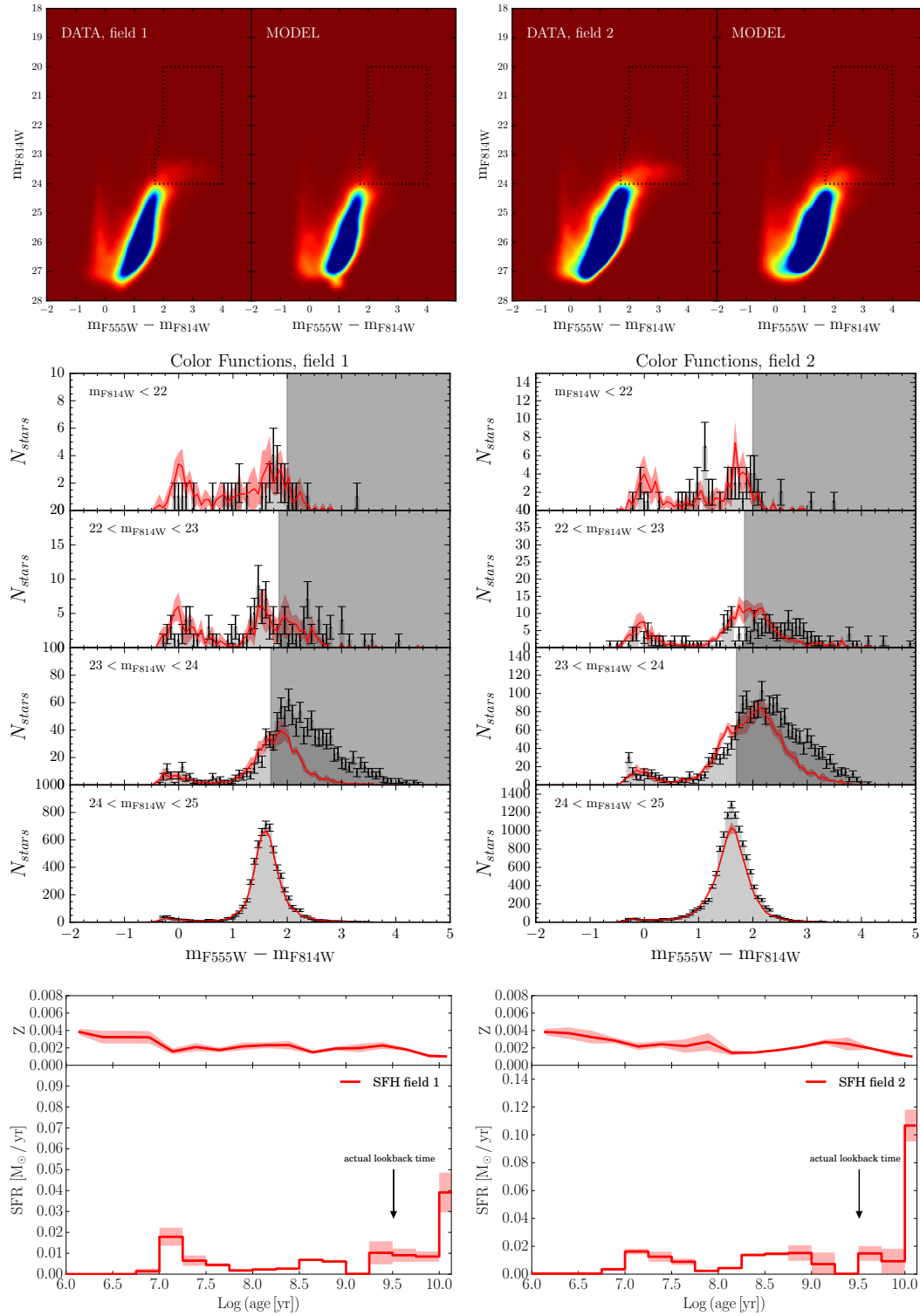


FIGURE 4.20: *Left panels.* Hess diagrams, color functions, age-metallicity relation and star formation history of Field 1. *Right panels.* Same for Field 2. Notice that the SFR scales are different from each other and from those of the other figures.

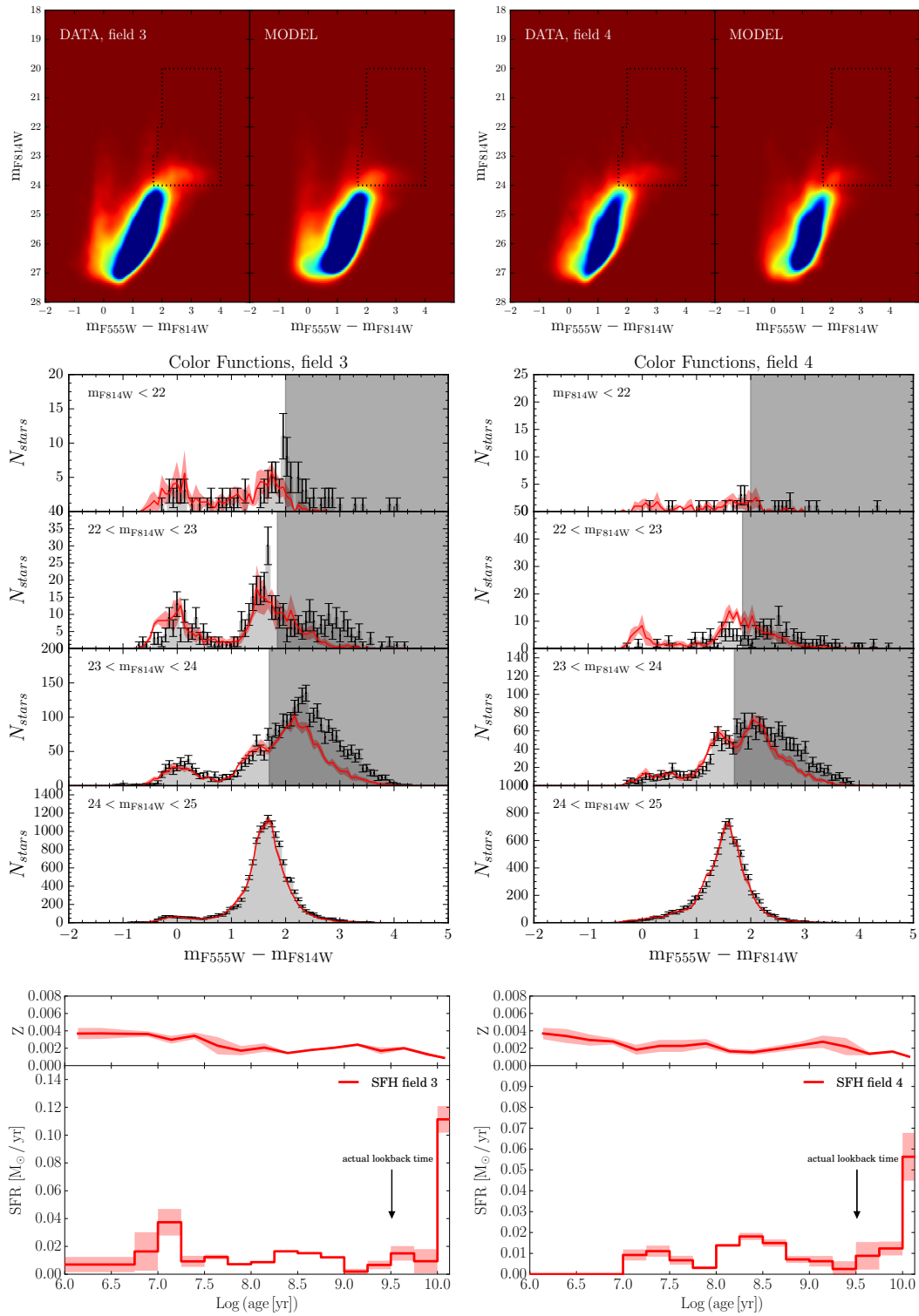


FIGURE 4.21: *Left panels.* Hess diagrams, color functions, age-metallicity relation and star formation history of Field 3. *Right panels.* Same for Field 4. Notice that the SFR scales are different from each other and from those of the other figures.

TABLE 4.1: Summary of the star formation rates and stellar masses in the different fields.

region	$\langle \text{SFR} \rangle$ [ $M_{\odot}/\text{yr}/\text{kpc}^2$ ]	$\text{SFR}_{\text{peak}}$ [ $M_{\odot}/\text{yr}/\text{kpc}^2$ ]	$\text{age}_{\text{peak}}$ [Myr]	$M_*(\text{age} \leq 10 \text{ Myr})$ [ $10^6 M_{\odot}$ ]	$M_*(\text{age} > 1 \text{ Gyr})$ [ $10^9 M_{\odot}$ ]
Total	$0.011 \pm 0.002$	$0.043 \pm 0.005$	7.8	$4.2 \pm 0.6$	$2.00 \pm 0.15$
Center	$0.069 \pm 0.009$	$0.254 \pm 0.027$	13.9	$0.9 \pm 0.1$	$0.59 \pm 0.08$
Clump 1	$0.025 \pm 0.003$	$0.111 \pm 0.008$	13.9	$0.7 \pm 0.2$	$0.36 \pm 0.03$
Clump 2	$0.015 \pm 0.002$	$0.079 \pm 0.005$	13.9	$0.03 \pm 0.04$	$0.23 \pm 0.03$
Field 1	$0.0018 \pm 0.0005$	$0.010 \pm 0.006$	$12 \times 10^3$	$0.006 \pm 0.006$	$0.21 \pm 0.04$
Field 2	$0.0033 \pm 0.0008$	$0.026 \pm 0.003$	$12 \times 10^3$	$0.017 \pm 0.007$	$0.46 \pm 0.06$
Field 3	$0.0056 \pm 0.0002$	$0.033 \pm 0.003$	$12 \times 10^3$	$0.11 \pm 0.06$	$0.48 \pm 0.05$
Field 4	$0.0048 \pm 0.0012$	$0.027 \pm 0.006$	$12 \times 10^3$	$< 10^{-4}$	$0.28 \pm 0.05$

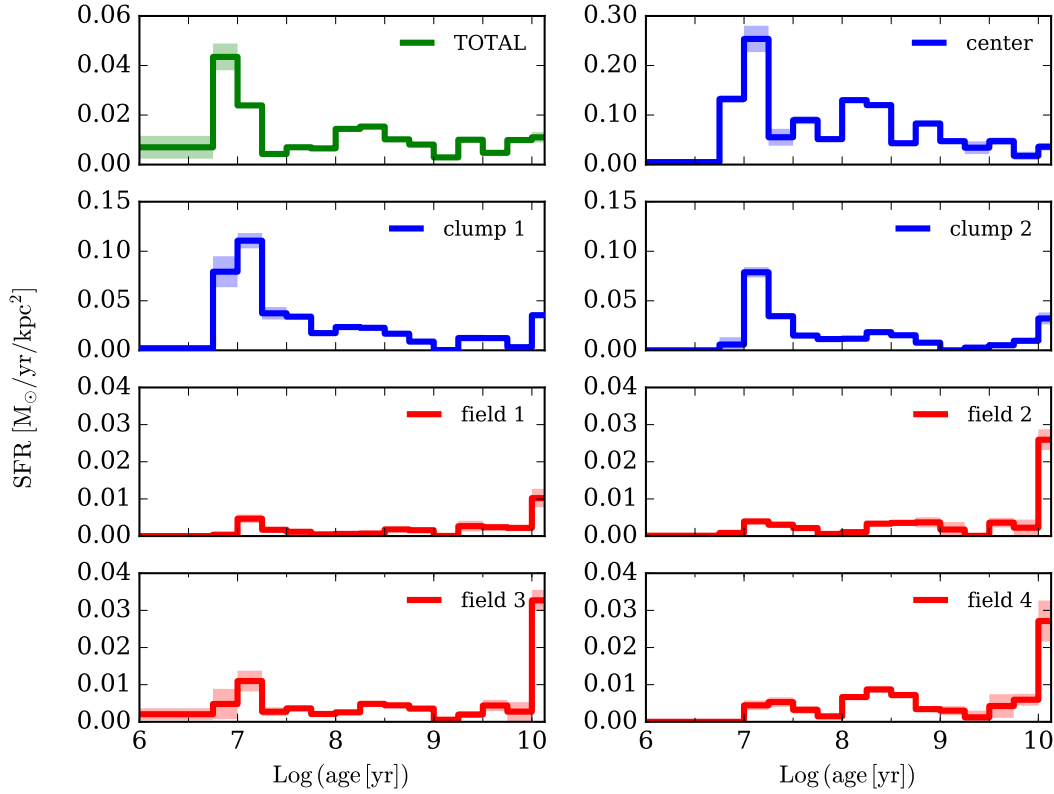


FIGURE 4.22: SFR surface densities (SFR/area) of the whole galaxy and the separate fields of NGC 4449. The colors indicate the total region (green), and the regions where we find a high (blue) and low (red) SF activity. Notice the different scales of the plots.

## 4.6 Results

In this Chapter we derived and analyzed the detailed star formation history of the Magellanic irregular galaxy NGC 4449 on the basis of its optical and UV color-magnitude diagrams. Here we summarize the main results and compare them with the literature, in order to place them in a broader context of the formation and evolution of this class of galaxy.

NGC 4449 is often considered a starburst galaxy and is indeed one of the most actively star-forming systems of the local Universe (Lee et al., 2009). However, there is no unique definition of a starburst, that may depend on the properties considered in the analysis. One definition is based on a short measured duration of the starburst activity and a current SFR that exceeds the average past value by a factor of at least 2 – 3 (McQuinn et al., 2010). In the case of NGC 4449 these values are less than  $\sim 20$  Myr and  $\sim 4$ , respectively. Another related quantity is the integrated  $H\alpha$  equivalent width, i.e. the  $H\alpha$  flux divided by the continuum flux density under the line. Lee et al. (2009) fix a threshold at 100 Å, that is not matched by NGC 4449 (which has an  $H\alpha$  equivalent width of  $\sim 72$  Å). However, since the  $H\alpha$  emission has a very short timescale, it might be tracing only starbursts with an enhanced activity in the last  $\sim 5$  Myr, which is indeed not the case of NGC 4449.

Our study shows that NGC 4449 has experienced a significant enhancement in the SF activity about 10 Myr ago, but we do not consider it a real burst, since its SFR is only a factor of  $\leq 4$  higher than in the quietest phases. We are inclined to consider a SF regime as “bursting” when the SFR of the burst is at least 10 times higher than average, its duration is short, and significantly long quiescent (or very quiet) phases are present. None of these conditions are met in NGC 4449.

Our results on the stellar populations and SFH clearly highlight the complexity of this galaxy, revealing a very peculiar boxy shape, a centrally concentrated S-shaped bar and H II regions in various clumps, also quite far from the most central region (at the edge of the optical galaxy). The SFH has a peak  $\sim 10$  Myr ago, lasting roughly until 20 Myr ago, in quite good agreement within the uncertainties with the results from McQuinn et al. (2010), which is the only other SFH available for this galaxy determined from optical photometric data (which are the same *HST* data we use here). They find another peak around 100 Myr that we don’t recover, mainly because of both the different stellar evolution models used and the fact that the TP-AGB phase is still not well-modeled. The SFH of the very central region shows excellent agreement with the SFH from our UV data, confirming the validity and consistency of our method and the robustness of our results.

Figure 4.22 shows the results for the SFHs of the whole galaxy and the sub-regions of NGC 4449, divided for the area of each region (chosen as the area including 90% of the stars in each field) in order to obtain a SFR surface density and to properly compare the SFH even among fields of very different spatial dimensions. In fact, even though smaller, the central region has the highest SFR density, as expected from the great amount of ionized emission. Both the clumps have also a significant recent activity, and Clump 1 shows signs of ongoing SF. These three regions together provide  $\sim 40\%$  of the SFR ( $\leq 10$  Myr) of the total galaxy. The external fields are

less active, showing a prevalence of older SF. Field 1 is the least active one, with a very low SF but some recent activity, while Fields 2 and 4 are quite similar and have a slightly higher activity except for Field 4 showing no sign of SF at recent epochs ( $< 10$  Myr). Field 3 is generally more active and shows a significant peak even in the recent bins. Clump 2 is overall more active than Field 3 but not in recent epochs, where also Clump 1 shows a higher peak. The Center is quite similar to Clump 1 but with a higher level of SF (see Table 4.1 for the details).

The UV data confirmed the “gaspings” scenario. In fact, no strong SF burst was detected in the last 180 Myr, with a SFR increasing, at most, by a factor of  $\approx 2$  over the 180 Myr-averaged SFR. The age resolution improves dramatically for ages less than 50 Myr, but strong variations over intervals of a few Myr are not observed either: we found peaks only  $\approx 2-3$  times higher than the 50 Myr-averaged SFR. This “flickering” SF mode is typically seen in the last 100 Myr of many high resolution studies (McQuinn et al., 2010; Weisz et al., 2008) and is probably connected with the formation of star clusters and associations. Multiple flickering events could then form the long-lasting ( $> 450$  Myr) bursts detected by McQuinn et al. (2010) in several dwarfs, whose origin is probably global.

It is remarkable that despite a number of differences, the stellar models PARSEC-COLIBRI and MIST provide consistent SFHs, indicating that evolutionary times of intermediate and massive stars are not significantly different. However, while all models generally reproduce the expected numbers of MS and post-MS stars in different magnitude bins, the color distributions show several issues which cannot be readily fixed by changing metallicity. The transition from MS and post-MS is especially problematic. At the bright end the total number of massive stars is well reproduced, but not the ratio between MS and post-MS, with a clear excess of the latter. This behavior is further complicated at the faint end of NGC 4449 ( $F336W > 23$ ), where all models predict a gap between MS and post-MS around  $F336W-F555W \approx -1$ , whereas the observational CMD shows a smooth transition. We also found that NGC 4449 is affected by a significant differential reddening, that may have a role behind the mismatches. This could be also due to the metallicity, suggesting a difficulty of models in matching the BL length at higher metallicity.

## 4.7 Discussion

The results presented above suggest the impact of possible recent phenomena to be stronger in the Northern regions, on a East-West axis (crossing Center, Clump 1, Field 3). Interestingly, this trend resembles what was discussed by Annibali et al. (2011) in their analysis of the cluster population of this galaxy (shown in Figure 4.6): they find that some old stellar clusters in NGC 4449, instead of following a uniform distribution across the galaxy as one would expect, seem to follow some linear structures possibly linked to a past accretion event (see their Figure 16). One of these structures crosses the regions where we find the highest activity and is roughly perpendicular to the structure in Clump 1. All these hints could again be evidence of a common event triggering significant activity in these regions, a scenario also suggested by Valdez-Gutiérrez et al. (2002) on the basis of their kinematic and dynamical study of the high perturbed velocity field of the ionized gas in NGC 4449. Very young clusters (age  $< 10$  Myr) are instead found only in the very central regions (six in Center, two in Clump 1 and one in Clump 2) and, as expected, tightly follow the distribution of the  $H\alpha$  emission (Annibali et al., 2011; Gelatt, Hunter, and Gallagher, 2001); here Reines, Johnson, and Goss (2008) also detected 13 embedded massive star clusters with thermal radio emission.

The elongated structure shown in Figure 4.6 and included in Clump 1 seems to be a coeval population probably formed as a result of the interaction, possibly a merging, with a smaller galaxy tidally disrupted by the main body of NGC 4449. Both the luminosity of these stars and the SFH we recover (see the results for Clump 1 in Figure 4.18) suggest an age of a few tens of Myr, while the embedded massive WR cluster, also contained here, has a minimum age of  $\sim 3$  Myr (Sokal et al., 2015). Indeed, Theis and Kohle (2001) performed several N-body simulations to reproduce the H I morphology of NGC 4449, finding that the observed features could be created by an encounter with a smaller dwarf galaxy. Moreover, as discussed by Lelli, Fraternali, and Verheijen (2014) and Lelli, Verheijen, and Fraternali (2014b), galaxies with young ( $\lesssim 100$  Myr) bursts of star formation usually show a very asymmetric H I morphology, which is also related to past and ongoing interaction/accretion events.

In many works it is outlined how starburst dwarf galaxies usually show very different morphological, dynamical and environmental characteristics. Among them, Lelli, Verheijen, and Fraternali (2014b) explore the H I morphology of several active dwarf irregulars (NGC 4449 included), trying to understand the main process triggering the starburst activity. They find that this enhanced activity usually correlates well with a disturbed H I morphology, suggesting that the starburst is likely triggered by external mechanisms (merging/gas inflow) rather than by internal ones (stellar feedback). The discovery of a stellar tidal stream from a disrupted dwarf galaxy in the halo of NGC 4449 (Rich et al., 2012; Martínez-Delgado et al., 2012) and of a possible remnant of a gas-rich accreted satellite (Annibali et al., 2012) also points at this scenario, and the dynamical timescale to see the tidal features of the encounters ( $< 10^8$  yr from Peñarrubia et al., 2009) is compatible with the beginning of the higher SF activity we find in the galaxy. The H I tails are possibly led also by the companion galaxy DDO 125, an irregular galaxy at a projected distance of 41 kpc from NGC 4449.

On the other hand, El-Badry et al. (2016) investigated through cosmological hydrodynamic simulations the effect that stellar feedback has on the stellar component of isolated dwarf galaxies; they find that gas outflows and inflows can severely affect the stellar kinematics and radial gradients in low-mass galaxies ( $M_* \sim 10^{7-9.6}$ ). The two effects might indeed be in action at the same time: stellar feedback on small scales (less than 10 kpc) where we actually see the stellar component of the galaxy, and external mechanisms on scales where the H I component becomes dominant (several 10 kpc).

As mentioned before, LEGUS is also studying in detail the star clusters in NGC 4449 (Adamo et al., in preparation, Cook et al., in preparation), with a multi-band approach that should provide soon a clearer scenario not only on their formation and evolution, but also on that of the whole galaxy.

Even though our photometry can constrain populations as old as a few Gyr only, there are several spectroscopic studies revealing features from older stars. Strader, Seth, and Caldwell (2012) found globular clusters consistent with ages of 7 – 10 Gyr; Karczewski et al. (2013) performed a fit to the multi-wavelength spectral energy distribution of NGC 4449, from the far-ultraviolet to the submillimetre, and found models consistent with a first onset of star formation around 12 Gyr ago. They assumed a simplified SFH consisting of only three episodes, old (between 12 Gyr and 400 Myr ago) with a SFR of  $0.09 M_\odot \text{ yr}^{-1}$ , intermediate (between 400 and 10 Myr ago) with a SFR of  $0.14 M_\odot \text{ yr}^{-1}$ , young (last 10 Myr) with a SFR of  $0.28 M_\odot \text{ yr}^{-1}$ . If we average our results to compare them with the listed ones, we find slightly higher values (old:  $0.16 M_\odot \text{ yr}^{-1}$ , intermediate  $0.24 M_\odot \text{ yr}^{-1}$ , young  $0.42 M_\odot \text{ yr}^{-1}$ ) but consistent within the uncertainties.

To statistically increase the comparison with other galaxies, we consider the work by Weisz et al. (2011), who provide the SFHs of 60 dwarf galaxies within the ANGST program. They find a huge diversity in the evolution of the SF among different morphological types, and also within the dwarf irregular sub-sample (see their Figures 3 and 4). However, all the galaxies in the sample seem to have formed the bulk of their stars earlier than  $\sim 1$  Gyr ago, in agreement with what we find for NGC 4449.

The LEGUS UV data highlight a SF enhancement in the last 50 Myr, followed by a minor activity in the last 10 Myr. An interesting question is whether or not the most recent peak is a unique event in the recent history of the galaxy. Simulations taking into account feedback processes illustrate that star formation in isolated dwarf galaxies can exhibit episodic or cyclic behavior (Stinson et al., 2007). Here, the starburst is terminated by the expulsion of gas through supernova winds. If the gas later accretes back to the galaxy, a new starburst could be ignited. In our case, the answer depends on the look-back time. In the last 16 Myr, NGC 4449 assembled about  $8.4 \times 10^6 M_\odot$  (according to the PARSEC-COLIBRI solution). If we dilute this mass between 40 and 63 Myr ago, the resulting SFR ( $\approx 0.36 M_\odot/\text{yr}$ ) would be *higher* than the measured rate ( $\approx 0.25 M_\odot/\text{yr}$ ), whereas between 63 and 100 Myr ago the resulting SFR would be *lower* than the measured rate (hence we can not exclude multiple events like the current one or stronger). Taking these numbers at face value and considering the error bars of our SFH, we find unlikely that another SF enhancement similar to the most recent one has taken place in NGC 4449 in the past 50 Myr, whereas at older epochs the situation is much more uncertain. In other words, the

recent enhancement of NGC 4449 is probably a unique event in the last 50 Myr, but nothing can be said for the earlier epochs. From this point of view, a SFH composed by periodic bursts with duration 5 Myr, period 50 Myr and peak rate like the current one, would be indistinguishable from a constant activity prior to 50 Myr ago.

An obvious question is what triggered the SF enhancement. If it is a cold flow accretion or a merger event, nearby H I gas maps might show morphologically disturbed features. Indeed, the global dynamics of the H I associated with NGC 4449 show large distortions. A key observational feature for this galaxy is neutral hydrogen extending to 6 times its Holmberg radius (van Woerden, Bosma, and Mebold, 1975; Hunter et al., 1998), characterized by an elongated ellipse of lower column density with a major axis of 35 kpc. Beyond the ellipse, there is a complex distribution of clouds and streamers that wrap around the galaxy. From a kinematical point of view, the gas in the central 4 kpc diameter, which corresponds to the brighter part of the optical galaxy, is seen to exhibit rotation in the opposite direction to that of the ellipse and streamers. Moreover, Hunter, van Woerden, and Gallagher (1999) found that the regions with the highest velocity dispersions in H I are located outside the regions of SF and in some cases beyond the bright part of the optical galaxy.

All these characteristics are consistent with a picture in which NGC 4449 has been disturbed by an external perturber, and the gas has not yet returned to equilibrium. However, in contrast to the disturbed morphology of the gas, NGC 4449 is a fairly isolated system. Its closer neighbor, DDO 125, located at an apparent separation of 41 kpc from the center of NGC 4449, does not show signs of damage and its global gas and optical properties are typical of irregular galaxies (Hunter, 1997). Between NGC 4449 and DDO 125 no clear bridge has been detected. As discussed in Hunter et al. (1998), with an H I mass of only  $10^8 M_{\odot}$ , it would have to have lost 90% of its H I mass in order to account for all of the mass in the streamers. More recently Martínez-Delgado et al. (2012) and Rich et al. (2012) detected and analyzed a stellar tidal stream in the halo of NGC 4449, arguing that this object is the result of the ongoing disruption of a dSph galaxy, while Annibali et al. (2012) found a globular cluster of NGC 4449 which appears associated with two tails of blue stars, possibly the nucleus of a former gas-rich satellite galaxy undergoing tidal disruption by NGC 4449. Finally, using metallicity measurements of the stream, Toloba et al. (2016) suggested a progenitor as massive as Fornax or Sagittarius. Interestingly, an interaction like that could have had a substantial impact on NGC 4449.

*The work presented in this Chapter has been reported in the following publications:*  
Sacchi et al. (2017, submitted)  
Cignoni et al. (2017, submitted)

## 5. THE SPIRAL: NGC 7793

---

In this Chapter, we present the analysis of NGC 7793, a flocculent spiral (morphological type SA(s)d) part of the Sculptor group, located at a distance of  $3.7 \pm 0.1$  Mpc (Radburn-Smith et al., 2011). NGC 7793 is a typical late-type Sd galaxy, with a very tiny bulge and a filamentary spiral structure; its stellar mass is  $M_* \sim 3.2 \times 10^9 M_\odot$  (Leroy et al., 2008) while the neutral gas mass is  $M_{\text{HI}} \sim 7.8 \times 10^8 M_\odot$  (Calzetti et al., 2015). The Sculptor group has the interesting characteristics of being at a high galactic latitude ( $-77^\circ 2$ ), that minimizes foreground extinction and contamination from the Milky Way, of containing mainly isolated disk systems, and of being at a distance that allows resolved stellar population studies of its member galaxies (it is indeed the closest group of galaxies outside the Local Group). The outer disk of NGC 7793 is particularly well studied, since it exhibits a discontinuity in the metallicity gradient which becomes positive beyond the disk break (Vlajić, Bland-Hawthorn, and Freeman, 2011). Also the radial surface brightness profiles of different stellar populations have a disk break that appears at a constant radius for all stellar ages, but older stars show a steeper profile internal to the break and a shallower profile beyond the break in comparison to younger stars, indicative of high levels of stellar radial migration (Radburn-Smith et al., 2012).

Bibby and Crowther (2010) studied the population of Wolf-Rayet (WR) stars in NGC 7793, i.e. helium burning stars descendants of massive O stars with very strong stellar winds. They find 52 of these sources, and with additional slits on the H II regions, they estimate a metallicity gradient using strong line calibrations of  $12 + \log(O/H) = 8.61 \pm 0.05 - (0.36 \pm 0.10) r/R_{25}$  and a SFR of  $0.45 M_\odot \text{ yr}^{-1}$ . Another study by Stanghellini, Magrini, and Casasola (2015) analyzed the strong-line oxygen abundances in the H II regions of the galaxy, finding similar radial metallicity gradients, inside  $R_{25} = 5.24 \pm 0.24$  arcmin, also in agreement with the previous study by Edmunds and Pagel (1984).

From VLA H I observations Carignan and Puche (1990) derived the rotation curve out to  $\sim 8'$ . A remarkable result of those observations is that, contrary to most spirals, the rotation curve is not flat in the outer parts but appears to be declining ( $\Delta V_{\text{rot}} \simeq 30$  km/s or 25% of  $V_{\text{max}}$  between the maximum velocity and the last point of the rotation curve), even after a careful modeling (tilted-ring model) of the warp in the outer H I disk. Although the rotation curve is declining in the outer parts, it is flatter than a pure Keplerian decline, and a dark halo is still needed to properly model the mass distribution. Dicaire et al. (2008) followed up this study and confirmed the uniqueness of this rotation curve with independent observations using the H $\alpha$  as tracer.

We used new LEGUS observations to study the stellar populations of this galaxy and infer for the first time its star formation history.

## 5.1 Observations and Data

LEGUS observed NGC 7793 with the *HST*/WFC3 UVIS channel, in the filters F275W, F336W, F438W, F555W, F814W, and F657N, in the two fields shown in Figure 5.1. The images were aligned, combined, and finally processed with the photometric package DOLPHOT version 2.0 (Dolphin, 2016).

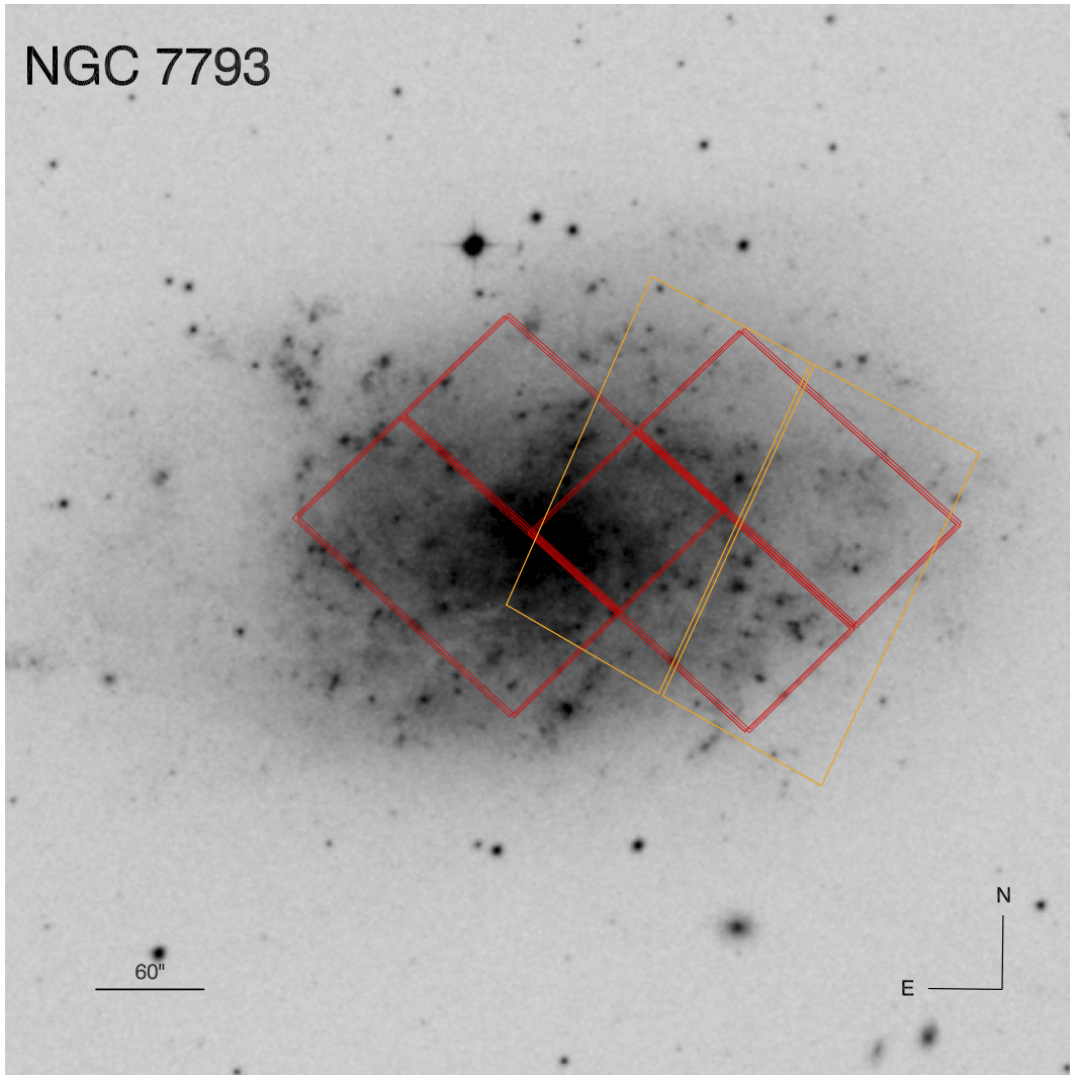


FIGURE 5.1: UVIS (red) and ACS (orange) footprints on a DSS image of NGC 7793 ( $10 \times 10$  arcmin). The angular scale and orientation of the image are also indicated.

For each star DOLPHOT provides the position relative to the drizzled image, the magnitude and a series of diagnostics to evaluate the quality of the photometry, including signal-to-noise (S/N) ratio, photometric error,  $\chi^2$  for the fit of the PSF, roundness (which can be used to identify extended objects), object type (which describes the shape of the source), and an error flag, which is larger than zero whenever there is an issue with the fitting (i.e., because of saturation or extension of the source

beyond the detector field of view). To correctly interpret the properties of the stellar populations found in the galaxy, we need to differentiate as much as possible the bona fide apparently single stars from extended objects, blended sources, and spurious detections. Thus, we used these output parameters to select our data, using the following criteria, to retain a source: photometric error  $\sigma \leq 0.2$ , squared sharpness  $\leq 0.2$ , crowding  $\leq 2.25$ , object type  $\leq 2$  for the F555W and F814W catalogs; photometric error  $\sigma \leq 0.2$ , squared sharpness  $\leq 0.15$ , crowding  $\leq 1.3$ , object type  $\leq 2$  for the F336W and F555W catalogs (following Williams et al., 2014).

Our final optical catalogs contain  $\sim 266\,000$  stars in both F555W and F814W for the eastern field of NGC 7793, and  $\sim 275\,000$  stars for the western field; the UV catalogs contain  $\sim 57\,000$  stars in both F336W and F555W for the eastern field, and  $\sim 41\,000$  stars for the western field. Notice that the western field contains more stars in the optical selection, but not in the UV one; this is due to its more external position with respect to the disk of the galaxy, which contains the majority of the young SF.

The CMDs corresponding to the four catalogs are shown in Figures 5.2 and 5.3.

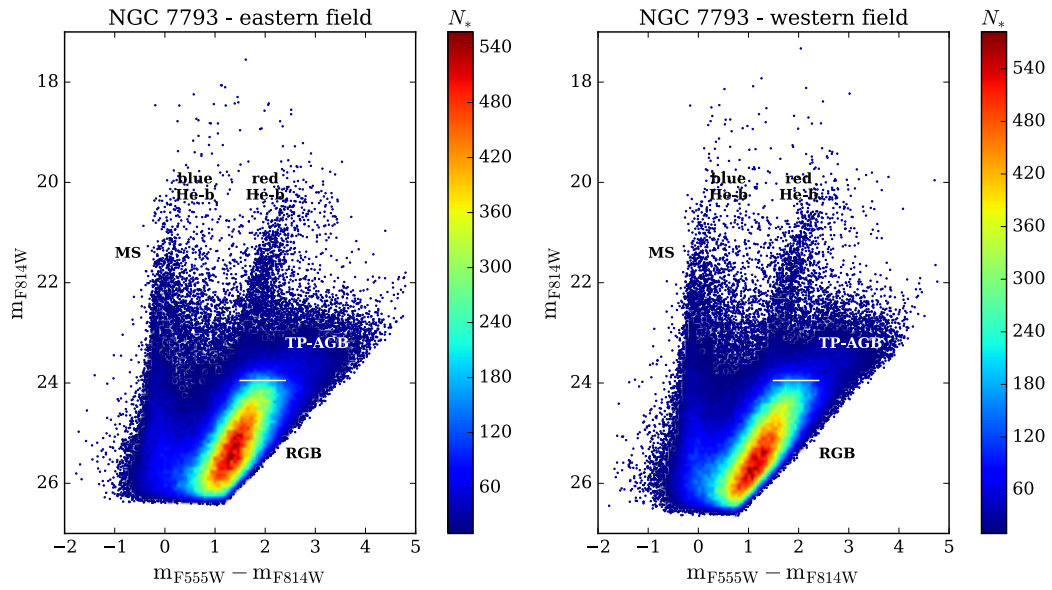


FIGURE 5.2: Optical Color-Magnitude Diagrams (after the quality cuts) of the two fields of NGC 7793 covered by the WFC3 and ACS imaging. The high density regions have been binned and color coded by number density (see the color-scale bar on the right of each panel) for a better visualization of the evolutionary features in the diagram. The main stellar evolutionary phases are indicated (see Section 4.3). The horizontal white line represents the magnitude of the red giant branch tip.

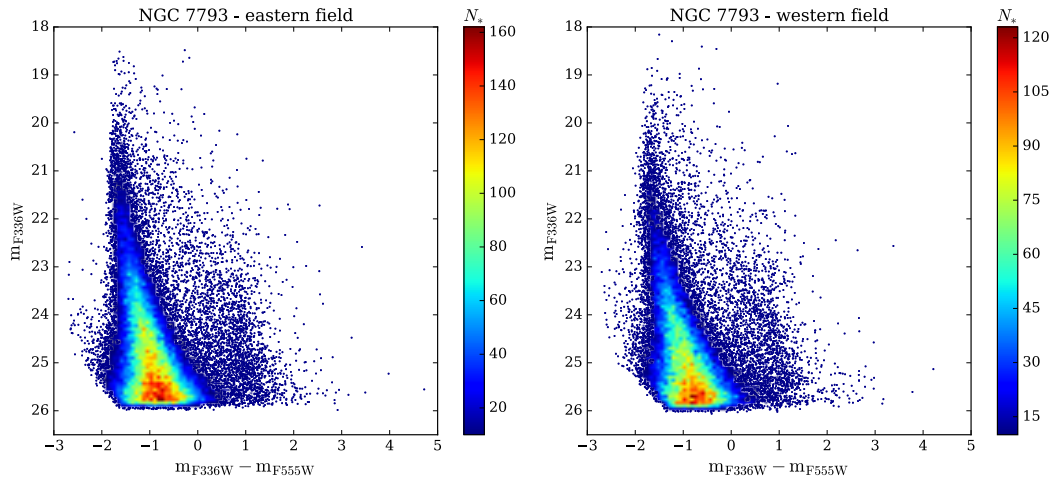


FIGURE 5.3: UV Color-Magnitude Diagrams (after the quality cuts) of the two fields of NGC 7793 covered by the WFC3 imaging. The high density regions have been binned and color coded by number density as in Figure 5.2.

## 5.2 Distribution of the stellar populations

Figure 5.4 shows a color combined image of the eastern field, which includes in red the  $H\alpha$  emission (F657N filter), tracing the star forming H II regions of the galaxy. The figure highlights very well the spiral but flocculent morphology of the galaxy, characterized by very clumpy emission both in F336W (blue) and F657N (red).

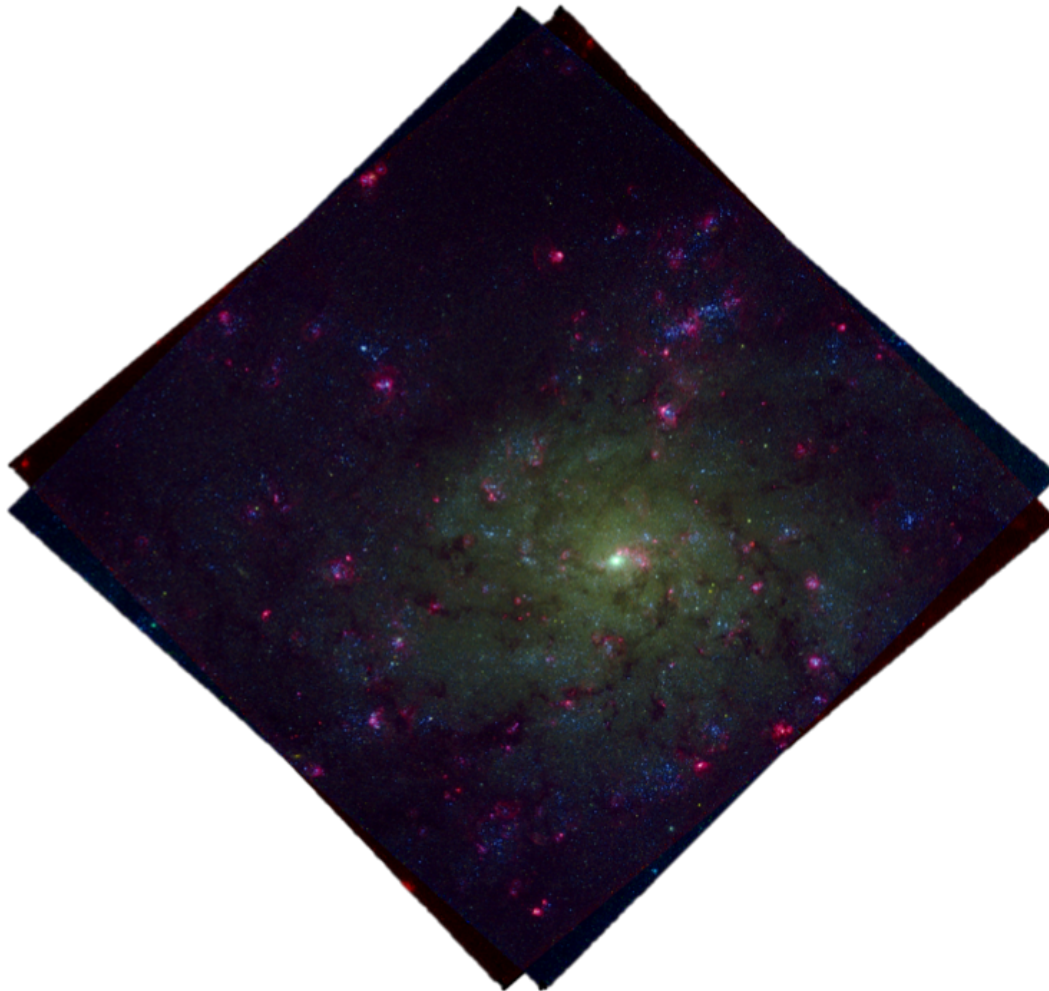


FIGURE 5.4: Three color combined image of the eastern field of NGC 7793 (F336W in blue, F555W in green, F657N in red).

Figure 5.2 shows the F814W versus F555W–F814W CMDs for the two fields we observed of the galaxy. They are very similar, but an accurate analysis reveals also some differences. First, it can be noticed that the western field CMD is deeper (by  $\sim 0.25$  mag), due to a higher level of completeness, as expected for a more external field. Moreover, the eastern field has a broader MS, and the whole CMD is slightly redder ( $\Delta\text{mag} \sim 0.2$ ), suggesting higher levels of both extinction and differential reddening, again in agreement with the position of the fields with respect to the galaxy dusty disk.

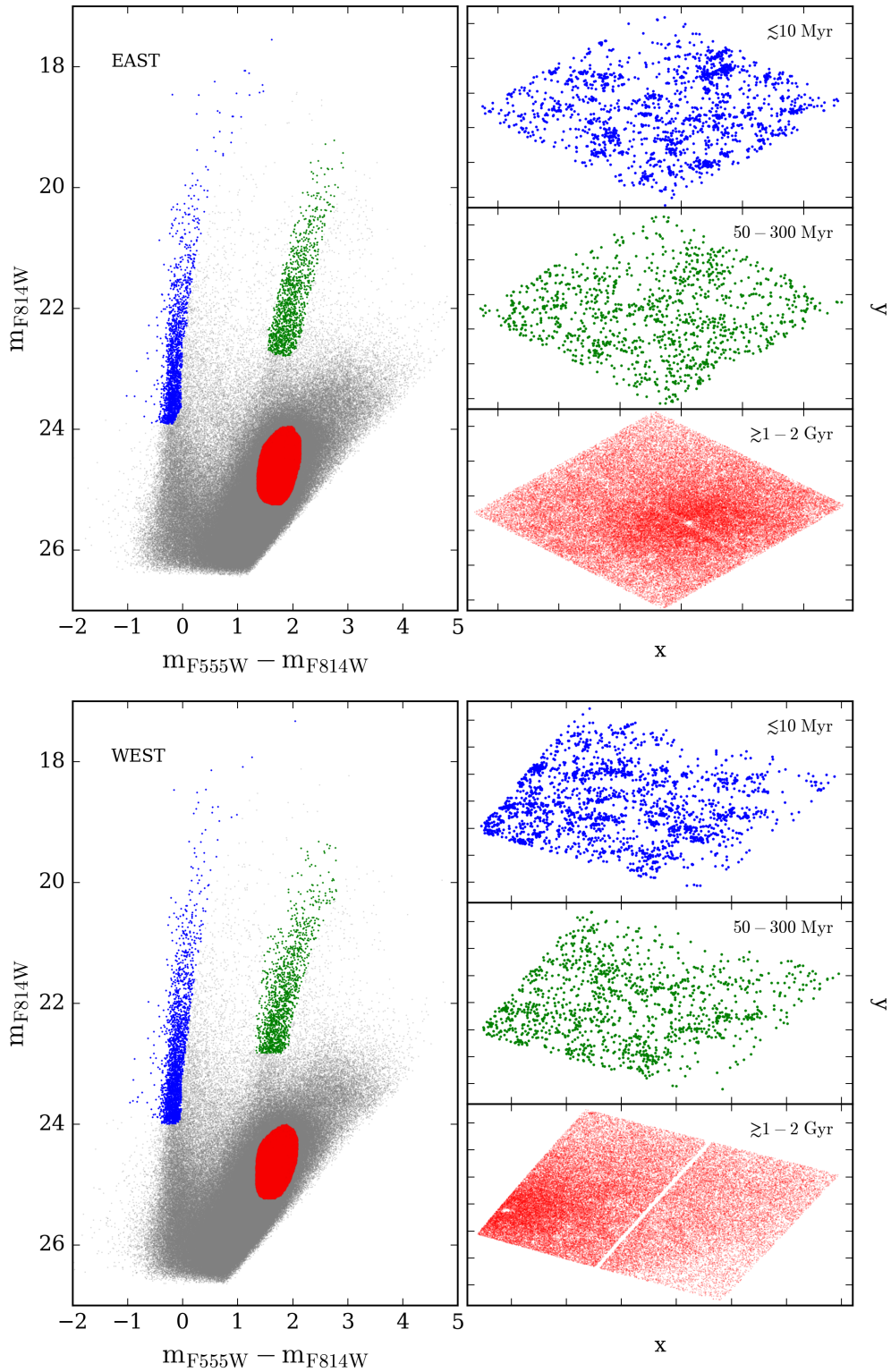


FIGURE 5.5: *Left panels.* Selection of three different stellar populations in the CMDs: in blue, stars with ages  $\lesssim 10$  Myr; in green, stars with intermediate ages between  $\sim 50$  and  $\sim 300$  Myr; in red, stars older than  $\sim 1 - 2$  Gyr. *Right panels.* Spatial distribution of the age-selected stars.

The main stellar evolutionary phases are clearly recognizable in both CMDs, and are typical of galaxies with a continuous star formation, from ancient to recent epochs. We see a well-populated blue plume, with MS and hot core He-burning stars, the red plume with mainly red He-burning stars, some BL stars between the two plumes, the horizontal feature characteristics of TP-AGB stars, and finally the RGB, our older age signature.

As we did for the other galaxies, we isolated three age intervals in the CMD and checked how the populations are distributed across the galaxy. The results are shown in Figure 5.5.

The distribution of the stellar populations in this spiral galaxy is very different from what was found for the irregulars DDO 68 and NGC 4449. The young stars here follow the structure of the flocculent spiral “arms”, spread all over the disk of the galaxy; almost all the sources found in this age interval also have a measured flux in the F336W filter. As expected, the slightly older population shows a similar, but less clumpy distribution. The oldest stars reveal an elliptical shape that traces the halo of the galaxy, with a central hole due to the incompleteness of the most crowded region.

To study the spatial variations of the SF across the body of the galaxy, we followed this elliptical contours to divide the galaxy in three sub-regions, shown in Figure 5.6.

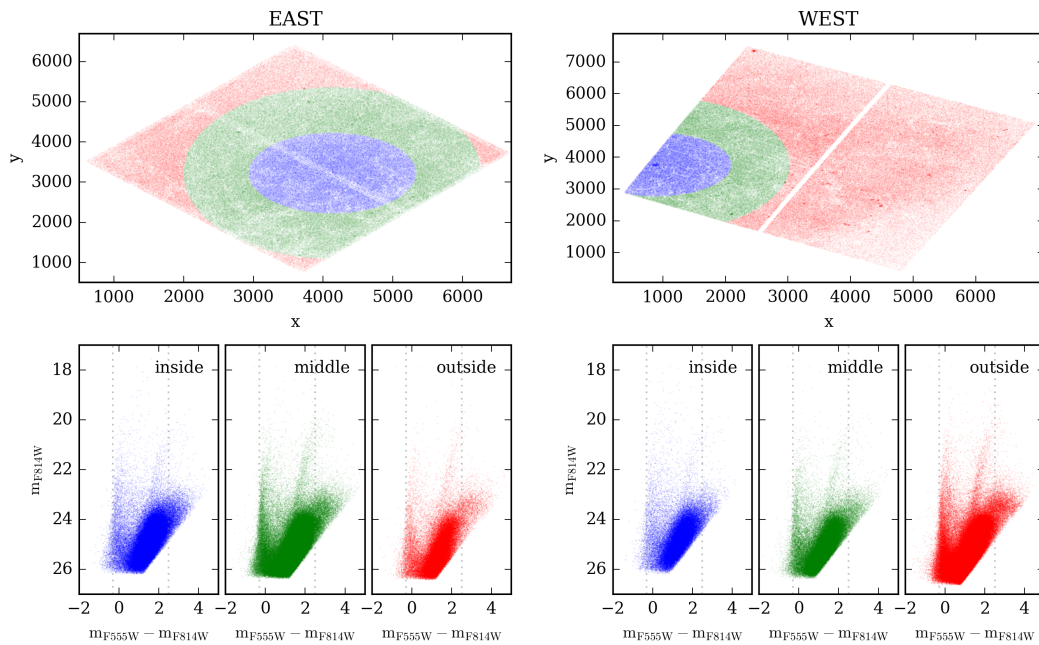


FIGURE 5.6: Maps and corresponding CMDs of the 3 regions we identified in the galaxy and used to recover the SFH; the dotted vertical lines are a rough reference of the blue edge of the MS ( $m_{F555W} - m_{F814W} = -0.3$ ) and the red edge of the RGB ( $m_{F555W} - m_{F814W} = 2.5$ ).

### 5.3 Distribution of dust

Using these same LEGUS data, Kahre et al. (in preparation) studied the dust distribution across the body of NGC 7793.

Dust has large and varied impacts on studies of star formation, chemical evolution, and galaxy evolution. The most obvious effect is the absorption and scattering of optical and UV light. Typically, up to 50% of the total stellar energy in a galaxy is attenuated by dust, hampering the interpretation of galaxy spectral energy distributions (SEDs) for their fundamental parameters, such as age, stellar population mix, star formation rates, and stellar initial mass functions (Calzetti, 2001). This, in turn, impacts our ability to obtain correct star formation histories and constrain theories of galaxy evolution and star formation.

Dust also plays a major role in star formation, both as a means of radiative feedback and as a catalyst for the formation of molecular hydrogen and other molecules (Mathis, 1990; Draine, 2003; Cazaux and Spaans, 2009; McKinnon, Torrey, and Vogelsberger, 2016). Finally, dust and the dust-to-gas ratio have effects on galaxy and chemical evolution models, since dust acts as a sink for many metals (McKinnon, Torrey, and Vogelsberger, 2016; Aoyama et al., 2017).

Extinction, as measured towards individual stars, includes effects of absorption and scattering. The ability to correct photometry for dust is vital for extragalactic studies of the interstellar medium (ISM) and stellar populations. Extinction maps are a useful tool for studying the differences between the diffuse ionized gas and H II regions, including extinction, ionization sources, and stellar populations. They can be further used to measure the dust content in a galaxy independent of the choice of the CO to H<sub>2</sub> conversion factor ( $X_{CO}$ ) and the dust-to-gas ratio, in order to place better constraints on these values. Finally, they can be used to correct optical, particularly H $\alpha$ , and UV fluxes for the effects of dust in order to better determine star formation rates and histories in nearby galaxies. This is particularly important for studies of the IMF and mass-to-light ratios, as classifying young massive stars often relies heavily on the UV, where extinction is severe.

Kahre et al. (in preparation) generated the extinction maps of NGC 7793 using the isochrone-matching method (Kim et al., 2012) on the individual stellar extinctions in all the 5 available bands.

Figure 5.7 shows their results. As expected, the peaks of the extinction are correlated with the location of the spiral arms and H $\alpha$  emission. Moreover, even though the maximum extinction is lower in the west field ( $E(V - I) = 0.75$ , while in the east field the maximum is  $E(V - I) = 0.80$ ) as we supposed from the analysis of the CMD, the right panels of Figure 5.7 reveal that high levels of extinction are more diffuse and irregular in the west field.

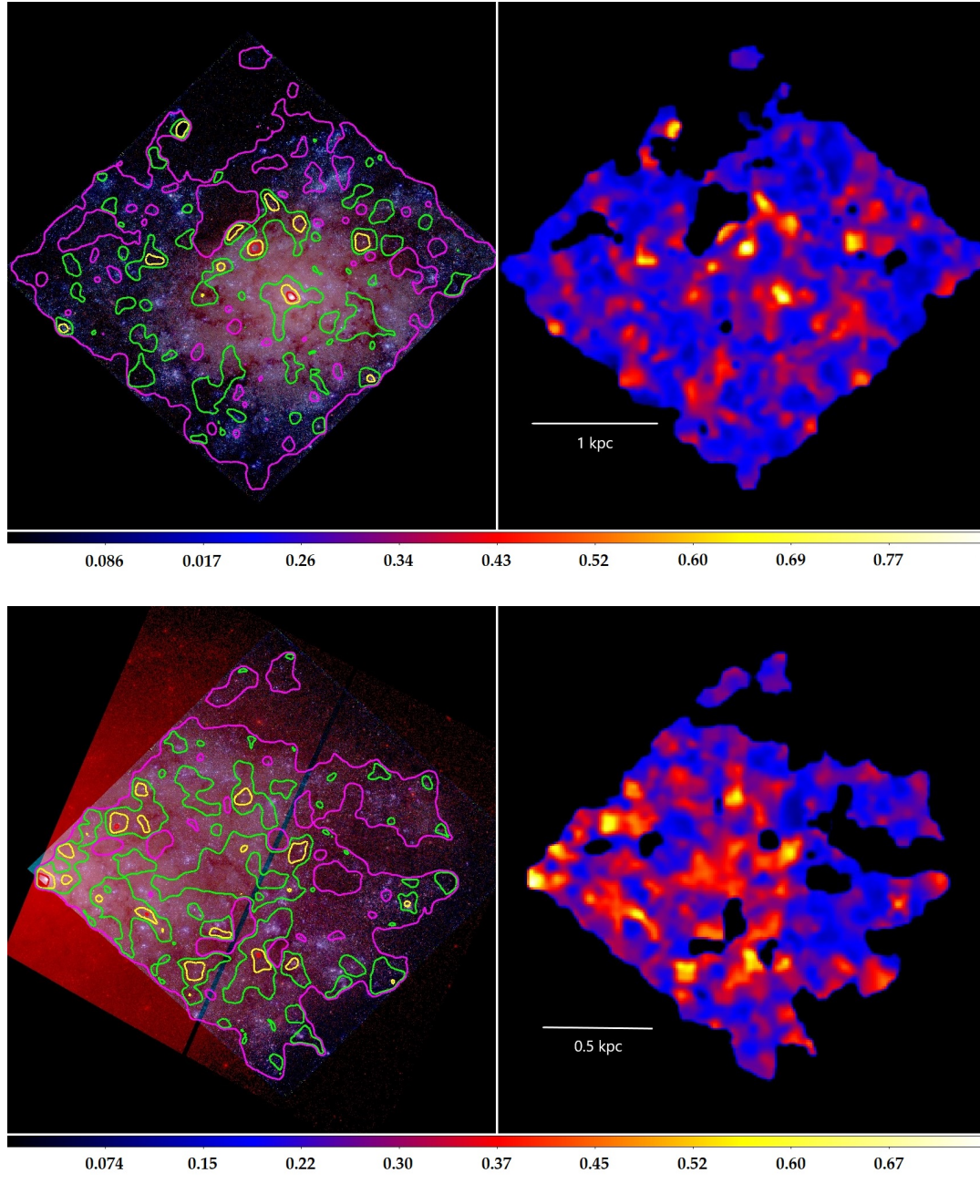


FIGURE 5.7: *Left panels.* 3-color *HST* image, using the filters F336W, F438W, and F814W. The scale for the extinction maps is shown below both images. Colored contours are at 20% (magenta), 40% (green), 60% (yellow), and 80% (red) of the maximum extinction ( $E(V - I) = 0.80$  for the eastern field and  $E(V - I) = 0.75$  for the western field). *Right panels.* Adaptive resolution weighted average extinction maps, smoothed with a  $3''$  Gaussian.  $E(V - I)$  increases going from blue to yellow/white. The top panels refer to the eastern field and the bottom panels to the western field of the galaxy.

## 5.4 Star Formation History

Since there are no steep density gradients in the spatial distribution of stars in NGC 7793, we adopted the conventional method for the artificial star tests, i.e. we used a uniform distribution of artificial stars which were put, one at a time, on the real images following the procedure described in Chapter 2. We thus estimated the completeness in each filter using the ratio between output and input stars as a function of magnitude, and used the  $m_{\text{output}} - m_{\text{input}}$  versus  $m_{\text{input}}$  distribution as an estimate of the photometric errors.

We used this information to build the basis functions for the synthetic CMDs, together with the galaxy's distance modulus, 27.87 (Radburn-Smith et al., 2011), which is allowed to vary from the chosen literature value, and metallicity,  $Z = 0.0015 - 0.0191$ , or  $[M/H]$  from  $-1.0$  to  $0.1$ , adopting the approximation  $[M/H] \simeq \log(Z/Z_{\odot})$ . In the most recent bins, the metallicity was allowed to vary in a small range around the value inferred from spectroscopy of the H II regions of the galaxy (Bibby and Crowther, 2010).

The models were created from the PARSEC-COLIBRI (Bressan et al., 2012; Marigo et al., 2017) and MIST (Choi et al., 2016) isochrones using a Kroupa (2001) IMF from  $0.1$  to  $300 M_{\odot}$  and 30% of binary stars.

In the western field, due to the much more asymmetrical shape of the spiral arms and dust distribution (see Section 5.3), the treatment of completeness and extinction requires a more specific analysis that will be performed by the LEGUS team in the near future. Thus, in what follows, we show only the results for the eastern field.

### 5.4.1 Inner region

Figure 5.8 shows the results obtained for the inner region of NGC 7793 with the two sets of stellar models. In the top panels we show the observed and recovered CMDs as Hess diagrams, together with the  $\sim 50\%$  completeness limit that we used as limiting magnitude to search for the best SFH. In the middle panels, the color functions in luminosity slices are shown. In the bottom panel, we show the star formation history and the evolution of the metallicity as a function of the age for both the COLIBRI and MIST isochrones, together with the SFH recovered using the F336W versus F336W–F555W CMD.

Both synthetic CMDs well reproduce the observational one, in particular the one based on the COLIBRI isochrones. The very red stars at  $22.5 < m_{F814W} < 23.5$ ,  $m_{F555W} - m_{F814W} \gtrsim 2.25$  are slightly underestimated, and the agreement worsens with the MIST-based CMD. This is the region of the TP-AGB stars, that are really hard to model, as mentioned in the previous Chapters. The MIST CMD also overestimates stars at  $m_{F814W} < 22.5$ ,  $m_{F555W} - m_{F814W} \sim 1.5$  and underestimates stars at  $23.5 < m_{F814W} < 24.5$ ,  $m_{F555W} - m_{F814W} \sim 1.75$ , which are instead well matched in the COLIBRI solution.

As expected, the star formation activity in this central region of the galaxy is prevalently old, but it continues until recent epochs, in agreement with the H $\alpha$  emission

that we see in Figure 5.4. The two solutions show similar trends, and also the optical and UV SFHs in the most recent  $\sim 150$  Myr reasonably agree, although the UV SFR is higher than the optical SFR (derived with the same stellar models) at the most recent epoch, as we already found for NGC 4449 (see Section 4.5.2). The metallicity trends show a different behavior between  $\sim 100$  and 400 Myr ago, again in the typical lifetime range of TP-AGB stars.

### 5.4.2 Middle region

Figure 5.9 shows the results of the SFH recovery process for the middle ring-shaped region of the galaxy. The observational CMD exhibits a much more populated MS with respect to that of the inner region, as expected from the presence of many star forming regions and  $H\alpha$  emission in the spiral arms. Indeed, the recent SFR is higher ( $\sim$  twice as much) than the one in Figure 5.8 (notice that the SFR scale is different), and the ratio between old and young SF is much lower. On average the SFH is almost constant, and there is a good agreement between the solutions from the two sets of models. Once again, the UV SFH agrees with the optical one, except for providing a higher SFR at the most recent epoch. The oldest UV SFH bin is very uncertain, due to the severe incompleteness in this age range in the UV CMD.

The CMDs and color functions show a very good match for the COLIBRI solution, with the only caveat that the model is broader than the data in the upper MS, at  $m_{F814W} < 23.5$ ,  $m_{F555W} - m_{F814W} \lesssim -0.25$ ; this is probably due to the higher reddening we find in this region of the galaxy, which introduces the difficulties already seen in the previous Chapter for NGC 4449. The solution also under predicts the number of TP-AGB stars, at  $22.5 < m_{F814W} < 23.5$ ,  $m_{F555W} - m_{F814W} \gtrsim 2.5$ . The MIST solution has the same issues, with the additional mismatches seen for the inner region in the bright red part of the CMD (stars at  $m_{F814W} < 22.5$ ,  $m_{F555W} - m_{F814W} \sim 1.5$  are overestimated), thus suggesting a systematic effect in the models.

### 5.4.3 Outer region

Figure 5.10 shows the CMDs, color functions, metallicity and SFH for both COLIBRI and MIST solutions. In both cases the observational CMD features are well reproduced by the synthetic ones, with the only relevant exception of the TP-AGB stars, as in the other regions. The SFR is generally lower here, with two higher episodes around 15 and 750 Myr ago. Given the paucity of massive stars, the UV SFH was not statistically relevant, so we do not include it in our analysis.

A summary of the SFRs and stellar masses formed in different epochs in the three different regions of the galaxy is given in Table 5.1.

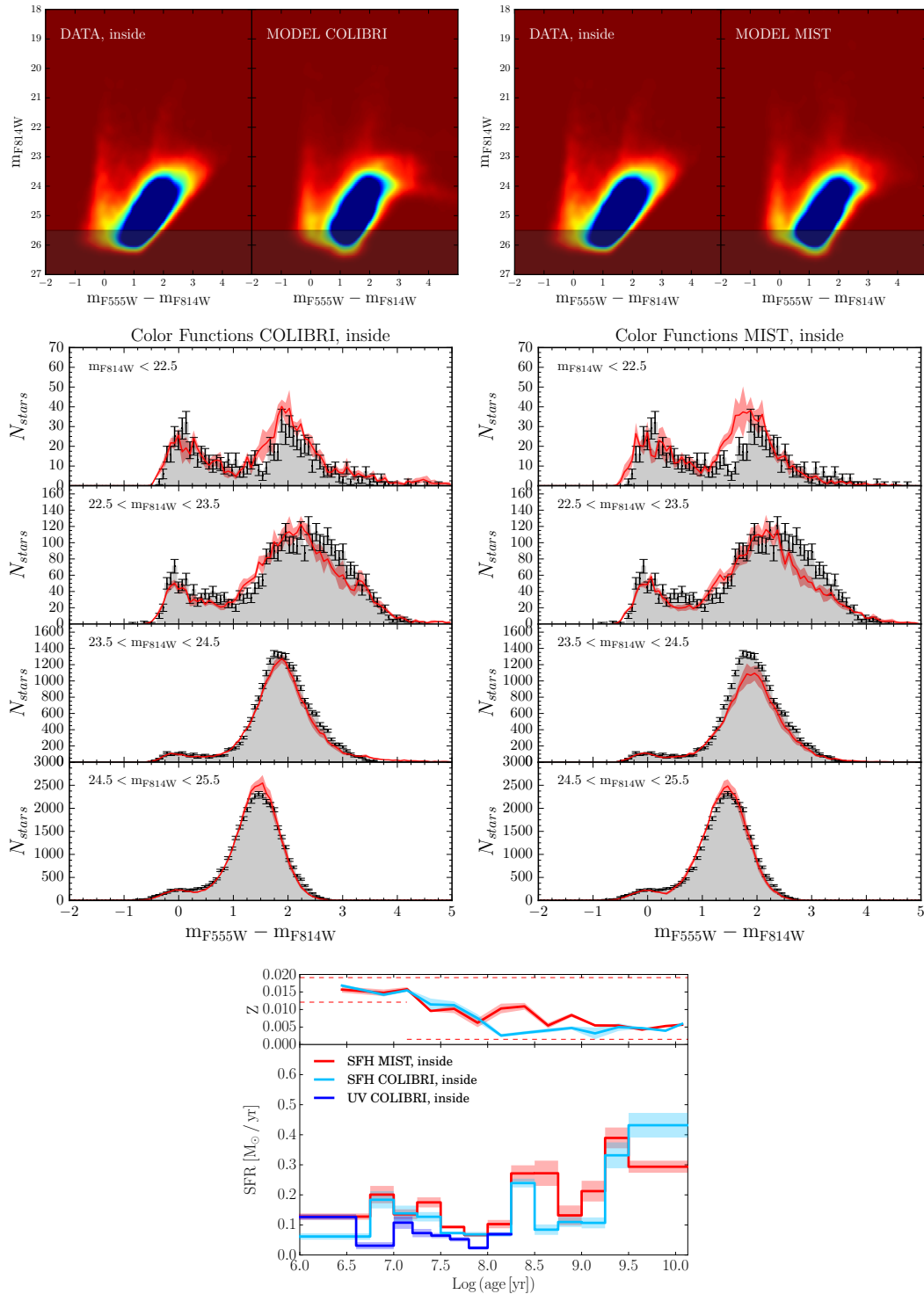


FIGURE 5.8: *Top panels.* Hess diagrams of the inner region of NGC 7793: the observational one is on the left and the one reconstructed on the basis of different sets of models on the right; the shaded part corresponds to the magnitude limit for the SFH recovery. *Middle panels.* Color functions of the CMDs in different luminosity bins; the data are the grey histograms with a Poissonian uncertainty, while the models are the red lines with the uncertainty from a bootstrap technique. *Bottom panel.* Recovered SFH and metallicity (the dashed lines show the allowed ranges); in blue, the UV SFH.

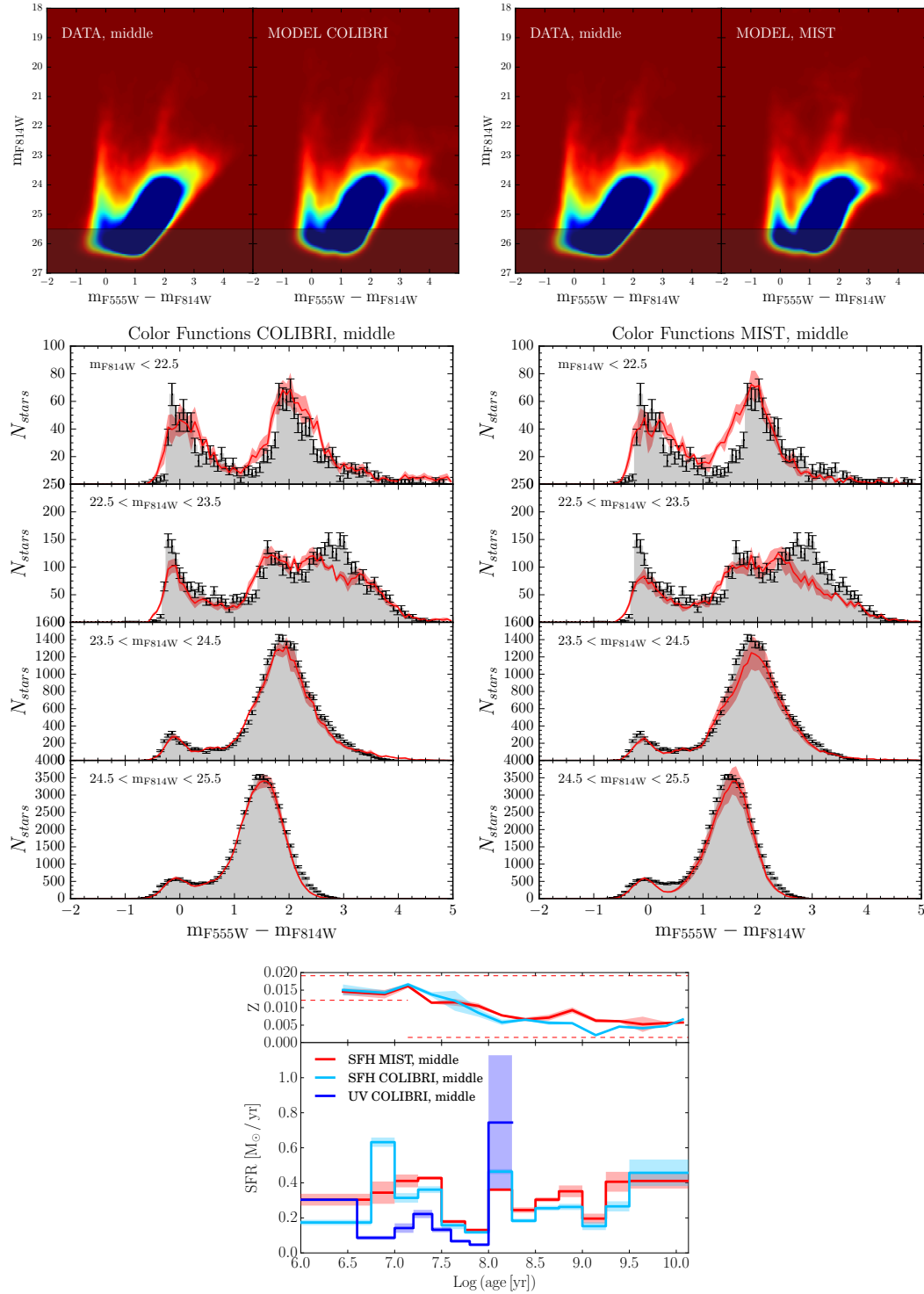


FIGURE 5.9: Same as Figure 5.8 but for the middle region of NGC 7793. Notice that the SFR scale is different from that in Figure 5.8.

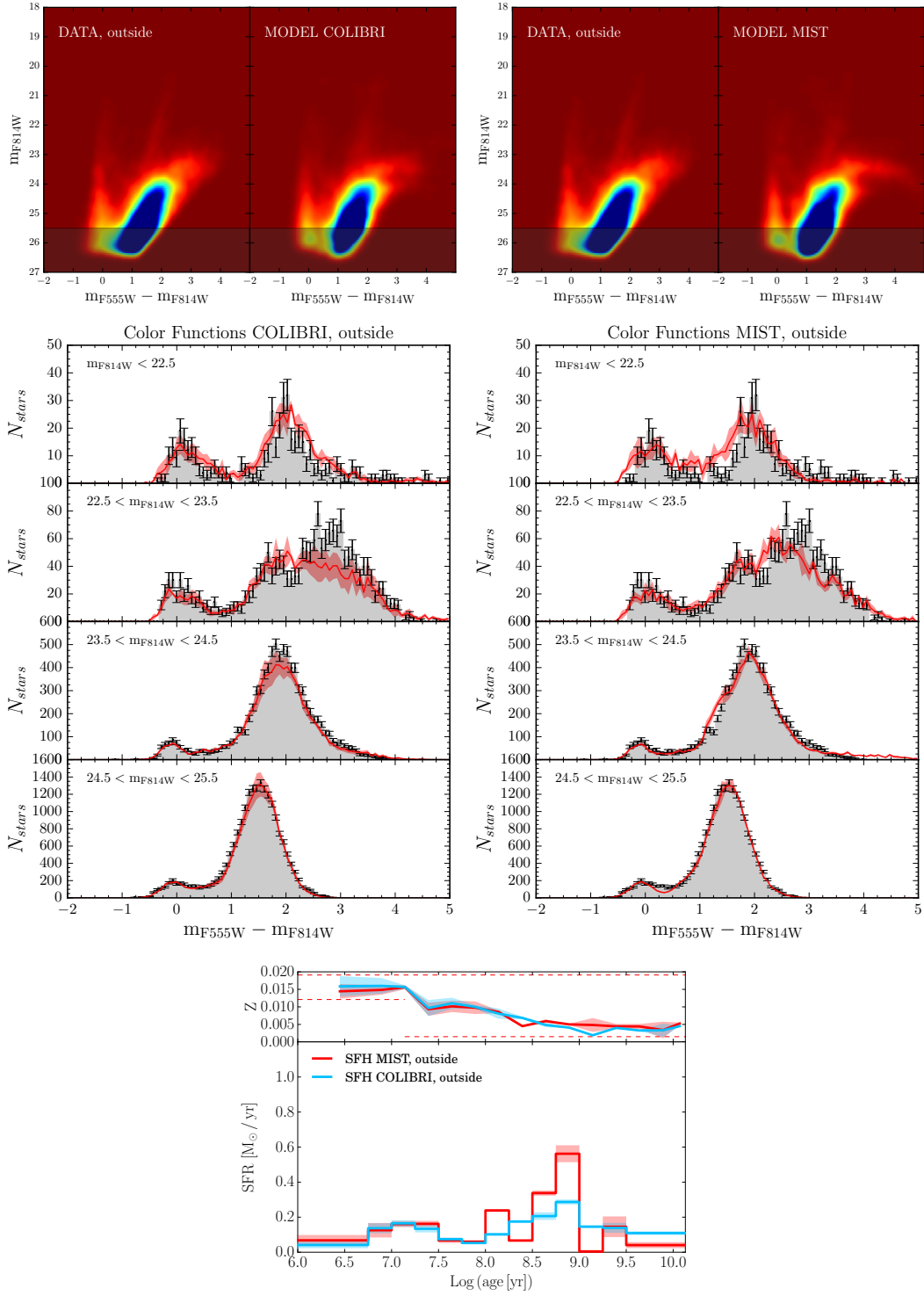


FIGURE 5.10: Same as Figures 5.8 and 5.9 but for the outer region of NGC 7793.

## 5.5 Discussion

Spiral galaxies have a major role in the universe today, with disk galaxies dominating star formation in the low-redshift universe (Brinchmann et al., 2004). Spiral galaxies have also been shown to operate at the peak baryon efficiency, more readily converting their gas into stars than galaxies at higher and lower masses (Guo et al., 2010). In addition, they provide an important laboratory for studying star formation due to the synchronization of star formation by density waves, which is essential to determine the timescales in the cloud formation – star formation – cloud disruption cycle. Understanding the processes that convert raw molecular material into stars and how star formation feeds back on galaxies and their environments in spiral galaxies is of great interest.

The spiral structure and strength of the density waves may affect molecular cloud properties in a variety of ways. For example, simulations find that the longest lived clouds tend to be the most massive and bound, with these clouds surviving into the inter-arm regions and containing relatively older massive clusters (Dobbs, Pringle, and Naylor, 2014). Clouds in the spiral arms, where they are likely more affected by feedback, tend to be destroyed (and have shorter lifetimes), or merge to form more massive clouds. If the galaxy is a grand design spiral, then the clouds may well show a sequence across the spiral arms, with clouds forming from  $H_2$ , then stars forming, then clusters. In flocculent galaxies, a more random distribution of clouds and evolution is expected (Dobbs and Pringle, 2010), but age spreads in simulations are found to be even shorter than grand design galaxies (Dobbs, Pringle, and Naylor, 2014).

In this Chapter, we presented the spatially resolved SFH of the central part of NGC 7793, a face-on flocculent spiral galaxy which we studied in the F336W, F555W and F814W filters thanks to new LEGUS data. The galaxy has also been re-observed with ALMA (Atacama Large Millimeter Array, PI: Kelsey Johnson) in order to study the impact of spiral structure and feedback from stellar populations on molecular clouds, and the spatial correlation between the star clusters and molecular gas. Figure 5.11 shows the UVIS  $V$ -band image of the two pointings of NGC 7793, overlaid with the giant molecular clouds (GMCs, blue ellipses), star clusters (SCs, circles, color-coded by age), and the outline of the ALMA coverage (gray box). We can see how younger star clusters are substantially closer to molecular clouds than older star clusters, and, as expected, preferentially located on the spiral arms.

TABLE 5.1: Summary of the star formation rates and stellar masses in the three different regions of the galaxy.

region	$\langle \text{SFR} \rangle$ [ $M_{\odot}/\text{yr}/\text{kpc}^2$ ]	$\text{SFR}_{\text{peak}}$ [ $M_{\odot}/\text{yr}/\text{kpc}^2$ ]	$\text{age}_{\text{peak}}$ [Gyr]	$M_*(\text{age} \leq 10 \text{ Myr})$ [ $10^6 M_{\odot}$ ]	$M_*(\text{age} > 1 \text{ Gyr})$ [ $10^9 M_{\odot}$ ]
Inner	$0.24 \pm 0.02$	$0.28 \pm 0.03$	6.5	$1.15 \pm 0.14$	$2.50 \pm 0.13$
Middle	$0.09 \pm 0.01$	$0.13 \pm 0.04$	6.5	$3.74 \pm 0.14$	$1.21 \pm 0.23$
Outer	$0.07 \pm 0.01$	$0.16 \pm 0.01$	0.8	$0.83 \pm 0.16$	$0.71 \pm 0.05$

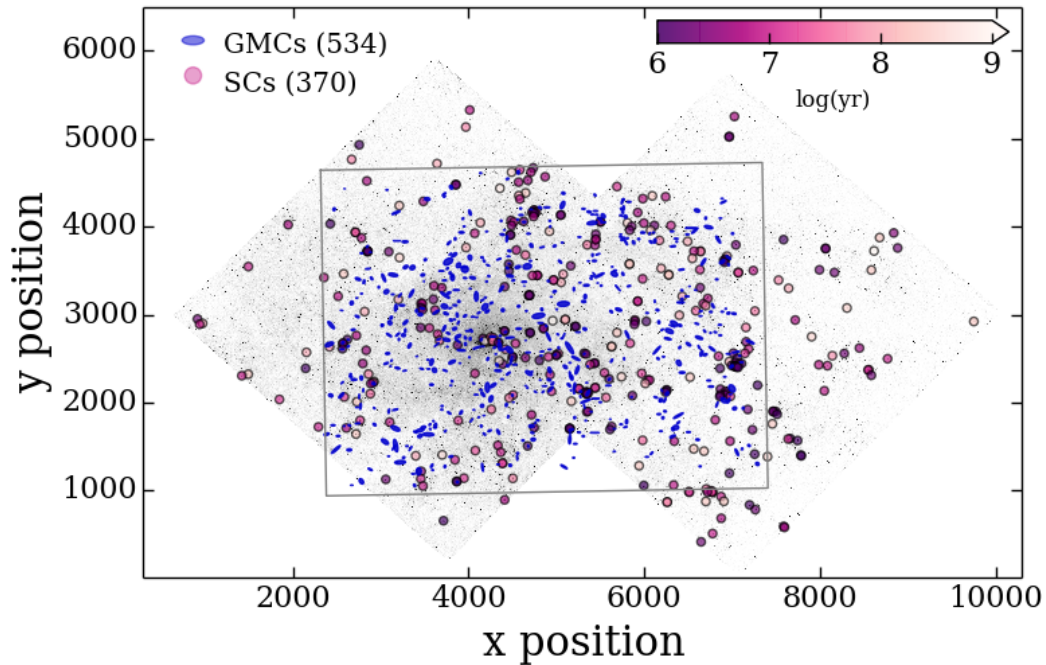


FIGURE 5.11: V-band image of the UVIS central/west pointings of NGC 7793, overlaid with the GMCs (blue ellipses), star clusters (circles, color-coded by age), and the outline of the ALMA coverage (gray box).

In order to ease the comparison among the different sub-regions of NGC 7793, Figure 5.12 and Table 5.1 show the SFHs of the three analyzed regions normalized to the corresponding area<sup>1</sup>. Even though we cover only the central part of the galaxy, there is a striking difference among the three SFHs: the ratio of present-to-past averaged star formation rate is much higher in the outermost sub-region, suggesting an “inside-out” growth scenario for the disk of NGC 7793, a mechanism originally introduced in the theory of galaxy evolution on the basis of chemical evolution arguments (see, e.g., Larson, 1976; Matteucci and Franco, 1989), and used as a basis for semi-analytic modeling of disk galaxies in the context of cold dark matter cosmologies (Kauffmann, 1996; van den Bosch, 1998). Under the assumption of detailed angular momentum conservation, the inside-out picture reflects the distribution of specific angular momentum of the protogalaxy: gas accreted at late times has a higher specific angular momentum and settles in the outer regions of the galaxies, therefore the outskirts of spiral galaxies are expected to form later. However, hydrodynamical simulations of the formation of disk galaxies indicate that angular momentum is not conserved and disks do not always form from the inside out (Sommer-Larsen, Götz, and Portinari, 2003).

<sup>1</sup>Chosen to include 90% of the stars.

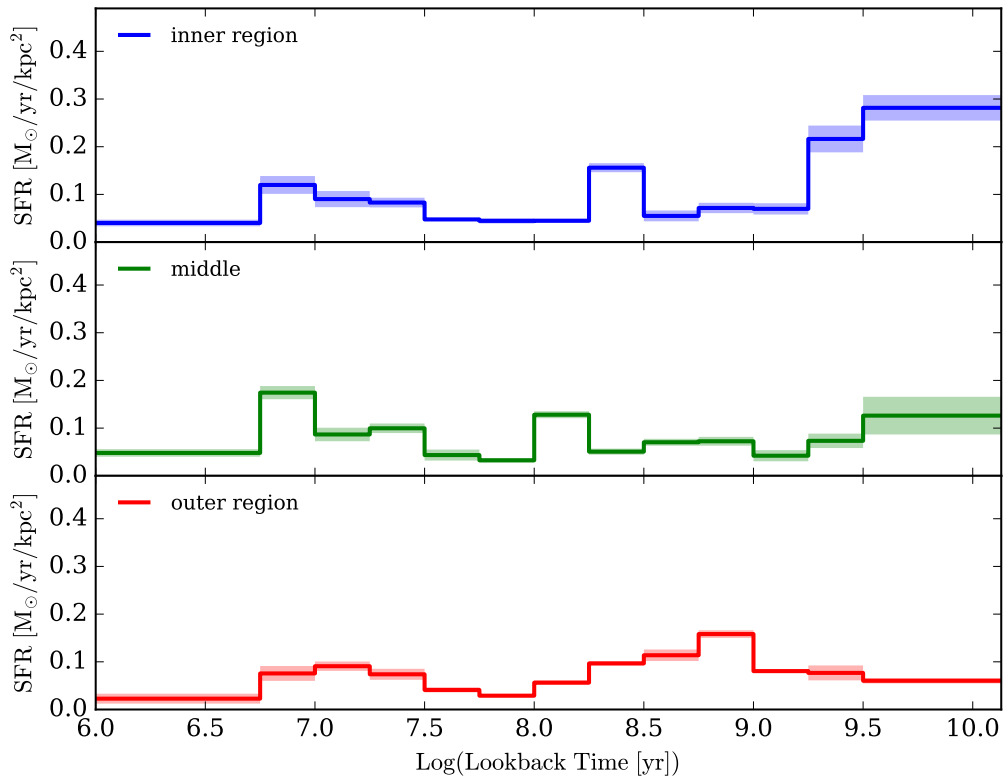


FIGURE 5.12: SFR surface densities (SFR/area) of the three regions we selected in NGC 7793.

From an observational point of view, there are several evidences of the inside-out mechanism. Pohlen and Trujillo (2006) studied a sample of 90 local disk galaxies using imaging data from the SDSS survey and found that 60% of them have inner exponential profiles followed by a steeper outer exponential profile, while 30% have a shallower (upward bending) outer profile. Azzollini, Trujillo, and Beckman (2008) found that for a given stellar mass, the radial position of this break has increased with cosmic time by a factor of  $1.3 \pm 0.1$  between  $z = 1$  and 0, suggesting a moderate inside-out growth of disk galaxies over the last  $\sim 8$  Gyr. Using the color profiles of 86 face-on spiral galaxies, de Jong (1996) found that the outer regions of disks are on average younger and have lower metallicity. Muñoz-Mateos et al. (2007) studied specific SFR (i.e. SFR per unit of galaxy stellar mass) profiles of a sample of 160 nearby spiral galaxies from the GALEX atlas of nearby galaxies (Gil de Paz et al., 2007) and found a large dispersion in the slope of the specific SFR profiles, with a slightly positive mean value, which they interpreted as implying moderate net inside-out disk formation. Moreover, studying the relationship between age, metallicity, and  $\alpha$ -enhancement of FGK stars in the disk of our Galaxy, Bergemann et al. (2014) found older, more  $\alpha$ -rich, and more metal-poor stars in the inner disk, hence supporting the inside-out mechanism. Finally, Pezzulli et al. (2015) measured the instantaneous mass and radial growth of the stellar disks of a sample of 35 nearby spiral galaxies that includes NGC 7793, finding clear signatures of its inside-out growth.

One interesting question is whether spiral arms trigger star formation, or whether they simply “rearrange” young stars, or molecular clouds in the galaxy. Roberts (1969) considered the response of gas to stellar spiral arms and showed that the gas experiences a strong shock. The sharp rise in density naturally means that the densities required to produce molecular gas, and gravitational collapse to form stars are reached, so the idea that spiral arms trigger star formation was proposed. However various observational results queried spiral arm triggering of star formation. Elmegreen and Elmegreen (1986) compared the star formation rates in flocculent and grand design galaxies, and found that there was little difference despite the different spiral arms. More recent observations still debate this: Eden et al. (2013) and Foyle et al. (2010) find little difference in the star formation efficiencies in spiral arms and inter-arm regions, while Seigar and James (2002) do find a dependence of star formation rate on the strength of spiral arms.

The comparison of our results for NGC 7793 with other analyses of different spiral galaxies will contribute to this debate, hopefully helping to understand the role and impact of spiral arms on the triggering and efficiency of star formation.

# 6. A PICTURE OF STAR FORMATION IN NEARBY GALAXIES

---

Over the past several years, it has become increasingly clear that the large-scale star formation is determined by a hierarchy of processes spanning a vast range of physical scales: the accretion of gas onto disks from satellite objects and the intergalactic medium (megaparsecs), the cooling of this gas to form a cool neutral phase (kiloparsecs), the formation of molecular clouds ( $\sim 10 - 100$  pc), the fragmentation and accretion of this molecular gas to form progressively denser structures such as clumps ( $\sim 1$  pc) and cores ( $\sim 0.1$  pc), and the subsequent contraction of the cores to form stars (solar radius) and planets (astronomical units). However, all these processes occur at the boundaries between different scales, and the coupling between them is not well understood yet.

Indeed, different physical processes may lead to star formation in different interstellar and galactic environments. An interesting strategy would be to find a unified approach to understand how star formation works, one that incorporates observational astrophysical constraints on star formation efficiencies, mass functions, gas accretion, from small-scale studies, along with a much deeper understanding of the processes that trigger and regulate the formation of star forming clouds on galactic scales, which, in turn, set the boundary conditions for star formation within clouds.

Observationally, we measure a very tight relation between the gas surface density  $\Sigma_{\text{gas}}$ <sup>1</sup> and the SFR surface density  $\Sigma_{\text{SFR}}$  of galaxies, known as the Schmidt-Kennicutt (SK) law (Schmidt, 1959; Schmidt, 1963; Kennicutt, 1998; Kennicutt and Evans, 2012), which is nicely described by a power-law of the form:

$$\Sigma_{\text{SFR}} \propto \Sigma_{\text{gas}}^N \tag{6.1}$$

where  $N \sim 1.4 - 1.5$ , even though the precise form of this relation depends on assumptions about how  $\Sigma_{\text{gas}}$  is derived from the observations.

The correlations between SFR and gas surface densities (and masses) are not the only scaling laws that are observed. Kennicutt (1998) pointed out that the SFR surface densities also correlate tightly with the ratio of the gas surface density to the local dynamical time, defined in that case to be the average orbit time. This prescription is especially useful for numerical simulations and semi-analytical models of galaxy evolution. Other SFR scaling laws can be understood as arising from an underlying

---

<sup>1</sup>The total gas density is assumed to be  $\Sigma_{\text{gas}} = 1.41 (\Sigma_{\text{H}_1} + \Sigma_{\text{H}_2})$  to take into account the fraction of helium that certainly accompanies hydrogen.

SK law. The best known of these is a strong correlation between characteristic dust attenuation in a star-forming galaxy and the SFR, with the consequence that galaxies with the highest absolute SFRs are nearly all dusty luminous and ultra-luminous infrared galaxies (e.g., Wang & Heckman 1996, Martin et al. 2005b, Bothwell et al. 2011). This opacity versus SFR relation is partly a manifestation of the SK law since the most intense star formation in galaxies takes place in regions with very high gas surface densities and, thus, also in regions with very high dust surface densities. The other factor underlying the SFR versus opacity correlation is the prevalence of highly concentrated circumnuclear star formation in the most intense starbursts observed in the present-day Universe; this may not necessarily be the case for starburst galaxies at early cosmic epochs (Kennicutt and Evans, 2012).

Although the general idea that gas is the input driver for star formation may seem obvious, there are still many questions that we need to answer to formulate a complete and consistent theory of star formation, such as understanding why the gas-SFR link we see at large scales is not easily recovered at small scales, what determines the H I–H<sub>2</sub>–dense gas–SFR transition fractions, what changes the efficiency of gas-to-star conversion and on what time scales, how feedback works and affects all these processes.

Trying to find such answers or at least connect some of these dots is indeed one of the main scientific goals of LEGUS, which takes advantage of the multi-wavelength, spatially resolved, and high temporal resolution approaches.

Here we summarize the main results discussed in the previous chapters in order to reach some conclusions on the star formation processes and to embed this work in a more general context on galactic formation and evolution.

## 6.1 Three different galaxies: a comparative study

In this thesis I showed the results obtained for three galaxies of different morphological type, stellar mass, metallicity and environment, i.e. DDO 68, NGC 4449, and NGC 7793. This study has been carried out in parallel using both LEGUS and archival optical observations, covering a timescale of several Gyr, and new UV LEGUS data, to improve the time resolution of the SFH in the last few hundreds Myr. In Table 6.1 there is a summary of the main properties of these three galaxies, both from the literature and from our results.

DDO 68 is a dwarf irregular galaxy, with an extremely low metallicity and in a very isolated location. Despite its isolation, we detected some faint stellar streams probably in interaction with the main body of the galaxy, and connected to the SF peak we find between  $\sim 30$  Myr and  $\sim 50$  Myr ago. Its SF regime is rather continuous, although with peaks and dips. It was definitely already active at the reached look-back time.

NGC 4449 is a Magellanic irregular galaxy with a very disturbed morphology, due to continuous interactions with neighboring galaxies. Its star formation is ongoing, with the major peak of activity around  $\sim 10$  Myr ago. Its SF regime is also rather continuous, although with significant peaks and dips, and its SFR is always higher than in DDO 68. Its SF activity was significant also at the earlier epochs.

NGC 7793 is a flocculent spiral galaxy member of the Sculptor group. Its SFH is typical of spiral galaxies, prevalently old but effective at all epochs. We find a radial SF trend which supports the inside-out formation scenario, with the inner parts of the galaxy being the oldest and more metal-rich ones.

TABLE 6.1: Fundamental properties of DDO 68, NGC 4449 and NGC 7793.

Galaxy	Type	$D$ [Mpc]	$r_{25}$ [kpc]	$12 + \log(O/H)$	$M_*$ [ $M_\odot$ ]	$M_{\text{HI}}$ [ $M_\odot$ ]	SFR <sub>UV</sub> [ $M_\odot/\text{yr}$ ]
DDO 68	Im	12.65	3.6	7.15	$1.3 \times 10^8$	$1.0 \times 10^9$	0.02
NGC 4449	IBm	3.82	2.8	8.37	$2.2 \times 10^9$	$3.0 \times 10^9$	0.94
NGC 7793	SA(s)d	3.7	6.0	8.61	$4.4 \times 10^9$	$7.8 \times 10^8$	0.52

In Figure 6.1 we show the comparison among the SFR densities of the three analyzed galaxies. The evolution is clearly different between the two irregulars, whose peak SFR is more recent than 50 Myr ago, and the spiral which had the bulk of its SF at much older epochs.

The quality of our *HST* data allowed us to perform a spatially resolved analysis of all the three galaxies. DDO 68 and NGC 4449 have the peak of recent activity in their central part, although young SF is present also in more external regions. In particular, DDO 68 is very active in what we called the Tail, an arc-shaped structure connected to the main body of the galaxy and likely originated from the merging of a smaller satellite. Analogously, NGC 4449 shows peaks of recent SF in many clumps, and even in this case the most probable interpretation is that they were triggered by an interaction, also suggested by the complex shape of its neutral gas.

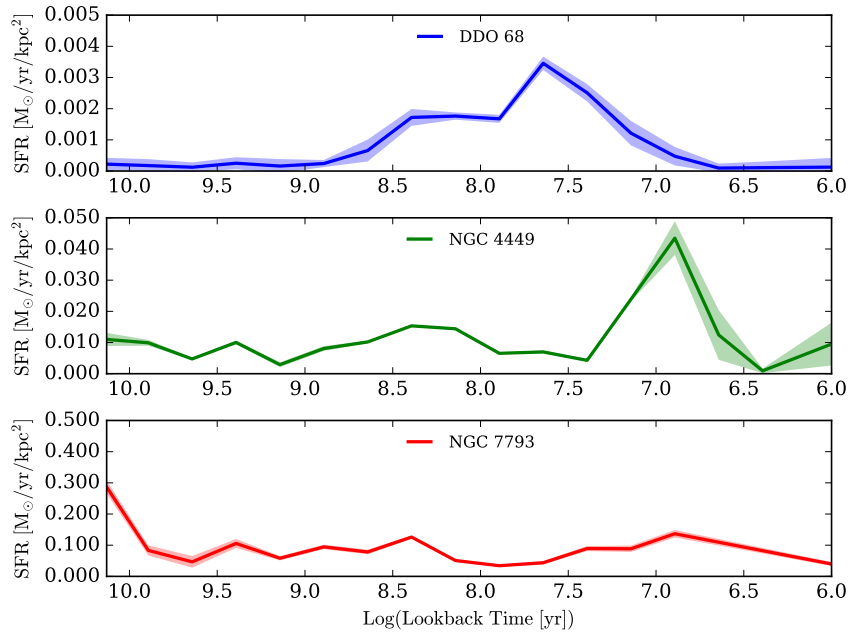


FIGURE 6.1: Comparison among the SFHs of the three analyzed galaxies (DDO 68 in blue, NGC 4449 in green, NGC 7793 in red) normalized over the area containing 90% of the stars in each galaxy.

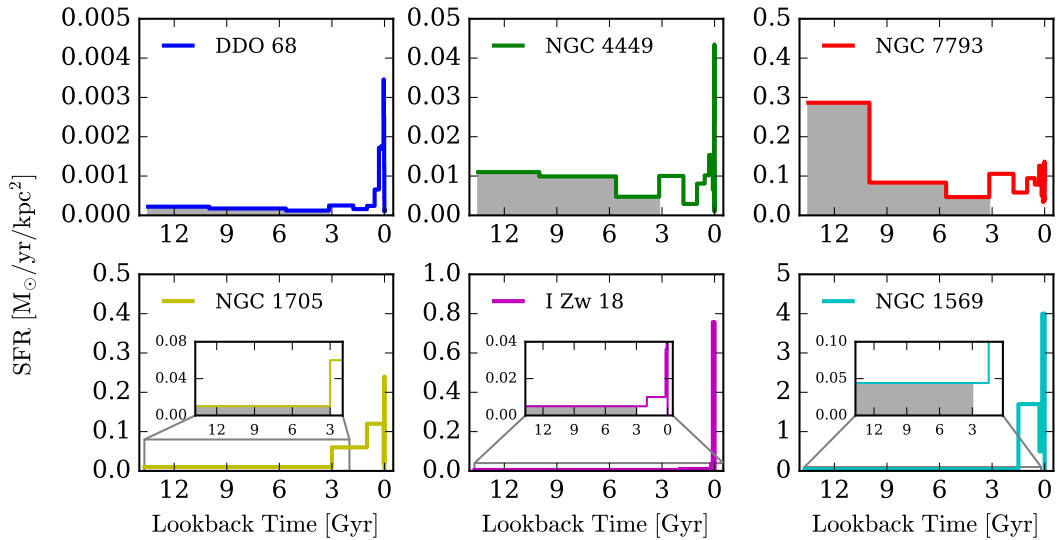


FIGURE 6.2: Comparison among the SFR densities of DDO 68, NGC 4449, NGC 7793, NGC 1705 (Annibali et al., 2003; Annibali et al., 2009), I Zw 18 (Annibali et al., 2013), and NGC 1569 (Greggio et al., 1998; Angeretti et al., 2005). In the bottom panels some blow-ups of the oldest time bins are present, to highlight SFRs barely visible in the main graphs. The gray areas indicate a less robust SFH given that the oldest stars reached by the photometry are in the RGB phase. Notice the very different scales but very similar morphologies (except for NGC 7793, which is a spiral galaxy).

NGC 7793 instead exhibits the typical features of the majority of spiral galaxies, with the ratio of recent over past star formation rates much higher in the outer region, in agreement with an inside-out growth of its disk.

Figure 6.2 shows the global SFR density of DDO 68, NGC 4449, and NGC 7793 together with those of 3 other starburst dwarfs for which *HST* allowed to derive the SFH within the look-back time given by the resolved RGB stars (formally  $> 1$  Gyr, but in all cases taken as  $\sim 3$  Gyr, thanks to the low metallicity of these galaxies). It is important to notice that at distances larger than a couple of Mpc neither the old MSTO nor the HB are measurable, and the SFH older than 1 Gyr necessarily relies only on RGB stars, therefore the corresponding uncertainties are huge (see Appendix B of Weisz et al. 2011). We include in this comparison NGC 1705 (Annibali et al., 2003; Annibali et al., 2009), I Zw 18 (Annibali et al., 2013), and NGC 1569 (Greggio et al., 1998; Angeretti et al., 2005). The shown galaxies are too far away even to detect the He-burning phase of stars with ages between 0.5 and 1 Gyr, hence the resulting SFHs are rather uncertain also in that age range. However, within the uncertainties, the resulting scenario is correct. Apart from the spiral, all these galaxies show a well defined very recent burst and moderate ancient SFRs, as old as the look-back time reached by the photometry, with no evidence for interruptions in the SF. Similar results are also found in other studies of dIrr galaxies (McQuinn et al., 2010; Weisz et al., 2011) which typically show a significant SF at old epochs plus, in the case of starburst galaxies, elevated levels of recent SF. The details of the SFHs, however, can considerably vary from galaxy to galaxy, and even though the SFH morphologies are remarkably similar, the SFR scale is very different from one galaxy to another, spanning  $\sim 3$  orders of magnitude.

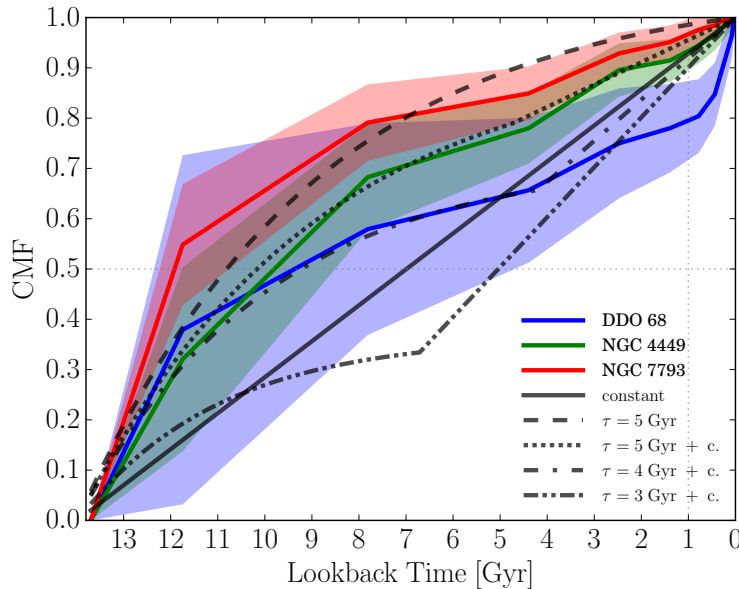


FIGURE 6.3: Cumulative stellar mass fractions of the galaxies (with  $3\sigma$  errors) compared with some simple SFH models (constant SFR, exponentially declining  $\tau$ -model, and a combination of the two); the dotted vertical line indicates an age of 1 Gyr whilst the dotted horizontal line shows 50% of the total mass.

Following Weisz et al. (2014), in Figure 6.3 we compare the cumulative stellar mass fractions of the galaxies with some simple SFH models, i.e. a constant SFH, an exponentially declining  $\tau$ -model, and a combination of the two. We can clearly see that all the three galaxies formed 50% of their mass well before the predictions of a constant SFH, between  $\sim 9$  and 12 Gyr ago. The CMF of NGC 4449 is well represented by an exponentially declining SFH with  $\tau = 5$  Gyr followed by a constant SFH, in quite good agreement with the findings of Weisz et al. (2014) for irregulars, even though from the SFH in Figure 6.1 we see the very recent peak which is averaged out in the cumulative distribution and obviously cannot be produced either with an exponentially decreasing or with a constant law of SF. For the other two galaxies there is no combination of these two models able to reproduce the full mass assembly history; until  $\sim 4$  Gyr ago the mass function of DDO 68 follows the profile with  $\tau = 4$  Gyr, but from then on the evolution is much more complicated.

The lack of information coming from the oldest MSTO and the age-metallicity degeneracy affecting the RGB phase, strongly hamper the possibility of constraining the chemical evolution of our targets. Indeed, in our procedure we impose that metallicity grows with time and matches the spectroscopic value in the most recent time bins. On this side, a promising route could be the synergy of our method for the SFH recovery with chemical evolution models as already done for closer galaxies, as the dwarf spheroidal Sculptor (see, e.g., Vincenzo et al., 2016).

## 6.2 The Schmidt-Kennicutt law

Using our results on the SFH, and with literature values for the gas component, we estimated the  $\Sigma_{\text{SFR}}$  versus  $\Sigma_{\text{gas}}$  for the three galaxies, as shown in Figure 6.4 (yellow stars). We adopted the conversion  $\Sigma_{\text{gas}} = 1.41 (\Sigma_{\text{H I}} + \Sigma_{\text{H}_2})$  to take into account the presence of helium. The original Figure is from Kennicutt and Evans (2012), and represents an updated version of the global Schmidt law in galaxies. Each point is an individual galaxy with the surface density defined as the total gas mass (molecular plus atomic) or SFR normalized to the radius of the main star-forming disk. For simplicity, a constant  $X_{\text{CO}}$  factor  $2.3 \times 10^{20} (\text{K km s}^{-1})^{-1}$  was applied to all the galaxies. This sample of galaxies was enlarged from that studied by Kennicutt (1998), and all the H $\alpha$ -based SFR measurements were improved by incorporating individual (IR-based) corrections for dust attenuation and [N II] contamination. Most of the galaxies form a tight relation; the dispersion of the normal galaxies (purple points) from the average relation ( $\pm 0.30$  dex rms) is considerably higher than what can be attributed to observational uncertainties, which suggests that much of the dispersion is physical. Above  $\Sigma_{\text{gas}} \sim 10 M_{\odot} \text{ pc}^{-2}$ , the form of this integrated Schmidt law appears to be surprisingly insensitive to the SFR environment and parameters such as the atomic versus molecular fraction, but some metal-poor galaxies (defined as  $Z < 0.3 Z_{\odot}$ , which includes DDO 68) deviate systematically from the main relation (blue open circles). These deviations could arise from a physical change in the star-formation law but more likely reflect a breakdown in the application of a constant  $X_{\text{CO}}$  factor (Leroy et al., 2011). Adopting higher values of  $X_{\text{CO}}$  for metal-poor galaxies would be more physically meaningful (since there is no reason why H $_2$  should scale with the metallicity) and would bring them much more into agreement with the main relation. Observations of low-surface-brightness spiral galaxies (magenta crosses) by Wyder et al. (2009) extended the measurements of the integrated star-formation law to even lower mean surface densities. A clear turnover is present, which is consistent with breaks seen in spatially resolved observations of the star-formation law (Kennicutt and Evans, 2012).

These observations, in particular, seem to suggest that the turnover at gas densities of about  $10 M_{\odot} \text{ pc}^{-2}$  reflects a transition from H I dominated to H $_2$  dominated regime: above the transition density, the ISM is mostly H $_2$  and the SFR strongly correlates with the H $_2$  density (see Leroy et al., 2013); below the transition density, the ISM is mostly H I and the SFR drops precipitously. In order to explain this point we need to introduce the concept of star formation efficiency (SFE).

So far, we referred to the quantitative relationship between neutral gas and the SFR as the *star formation law*. However, to predict the SFR over an entire galactic disk, it is also necessary to know which gas actively forms stars. This topic is often phrased as the *star formation threshold*, but may be more generally thought of as the problem of where a cold phase ( $n \sim 4 - 80 \text{ cm}^{-3}$ ,  $T \sim 50 - 200 \text{ K}$ ) or gravitationally bound clouds can form; both are thought to be prerequisites to star formation.

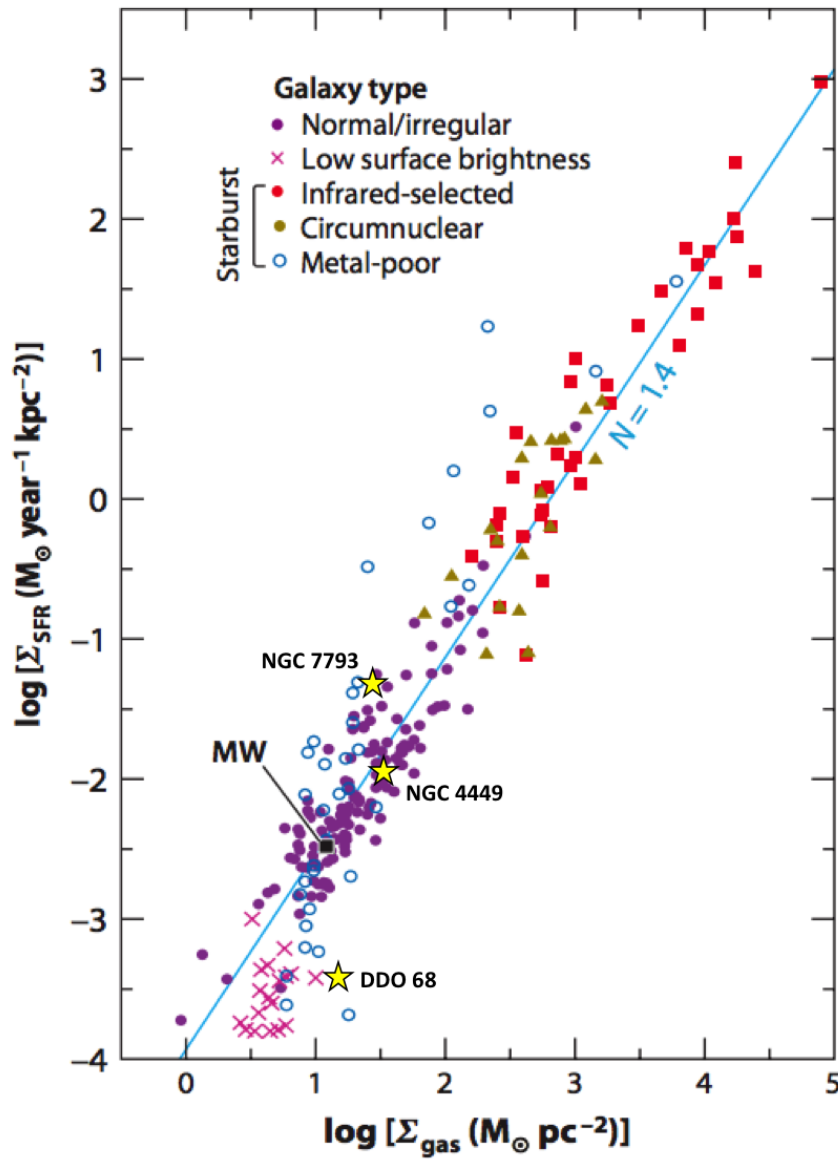


FIGURE 6.4: Relationship between the disk-averaged surface densities of star formation and gas (atomic and molecular) for different classes of star-forming galaxies. Each point represents an individual galaxy, with the SFRs and gas masses normalized to the radius of the main star-forming disk. Purple points represent normal spiral and irregular galaxies, red points infrared-selected starburst galaxies (mostly luminous and ultra-luminous infrared galaxies), and dark yellow points denote circumnuclear starbursts. The Milky Way (black square) fits well on the main trend seen for other nearby normal galaxies. Magenta crosses represent nearby low-surface brightness galaxies. Open blue circles denote low-mass irregular and starburst galaxies with estimated metal (oxygen) abundances less than  $0.3 Z_{\odot}$ , indicating a systematic deviation from the main relation. The light blue line shows a fiducial relation with slope  $N = 1.4$  (not intended as a fit to the data). The three yellow stars are DDO 68, NGC 4449 and NGC 7793, as labeled. Original figure from Kennicutt and Evans (2012).

There are many definitions for the SFE, but here we refer to it as the SFR surface density per unit neutral gas surface density along a line of sight, that is:

$$\text{SFE} = \frac{\Sigma_{\text{SFR}}}{\Sigma_{\text{gas}}} \quad [\text{yr}^{-1}] \quad . \quad (6.2)$$

The SFE is the inverse of the gas depletion time, the timescale required for present-day star formation to consume the gas reservoir. It results from the combination of the real timescale for neutral gas to form stars and the fraction of gas that ends up in stars. Because it is normalized by  $\Sigma_{\text{gas}}$ , the SFE is more useful than  $\Sigma_{\text{SFR}}$  alone to identify where conditions are conducive to star formation i.e., where gas is “good at forming stars”.

In terms of depletion time and SFE, the turnover below  $10 M_{\odot} \text{pc}^{-2}$  seems to reflect the transition between the extremely long depletion time of the H I dominated phase, typically about 100 Gyr (low SFE), and the depletion time of the H<sub>2</sub> dominated phase, about 2 Gyr (high SFE). In this context, the position of DDO 68 below the SK law could indicate that this system has not yet reached any sort of equilibrium between cosmological infall of gas and star formation. Instead, its time-averaged accretion rate from the intergalactic medium up to this point in cosmic time may have exceeded the rate at which the galaxy is capable of processing that gas into stars.

To explore the correlation of the SFE with different galactic properties, Leroy et al. (2008) analyzed the optical disks of 23 nearby spiral and irregular galaxies using very high quality H I, far ultraviolet, infrared, and CO data. Their analysis includes also NGC 4449 and NGC 7793 (see Figures 6.5 and 6.6).

As a general result, they do not find huge differences between the SFE of spiral and dwarf galaxies, and typically in the outer parts of spirals and throughout dwarf galaxies the SFE declines steadily with increasing radius, with an exponential scale length of  $\sim 0.2 - 0.25 r_{25}$ . However, the situation is very different from one galaxy to another, and these data do not identify a unique driver for the SFE, but suggest that the ISM physics below the available resolution - balance between warm and cold H I phases, H<sub>2</sub> formation, and perhaps shocks and turbulent fluctuations driven by stellar feedback - governs the ability of the ISM to effectively form stars.

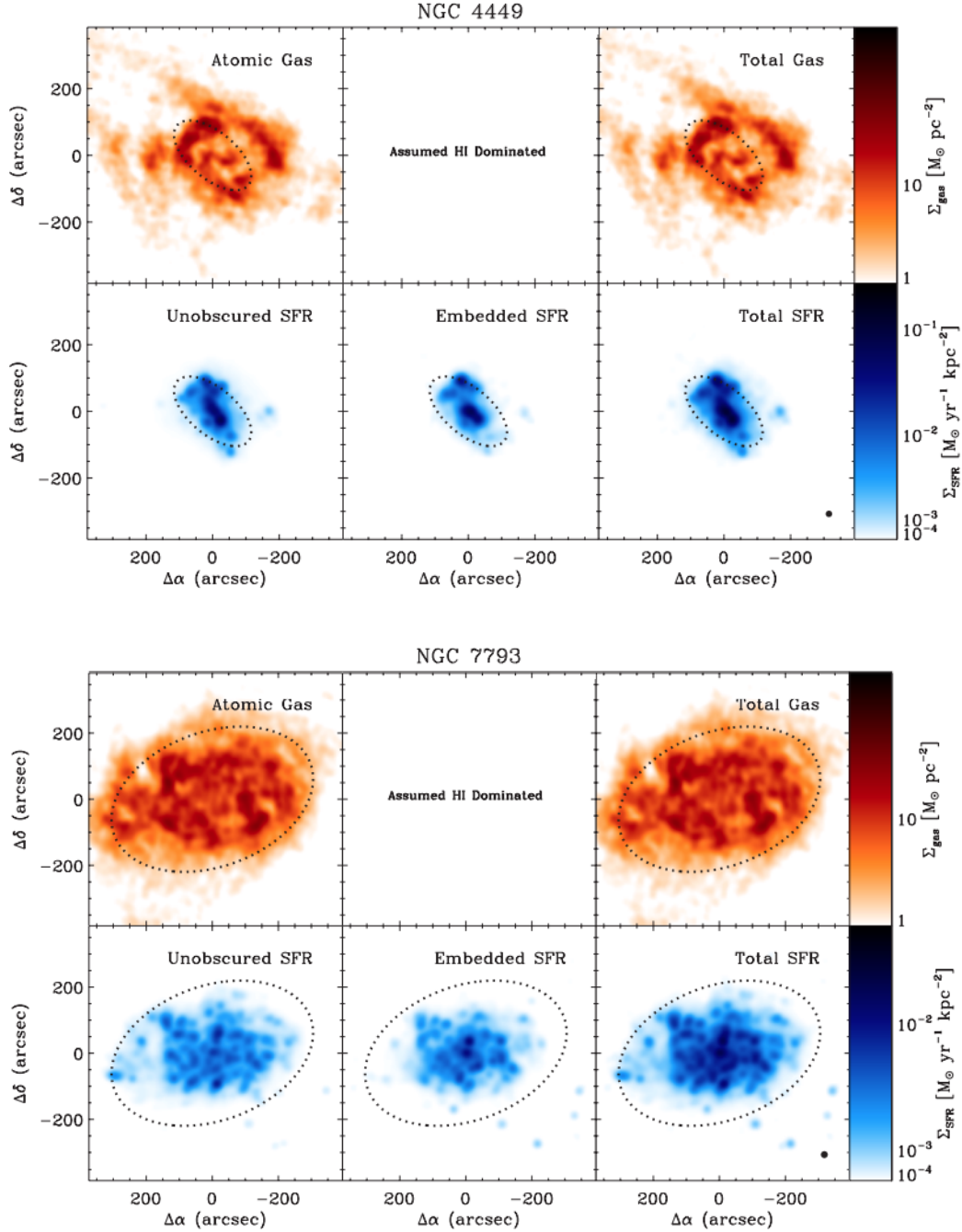


FIGURE 6.5: *Top panels.* Maps of atomic gas  $\Sigma_{\text{H I}}$ , molecular gas  $\Sigma_{\text{H}_2}$ , and total gas  $\Sigma_{\text{gas}} = 1.36 (\Sigma_{\text{H I}} + \Sigma_{\text{H}_2})$  for each galaxy. *Bottom panels.* Unobscured (FUV), dust-embedded ( $24 \mu\text{m}$ ), and total star formation surface density  $\Sigma_{\text{SFR}}$ . The color scheme is indicated on the right of each row. The dotted circle indicates the optical radius,  $r_{25}$ , in the plane of the galaxy. The small black circle in the bottom right panel shows the angular resolution. Original figure from Leroy et al. (2008).

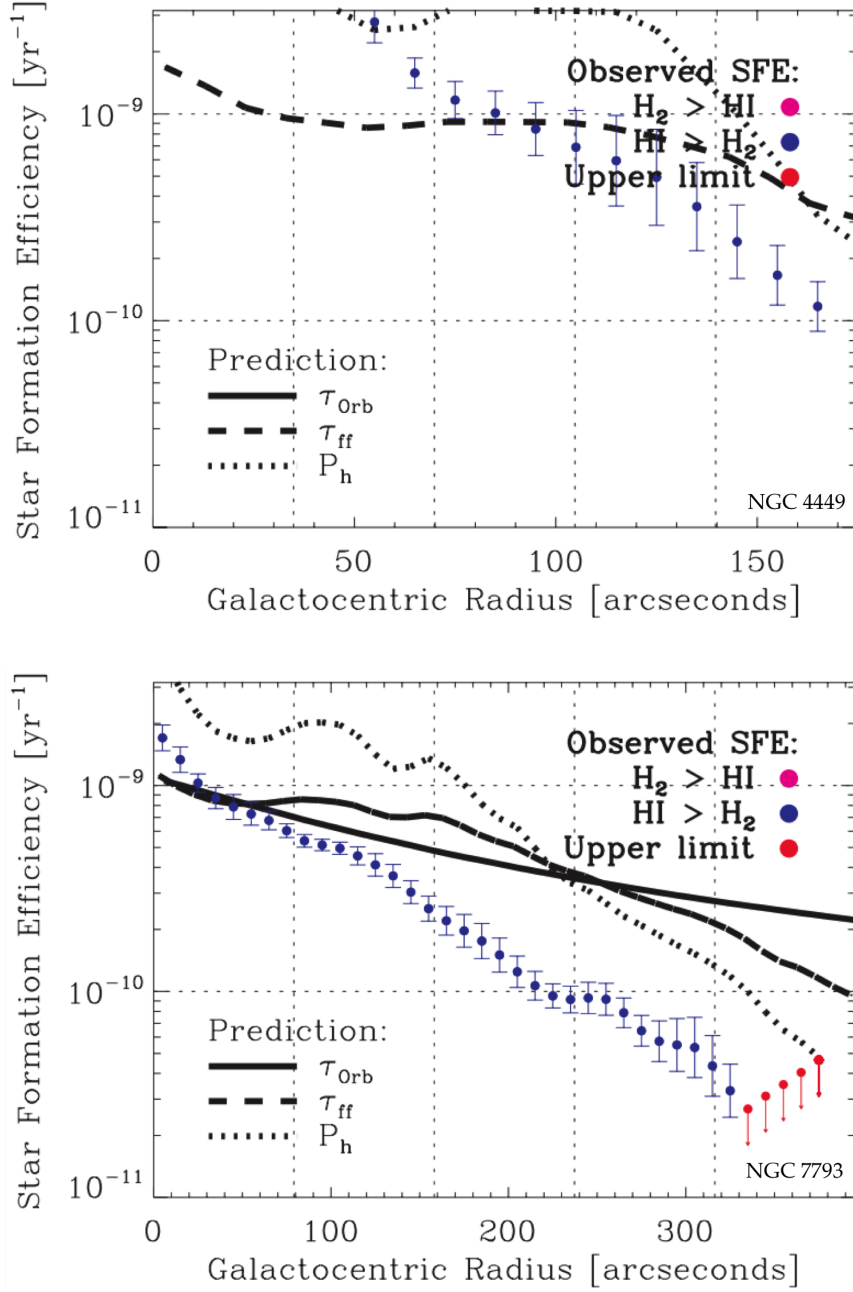


FIGURE 6.6: Observed SFE for NGC 4449 (top) and NGC 7793 (bottom). Magenta points indicate rings where  $\Sigma_{\text{H}_2} > \Sigma_{\text{HI}}$ , blue points show rings where  $\Sigma_{\text{H}_2} < \Sigma_{\text{HI}}$ , and red arrows indicate upper limits. Solid, dashed, and dotted lines show the SFE predicted following different methods described in Leroy et al. (2008). Vertical dotted lines indicate 0.25, 0.5, 0.75, and 1.0 times  $r_{25}$ . Horizontal dotted lines show fixed SFE. Original figure from Leroy et al. (2008).

### 6.3 The Role of Interaction

Another important aspect that can strongly influence star formation is galaxy interaction. Mergers between massive galaxies provide an important mode of galaxy evolution that can drive morphological changes from gas-rich disk galaxies to red, quiescent systems, while triggering starbursts and quasar activity (e.g. Toomre and Toomre, 1972; Sanders et al., 1988). At low redshift, massive galaxy interactions and mergers are observed to produce diluted metals, enhanced star formation, bluer colors, and higher active galactic nucleus fractions relative to their isolated counterparts (e.g., Armus, Heckman, and Miley, 1987; Sanders et al., 1988; Woods et al., 2010; Ellison et al., 2011; Ellison et al., 2013; Patton et al., 2011; Patton et al., 2013; Rich et al., 2012; Scudder et al., 2012). These observed effects are consistent with numerical simulations of merging galaxies, which predict that close pericentric passages between massive galaxies can trigger gas inflows, starbursts, and the activation of central supermassive black holes (e.g., Toomre and Toomre, 1972; Hernquist, 1989; Barnes and Hernquist, 1991; Mihos and Hernquist, 1994; Mihos and Hernquist, 1996; Torrey et al., 2012).

These effects are particularly interesting in low-mass galaxies, which differ from their more massive counterparts, as their dark matter to baryonic matter ratio tends to be larger, they are much fainter ( $10 - 10^5$  times fainter than MW-type galaxies) and they are less efficient at forming stars from their large gas reservoirs (Blanton et al., 2001; Robertson and Kravtsov, 2008). It is therefore unclear whether the same processes observed in massive galaxies scale down to the dwarf regime. Since dwarf galaxies dominate the galaxy population of the Universe at all times, the interactions and mergers between them occur more frequently in a given volume than for massive galaxies (Fakhouri, Ma, and Boylan-Kolchin, 2010; Deason, Wetzel, and Garrison-Kimmel, 2014) and they play a crucial role in the hierarchical build up of dark matter and stellar halos.

Dwarf groups have been recently observed by Stierwalt et al. (2017) using the panchromatic Tiny Titans survey (Stierwalt et al., 2015), a systematic study of SF in interacting dwarf galaxies. According to this study, the interaction between dwarfs could be quantitatively different as compared to their more massive counterparts. In fact, both paired dwarfs and paired massive galaxies show enhanced SF out to separations of  $\sim 100$  kpc (Patton et al., 2013; Stierwalt et al., 2015), but the effect in dwarfs is stronger by a factor of 1.3 and involves a larger fraction of the virial radius. Dwarfs are therefore more globally affected by small companions.

A large fraction of interacting dwarfs are starbursting, too. If one defines starbursts those regions with global  $H\alpha$  equivalent width  $> 100 \text{ \AA}$ , Stierwalt et al. (2017) found that starbursts occur in 20% of the isolated galaxy pairs, compared to only 6% of the matched isolated single dwarfs, suggesting that dwarf-dwarf interactions play a key role in triggering starbursts in dwarfs. Interestingly, the final coalescence stage of the dwarf-dwarf merger is not required to produce starbursts, but rather they are triggered at earlier stages of the interaction. Finally, collisions between dwarfs and satellites predominantly star-free, or even dark, could explain the strong bursts of SF that in some dwarfs occur without apparent cause (Starkeburg, Helmi, and Sales, 2016).

Many other studies have investigated possible mechanisms leading to the formation of a starburst, such as tidal interactions, mergers, or gas accretion (Lelli, Verheijen, and Fraternali, 2014b), highlighting the close link between environment, gas distribution and star formation. On the other hand, simulations show that stellar feedback (gas out/in-flows) also play an important role in determining the stellar kinematics and radial gradients in low-mass ( $M_* \sim 10^{7-9.6} M_\odot$ ) galaxies (El-Badry et al., 2016).

We find clear correlations of SF enhancement with merging and interactions in the two dwarf galaxies we studied. In DDO 68, we see a peak in the star formation activity between  $\sim 30$  Myr and  $\sim 50$  Myr even at very large galactocentric distances, suggesting an event which triggered the SF; we indeed find evidence of stellar streams which are merging with the main body of the galaxy, that could also explain the arc-shaped morphology of the outer part of the galaxy (see Chapter 3). Analogously, the SFH of NGC 4449 shows a peak in the last  $\sim 10$  Myr, likely triggered by a cold flow accretion or a merger event, as supported by the large distortions observed in its H I gas map (see Chapter 4).



# 7. CONCLUDING REMARKS

---

This thesis described the analysis of the resolved stellar populations of three star-forming galaxies in the local Universe.

In Chapter 1, starting from a general overview of the properties of nearby galaxies, I described the past surveys that performed this kind of studies, and finally LEGUS, the new survey on which this work is based, and whose aim is to provide a homogeneous imaging data set in five bands (from the near ultraviolet to the near infrared) of a sample of 50 local (closer than 12 Mpc) star-forming galaxies, in a range of different galactic properties.

In Chapter 2 I revised the main aspects of stellar evolution theory, relevant for the interpretation of the color-magnitude diagram in terms of SFH. SFERA, the new code I used, was then extensively described, together with the practical steps needed for this analysis, and the main strengths and uncertainties related to this method.

Chapters 3, 4 and 5 contain the detailed description and results for the three galaxies I studied, DDO 68, NGC 4449, and NGC 7793. The most relevant conclusions we can draw are here summarized.

- For all the three galaxies, we obtained consistent results adopting the PARSEC-COLIBRI and MIST stellar evolutionary models. However, there are stellar evolution phases that are still not reliably modeled, and need to be treated very carefully (e.g. the TP-AGB phase). This new study also revealed that when high levels of reddening and differential reddening are present, the smooth transition observed between MS and post-MS stars is difficult to reproduce, probably due to a poor modeling of both the reddening distribution and the length of the loops during the He-burning phase in the adopted isochrones.
- The UV SFHs are in good agreement with the optical ones and provide a much better time resolution in the last  $\sim 150$  Myr.
- We find that the three galaxies (even the extremely metal-poor DDO 68) were already active at the oldest look-back time reached by our photometry ( $\sim 3$  Gyr) and possibly even before.
- They show rather continuous SFHs, although with the alternation of peaks and dips.
- The spiral, NGC 7793, has a more continuous SFH with respect to the two irregulars, and it exhibits the gradients observed also in the MW, suggesting an inside-out growth scenario.
- The average SFR follows the mass of the galaxy, with DDO 68 having the lowest one and NGC 7793 the highest one.

Finally, in Chapter 6 I embedded these results in a more general picture of star formation in nearby galaxies, in the attempt to a better understanding of the star formation process and its relation with galaxy formation and evolution.

- We did not find a simple model to describe the SFHs of the three analyzed galaxies. Only the SFH of NGC 4449 can be roughly approximated with an exponentially declining SFH with  $\tau = 5$  Gyr followed by a constant SFH, while the other two galaxies show a much more complicated evolution.
- NGC 4449 and NGC 7793 follow the SK relation between  $\Sigma_{\text{SFR}}$  and  $\Sigma_{\text{gas}}$ , while DDO 68 significantly deviates from the main relation, as found for other metal poor and low-surface-brightness galaxies.
- Interaction has a central role in regulating the SF activity even of the smallest systems.

Further investigation on this subject will be performed on the remaining LEGUS galaxies. Other than the comparison between different bands, a step forward in this kind of studies could be the combination of CMD-based SFHs and chemical evolution models to better constrain the metallicity of the analyzed galaxies. Moreover, it may be worth including different morphological types such as early-type spirals or ultra faint dwarfs.

# ACKNOWLEDGEMENTS

---

*Any work is hardly the effort of one person only. Luckily, I have met many people along the path that brought me here, who helped me in many different ways.*

*This is my chance to thank them.*

*Difficilmente un lavoro viene dall'impegno di una sola persona. Per mia fortuna, ho incontrato molte persone nel cammino che mi ha portato fin qui, che mi hanno aiutato in vari modi. Questa è la mia occasione per ringraziarle.*

First of all, Monica, thank you for reading (many times!) every single word of this thesis, for the respect and affection you always showed me, for being the perfect combination of authority and humanity that a supervisor should be.

Michele, I don't even know where to start. You are to me a mentor, a colleague, a friend, almost a brother, and the moments we shared both in work and personal life made these three years not only challenging and interesting, but also funny. Thank you for being there *literally* whenever I needed you, for listening even when you pretended not to, for being so annoying but so profoundly kind and talented. If there is one certainty in my scientific path, is that I can always count on you.

Francesca, thank you for taking me through the first steps of my PhD, with the great patience that characterizes you.

Alessandra, thank you for your help both in my work and in my days at STScI, for being a landmark in a land I didn't know, for your friendly and chatty attitude.

A special thanks to the Space Telescope Science Institute, for the past and future possibilities that were given to me, for being such an incredible and exciting environment to work.

Thanks to the whole LEGUS team, in particular to Daniela and Janice, for all the work in coordinating so many different people, for always listening to each one of us, for letting us feel as we were part of something bigger.

To Baltimore, for being a real city, with its pros and cons, and especially for giving me amazing friends. Camilla, I can't wait to see in which crazy situations we are going to end up, thank you for your help and your friendship, it is one of the reasons why I'm glad to come back.

Un ringraziamento particolare a tutti i miei maestri, professori, insegnanti, perché una grandissima parte del merito della mia formazione è vostra. Maestra Antonietta, prof. Malavolta, prof. Giuliani e prof. Bonifazi, grazie per avermi dato le basi di quell'incredibile linguaggio che è la matematica, per avermi fatto capire il suo alfabeto e le sue intime connessioni con la scienza, per aver sempre alimentato quella curiosità che tuttora mi spinge a continuare. Prof. Agostini, grazie per i tre anni in

cui hai letteralmente formato la mia mente, per avermi trasmesso la passione per la grammatica e la rigosità della logica, per essere stata un esempio e un punto di riferimento. Prof. Castiglioni e prof. Moriconi, le vostre materie sono quelle che rimpiango di più di avere abbandonato nei miei studi, sia per il loro splendore intrinseco che per il modo in cui me le avete tramesse. Prof. Moscardini, prof. Ciotti, prof. Fraternali, non solo siete stati degli ottimi insegnanti, avete anche lasciato qualcosa in più, lo stupore e la sete di conoscenza che sono alla base della ricerca.

Lungo un cammino non servono solo brave guide, ma anche i giusti compagni di viaggio... Lorenzo, Gabriele, Enrico, grazie per aver reso il mio primo anno di dottorato tra i più belli della mia vita, per le vostre menti brillanti, per le discussioni infinite su tutto lo scibile umano. Lucia, grazie per la tua incredibile dolcezza, per i tuoi occhioni da cerbiatto, per essere stata una splendida compagna d'ufficio. Bobo, ti ho visto la prima volta prendere appunti sull'ipad ad una lezione di cosmologia, ho pensato che te la tirassi perché non mi salutavi quando ci incontravamo in dipartimento, ho imparato che il tuo campo visivo è limitato, che il pecorino romano lo fanno a Macomer, che quando si brinda non si rischia di essere avvelenati, che sotto il tuo fare socievole e chiacchierone c'è un universo di introspezione, una fragilità ed una sensibilità che spesso nascondi, ma che ti rendono non solo una persona stupenda, ma anche un amico sincero; mi mancherai moltissimo, dalle critiche al fatto che mangio troppe verdure alle giornate passate a non lavorare in ufficio, e anche se fai finta di non ricordartelo, sai che ti voglio bene e che la distanza non cambierà il rapporto che abbiamo costruito. Matthew von Bauer, sei stato un'aggiunta preziosa alla nostra associazione a delinquere; grazie per il tuo punto di vista brillante e mai scontato, per le serate passate insieme, per le nostre somiglianze e differenze, per la grande sintonia che abbiamo trovato in così poco tempo. E comunque, C033 rulez! Ale, grazie per i tuoi sorrisi, per le tue chiacchiere, per la tua polemica, per il tuo essere così spumeggiante, per la tua indole socievole che contagia chiunque ti sia accanto. Marieddu, Lix, Giuls, Alb, Alfo, trovare la sintonia che abbiamo avuto essendo persone così diverse non è banale; grazie per aver reso il nostro posto di lavoro un ambiente così familiare e piacevole, un posto in cui voler tornare.

Vale, Meli, la nostra strada è iniziata all'università, ma continua e continuerà molto oltre. Grazie per la vostra amicizia sincera e spontanea, per esser sempre lì anche tra mille impegni, per la sicurezza che continueremo ad essere unite anche se le nostre strade si separeranno.

Bà, non è facile ringraziarti. Non perché ci siano pochi motivi per farlo, ma perché ce ne sono troppi. Grazie per le sfide continue che mi hai posto davanti, per i nostri battibecchi e le nostre bevute insieme, per il fatto che ti dai al 101% ad ogni tuo allievo, per questi 5 anni in cui non hai smesso di credere in me e nelle mie potenzialità. Grazie per le cose che mi hai insegnato e che hai lasciato che ti insegnassi, per questo nostro rapporto in continua evoluzione ed espansione, per le cose incredibili che certamente faremo ancora insieme. E naturalmente, grazie a voi, svoline e svolini, per i sorrisi, le ansie e i tantissimi momenti che abbiamo condiviso, perché ormai siete diventati una presenza costante nelle mie settimane, e mi mancherete incredibilmente.

A tutti i miei amici, sparsi per il mondo, sarete sempre con me in un modo o nell'altro. To my friends, all around the world, you will be here with me, always.

Mamma, papà, rospo, questa tesi è dedicata a voi perché senza di voi non sarei qui. Non solo in senso letterale, o materiale, ma anche e soprattutto per tutto quello che mi avete insegnato in questi quasi 27 anni, amore, sincerità, passione, libertà, perseveranza, coraggio. Avete sempre creduto in me, ed io in voi, plasmando ed incoraggiando la mia voglia di sapere e le mie attitudini e passioni. Il mio pensiero felice siamo noi, il 24 dicembre, davanti ad un albero di Natale.

Cri, Fra, siete sempre stati i miei eroi, le persone che aspettavo con ansia di rivedere Natale dopo Natale, festa dopo festa. Continuate ad esserlo in modi e per motivi sempre più profondi e complessi, man mano che cresciamo insieme. Il coraggio e l'energia che mettete nell'affrontare la vita hanno qualcosa di trascendente. Siete stati e sarete sempre per me un'ispirazione e un esempio. Così diversi, ma così uguali.

Alla mia famiglia, grazie perché mi ricordate sempre che la pazzia e il genio vanno di pari passo.

Annucchia, Ut, Fra, Vissi, non so per quale incredibile congiunzione cosmica ci siamo incontrate, so solo che mi avete dato così tanto che i miei ringraziamenti non basteranno mai. Sopra ogni cosa, mi avete mostrato che l'amicizia non conosce distanze o confini, non viene scalfita dal tempo che passa né dalle esperienze che cambiano. Siete una presenza costante anche quando non me ne rendo conto, siete la forza che mi da sicurezza in ogni momento, siete una parte di me. Spero che ricordiate sempre che persone incredibili siete, e soprattutto quanto vi voglio bene.

Matte. 7 anni sono più di quanto avrei mai pensato che qualcuno potesse sopportarmi e che io potessi sopportare qualcuno. Hai cambiato la mia visione della vita, anche se non lo credi hai allargato i miei orizzonti a possibilità che non avevo mai considerato, mi hai tenuto per mano davanti a tutti gli ostacoli di questo lungo cammino. Come mi disse una volta il prof. di filosofia, *la vita, come la danza, è un equilibrio continuamente perso e ritrovato*. E so che, come in passato, continueremo a perderlo e a ritrovarlo, perché questo è quello che ci fa crescere e migliorare. Nonostante la vertigine iniziale. Nonostante il senso di smarrimento. Nonostante le nostre paure. Grazie, perché ci sei, e so che ce la faremo, insieme.

Bologna, ovvero quasi un terzo della mia vita. Sei stata la prima casa che ho scelto, la prima esperienza di libertà e indipendenza. Mi mancherai come una necessità, mi mancherà la tua storia, scritta in miliardi di mattoncini rossi, mi mancheranno le tue strade, i tuoi odori, la vita che offri a chi ti abita, le persone che mi hai fatto incontrare, le possibilità che mi hai dato in questi otto anni. Grazie.



# BIBLIOGRAPHY

---

- Aloisi, A. et al. (2007). "I Zw 18 Revisited with HST ACS and Cepheids: New Distance and Age". In: *ApJ* 667, pp. L151–L154. DOI: [10.1086/522368](https://doi.org/10.1086/522368). arXiv: [0707.2371](https://arxiv.org/abs/0707.2371).
- Anderson, J. and L. R. Bedin (2010). "An Empirical Pixel-Based Correction for Imperfect CTE. I. HST's Advanced Camera for Surveys". In: *PASP* 122, pp. 1035–1064. DOI: [10.1086/656399](https://doi.org/10.1086/656399). arXiv: [1007.3987](https://arxiv.org/abs/1007.3987) [[astro-ph.IM](https://arxiv.org/abs/1007.3987)].
- Angeretti, L. et al. (2005). "The Complex Star Formation History of NGC 1569". In: *AJ* 129, pp. 2203–2216. DOI: [10.1086/429677](https://doi.org/10.1086/429677). eprint: [astro-ph/0504281](https://arxiv.org/abs/astro-ph/0504281).
- Annibali, F. et al. (2003). "The Star Formation History of NGC 1705: A Poststarburst Galaxy on the Verge of Activity". In: *AJ* 126, pp. 2752–2773. DOI: [10.1086/379556](https://doi.org/10.1086/379556). eprint: [astro-ph/0309265](https://arxiv.org/abs/astro-ph/0309265).
- Annibali, F. et al. (2008). "Starbursts in the Local Universe: New Hubble Space Telescope Advanced Camera for Surveys Observations of the Irregular Galaxy NGC 4449". In: *AJ* 135, pp. 1900–1916. DOI: [10.1088/0004-6256/135/5/1900](https://doi.org/10.1088/0004-6256/135/5/1900).
- Annibali, F. et al. (2009). "Young Stellar Populations and Star Clusters in NGC 1705". In: *AJ* 138, pp. 169–183. DOI: [10.1088/0004-6256/138/1/169](https://doi.org/10.1088/0004-6256/138/1/169). arXiv: [0904.3257](https://arxiv.org/abs/0904.3257).
- Annibali, F. et al. (2011). "The Cluster Population of the Irregular Galaxy NGC 4449 as Seen by the Hubble Advanced Camera for Surveys". In: *AJ* 142, 129, p. 129. DOI: [10.1088/0004-6256/142/4/129](https://doi.org/10.1088/0004-6256/142/4/129). arXiv: [1108.0694](https://arxiv.org/abs/1108.0694).
- Annibali, F. et al. (2012). "Cluster 77 in NGC 4449: The Nucleus of a Satellite Galaxy Being Transformed into a Globular Cluster?" In: *ApJ* 745, L1, p. L1. DOI: [10.1088/2041-8205/745/1/L1](https://doi.org/10.1088/2041-8205/745/1/L1). arXiv: [1201.0811](https://arxiv.org/abs/1201.0811) [[astro-ph.SR](https://arxiv.org/abs/1201.0811)].
- Annibali, F. et al. (2013). "The Star Formation History of the Very Metal-poor Blue Compact Dwarf I Zw 18 from HST/ACS Data". In: *AJ* 146, 144, p. 144. DOI: [10.1088/0004-6256/146/6/144](https://doi.org/10.1088/0004-6256/146/6/144). arXiv: [1303.3909](https://arxiv.org/abs/1303.3909).
- Annibali, F. et al. (2016). "DDO 68: A Flea with Smaller Fleas that on Him Prey". In: *ApJ* 826, L27, p. L27. DOI: [10.3847/2041-8205/826/2/L27](https://doi.org/10.3847/2041-8205/826/2/L27). arXiv: [1607.02628](https://arxiv.org/abs/1607.02628).
- Annibali, F. et al. (2017). "Planetary Nebulae and H ii Regions in the Starburst Irregular Galaxy NGC 4449 from LBT MODS Data". In: *ApJ* 843, 20, p. 20. DOI: [10.3847/1538-4357/aa7678](https://doi.org/10.3847/1538-4357/aa7678). arXiv: [1706.02108](https://arxiv.org/abs/1706.02108).
- Aoyama, S. et al. (2017). "Galaxy simulation with dust formation and destruction". In: *MNRAS* 466, pp. 105–121. DOI: [10.1093/mnras/stw3061](https://doi.org/10.1093/mnras/stw3061). arXiv: [1609.07547](https://arxiv.org/abs/1609.07547).
- Aparicio, A. and C. Gallart (2004). "IAC-STAR: A Code for Synthetic Color-Magnitude Diagram Computation". In: *AJ* 128, pp. 1465–1477. DOI: [10.1086/382836](https://doi.org/10.1086/382836). eprint: [astro-ph/0407589](https://arxiv.org/abs/astro-ph/0407589).

- Aparicio, A. and S. L. Hidalgo (2009). "IAC-pop: Finding the Star Formation History of Resolved Galaxies". In: *AJ* 138, pp. 558–567. DOI: [10.1088/0004-6256/138/2/558](https://doi.org/10.1088/0004-6256/138/2/558). arXiv: [0906.0712](https://arxiv.org/abs/0906.0712).
- Armus, L., T. Heckman, and G. Miley (1987). "Multicolor optical imaging of powerful far-infrared galaxies - More evidence for a link between galaxy mergers and far-infrared emission". In: *AJ* 94, pp. 831–846. DOI: [10.1086/114517](https://doi.org/10.1086/114517).
- Azzollini, R., I. Trujillo, and J. E. Beckman (2008). "Cosmic Evolution of Stellar Disk Truncations: From  $z \sim 1$  to the Local Universe". In: *ApJ* 684, 1026–1047, pp. 1026–1047. DOI: [10.1086/590142](https://doi.org/10.1086/590142). arXiv: [0805.2259](https://arxiv.org/abs/0805.2259).
- Barnes, J. E. and L. E. Hernquist (1991). "Fueling starburst galaxies with gas-rich mergers". In: *ApJ* 370, pp. L65–L68. DOI: [10.1086/185978](https://doi.org/10.1086/185978).
- Bellazzini, M. et al. (2004). "The calibration of the RGB Tip as a Standard Candle. Extension to Near Infrared colors and higher metallicity". In: *A&A* 424, pp. 199–211. DOI: [10.1051/0004-6361:20035910](https://doi.org/10.1051/0004-6361:20035910). eprint: [astro-ph/0404572](https://arxiv.org/abs/astro-ph/0404572).
- Bellazzini, M. et al. (2013). "Dwarfs walking in a row. The filamentary nature of the NGC 3109 association". In: *A&A* 559, L11, p. L11. DOI: [10.1051/0004-6361/201322744](https://doi.org/10.1051/0004-6361/201322744). arXiv: [1310.6365](https://arxiv.org/abs/1310.6365).
- Belokurov, V. et al. (2007). "Cats and Dogs, Hair and a Hero: A Quintet of New Milky Way Companions". In: *ApJ* 654, pp. 897–906. DOI: [10.1086/509718](https://doi.org/10.1086/509718). eprint: [astro-ph/0608448](https://arxiv.org/abs/astro-ph/0608448).
- Belokurov, V. et al. (2010). "Big Fish, Little Fish: Two New Ultra-faint Satellites of the Milky Way". In: *ApJ* 712, pp. L103–L106. DOI: [10.1088/2041-8205/712/1/L103](https://doi.org/10.1088/2041-8205/712/1/L103). arXiv: [1002.0504](https://arxiv.org/abs/1002.0504).
- Berg, D. A. et al. (2012). "Direct Oxygen Abundances for Low-luminosity LVL Galaxies". In: *ApJ* 754, 98, p. 98. DOI: [10.1088/0004-637X/754/2/98](https://doi.org/10.1088/0004-637X/754/2/98). arXiv: [1205.6782](https://arxiv.org/abs/1205.6782).
- Bergemann, M. et al. (2014). "The Gaia-ESO Survey: radial metallicity gradients and age-metallicity relation of stars in the Milky Way disk". In: *A&A* 565, A89, A89. DOI: [10.1051/0004-6361/201423456](https://doi.org/10.1051/0004-6361/201423456). arXiv: [1401.4437](https://arxiv.org/abs/1401.4437).
- Bibby, J. L. and P. A. Crowther (2010). "A Very Large Telescope imaging and spectroscopic survey of the Wolf-Rayet population in NGC7793". In: *MNRAS* 405, pp. 2737–2753. DOI: [10.1111/j.1365-2966.2010.16659.x](https://doi.org/10.1111/j.1365-2966.2010.16659.x). arXiv: [1004.1549](https://arxiv.org/abs/1004.1549) [[astro-ph](https://arxiv.org/abs/astro-ph).SR].
- Blanton, M. R. et al. (2001). "The Luminosity Function of Galaxies in SDSS Commissioning Data". In: *AJ* 121, pp. 2358–2380. DOI: [10.1086/320405](https://doi.org/10.1086/320405). eprint: [astro-ph/0012085](https://arxiv.org/abs/astro-ph/0012085).
- Bohlin, R. C. (2012). *Flux Calibration of the ACS CCD Cameras IV. Absolute Fluxes*. Tech. rep.
- Boyer, M. L. et al. (2009). "A Spitzer Study of Asymptotic Giant Branch Stars. III. Dust Production and Gas Return in Local Group Dwarf Irregular Galaxies". In: *ApJ* 697, pp. 1993–2014. DOI: [10.1088/0004-637X/697/2/1993](https://doi.org/10.1088/0004-637X/697/2/1993). arXiv: [0903.3871](https://arxiv.org/abs/0903.3871) [[astro-ph](https://arxiv.org/abs/astro-ph).GA].
- Bressan, A. et al. (2012). "PARSEC: stellar tracks and isochrones with the PAdova and TRieste Stellar Evolution Code". In: *MNRAS* 427, pp. 127–145. DOI: [10.1111/j.1365-2966.2012.21948.x](https://doi.org/10.1111/j.1365-2966.2012.21948.x). arXiv: [1208.4498](https://arxiv.org/abs/1208.4498) [[astro-ph](https://arxiv.org/abs/astro-ph).SR].
- Bressan, A. et al. (2015). "Uncertainties in Stellar Evolution Models: Convective Overshoot". In: *Asteroseismology of Stellar Populations in the Milky Way*. Ed. by

- A. Miglio et al. Vol. 39. *Astrophysics and Space Science Proceedings*, p. 25. DOI: [10.1007/978-3-319-10993-0\\_3](https://doi.org/10.1007/978-3-319-10993-0_3). arXiv: [1409.2268](https://arxiv.org/abs/1409.2268) [astro-ph.SR].
- Brinchmann, J. et al. (2004). "The physical properties of star-forming galaxies in the low-redshift Universe". In: *MNRAS* 351, pp. 1151–1179. DOI: [10.1111/j.1365-2966.2004.07881.x](https://doi.org/10.1111/j.1365-2966.2004.07881.x). eprint: [astro-ph/0311060](https://arxiv.org/abs/astro-ph/0311060).
- Brown, T. M. et al. (2014). "The Quenching of the Ultra-faint Dwarf Galaxies in the Reionization Era". In: *ApJ* 796, 91, p. 91. DOI: [10.1088/0004-637X/796/2/91](https://doi.org/10.1088/0004-637X/796/2/91). arXiv: [1410.0681](https://arxiv.org/abs/1410.0681).
- Caffau, E. et al. (2008). "The photospheric solar oxygen project. I. Abundance analysis of atomic lines and influence of atmospheric models". In: *A&A* 488, pp. 1031–1046. DOI: [10.1051/0004-6361:200809885](https://doi.org/10.1051/0004-6361:200809885). arXiv: [0805.4398](https://arxiv.org/abs/0805.4398).
- Calzetti, D. (2001). "The Dust Opacity of Star-forming Galaxies". In: *PASP* 113, pp. 1449–1485. DOI: [10.1086/324269](https://doi.org/10.1086/324269). eprint: [astro-ph/0109035](https://arxiv.org/abs/astro-ph/0109035).
- Calzetti, D. et al. (2015). "Legacy Extragalactic UV Survey (LEGUS) With the Hubble Space Telescope. I. Survey Description". In: *AJ* 149, 51, p. 51. DOI: [10.1088/0004-6256/149/2/51](https://doi.org/10.1088/0004-6256/149/2/51). arXiv: [1410.7456](https://arxiv.org/abs/1410.7456).
- Cannon, J. M. et al. (2014). "Discovery of a Gas-rich Companion to the Extremely Metal-poor Galaxy DDO 68". In: *ApJ* 787, L1, p. L1. DOI: [10.1088/2041-8205/787/1/L1](https://doi.org/10.1088/2041-8205/787/1/L1). arXiv: [1404.3540](https://arxiv.org/abs/1404.3540).
- Carignan, C. and D. Puche (1990). "H I studies of the Sculptor group galaxies. II - NGC 7793". In: *AJ* 100, pp. 394–402. DOI: [10.1086/115523](https://doi.org/10.1086/115523).
- Cash, W. (1979). "Parameter estimation in astronomy through application of the likelihood ratio". In: *ApJ* 228, pp. 939–947. DOI: [10.1086/156922](https://doi.org/10.1086/156922).
- Cazaux, S. and M. Spaans (2009). "HD and H<sub>2</sub> formation in low-metallicity dusty gas clouds at high redshift". In: *A&A* 496, pp. 365–374. DOI: [10.1051/0004-6361:200811302](https://doi.org/10.1051/0004-6361:200811302). arXiv: [0901.0514](https://arxiv.org/abs/0901.0514) [astro-ph.CO].
- Choi, J. et al. (2016). "Mesa Isochrones and Stellar Tracks (MIST). I. Solar-scaled Models". In: *ApJ* 823, 102, p. 102. DOI: [10.3847/0004-637X/823/2/102](https://doi.org/10.3847/0004-637X/823/2/102). arXiv: [1604.08592](https://arxiv.org/abs/1604.08592) [astro-ph.SR].
- Cignoni, M. and M. Tosi (2010). "Star Formation Histories of Dwarf Galaxies from the Colour-Magnitude Diagrams of Their Resolved Stellar Populations". In: *Advances in Astronomy 2010*, 158568, p. 158568. DOI: [10.1155/2010/158568](https://doi.org/10.1155/2010/158568). arXiv: [0909.4234](https://arxiv.org/abs/0909.4234).
- Cignoni, M. et al. (2010). "Pre-main-sequence Turn-On as a Chronometer for Young Clusters: NGC 346 as a Benchmark". In: *ApJ* 712, pp. L63–L68. DOI: [10.1088/2041-8205/712/1/L63](https://doi.org/10.1088/2041-8205/712/1/L63). arXiv: [1001.4442](https://arxiv.org/abs/1001.4442) [astro-ph.SR].
- Cignoni, M. et al. (2012). "Star Formation History in Two Fields of the Small Magellanic Cloud Bar". In: *ApJ* 754, 130, p. 130. DOI: [10.1088/0004-637X/754/2/130](https://doi.org/10.1088/0004-637X/754/2/130). arXiv: [1206.0733](https://arxiv.org/abs/1206.0733).
- (2013). "Mean Age Gradient and Asymmetry in the Star Formation History of the Small Magellanic Cloud". In: *ApJ* 775, 83, p. 83. DOI: [10.1088/0004-637X/775/2/83](https://doi.org/10.1088/0004-637X/775/2/83). arXiv: [1308.1409](https://arxiv.org/abs/1308.1409).
- Cignoni, M. et al. (2015). "Hubble Tarantula Treasury Project. II. The Star-formation History of the Starburst Region NGC 2070 in 30 Doradus". In: *ApJ* 811, 76, p. 76. DOI: [10.1088/0004-637X/811/2/76](https://doi.org/10.1088/0004-637X/811/2/76).
- Cignoni, M. et al. (2016). "Hubble Tarantula Treasury Project V. The Star Cluster Hodge 301: The Old Face of 30 Doradus". In: *ApJ* 833, 154, p. 154. DOI: [10.3847/1538-4357/833/2/154](https://doi.org/10.3847/1538-4357/833/2/154). arXiv: [1610.06180](https://arxiv.org/abs/1610.06180) [astro-ph.SR].

- Cioni, M.-R. L. et al. (2000). “The tip of the red giant branch and distance of the Magellanic Clouds: results from the DENIS survey”. In: *A&A* 359, pp. 601–614. eprint: [astro-ph/0003223](#).
- Cole, A. A. et al. (2007). “Leo A: A Late-blooming Survivor of the Epoch of Reionization in the Local Group”. In: *ApJ* 659, pp. L17–L20. DOI: [10.1086/516711](#). eprint: [astro-ph/0702646](#).
- Cole, A. A. et al. (2014). “Delayed Star Formation in Isolated Dwarf galaxies: Hubble Space Telescope Star Formation History of the Aquarius Dwarf Irregular”. In: *ApJ* 795, 54, p. 54. DOI: [10.1088/0004-637X/795/1/54](#). arXiv: [1409.1630](#).
- Dalcanton, J. J. et al. (2009). “The ACS Nearby Galaxy Survey Treasury”. In: *ApJS* 183, pp. 67–108. DOI: [10.1088/0067-0049/183/1/67](#). arXiv: [0905.3737](#) [[astro-ph.GA](#)].
- de Jong, R. S. (1996). “Near-infrared and optical broadband surface photometry of 86 face-on disk dominated galaxies. IV. Using color profiles to study stellar and dust content of galaxies.” In: *A&A* 313, pp. 377–395. eprint: [astro-ph/9604010](#).
- Deason, A., A. Wetzel, and S. Garrison-Kimmel (2014). “Satellite Dwarf Galaxies in a Hierarchical Universe: The Prevalence of Dwarf-Dwarf Major Mergers”. In: *ApJ* 794, 115, p. 115. DOI: [10.1088/0004-637X/794/2/115](#). arXiv: [1406.3344](#).
- Deason, A. J. et al. (2015). “Satellites of LMC-mass dwarfs: close friendships ruined by Milky Way mass haloes”. In: *MNRAS* 453, pp. 3568–3574. DOI: [10.1093/mnras/stv1939](#). arXiv: [1504.04372](#).
- Dicaire, I. et al. (2008). “Deep Fabry-Perot H $\alpha$  Observations of NGC 7793: A Very Extended H $\alpha$  Disk and A Truly Declining Rotation Curve”. In: *AJ* 135, pp. 2038–2047. DOI: [10.1088/0004-6256/135/6/2038](#). arXiv: [0802.2545](#).
- Dobbs, C. L. and J. E. Pringle (2010). “Age distributions of star clusters in spiral and barred galaxies as a test for theories of spiral structure”. In: *MNRAS* 409, pp. 396–404. DOI: [10.1111/j.1365-2966.2010.17323.x](#). arXiv: [1007.1399](#).
- Dobbs, C. L., J. E. Pringle, and T. Naylor (2014). “The dependence of stellar age distributions on giant molecular cloud environment”. In: *MNRAS* 437, pp. L31–L35. DOI: [10.1093/mnrasl/slt134](#). arXiv: [1309.6244](#).
- Dohm-Palmer, R. C. et al. (1997). “The Dwarf Irregular Galaxy Sextans A. II. Recent Star Formation History”. In: *AJ* 114, p. 2527. DOI: [10.1086/118665](#).
- Dolphin, A. (2016). *DOLPHOT: Stellar photometry*. Astrophysics Source Code Library. ascl: [1608.013](#).
- Dolphin, A. E. (2002). “Numerical methods of star formation history measurement and applications to seven dwarf spheroidals”. In: *MNRAS* 332, pp. 91–108. DOI: [10.1046/j.1365-8711.2002.05271.x](#). eprint: [astro-ph/0112331](#).
- (2013). “On the Estimation of Random Uncertainties of Star Formation Histories”. In: *ApJ* 775, 76, p. 76. DOI: [10.1088/0004-637X/775/1/76](#). arXiv: [1308.1740](#) [[astro-ph.IM](#)].
- D’Onghia, E. and G. Lake (2008). “Small Dwarf Galaxies within Larger Dwarfs: Why Some Are Luminous while Most Go Dark”. In: *ApJ* 686, L61, p. L61. DOI: [10.1086/592995](#). arXiv: [0802.0001](#).
- Draine, B. T. (2003). “Interstellar Dust Grains”. In: *ARA&A* 41, pp. 241–289. DOI: [10.1146/annurev.astro.41.011802.094840](#). eprint: [astro-ph/0304489](#).
- Eden, D. J. et al. (2013). “Star formation in Galactic spiral arms and the interarm regions”. In: *MNRAS* 431, pp. 1587–1595. DOI: [10.1093/mnras/stt279](#). arXiv: [1302.2874](#).

- Edmunds, M. G. and B. E. J. Pagel (1984). "On the composition of H II regions in southern galaxies. III - NGC 2997 and 7793". In: MNRAS 211, pp. 507–519. DOI: [10.1093/mnras/211.3.507](https://doi.org/10.1093/mnras/211.3.507).
- El-Badry, K. et al. (2016). "Breathing FIRE: How Stellar Feedback Drives Radial Migration, Rapid Size Fluctuations, and Population Gradients in Low-mass Galaxies". In: ApJ 820, 131, p. 131. DOI: [10.3847/0004-637X/820/2/131](https://doi.org/10.3847/0004-637X/820/2/131). arXiv: [1512.01235](https://arxiv.org/abs/1512.01235).
- Ellison, S. L. et al. (2011). "Galaxy pairs in the Sloan Digital Sky Survey - IV. Interactions trigger active galactic nuclei". In: MNRAS 418, pp. 2043–2053. DOI: [10.1111/j.1365-2966.2011.19624.x](https://doi.org/10.1111/j.1365-2966.2011.19624.x). arXiv: [1108.2711](https://arxiv.org/abs/1108.2711).
- Ellison, S. L. et al. (2013). "Galaxy pairs in the Sloan Digital Sky Survey - VIII. The observational properties of post-merger galaxies". In: MNRAS 435, pp. 3627–3638. DOI: [10.1093/mnras/stt1562](https://doi.org/10.1093/mnras/stt1562). arXiv: [1308.3707](https://arxiv.org/abs/1308.3707).
- Elmegreen, B. G. and D. M. Elmegreen (1986). "Do density waves trigger star formation?" In: ApJ 311, pp. 554–562. DOI: [10.1086/164795](https://doi.org/10.1086/164795).
- Fagotto, F. et al. (1994). "Evolutionary sequences of stellar models with new radiative opacities. III. Z=0.0004 and Z=0.05". In: A&AS 104, pp. 365–376.
- Fakhouri, O., C.-P. Ma, and M. Boylan-Kolchin (2010). "The merger rates and mass assembly histories of dark matter haloes in the two Millennium simulations". In: MNRAS 406, pp. 2267–2278. DOI: [10.1111/j.1365-2966.2010.16859.x](https://doi.org/10.1111/j.1365-2966.2010.16859.x). arXiv: [1001.2304](https://arxiv.org/abs/1001.2304) [astro-ph.CO].
- Foyle, K. et al. (2010). "Arm and Interarm Star Formation in Spiral Galaxies". In: ApJ 725, pp. 534–541. DOI: [10.1088/0004-637X/725/1/534](https://doi.org/10.1088/0004-637X/725/1/534). arXiv: [1010.0678](https://arxiv.org/abs/1010.0678).
- Fruchter, A. S. et al. (2009). "Multidrizzle – New and Improved". In: *American Astronomical Society Meeting Abstracts #213*. Vol. 41. Bulletin of the American Astronomical Society, p. 467.02.
- Gallart, C. (2008). "The ACS LCID Project: Old Main Sequence Turnoff Photometry of Isolated Local Group Dwarf Galaxies". In: *Pathways Through an Eclectic Universe*. Ed. by J. H. Knapen, T. J. Mahoney, and A. Vazdekis. Vol. 390. Astronomical Society of the Pacific Conference Series, p. 278.
- Gallart, C., M. Zoccali, and A. Aparicio (2005). "The Adequacy of Stellar Evolution Models for the Interpretation of the Color-Magnitude Diagrams of Resolved Stellar Populations". In: ARA&A 43, pp. 387–434. DOI: [10.1146/annurev.astro.43.072103.150608](https://doi.org/10.1146/annurev.astro.43.072103.150608).
- Gallart, C. et al. (2015). "The ACS LCID Project: On the Origin of Dwarf Galaxy Types: A Manifestation of the Halo Assembly Bias?" In: ApJ 811, L18, p. L18. DOI: [10.1088/2041-8205/811/2/L18](https://doi.org/10.1088/2041-8205/811/2/L18). arXiv: [1507.08350](https://arxiv.org/abs/1507.08350).
- Gelatt, A. E., D. A. Hunter, and J. S. Gallagher (2001). "The Star Clusters in the Irregular Galaxy NGC 4449". In: PASP 113, pp. 142–153. DOI: [10.1086/318613](https://doi.org/10.1086/318613). eprint: [astro-ph/0010515](https://arxiv.org/abs/astro-ph/0010515).
- Gil de Paz, A. et al. (2007). "The GALEX Ultraviolet Atlas of Nearby Galaxies". In: ApJS 173, pp. 185–255. DOI: [10.1086/516636](https://doi.org/10.1086/516636). eprint: [astro-ph/0606440](https://arxiv.org/abs/astro-ph/0606440).
- Giovanelli, R. et al. (2013). "ALFALFA Discovery of the Nearby Gas-rich Dwarf Galaxy Leo P. I. HI Observations". In: AJ 146, 15, p. 15. DOI: [10.1088/0004-6256/146/1/15](https://doi.org/10.1088/0004-6256/146/1/15). arXiv: [1305.0272](https://arxiv.org/abs/1305.0272).
- Gottlöber, S. et al. (2003). "The structure of voids". In: MNRAS 344, pp. 715–724. DOI: [10.1046/j.1365-8711.2003.06850.x](https://doi.org/10.1046/j.1365-8711.2003.06850.x). eprint: [astro-ph/0305393](https://arxiv.org/abs/astro-ph/0305393).

- Gouliermis, D. A. et al. (2017). "Hierarchical star formation across the grand design spiral NGC1566". In: *ArXiv e-prints*. arXiv: 1702.06006.
- Greggio, L. et al. (1998). "The Resolved Stellar Population of the Poststarburst Galaxy NGC 1569". In: *ApJ* 504, pp. 725–742. DOI: 10.1086/306100. eprint: astro-ph/9803326.
- Grocholski, A. J. et al. (2012). "HST/ACS Photometry of Old Stars in NGC 1569: The Star Formation History of a nearby Starburst". In: *AJ* 143, 117, p. 117. DOI: 10.1088/0004-6256/143/5/117. arXiv: 1204.0989.
- Guo, Q. et al. (2010). "How do galaxies populate dark matter haloes?" In: *MNRAS* 404, pp. 1111–1120. DOI: 10.1111/j.1365-2966.2010.16341.x. arXiv: 0909.4305 [astro-ph.CO].
- Harris, J. and D. Zaritsky (2001). "A Method for Determining the Star Formation History of a Mixed Stellar Population". In: *ApJS* 136, pp. 25–40. DOI: 10.1086/321792. eprint: astro-ph/0104202.
- (2004). "The Star Formation History of the Small Magellanic Cloud". In: *AJ* 127, pp. 1531–1544. DOI: 10.1086/381953. eprint: astro-ph/0312100.
- Harris, J., D. Zaritsky, and I. Thompson (1997). "On the Distribution of Dust in the Large Magellanic Cloud". In: *AJ* 114, p. 1933. DOI: 10.1086/118615. eprint: astro-ph/9709043.
- Hernquist, L. (1989). "Tidal triggering of starbursts and nuclear activity in galaxies". In: *Nature* 340, pp. 687–691. DOI: 10.1038/340687a0.
- Hidalgo, S. L. et al. (2013). "The ACS LCID Project. IX. Imprints of the Early Universe in the Radial Variation of the Star Formation History of Dwarf Galaxies". In: *ApJ* 778, 103, p. 103. DOI: 10.1088/0004-637X/778/2/103. arXiv: 1309.6130.
- Hill, R. S. et al. (1994). "Star formation in NGC 4449: MAMA-detector UV imagery and Fabry-Perot Balmer-line imagery". In: *ApJ* 430, pp. 568–580. DOI: 10.1086/174431.
- Hoefl, M. et al. (2006). "Dwarf galaxies in voids: suppressing star formation with photoheating". In: *MNRAS* 371, pp. 401–414. DOI: 10.1111/j.1365-2966.2006.10678.x. eprint: astro-ph/0501304.
- Hunter, D. (1997). "Star Formation in Irregular Galaxies: A Review of Several Key Questions". In: *PASP* 109, pp. 937–950. DOI: 10.1086/133965.
- Hunter, D. A., H. van Woerden, and J. S. Gallagher (1999). "Neutral Hydrogen and Star Formation in the Irregular Galaxy NGC 4449". In: *AJ* 118, pp. 2184–2210. DOI: 10.1086/301096.
- Hunter, D. A. et al. (1998). "The Nature of the Extended H I Gas around NGC 4449: The Dr. Jekyll/Mr. Hyde of Irregular Galaxies". In: *ApJ* 495, pp. L47–L50. DOI: 10.1086/311213.
- Izotov, Y. I. and T. X. Thuan (1999). "Heavy-Element Abundances in Blue Compact Galaxies". In: *ApJ* 511, pp. 639–659. DOI: 10.1086/306708. eprint: astro-ph/9811387.
- (2002). "Hubble Space Telescope Observations of the Cometary Blue Compact Dwarf Galaxy UGC 4483: A Relatively Young Galaxy?" In: *ApJ* 567, pp. 875–891. DOI: 10.1086/338752. eprint: astro-ph/0111307.
- (2004). "Deep Hubble Space Telescope ACS Observations of I Zw 18: a Young Galaxy in Formation". In: *ApJ* 616, pp. 768–782. DOI: 10.1086/424990. eprint: astro-ph/0408391.

- (2009). “Luminous Blue Variable Stars in the two Extremely Metal-Deficient Blue Compact Dwarf Galaxies DDO 68 and PHL 293B”. In: *ApJ* 690, pp. 1797–1806. DOI: [10.1088/0004-637X/690/2/1797](https://doi.org/10.1088/0004-637X/690/2/1797). arXiv: [0809.3077](https://arxiv.org/abs/0809.3077).
- James, B. L. et al. (2015). “Uncovering blue diffuse dwarf galaxies”. In: *MNRAS* 448, pp. 2687–2703. DOI: [10.1093/mnras/stv175](https://doi.org/10.1093/mnras/stv175). arXiv: [1411.7371](https://arxiv.org/abs/1411.7371).
- Karczewski, O. Ł. et al. (2013). “A multiwavelength study of the Magellanic-type galaxy NGC 4449 - I. Modelling the spectral energy distribution, the ionization structure and the star formation history”. In: *MNRAS* 431, pp. 2493–2512. DOI: [10.1093/mnras/stt345](https://doi.org/10.1093/mnras/stt345). arXiv: [1302.5430](https://arxiv.org/abs/1302.5430) [[astro-ph.CO](https://arxiv.org/archive/astro-ph)].
- Kauffmann, G. (1996). “The age of elliptical galaxies and bulges in a merger model”. In: *MNRAS* 281, pp. 487–492. DOI: [10.1093/mnras/281.2.487](https://doi.org/10.1093/mnras/281.2.487). eprint: [astro-ph/9502096](https://arxiv.org/abs/astro-ph/9502096).
- Kennicutt, R. C. and N. J. Evans (2012). “Star Formation in the Milky Way and Nearby Galaxies”. In: *ARA&A* 50, pp. 531–608. DOI: [10.1146/annurev-astro-081811-125610](https://doi.org/10.1146/annurev-astro-081811-125610). arXiv: [1204.3552](https://arxiv.org/abs/1204.3552).
- Kennicutt Jr., R. C. (1998). “The Global Schmidt Law in Star-forming Galaxies”. In: *ApJ* 498, pp. 541–552. DOI: [10.1086/305588](https://doi.org/10.1086/305588). eprint: [astro-ph/9712213](https://arxiv.org/abs/astro-ph/9712213).
- Kim, H. et al. (2012). “The Resolved Stellar Population in 50 Regions of M83 from HST/WFC3 Early Release Science Observations”. In: *ApJ* 753, 26, p. 26. DOI: [10.1088/0004-637X/753/1/26](https://doi.org/10.1088/0004-637X/753/1/26). arXiv: [1204.6045](https://arxiv.org/abs/1204.6045).
- Kormendy, J. and R. Bender (2012). “A Revised Parallel-sequence Morphological Classification of Galaxies: Structure and Formation of S0 and Spheroidal Galaxies”. In: *ApJS* 198, 2, p. 2. DOI: [10.1088/0067-0049/198/1/2](https://doi.org/10.1088/0067-0049/198/1/2). arXiv: [1110.4384](https://arxiv.org/abs/1110.4384).
- Kroupa, P. (2001). “On the variation of the initial mass function”. In: *MNRAS* 322, pp. 231–246. DOI: [10.1046/j.1365-8711.2001.04022.x](https://doi.org/10.1046/j.1365-8711.2001.04022.x). eprint: [astro-ph/0009005](https://arxiv.org/abs/astro-ph/0009005).
- Larson, R. B. (1976). “Models for the formation of disc galaxies”. In: *MNRAS* 176, pp. 31–52. DOI: [10.1093/mnras/176.1.31](https://doi.org/10.1093/mnras/176.1.31).
- Lee, J. C. et al. (2009). “Dwarf Galaxy Starburst Statistics in the Local Volume”. In: *ApJ* 692, 1305–1320, pp. 1305–1320. DOI: [10.1088/0004-637X/692/2/1305](https://doi.org/10.1088/0004-637X/692/2/1305). arXiv: [0810.5132](https://arxiv.org/abs/0810.5132).
- Leitherer, C. et al. (1999). “Starburst99: Synthesis Models for Galaxies with Active Star Formation”. In: *ApJS* 123, pp. 3–40. DOI: [10.1086/313233](https://doi.org/10.1086/313233). eprint: [astro-ph/9902334](https://arxiv.org/abs/astro-ph/9902334).
- Lelli, F., F. Fraternali, and M. Verheijen (2014). “Evolution of dwarf galaxies: a dynamical perspective”. In: *A&A* 563, A27, A27. DOI: [10.1051/0004-6361/201322658](https://doi.org/10.1051/0004-6361/201322658). arXiv: [1311.4556](https://arxiv.org/abs/1311.4556) [[astro-ph.GA](https://arxiv.org/archive/astro-ph)].
- Lelli, F., M. Verheijen, and F. Fraternali (2014a). “Dynamics of starbursting dwarf galaxies. III. A H I study of 18 nearby objects”. In: *A&A* 566, A71, A71. DOI: [10.1051/0004-6361/201322657](https://doi.org/10.1051/0004-6361/201322657). arXiv: [1404.6252](https://arxiv.org/abs/1404.6252).
- (2014b). “The triggering of starbursts in low-mass galaxies”. In: *MNRAS* 445, pp. 1694–1712. DOI: [10.1093/mnras/stu1804](https://doi.org/10.1093/mnras/stu1804). arXiv: [1409.1239](https://arxiv.org/abs/1409.1239).
- Leroy, A. K. et al. (2008). “The Star Formation Efficiency in Nearby Galaxies: Measuring Where Gas Forms Stars Effectively”. In: *AJ* 136, pp. 2782–2845. DOI: [10.1088/0004-6256/136/6/2782](https://doi.org/10.1088/0004-6256/136/6/2782). arXiv: [0810.2556](https://arxiv.org/abs/0810.2556).

- Leroy, A. K. et al. (2011). “The CO-to-H<sub>2</sub> Conversion Factor from Infrared Dust Emission across the Local Group”. In: *ApJ* 737, 12, p. 12. DOI: [10.1088/0004-637X/737/1/12](https://doi.org/10.1088/0004-637X/737/1/12). arXiv: [1102.4618](https://arxiv.org/abs/1102.4618).
- Leroy, A. K. et al. (2013). “Molecular Gas and Star Formation in nearby Disk Galaxies”. In: *AJ* 146, 19, p. 19. DOI: [10.1088/0004-6256/146/2/19](https://doi.org/10.1088/0004-6256/146/2/19). arXiv: [1301.2328](https://arxiv.org/abs/1301.2328).
- Lewis, A. R. et al. (2015). “The Panchromatic Hubble Andromeda Treasury. XI. The Spatially Resolved Recent Star Formation History of M31”. In: *ApJ* 805, 183, p. 183. DOI: [10.1088/0004-637X/805/2/183](https://doi.org/10.1088/0004-637X/805/2/183). arXiv: [1504.03338](https://arxiv.org/abs/1504.03338).
- Li, Y.-S. and A. Helmi (2008). “Infall of substructures on to a Milky Way-like dark halo”. In: *MNRAS* 385, pp. 1365–1373. DOI: [10.1111/j.1365-2966.2008.12854.x](https://doi.org/10.1111/j.1365-2966.2008.12854.x). arXiv: [0711.2429](https://arxiv.org/abs/0711.2429).
- Marconi, G. et al. (1995). “Star formation in dwarf irregular galaxies NGC 6822”. In: *AJ* 109, pp. 173–199. DOI: [10.1086/117265](https://doi.org/10.1086/117265). eprint: [astro-ph/9409013](https://arxiv.org/abs/astro-ph/9409013).
- Marigo, P. et al. (2013). “Evolution of thermally pulsing asymptotic giant branch stars - I. The COLIBRI code”. In: *MNRAS* 434, pp. 488–526. DOI: [10.1093/mnras/stt1034](https://doi.org/10.1093/mnras/stt1034). arXiv: [1305.4485](https://arxiv.org/abs/1305.4485) [[astro-ph](https://arxiv.org/abs/astro-ph).SR].
- Marigo, P. et al. (2017). “A New Generation of PARSEC-COLIBRI Stellar Isochrones Including the TP-AGB Phase”. In: *ApJ* 835, 77, p. 77. DOI: [10.3847/1538-4357/835/1/77](https://doi.org/10.3847/1538-4357/835/1/77). arXiv: [1701.08510](https://arxiv.org/abs/1701.08510) [[astro-ph](https://arxiv.org/abs/astro-ph).SR].
- Martínez-Delgado, D. et al. (2012). “Dwarfs Gobbling Dwarfs: A Stellar Tidal Stream around NGC 4449 and Hierarchical Galaxy Formation on Small Scales”. In: *ApJ* 748, L24, p. L24. DOI: [10.1088/2041-8205/748/2/L24](https://doi.org/10.1088/2041-8205/748/2/L24). arXiv: [1112.2154](https://arxiv.org/abs/1112.2154).
- Mathis, J. S. (1990). “Interstellar dust and extinction”. In: *ARA&A* 28, pp. 37–70. DOI: [10.1146/annurev.aa.28.090190.000345](https://doi.org/10.1146/annurev.aa.28.090190.000345).
- Matteucci, F. and P. Francois (1989). “Galactic chemical evolution - Abundance gradients of individual elements”. In: *MNRAS* 239, pp. 885–904. DOI: [10.1093/mnras/239.3.885](https://doi.org/10.1093/mnras/239.3.885).
- McKinnon, R., P. Torrey, and M. Vogelsberger (2016). “Dust formation in Milky Way-like galaxies”. In: *MNRAS* 457, pp. 3775–3800. DOI: [10.1093/mnras/stw253](https://doi.org/10.1093/mnras/stw253). arXiv: [1505.04792](https://arxiv.org/abs/1505.04792).
- McQuinn, K. B. W. et al. (2010). “The Nature of Starbursts. I. The Star Formation Histories of Eighteen Nearby Starburst Dwarf Galaxies”. In: *ApJ* 721, pp. 297–317. DOI: [10.1088/0004-637X/721/1/297](https://doi.org/10.1088/0004-637X/721/1/297). arXiv: [1008.1589](https://arxiv.org/abs/1008.1589).
- McQuinn, K. B. W. et al. (2011). “Observational Constraints on Red and Blue Helium Burning Sequences”. In: *ApJ* 740, 48, p. 48. DOI: [10.1088/0004-637X/740/1/48](https://doi.org/10.1088/0004-637X/740/1/48). arXiv: [1108.1405](https://arxiv.org/abs/1108.1405).
- McQuinn, K. B. W. et al. (2012). “The Nature of Starbursts. III. The Spatial Distribution of Star Formation”. In: *ApJ* 759, 77, p. 77. DOI: [10.1088/0004-637X/759/1/77](https://doi.org/10.1088/0004-637X/759/1/77). arXiv: [1210.0552](https://arxiv.org/abs/1210.0552).
- McQuinn, K. B. W. et al. (2015). “Leo P: An Unquenched Very Low-mass Galaxy”. In: *ApJ* 812, 158, p. 158. DOI: [10.1088/0004-637X/812/2/158](https://doi.org/10.1088/0004-637X/812/2/158). arXiv: [1506.05495](https://arxiv.org/abs/1506.05495).
- Meynet, G. and A. Maeder (1997). “Stellar evolution with rotation. I. The computational method and the inhibiting effect of the  $\mu$ -gradient.” In: *A&A* 321, pp. 465–476.

- (2002). “Stellar evolution with rotation. VIII. Models at  $Z = 10^{-5}$  and CNO yields for early galactic evolution”. In: *A&A* 390, pp. 561–583. DOI: [10.1051/0004-6361:20020755](https://doi.org/10.1051/0004-6361:20020755). eprint: [astro-ph/0205370](https://arxiv.org/abs/astro-ph/0205370).
- Mighell, K. J. (1999). “Parameter Estimation in Astronomy with Poisson-distributed Data. I. The  $\chi^2_\gamma$  Statistic”. In: *ApJ* 518, pp. 380–393. DOI: [10.1086/307253](https://doi.org/10.1086/307253). eprint: [astro-ph/9903093](https://arxiv.org/abs/astro-ph/9903093).
- Mihos, J. C. and L. Hernquist (1994). “Ultraluminous starbursts in major mergers”. In: *ApJ* 431, pp. L9–L12. DOI: [10.1086/187460](https://doi.org/10.1086/187460).
- (1996). “Gasdynamics and Starbursts in Major Mergers”. In: *ApJ* 464, p. 641. DOI: [10.1086/177353](https://doi.org/10.1086/177353). eprint: [astro-ph/9512099](https://arxiv.org/abs/astro-ph/9512099).
- Monelli, M. et al. (2010). “The ACS LCID Project. III. The Star Formation History of the Cetus dSph Galaxy: A Post-reionization Fossil”. In: *ApJ* 720, pp. 1225–1245. DOI: [10.1088/0004-637X/720/2/1225](https://doi.org/10.1088/0004-637X/720/2/1225). arXiv: [1002.4300](https://arxiv.org/abs/1002.4300).
- Muñoz-Mateos, J. C. et al. (2007). “Specific Star Formation Rate Profiles in Nearby Spiral Galaxies: Quantifying the Inside-Out Formation of Disks”. In: *ApJ* 658, pp. 1006–1026. DOI: [10.1086/511812](https://doi.org/10.1086/511812). eprint: [astro-ph/0612017](https://arxiv.org/abs/astro-ph/0612017).
- Nipoti, C., P. Londrillo, and L. Ciotti (2003). “Galaxy merging, the fundamental plane of elliptical galaxies and the  $M_{BH}-\sigma_0$  relation”. In: *MNRAS* 342, pp. 501–512. DOI: [10.1046/j.1365-8711.2003.06554.x](https://doi.org/10.1046/j.1365-8711.2003.06554.x). eprint: [astro-ph/0302423](https://arxiv.org/abs/astro-ph/0302423).
- Noël, N. E. D. et al. (2009). “Old Main-Sequence Turnoff Photometry in the Small Magellanic Cloud. II. Star Formation History and its Spatial Gradients”. In: *ApJ* 705, pp. 1260–1274. DOI: [10.1088/0004-637X/705/2/1260](https://doi.org/10.1088/0004-637X/705/2/1260). arXiv: [0909.2873](https://arxiv.org/abs/0909.2873).
- Olsen, K. A. G. (1999). “Star Formation Histories from Hubble Space Telescope Color-Magnitude Diagrams of Six Fields of the Large Magellanic Cloud”. In: *AJ* 117, pp. 2244–2267. DOI: [10.1086/300854](https://doi.org/10.1086/300854). eprint: [astro-ph/9902031](https://arxiv.org/abs/astro-ph/9902031).
- Patton, D. R. et al. (2011). “Galaxy pairs in the Sloan Digital Sky Survey - III. Evidence of induced star formation from optical colours”. In: *MNRAS* 412, pp. 591–606. DOI: [10.1111/j.1365-2966.2010.17932.x](https://doi.org/10.1111/j.1365-2966.2010.17932.x). arXiv: [1010.5778](https://arxiv.org/abs/1010.5778).
- Patton, D. R. et al. (2013). “Galaxy pairs in the Sloan Digital Sky Survey - VI. The orbital extent of enhanced star formation in interacting galaxies”. In: *MNRAS* 433, pp. L59–L63. DOI: [10.1093/mnrasl/slt058](https://doi.org/10.1093/mnrasl/slt058). arXiv: [1305.1595](https://arxiv.org/abs/1305.1595).
- Peñarrubia, J. et al. (2009). “The Signature of Galactic Tides in Local Group Dwarf Spheroidals”. In: *ApJ* 698, pp. 222–232. DOI: [10.1088/0004-637X/698/1/222](https://doi.org/10.1088/0004-637X/698/1/222). arXiv: [0811.1579](https://arxiv.org/abs/0811.1579).
- Peebles, P. J. E. (2001). “The Void Phenomenon”. In: *ApJ* 557, pp. 495–504. DOI: [10.1086/322254](https://doi.org/10.1086/322254). eprint: [astro-ph/0101127](https://arxiv.org/abs/astro-ph/0101127).
- Pezzulli, G. et al. (2015). “The instantaneous radial growth rate of stellar discs”. In: *MNRAS* 451, pp. 2324–2336. DOI: [10.1093/mnras/stv1077](https://doi.org/10.1093/mnras/stv1077). arXiv: [1505.03544](https://arxiv.org/abs/1505.03544).
- Pohlen, M. and I. Trujillo (2006). “The structure of galactic disks. Studying late-type spiral galaxies using SDSS”. In: *A&A* 454, pp. 759–772. DOI: [10.1051/0004-6361:20064883](https://doi.org/10.1051/0004-6361:20064883). eprint: [astro-ph/0603682](https://arxiv.org/abs/astro-ph/0603682).
- Pustilnik, S. A., A. Y. Kniazev, and A. G. Pramskij (2005). “Study of DDO 68: nearest candidate for a young galaxy?” In: *A&A* 443, pp. 91–102. DOI: [10.1051/0004-6361:20053102](https://doi.org/10.1051/0004-6361:20053102). eprint: [astro-ph/0507658](https://arxiv.org/abs/astro-ph/0507658).

- Pustilnik, S. A. and A. L. Tepliakova (2011). "Study of galaxies in the Lynx-Cancer void - I. Sample description". In: *MNRAS* 415, pp. 1188–1201. DOI: [10.1111/j.1365-2966.2011.18733.x](https://doi.org/10.1111/j.1365-2966.2011.18733.x). arXiv: [1105.3034](https://arxiv.org/abs/1105.3034).
- Pustilnik, S. A., A. L. Tepliakova, and A. Y. Kniazev (2008). "Study of the galaxy DDO 68: New evidence for its youth". In: *Astronomy Letters* 34, pp. 457–467. DOI: [10.1134/S1063773708070049](https://doi.org/10.1134/S1063773708070049).
- Radburn-Smith, D. J. et al. (2011). "The GHOSTS Survey. I. Hubble Space Telescope Advanced Camera for Surveys Data". In: *ApJS* 195, 18, p. 18. DOI: [10.1088/0067-0049/195/2/18](https://doi.org/10.1088/0067-0049/195/2/18).
- Radburn-Smith, D. J. et al. (2012). "Outer-disk Populations in NGC 7793: Evidence for Stellar Radial Migration". In: *ApJ* 753, 138, p. 138. DOI: [10.1088/0004-637X/753/2/138](https://doi.org/10.1088/0004-637X/753/2/138). arXiv: [1206.1057](https://arxiv.org/abs/1206.1057).
- Reines, A. E., K. E. Johnson, and W. M. Goss (2008). "Emerging Massive Star Clusters Revealed: High-Resolution Imaging of NGC 4449 from the Radio to the Ultraviolet". In: *AJ* 135, pp. 2222–2239. DOI: [10.1088/0004-6256/135/6/2222](https://doi.org/10.1088/0004-6256/135/6/2222). arXiv: [0804.0005](https://arxiv.org/abs/0804.0005).
- Rich, R. M. et al. (2012). "A tidally distorted dwarf galaxy near NGC 4449". In: *Nature* 482, pp. 192–194. DOI: [10.1038/nature10837](https://doi.org/10.1038/nature10837). arXiv: [1202.2316](https://arxiv.org/abs/1202.2316).
- Roberts, W. W. (1969). "Large-Scale Shock Formation in Spiral Galaxies and its Implications on Star Formation". In: *ApJ* 158, p. 123. DOI: [10.1086/150177](https://doi.org/10.1086/150177).
- Robertson, B. E. and A. V. Kravtsov (2008). "Molecular Hydrogen and Global Star Formation Relations in Galaxies". In: *ApJ* 680, 1083–1111, pp. 1083–1111. DOI: [10.1086/587796](https://doi.org/10.1086/587796). arXiv: [0710.2102](https://arxiv.org/abs/0710.2102).
- Rojas, R. R. et al. (2004). "Photometric Properties of Void Galaxies in the Sloan Digital Sky Survey". In: *ApJ* 617, pp. 50–63. DOI: [10.1086/425225](https://doi.org/10.1086/425225). eprint: [astro-ph/0307274](https://arxiv.org/abs/astro-ph/0307274).
- (2005). "Spectroscopic Properties of Void Galaxies in the Sloan Digital Sky Survey". In: *ApJ* 624, pp. 571–585. DOI: [10.1086/428476](https://doi.org/10.1086/428476). eprint: [astro-ph/0409074](https://arxiv.org/abs/astro-ph/0409074).
- Rosenfield, P. et al. (2016). "Evolution of Thermally Pulsing Asymptotic Giant Branch Stars. V. Constraining the Mass Loss and Lifetimes of Intermediate-mass, Low-metallicity AGB Stars". In: *ApJ* 822, 73, p. 73. DOI: [10.3847/0004-637X/822/2/73](https://doi.org/10.3847/0004-637X/822/2/73). arXiv: [1603.05283](https://arxiv.org/abs/1603.05283) [[astro-ph](https://arxiv.org/abs/astro-ph).SR].
- Sacchi, E. et al. (2016). "Stellar Populations and Star Formation History of the Metal-poor Dwarf Galaxy DDO 68". In: *ApJ* 830, 3, p. 3. DOI: [10.3847/0004-637X/830/1/3](https://doi.org/10.3847/0004-637X/830/1/3). arXiv: [1604.06239](https://arxiv.org/abs/1604.06239).
- Salpeter, E. E. (1955). "The Luminosity Function and Stellar Evolution." In: *ApJ* 121, p. 161. DOI: [10.1086/145971](https://doi.org/10.1086/145971).
- Sanders, D. B. et al. (1988). "Ultraluminous infrared galaxies and the origin of quasars". In: *ApJ* 325, pp. 74–91. DOI: [10.1086/165983](https://doi.org/10.1086/165983).
- Schlafly, E. F. and D. P. Finkbeiner (2011). "Measuring Reddening with Sloan Digital Sky Survey Stellar Spectra and Recalibrating SFD". In: *ApJ* 737, 103, p. 103. DOI: [10.1088/0004-637X/737/2/103](https://doi.org/10.1088/0004-637X/737/2/103). arXiv: [1012.4804](https://arxiv.org/abs/1012.4804) [[astro-ph](https://arxiv.org/abs/astro-ph).GA].
- Schlegel, D. J., D. P. Finkbeiner, and M. Davis (1998). "Maps of Dust Infrared Emission for Use in Estimation of Reddening and Cosmic Microwave Background Radiation Foregrounds". In: *ApJ* 500, pp. 525–553. DOI: [10.1086/305772](https://doi.org/10.1086/305772). eprint: [astro-ph/9710327](https://arxiv.org/abs/astro-ph/9710327).

- Schmidt, M. (1959). "The Rate of Star Formation." In: *ApJ* 129, p. 243. DOI: [10.1086/146614](https://doi.org/10.1086/146614).
- (1963). "The Rate of Star Formation. II. The Rate of Formation of Stars of Different Mass." In: *ApJ* 137, p. 758. DOI: [10.1086/147553](https://doi.org/10.1086/147553).
- Schulte-Ladbeck, R. E. et al. (2002). "The Oldest Stars of the Extremely Metal-Poor Local Group Dwarf Irregular Galaxy Leo A". In: *AJ* 124, pp. 896–914. DOI: [10.1086/341611](https://doi.org/10.1086/341611). eprint: [astro-ph/0205052](https://arxiv.org/abs/astro-ph/0205052).
- Scudder, J. M. et al. (2012). "Galaxy pairs in the Sloan Digital Sky Survey - V. Tracing changes in star formation rate and metallicity out to separations of 80 kpc". In: *MNRAS* 426, pp. 549–565. DOI: [10.1111/j.1365-2966.2012.21749.x](https://doi.org/10.1111/j.1365-2966.2012.21749.x). arXiv: [1207.4791](https://arxiv.org/abs/1207.4791).
- Seigar, M. S. and P. A. James (2002). "A test of arm-induced star formation in spiral galaxies from near-infrared and H $\alpha$  imaging". In: *MNRAS* 337, pp. 1113–1117. DOI: [10.1046/j.1365-8711.2002.06007.x](https://doi.org/10.1046/j.1365-8711.2002.06007.x). eprint: [astro-ph/0208401](https://arxiv.org/abs/astro-ph/0208401).
- Sirianni, M. et al. (2005). "The Photometric Performance and Calibration of the Hubble Space Telescope Advanced Camera for Surveys". In: *PASP* 117, pp. 1049–1112. DOI: [10.1086/444553](https://doi.org/10.1086/444553). eprint: [astro-ph/0507614](https://arxiv.org/abs/astro-ph/0507614).
- Skillman, E. D. and R. C. Kennicutt Jr. (1993). "Spatially resolved optical and near-infrared spectroscopy of I ZW 18". In: *ApJ* 411, pp. 655–666. DOI: [10.1086/172868](https://doi.org/10.1086/172868).
- Skillman, E. D. et al. (2013). "ALFALFA Discovery of the nearby Gas-rich Dwarf Galaxy Leo P. III. An Extremely Metal Deficient Galaxy". In: *AJ* 146, 3, p. 3. DOI: [10.1088/0004-6256/146/1/3](https://doi.org/10.1088/0004-6256/146/1/3). arXiv: [1305.0277](https://arxiv.org/abs/1305.0277).
- Sokal, K. R. et al. (2015). "An Emerging Wolf-Rayet Massive Star Cluster in NGC 4449". In: *AJ* 149, 115, p. 115. DOI: [10.1088/0004-6256/149/3/115](https://doi.org/10.1088/0004-6256/149/3/115). arXiv: [1501.05313](https://arxiv.org/abs/1501.05313).
- Sommer-Larsen, J., M. Götz, and L. Portinari (2003). "Galaxy Formation: Cold Dark Matter, Feedback, and the Hubble Sequence". In: *ApJ* 596, pp. 47–66. DOI: [10.1086/377685](https://doi.org/10.1086/377685). eprint: [astro-ph/0204366](https://arxiv.org/abs/astro-ph/0204366).
- Stanghellini, L., L. Magrini, and V. Casasola (2015). "Gas-phase Oxygen Abundances and Radial Metallicity Gradients in the Two nearby Spiral Galaxies NGC 7793 and NGC 4945". In: *ApJ* 812, 39, p. 39. DOI: [10.1088/0004-637X/812/1/39](https://doi.org/10.1088/0004-637X/812/1/39). arXiv: [1508.02754](https://arxiv.org/abs/1508.02754).
- Starkenburger, T. K., A. Helmi, and L. V. Sales (2016). "Dark influences. III. Structural characterization of minor mergers of dwarf galaxies with dark satellites". In: *A&A* 595, A56, A56. DOI: [10.1051/0004-6361/201528066](https://doi.org/10.1051/0004-6361/201528066). arXiv: [1601.00020](https://arxiv.org/abs/1601.00020).
- Stetson, P. B. (1987). "DAOPHOT - A computer program for crowded-field stellar photometry". In: *PASP* 99, pp. 191–222. DOI: [10.1086/131977](https://doi.org/10.1086/131977).
- Stierwalt, S. et al. (2015). "TiNy Titans: The Role of Dwarf-Dwarf Interactions in Low-mass Galaxy Evolution". In: *ApJ* 805, 2, p. 2. DOI: [10.1088/0004-637X/805/1/2](https://doi.org/10.1088/0004-637X/805/1/2). arXiv: [1412.4796](https://arxiv.org/abs/1412.4796).
- Stierwalt, S. et al. (2017). "Direct evidence of hierarchical assembly at low masses from isolated dwarf galaxy groups". In: *Nature Astronomy* 1, 0025, p. 0025. DOI: [10.1038/s41550-016-0025](https://doi.org/10.1038/s41550-016-0025). arXiv: [1701.01731](https://arxiv.org/abs/1701.01731).
- Stil, J. M. and F. P. Israel (2002a). "Neutral hydrogen in dwarf galaxies. I. The spatial distribution of HI". In: *A&A* 389, pp. 29–41. DOI: [10.1051/0004-6361:20020352](https://doi.org/10.1051/0004-6361:20020352). eprint: [astro-ph/0203128](https://arxiv.org/abs/astro-ph/0203128).

- Stil, J. M. and F. P. Israel (2002b). "Neutral hydrogen in dwarf galaxies. II. The kinematics of HI". In: *A&A* 389, pp. 42–57. DOI: [10.1051/0004-6361:20020353](https://doi.org/10.1051/0004-6361:20020353). eprint: [astro-ph/0203133](https://arxiv.org/abs/astro-ph/0203133).
- Stinson, G. S. et al. (2007). "Breathing in Low-Mass Galaxies: A Study of Episodic Star Formation". In: *ApJ* 667, pp. 170–175. DOI: [10.1086/520504](https://doi.org/10.1086/520504). arXiv: [0705.4494](https://arxiv.org/abs/0705.4494).
- Strader, J., A. C. Seth, and N. Caldwell (2012). "Old Massive Globular Clusters and the Stellar Halo of the Dwarf Starburst Galaxy NGC 4449". In: *AJ* 143, 52, p. 52. DOI: [10.1088/0004-6256/143/2/52](https://doi.org/10.1088/0004-6256/143/2/52). arXiv: [1112.3958](https://arxiv.org/abs/1112.3958).
- Tang, J. et al. (2014). "New PARSEC evolutionary tracks of massive stars at low metallicity: testing canonical stellar evolution in nearby star-forming dwarf galaxies". In: *MNRAS* 445, pp. 4287–4305. DOI: [10.1093/mnras/stu2029](https://doi.org/10.1093/mnras/stu2029). arXiv: [1410.1745](https://arxiv.org/abs/1410.1745) [[astro-ph](https://arxiv.org/abs/astro-ph).SR].
- Theis, C. and S. Kohle (2001). "Multi-method-modeling of interacting galaxies. I. A unique scenario for NGC 4449?" In: *A&A* 370, pp. 365–383. DOI: [10.1051/0004-6361:20010198](https://doi.org/10.1051/0004-6361:20010198). eprint: [astro-ph/0104304](https://arxiv.org/abs/astro-ph/0104304).
- Tikhonov, N. A., O. A. Galazutdinova, and V. S. Lebedev (2014). "Stellar content of the metal-poor galaxy DDO 68". In: *Astronomy Letters* 40, pp. 1–10. DOI: [10.1134/S1063773714010058](https://doi.org/10.1134/S1063773714010058).
- Toloba, E. et al. (2016). "New Spectroscopic Technique Based on Coaddition of Surface Brightness Fluctuations: NGC 4449 and its Stellar Tidal Stream". In: *ApJ* 824, 35, p. 35. DOI: [10.3847/0004-637X/824/1/35](https://doi.org/10.3847/0004-637X/824/1/35). arXiv: [1605.03967](https://arxiv.org/abs/1605.03967).
- Tolstoy, E., V. Hill, and M. Tosi (2009). "Star-Formation Histories, Abundances, and Kinematics of Dwarf Galaxies in the Local Group". In: *ARA&A* 47, pp. 371–425. DOI: [10.1146/annurev-astro-082708-101650](https://doi.org/10.1146/annurev-astro-082708-101650). arXiv: [0904.4505](https://arxiv.org/abs/0904.4505) [[astro-ph](https://arxiv.org/abs/astro-ph).CO].
- Tolstoy, E. et al. (1998). "Wide Field Planetary Camera 2 Observations of Leo A: A Predominantly Young Galaxy within the Local Group". In: *AJ* 116, pp. 1244–1262. DOI: [10.1086/300515](https://doi.org/10.1086/300515). eprint: [astro-ph/9805268](https://arxiv.org/abs/astro-ph/9805268).
- Toomre, A. and J. Toomre (1972). "Galactic Bridges and Tails". In: *ApJ* 178, pp. 623–666. DOI: [10.1086/151823](https://doi.org/10.1086/151823).
- Torrey, P. et al. (2012). "The Metallicity Evolution of Interacting Galaxies". In: *ApJ* 746, 108, p. 108. DOI: [10.1088/0004-637X/746/1/108](https://doi.org/10.1088/0004-637X/746/1/108). arXiv: [1107.0001](https://arxiv.org/abs/1107.0001).
- Tosi, M. (2009). "Star formation histories of resolved galaxies". In: *The Ages of Stars*. Ed. by E. E. Mamajek, D. R. Soderblom, and R. F. G. Wyse. Vol. 258. IAU Symposium, pp. 61–72. DOI: [10.1017/S1743921309031718](https://doi.org/10.1017/S1743921309031718). arXiv: [0901.1090](https://arxiv.org/abs/0901.1090).
- Tosi, M. et al. (1991). "Star formation in dwarf irregular galaxies - Sextans B". In: *AJ* 102, pp. 951–974. DOI: [10.1086/115925](https://doi.org/10.1086/115925).
- Tully, R. B. et al. (2006). "Associations of Dwarf Galaxies". In: *AJ* 132, pp. 729–748. DOI: [10.1086/505466](https://doi.org/10.1086/505466). eprint: [astro-ph/0603380](https://arxiv.org/abs/astro-ph/0603380).
- Valdez-Gutiérrez, M. et al. (2002). "Unveiling the Kinematics and Dynamics of Ionized Gas in the Nearby Irregular Galaxy NGC 4449". In: *AJ* 124, pp. 3157–3178. DOI: [10.1086/344304](https://doi.org/10.1086/344304). eprint: [astro-ph/0208338](https://arxiv.org/abs/astro-ph/0208338).
- van den Bosch, F. C. (1998). "The Formation of Disk-Bulge-Halo Systems and the Origin of the Hubble Sequence". In: *ApJ* 507, pp. 601–614. DOI: [10.1086/306354](https://doi.org/10.1086/306354). eprint: [astro-ph/9805113](https://arxiv.org/abs/astro-ph/9805113).
- van Woerden, H., A. Bosma, and U. Mebold (1975). "Distribution and Motions of Neutral Hydrogen in the Giant Irregular Galaxy NGC 4449". In: *La Dynamique des galaxies spirales*. Ed. by L. Weliachew. Vol. 241, p. 483.

- Vincenzo, F. et al. (2016). “Lighting up stars in chemical evolution models: the CMD of Sculptor”. In: MNRAS 460, pp. 2238–2244. DOI: [10.1093/mnras/stw1145](https://doi.org/10.1093/mnras/stw1145). arXiv: [1605.03606](https://arxiv.org/abs/1605.03606).
- Vlajić, M., J. Bland-Hawthorn, and K. C. Freeman (2011). “The Structure and Metallicity Gradient in the Extreme Outer Disk of NGC 7793”. In: ApJ 732, 7, p. 7. DOI: [10.1088/0004-637X/732/1/7](https://doi.org/10.1088/0004-637X/732/1/7). arXiv: [1101.0607](https://arxiv.org/abs/1101.0607).
- Weisz, D. R. et al. (2008). “The Recent Star Formation Histories of M81 Group Dwarf Irregular Galaxies”. In: ApJ 689, 160–183, pp. 160–183. DOI: [10.1086/592323](https://doi.org/10.1086/592323). arXiv: [0809.5059](https://arxiv.org/abs/0809.5059).
- Weisz, D. R. et al. (2011). “The ACS Nearby Galaxy Survey Treasury. VIII. The Global Star Formation Histories of 60 Dwarf Galaxies in the Local Volume”. In: ApJ 739, 5, p. 5. DOI: [10.1088/0004-637X/739/1/5](https://doi.org/10.1088/0004-637X/739/1/5). arXiv: [1101.1093](https://arxiv.org/abs/1101.1093).
- Weisz, D. R. et al. (2013). “Comparing the ancient star formation histories of the Magellanic Clouds”. In: MNRAS 431, pp. 364–371. DOI: [10.1093/mnras/stt1165](https://doi.org/10.1093/mnras/stt1165). arXiv: [1301.7422](https://arxiv.org/abs/1301.7422).
- Weisz, D. R. et al. (2014). “The Star Formation Histories of Local Group Dwarf Galaxies. I. Hubble Space Telescope/Wide Field Planetary Camera 2 Observations”. In: ApJ 789, 147, p. 147. DOI: [10.1088/0004-637X/789/2/147](https://doi.org/10.1088/0004-637X/789/2/147). arXiv: [1404.7144](https://arxiv.org/abs/1404.7144).
- Wheeler, C. et al. (2015). “Sweating the small stuff: simulating dwarf galaxies, ultra-faint dwarf galaxies, and their own tiny satellites”. In: MNRAS 453, pp. 1305–1316. DOI: [10.1093/mnras/stv1691](https://doi.org/10.1093/mnras/stv1691). arXiv: [1504.02466](https://arxiv.org/abs/1504.02466).
- Williams, B. F. et al. (2014). “The Panchromatic Hubble Andromeda Treasury. X. Ultraviolet to Infrared Photometry of 117 Million Equidistant Stars”. In: ApJS 215, 9, p. 9. DOI: [10.1088/0067-0049/215/1/9](https://doi.org/10.1088/0067-0049/215/1/9). arXiv: [1409.0899](https://arxiv.org/abs/1409.0899).
- Woods, D. F. et al. (2010). “Triggered Star Formation in Galaxy Pairs at  $z = 0.08$ – $0.38$ ”. In: AJ 139, pp. 1857–1870. DOI: [10.1088/0004-6256/139/5/1857](https://doi.org/10.1088/0004-6256/139/5/1857). arXiv: [1002.0386](https://arxiv.org/abs/1002.0386).
- Wyder, T. K. et al. (2009). “The Star Formation Law at Low Surface Density”. In: ApJ 696, pp. 1834–1853. DOI: [10.1088/0004-637X/696/2/1834](https://doi.org/10.1088/0004-637X/696/2/1834). arXiv: [0903.3015](https://arxiv.org/abs/0903.3015) [astro-ph.CO].
- Zaritsky, D., J. Harris, and I. Thompson (1997). “A digital photometric survey of the magellanic clouds: First results from one million stars.” In: AJ 114, pp. 1002–1013. DOI: [10.1086/118531](https://doi.org/10.1086/118531). eprint: [astro-ph/9706206](https://arxiv.org/abs/astro-ph/9706206).